DOE/ER-0313/74
ORNL/TM-2023/3142

FUSION MATERIALS
SEMIANNUAL PROGRESS REPORT
FOR THE PERIOD ENDING

June 30, 2023

Prepared for
DOE Office of Fusion Energy Sciences
(AT 60 20 10 0)

DATE PUBLISHED: October 2023

Prepared by
OAK RIDGE NATIONAL LABORATORY
Oak Ridge, Tennessee 37831
Managed by
UT-Battelle, LLC
For the
U.S. DEPARTMENT OF ENERGY

FOREWORD

This is the seventy-fourth in a series of semiannual technical progress reports on fusion materials science activity supported by the Fusion Energy Sciences Program of the U.S. Department of Energy. It covers the period ending June 30, 2023. This report focuses on research addressing the effects on materials properties and performance of exposure to the neutronic, thermal and chemical environments anticipated in the chambers of fusion experiments and energy systems. This research is a major element of the national effort to establish the materials knowledge base for an economically and environmentally attractive fusion energy source. Research activities on issues related to the interaction of materials with plasmas are reported separately.

The results reported are the products of a national effort involving a number of national laboratories and universities. A large fraction of this work, particularly in relation to fission reactor irradiations, is carried out collaboratively with partners in Japan, Russia, and the European Union. The purpose of this series of reports is to provide a working technical record for the use of program participants, and to provide a means of communicating the efforts of fusion materials scientists to the broader fusion community, both nationally and worldwide.

This report has been compiled by Stephanie Melton, Oak Ridge National Laboratory. Her efforts, and the efforts of the many persons who made technical contributions, are gratefully acknowledged.

Guinevere Shaw
Research Division
Office of Fusion Energy Sciences

TABLE OF CONTENTS

TABLE OF CONTENTS

TABLE OF CONTENTS

1. FERRITIC/MARTENSITIC STEEL DEVELOPMENT

1.1 CHARPY IMPACT TESTING OF CNA STEELS AFTER DIFFERENT TEMPERING HEAT TREATMENTS

—X. Chen, W. Zhong, Y. Yang (Oak Ridge National Laboratory)

OBJECTIVE

The Reduced-Activation Ferritic-Martensitic (RAFM) steels are essential candidate materials for first-wall/blanket applications of fusion energy. To overcome the limitations of the current benchmark RAFM steels, Castable Nanostructured Alloys (CNAs) have been developed and examined in laboratory-scale heats, which demonstrated improvements in various properties that are critical to fusion applications. To establish a US-RAFM steel based on the carbide-strengthened CNAs, it is vital to perform property and microstructure evaluation of industry-scale heats of CNAs and benchmark their performance against laboratory-scale CNAs and current RAFM steels, e.g., F82H and EUROFER97. In this task, we focus on the Charpy impact testing of CNA steels after different tempering heat treatments. We observed a relatively high and unfavorable ductile-to-brittle transition temperature (DBTT) of 2°C for a CNA rod material after a final tempering treatment at 710°C. Increasing the tempering treatment temperatures to 730-750°C reduced the DBTT and maintained the Vickers hardness values within the specification for the CNA rod.

SUMMARY

One CNA rod material after additional heat treatment (normalization at 1180°C for 10min -> water quench -> tempering at 710°C for 60min -> air cooling) was used for Charpy and miniCT specimen machined as shown in Figure 1. Standard full size Charpy specimens with a dimension of 55 x 10 x 10 mm^3 were machined in the LC orientation. Charpy impact testing was performed with an Instron Charpy frame equipment with an MPM in-situ heating/cooling stage as shown in Figure 2.

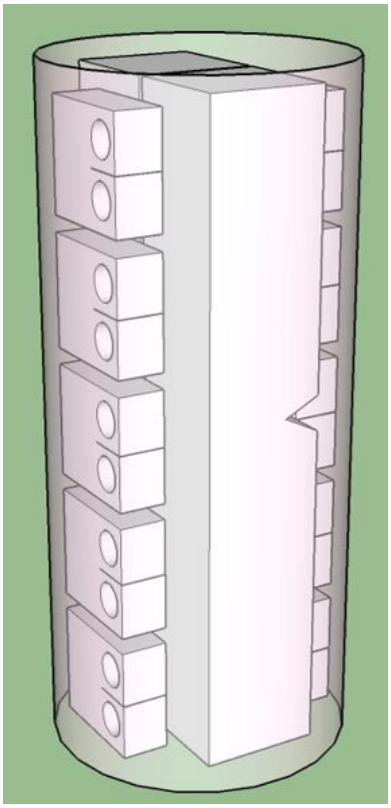

Figure 1. Schemati of Charpy and miniCT machining from a CNA rod sample.

Figure 2. Instron Charpy impact frame equipped with an MPM in-situ heating/cooling stage.

The Charpy impact energy results are shown in Figure 3. The CNA rod material exhibited the classic ductile to brittle transition behavior of ferritic steels. The 41J DBTT was 2°C and upper shelf energy (USE) was 308 J.

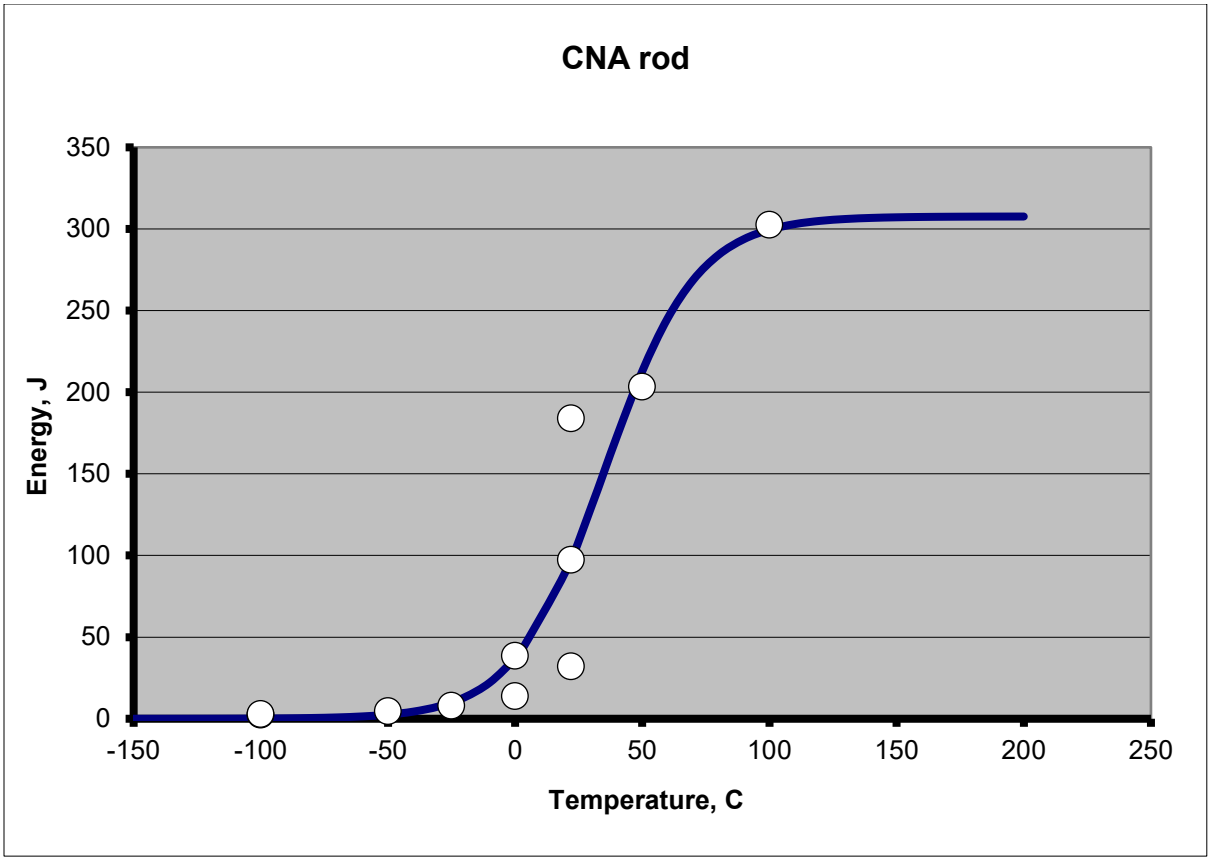

Figure 3. Charpy impact energy from a CNA rod after 710°C tempering heat treatment.

Compared with other grades of ferritic martensitic steels, the CNA rod exhibited higher DBTT and equivalent USE as shown in Table 1. Since a higher DBTT is not favorable for fusion applications due to irradiation embrittlement, we need to reduce the DBTT of the material. We speculated that the martensite formed after normalization was not fully tempered due to the low tempering temperature of 710°C, which resulted in a high density of fine precipitates in the material. Based on the work by Lee et al. [5], increasing the tempering temperature is beneficial to reduce the DBTT. Therefore, we performed two different heat treatments with higher tempering temperatures:

- V2: Normalization at 1170°C for 30min-> water quench -> tempered at 730°C for 60min -> air cooling
- V3: Normalization at 1170°C for 30min-> water quench -> tempered at 750°C for 60min -> air cooling

Room temperature Charpy impact testing was performed on specimens machined from the CNA rod with either V2 or V3 heat treatments and the Charpy impact energy results are compared with the original heat treatment as shown in Figure 4. Indeed, higher tempering temperature greatly increased the room temperature Charpy impact energy which means the corresponding DBTT of the material will be reduced. In addition, the higher tempering temperature didn't negatively affect the Vickers hardness results of the CNA rod with V2 Vickers hardness of HV245.6 ± 5.3 and V3 Vickers hardness of HV240.9 ± 3.7, both of which are within the specification for the CNA steel.

Table 1. Comparison of Charpy impact results between the CNA rod and literature results for other grades of ferritic martensitic steels

Material	Orientation	Heat Treatment	DBTT (°C)	USE (J)
CNA rod	**LC**	**1180°C 710°C***	**2**	**308**
F82H-IEA plate [1]	LT, TL	1040°C 750°C	-60°C to -10°C	NA
F82H-BA10 plate [2]	NA	1040°C 750°C	-150°C to -30°C	250-300
EUROFER97-1 plate [3]	LT, TL	980~1075°C 750~760°C	-85°C to -55°C	250-300
Gr. 91 steel plate [4]	TL	1040°C 760°C	-40°C to -30°C	190-200

*Prior to the final heat treatment, the CNA rod also went through normalization at 1050°C followed by tempering at 750°C.

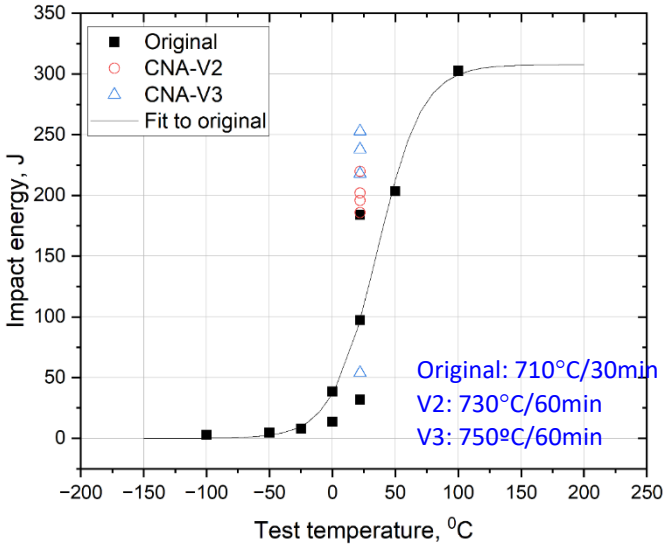

Figure 4. Comparison of Charpy impact energy results from a CNA rod after different tempering heat treatments.

References

[1] H. Sakasegawa, H. Tanigawa, Fusion Engineering and Design 109–111 (2016) 1724–1727.
[2] H. Sakasegawa et al., Fusion Engineering and Design 89 (2014) 1684–1687.
[3] M. Rieth et al., EUROFER97 Tensile, Charpy, Creep and Structural Tests, FZKA 6911, 2003.
[4] C. Brinkman, D. Alexander, P. Maziasz, Influence of Long-term Thermal Aging (50,000 h) on the Charpy V-notch Properties of Modified 9Cr-1Mo Steel, ORNL-6506, 1988.
[5] Chang-Hoon Lee, et al. Fusion Engineering and Design 124 (2017): 953-957.

1.2 PERFORMANCE EVALUATION OF MODIFIED 3CR-3WVTA BAINITIC STEELS—Y. Yamamoto (Oak Ridge National Laboratory)

OBJECTIVE

This work aims to evaluate the advantages in the mechanical performance of newly proposed, modified 3Cr-3WVTa bainitic steels developed at Oak Ridge National Laboratory. The proposed steel was designed to eliminate the need for post-weld heat treatment (PWHT), as well as providing improved mechanical properties of both base metal and weldments compared to those of existing commercial bainitic steels or ferritic martensitic (FM) steels. The target applications are high-temperature structural components in fusion reactors, such as helium-cooled vacuum vessels operating up to 450°C and blanket support structures operating up to 550°C. An optimization of thermomechanical treatment has been applied targeting the improvement of mechanical properties, especially for long-term creep performance as well as impact toughness after long-term isothermal exposure. The property improvements are to be measured by experimental approaches.

SUMMARY

There are two major updates on property evaluation of the “process-optimized” modified 3Cr-3WVTa steel: (1) the long-term creep-rupture tests of the base metal and cross-weld specimens, and (2) microstructure characterization and property evaluation of the isothermally aged modified 3Cr-3WVTa steel after applying an optimized thermomechanical treatment. A significant improvement of the base metal creep-rupture performance was observed in the process-optimized steel with more than doubled creep-rupture life at 550°C and 295 MPa in the normalized-and-tempered condition. The cross-weld specimens of the process-optimized steel also achieved ~20% improvement of the creep strength compared to non-optimized cross-weld specimens. The long-term isothermal aging at 500°C for up to 10,000 h resulted in almost no changes in the microstructure, and only a significantly small amount of hardness reduction compared to the same material tempered at 700°C for 1 h.

PROGRESS AND STATUS

A compositionally modified 3Cr-3WVTa bainitic ferritic steel (Mod. 3Cr-3WVTa steel, ID: MLC02T) was proposed with an advanced alloy design to achieve a reduced property inhomogeneity across the weldment in as-welded condition, targeting a PWHT-free bainitic ferritic steel for fusion structural applications. The nominal compositions of the original and modified steels are summarized in Table 1. Initial property evaluation of the modified steel suggested that the as-normalized MLC02T exhibited an improved room-temperature impact toughness compared to that after applying tempering, as opposed to the response in typical low-alloyed bainitic steels.

Table 1. Nominal composition of 3Cr-3WVTa base bainitic steels (balanced Fe)

Name	Alloy composition, wt.%	Remarks
MLC02T	3Cr-3W-0.2V-0.16Si-2.0Mn-0.1Ta-0.05C	Modified (newly proposed)
Original	3Cr-3W-0.2V-0.16Si-0.4Mn-0.1Ta-0.1C	Require PWHT, proposed in 1990’s [ref.]

[ref.] R.L. Klueh et al., Int. J. Pressure Vessels and Piping, 84 (2007) 29-36.

Based on the initial results, the focus of systematic performance evaluation has been shifted to the as-normalized condition. In addition, a refinement of the prior austenite grains (PAG) was also conducted through optimization of thermomechanical treatments as well as normalization temperature, as reported previously, targeting the improved room-temperature mechanical properties including both tensile and toughness. The present report summarizes the progress of property evaluation of MLC02T with the refined PAG in the as-normalized condition.

A cast ingot of MLC02T produced through vacuum-induction-melting was homogenized at 1200°C, followed by hot-rolling and normalization at 1000°C to prepare an as-normalized plate with ~15 mm thickness and average PAG size of ~40 μm. A small piece was sectioned from the plate which applied tempering at 700°C to compare the mechanical performance with and without tempering. Uni-axial tensile creep-rupture tests of the base metal in the as-normalized and normalized-and-tempered conditions were conducted at 500 and 550°C. A part of the as-normalized plate was machined to have a single V groove and then applied a gas tungsten arc weld (GTAW) with a compositionally matched weld filler metal strip. The creep-rupture performance across the weldment was also evaluated at 500 and 550°C.

Three creep-rupture tests at 500 and 550°C of the as-normalized MLC02T base metal with refined PAG and as-welded GTAW specimens are currently in progress, as summarized with Larson-Miller Parameter in Figure 1a. The creep-rupture strength of the as-normalized base metal showed ~35% improvement to date compared to that of previously evaluated MLC02T (normalized at 1100°C + tempered). Direct comparison of the creep-rupture curves of the normalized-and-tempered MLC02T tested at 550°C and 295 MPa (Figure 1b) indicated an apparent improvement of creep-deformation resistance by applying normalization at 1000°C, followed by tempering, with more than double creep-rupture life (6,274 h) compared to the non-optimized specimens (2,857 h). The as-normalized material of the process-optimized MLC02T specimen resulted in further improvement of creep-rupture life of 13,693 h at the given test condition. The cross-weld specimens of the process-optimized MLC02T steel also achieved ~20% improvement of the creep strength compared to non-optimized cross-weld specimens, indicating the effectiveness of the process optimization of the modified 3Cr-3WVTa steel in the creep performance of both base metal and the weldment.

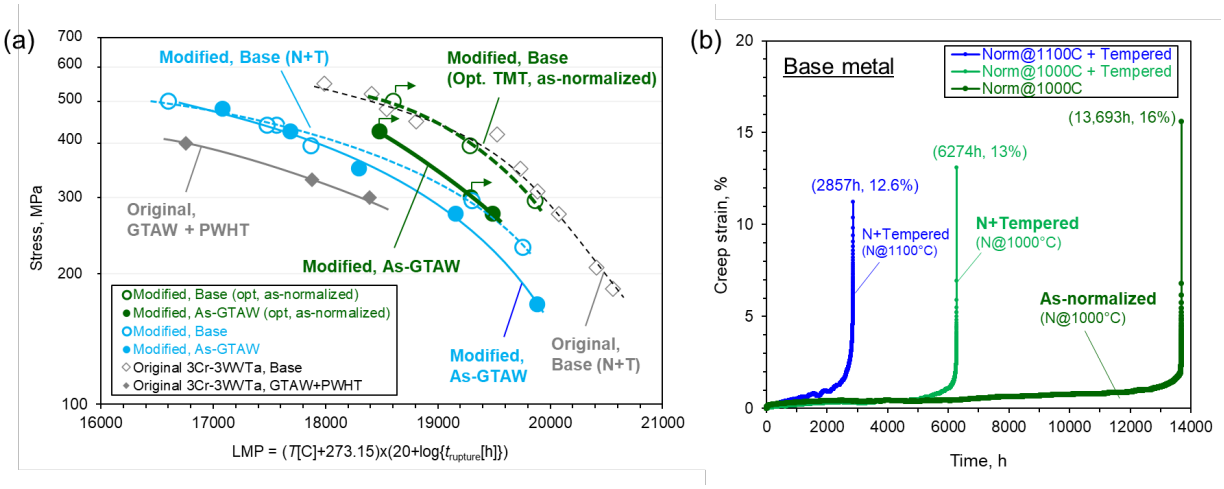

Figure 1. (a) Larson-Miller Parameter (LMP) plot of the process optimized MLC02T steel base metal and as-GTAW specimens, comparing with previously evaluated materials, and (b) creep-rupture curves of the modified 3Cr-3WVTa steel before and after re-normalization at 1,000°C, tested at 550°C and 295MPa.

Isothermal aging at 500°C in a laboratory air, for up to 10,000h, was conducted for evaluation of long-term thermal stability in microstructure and mechanical performance of the process-optimized MLC02T plate in the as-normalized condition. Figure 2 represents optical micrographs of the process-optimized MLC02T steel aged for 1,000h, 3,000h, and 10,000h compared to the as-normalized microstructure. The as-normalized specimen showed a fully bainitic microstructure, and the microstructural characteristics including PAG size and acicular bainite ferrite structure showed no significant changes including recrystallization or grain coarsening, even after 10,000 h exposure. Optical micrographs also indicated secondary phase precipitation inside the acicular bainite ferrite, although a detailed scanning electron microscope (SEM) characterization would require identifying the types of precipitates.

Figure 3 shows micro-Vickers hardness (HV0.5, averaged 25 indent measurements) of the process-optimized MLC02T steel plotted as a function of aging time at 500°C. The hardness values of the same

material after tempering at 680°C or 700°C for 1h are also plotted for comparison. The hardness showed very little change during aging, from 318 ± 9 HV in the as-normalized condition to 309 ± 10 HV after 10,000h aging. The amount of the hardness reduction was significantly smaller than the same material tempered at 700°C for 1h (244HV) or even at 680°C for 1h (300HV). Based on both microstructure characterization and hardness measurement, it is speculated that the microstructural stability of the process-optimized MLC02T steel at 500°C could be correlated with the little change in the hardness, which may also lead a potential of thermal stability of the other mechanical properties. The evaluation of Charpy impact toughness and tensile properties of the aged specimens are also planned, and the correlation with microstructural stability will be discussed in future.

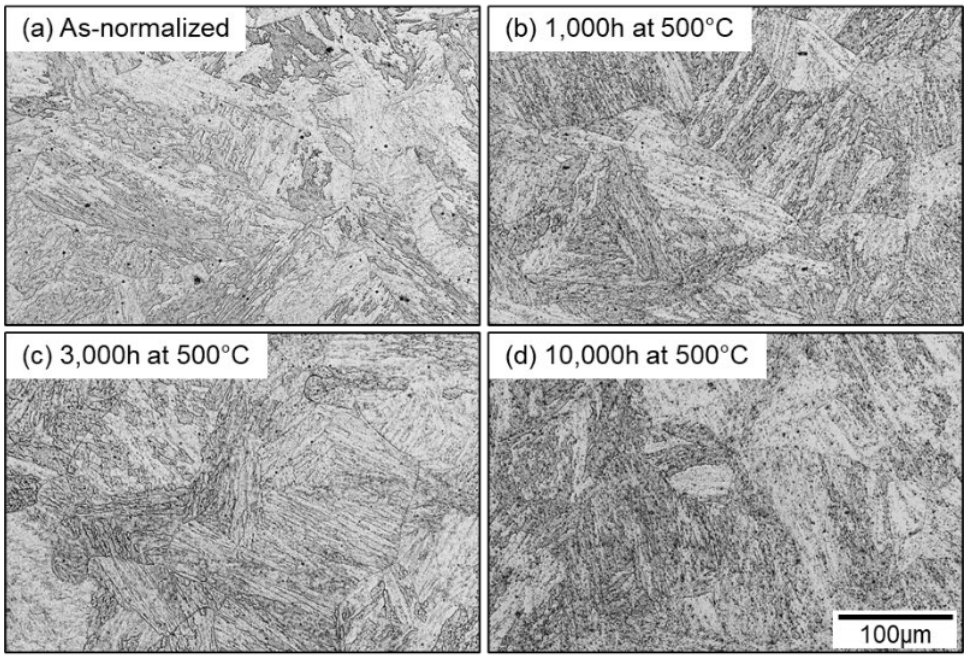

Figure 2. Optical micrographs showing fully bainitic structure of the process-optimized MLC02T before and after aging at 500°C: (a) as-normalized, (b) aged for 1,000h, (c) 3,000h, and (d) 10,000h.

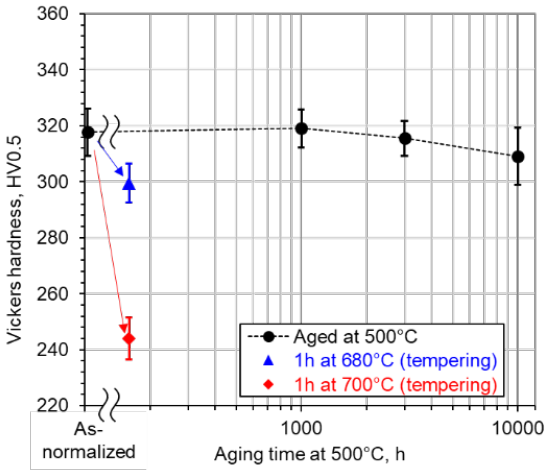

Figure 3. Micro-Vickers hardness plotted as a function of aging time at 500°C and compared with those after tempering at 680 and 700°C for 1h.

Future Plans

Detailed microstructure characterization of the long-term creep-ruptured and isothermally aged MLC02T will be conducted to be correlated with the process or test conditions. Evaluation of the creep-rupture performance will be continued, and Charpy impact toughness and tensile tests of the isothermally aged samples will also be conducted. A compositionally matched metal-core wire of MLC02T steel was produced and a wall has been printed through wire-DED process, so that the microstructure characterization and property evaluation will also be conducted.

1.3 IMPACT OF HELIUM ON THE NEUTRON IRRADIATION RESPONSE OF ISOTOPICALLY TAILORED F82H RAFM STEEL AT 86 DPA

—Y. Lin, T.S. Byun (Oak Ridge National Laboratory)

OBJECTIVE

The aim of this research is to investigate and quantify microstructural changes induced by neutrons and transmutation helium in High Flux Isotope Reactor (HFIR)-irradiated F82H Reduced-activation ferritic/martensitic (RAFM) steels and provide a deeper understanding of how these changes impact the deterioration of mechanical properties.

SUMMARY

Cavities (helium bubbles and voids) were observed in both F82H-Ni58 and F82H-Ni60 samples following mixed-spectrum neutron irradiation in HFIR at 300°C up to ~86 dpa. The F82H-Ni58 exhibited a higher cavity density with an elevated He per dpa ratio (11 appm He/dpa) compared to F82H-Ni60 (0.3 appm He/dpa). No distinct bimodal cavity size distribution was evident in either of the neutron-irradiated F82H samples. Both neutron-irradiated F82H samples displayed Ni-rich clusters, likely resulting from irradiation-induced or enhanced precipitation. These clusters included small, spherical Ni- or Cr-rich particles, as well as larger, rod-shaped clusters enriched in both Ni and Cr. Furthermore, the segregation of Ni/Cr was observed at grain boundaries and around cavities in both neutron-irradiated F82H materials.

PROGRESS AND STATUS

The RAFM steels are the primary candidates for the fusion reactor first wall and plasma-facing structures due to their attractive thermo-mechanical properties and demonstrated radiation tolerance. Although obtaining fusion-relevant helium generation rates in RAFM steels is practically challenging without a fusion prototypic neutron source, controlling helium generation in the mixed-energy neutron spectrum at HFIR using isotopically tailored alloying methods can be a plausible feasible approach. In the previous campaign, the F82H steels alloyed with Ni isotopes with different (n,α) reaction cross sections were HFIR-irradiated in different conditions. In this study at Low Activation Materials Development and Analysis (LAMDA), Oak Ridge National Laboratory (ORNL), we conducted transmission electron microscopy (TEM) characterization on the selected HFIR-irradiated F82H steels doped with 1.4% ^{58}Ni and 1.4% ^{60}Ni. The F82H steel with 1.4% ^{58}Ni generated approximately 936 appm helium (~11 appm He/dpa), while the steel with 1.4% ^{60}Ni steel produced about 26 appm helium (~0.3 appm He/dpa) at a dose of ~86.17 dpa.

Following neutron irradiation, the distribution of cavities was characterized in scanning transmission electron microscopy bright field (STEM-BF) mode for both the F82H-Ni58 and F82H-Ni60 samples, as depicted in Figure 1. The F82H-Ni58 sample exhibited a higher cavity density, featuring an elevated He per dpa ratio (11 appm He/dpa), in contrast to F82H-Ni60 (0.3 appm He/dpa). Notably, neither of the neutron-irradiated F82H samples displayed a bimodal cavity size distribution (with a higher density of fine bubbles and a lower density of larger voids). This is attributed to the complex microstructural changes that occur under neutron irradiation, affecting sink strength and blurring the critical radius boundary between bubbles and voids. The uniquely fine microstructure of the quenched and tempered F82H steels might also influence the evolution of cavities, possibly limiting formation of large cavities.

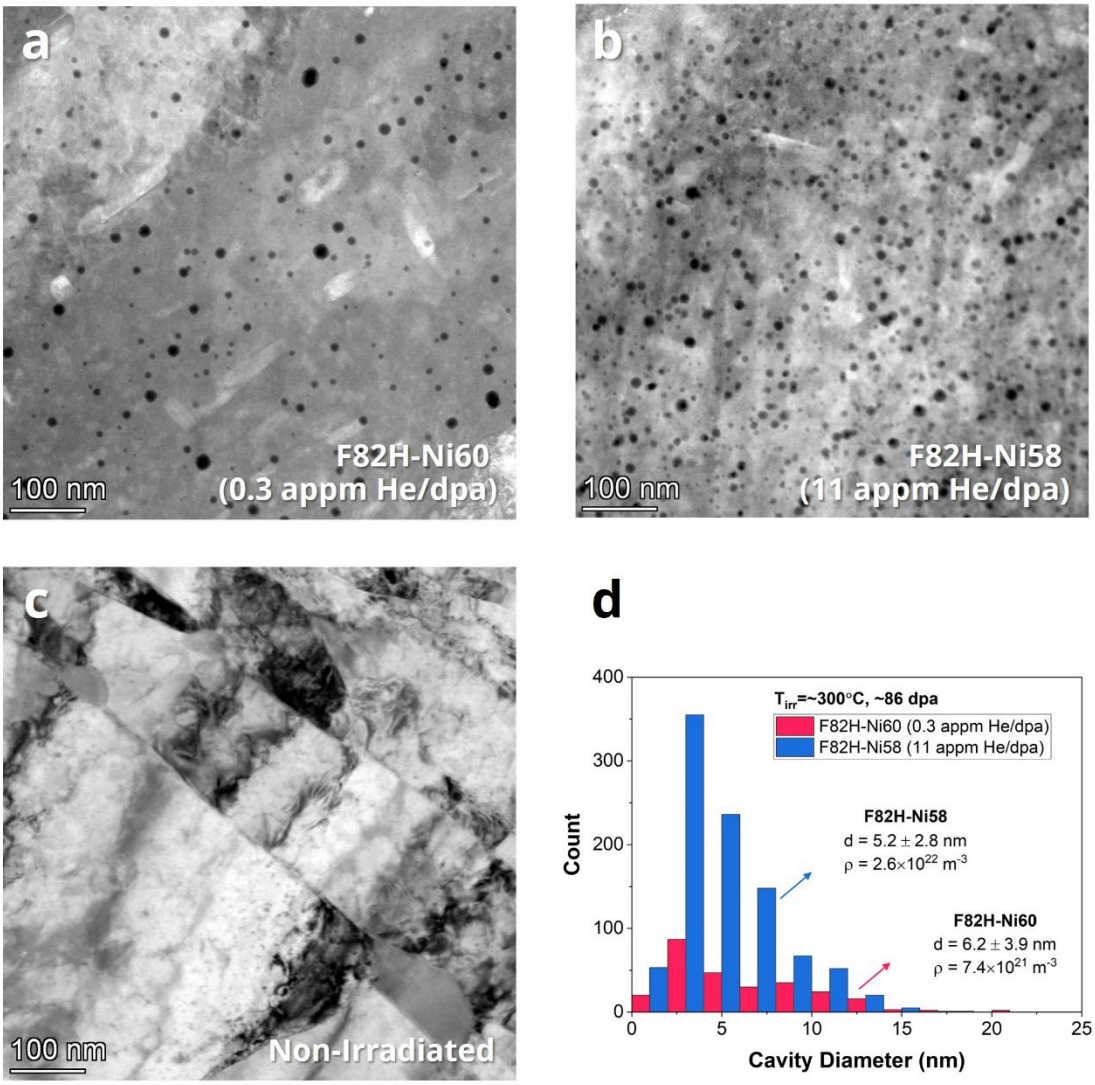

Figure 1. The STEM High-angle annular dark-field imaging (HAADF) images of cavities in (a) F82H-Ni60 and (b) F82H-Ni58; (c) STEM bright-field image of the non-irradiated F82H sample with no cavities observed; (d) Size distribution of cavities in F82H-Ni60 and F82H-Ni58.

In Figure 2, STEM energy dispersive X-ray spectroscopy (EDS) mapping has unveiled the presence of Ni/Cr-rich precipitates and clusters in both the neutron-irradiated F82H-Ni60 and F82H-Ni58 samples, which are absent in the non-irradiated sample. These Ni/Cr-rich precipitates and clusters are likely a result of irradiation-induced or -enhanced precipitation. They encompass small, spherical Ni- or Cr-rich particles as well as larger, rod-shaped clusters enriched in both Ni and Cr. The large Cr-rich particles in the non-irradiated F82H sample are $M_{23}C_6$ primitive particle.

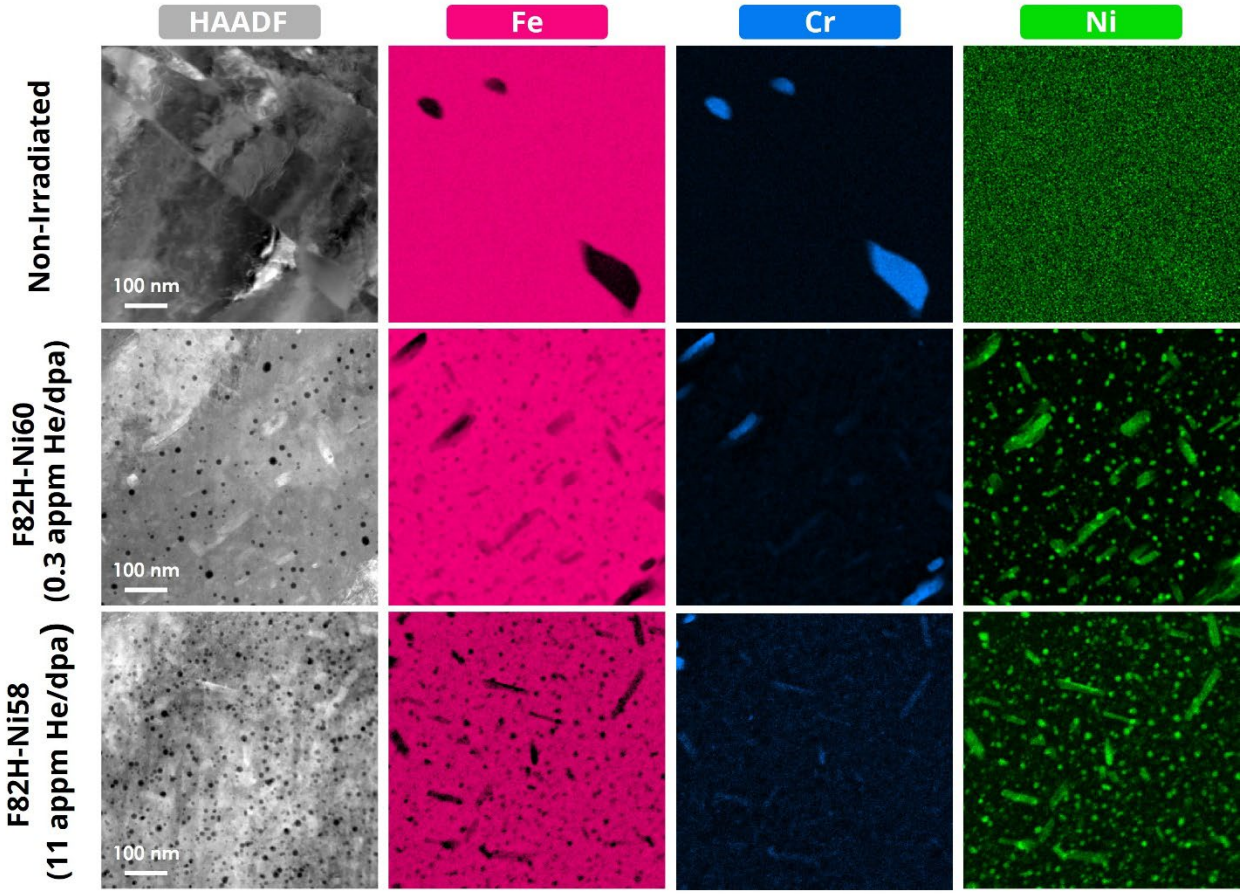

Figure 2. The STEM-HAADF image and elemental STEM-EDS maps for Fe, Cr, and Ni in the grain Interior of non-Irradiated F82H, and neutron irradiated Ni60/Ni58-alloyed F82H.

Upon closer examination with higher magnification STEM-EDS mapping near the grain boundary (Figure 3), we observed the segregation of Ni/Cr at grain boundaries and around cavities in both neutron-irradiated F82H materials. This observation aligns with the general concept of radiation-induced segregation (RIS), which is a non-equilibrium process occurring at point defect sinks during irradiation at intermediate temperatures and often coincides with cavity formation. It is worth noting that the segregation of Ni around the cavity surface has the potential to enhance the strengthening coefficient of cavities and subsequently increase irradiation hardening.

Results

This report presents invaluable and crucial data regarding neutron-irradiated RAFM steels doped with Ni up to ~86 dpa at 300°C. Achieving this final dose required approximately nine years of exposure to neutron irradiation in HFIR. The formation of high-density, fine Ni particles and the segregation of Ni within various features were unexpected outcomes from a 1.4% Ni doping. The increased density of cavities observed in the F82H-Ni58 sample, coupled with a higher helium production rate of 11 appm He/dpa compared to the 0.3 appm He/dpa in F82H-Ni58, is likely the primary contributor to the additional increase in yield strength observed in tensile tests. However, further quantification of all irradiation-induced microstructures, including cavities, dislocations, dislocation loops, and precipitates, is necessary to confirm the predominant factor contributing to radiation hardening in these samples.

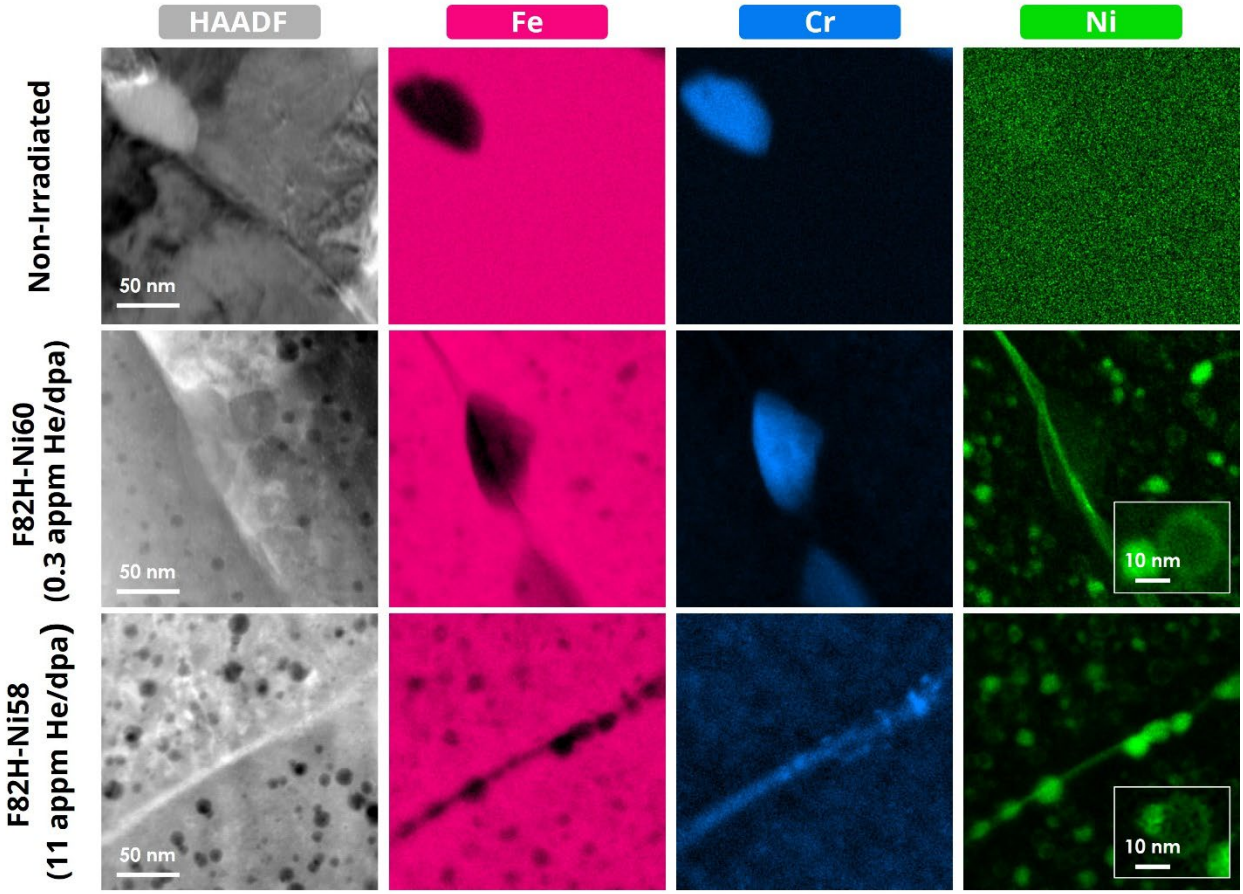

Figure 3. The STEM-HAADF image and elemental STEM-EDS maps for Fe, Cr, and Ni near the grain boundary of non-Irradiated F82H, and neutron irradiated Ni60/Ni58 F82H.

Future Work

Future work will focus on dislocation and dislocation loop analysis of the two neutron-irradiated F82H samples. In addition, we will employ selected area electron diffraction techniques to investigate the crystal structure and phase of the Ni/Cr clusters identified in the STEM-EDS results presented in this report. Furthermore, we will use S/TEM methods to study the effects of neutron irradiation on the primitive $M_{23}C_6$ particles.

Correlating the microstructure characterization results with measured mechanical properties will be also pursued. Effects of helium transmutation, displacement damage, and thermal recovery on mechanical property degradation will be focused.

1.4 WELDABILITY AND POST WELD HEAT TREATMENT STUDY OF THE CASTABLE NANOSTRUCTURED ALLOY—W. Tang, R. Miller, W. Zhong, D. Kyle, T. Graening, Y. Katoh, Y. Yang (Oak Ridge National Laboratory), E. Proehl (University of Tennessee)

OBJECTIVE

Castable nanostructured alloy (CNA) welding process development and welded joint characterization.

SUMMARY

A gas tungsten arc welding (GTAW) process was developed on CNA7 plates using welding wire produced from a 0.25-ton heat CNA. Visual, radiographic, and visible dye penetrant inspections were applied on the welded joint. Normalization and tempering post weld heat treatments (PWHTs) were performed on part of the weld deposit and welded joint. Optical microscopy observation, Rockwell B hardness testing, Vickers microhardness testing, and transverse room temperature tensile testing were performed on the as welded and post weld heat treated weld joint coupons and the weld deposit.

PROGRESS AND STATUS

Introduction

The CNAs are a newly developed United States reduced activation ferritic/martensitic (RAFM) steels for structural components in fusion reactors. Previous studies showed improved properties compared to conventional RAFM steels, including Eurofer97 and F82H. The CNAs from the laboratory-scale developmental heats exhibited the desired uniformly distributed precipitates with higher number densities. These microstructures resulted in enhanced yield strengths, creep resistances, and Charpy impact toughness. These alloys also displayed better helium management and reduced susceptibilities to transmutation-induced phase transformation. However, the weldability of the industrial scale CNAs has not been studied. In this work, we developed a GTAW process for CNA plates using the welding wire produced from the most recent generation of CNA. Microstructures and mechanical properties of the welded joint were evaluated in the as welded and post weld heat treated conditions.

Experimental Procedure

With welding wire produced from a 0.25-ton heat of CNA, a pair of previous generation CNA plates, CNA7 (0.78 in. thick), were joined by GTAW using a double vee groove. Meanwhile, an all-CNA weld metal deposit was produced on a A36 steel plate by GTAW. Visual, radiographic, and dye penetration inspections were performed on the CNA7 welded joint. The following PWHTs were applied on half of the CNA7 welded joint and some of the weld deposit:

1. Normalized + Tempered: 1180 °C × 10 min. + water cool + 710 °C × 60 min. + air cool (Applied on half of the welded joint and some weld deposit).
2. Tempered Only: 710 °C × 60 min. + air cool (Only applied on some of the weld deposit).

Optical microscopy observation, Rockwell B hardness testing, Vickers microhardness testing, and transverse room temperature tensile testing were performed on the as welded and post weld heat treated weld joint coupons and the weld deposit.

Results

No relevant indications were identified on the welded joint by visual, radiographic, and visible dye penetrant inspections. Typical lath martensitic microstructures were observed in the weld without PWHT, and more tempered martensite presented at the weld root area. After the normalization and tempering PWHT, grain structures in the weld were similar to the normalized and tempered base metal.

The Vickers microhardness measurements were performed along three horizontal lines across the weld, close to the weld crown, along the plate middle thickness across the weld root, and along the ¼ plate thickness. In the as-welded condition, the hardness values close to the weld crown and at ¼ plate thickness were higher than that of the base metal (BM) due to the martensite formation. The hardness of the fusion zone (FZ) along the plate middle thickness was lower than the BM hardness by the over tempering effect from multi-pass welding thermal cycles. In addition, hardness at some locations close to the weld crown were measured very low, almost to the BM hardness level. Optical microscopy observation indicated that this phenomenon was caused by the presence of δ-ferrite, a very soft phase vs. martensite, and scanning electron microscopy (SEM) characterization will be performed for confirmation. Reduced hardness valleys were presented in the heat affected zones (HAZs) on both sides of the FZ for all three lines of measurements. It is believed that the decrease of hardness in HAZ was associated with over-tempering from the welding heat input. Hardness measurements in the FZ and HAZ of the post weld heat treated joint exhibited similar values with the BM, indicating relatively homogenized microstructures and hardness along the whole welded joint.

Transverse tensile tests were performed on welded joint specimens with the as welded and post weld heat treated conditions. Specimens received PWHT exhibited ~5% higher yield strength than the as-welded condition, and they all exhibited similar tensile strength. However, the elongation and reduction of area (RoA) of the post weld heat treated specimens resulted in an ~40% increase compared with the as welded condition. This improvement is believed to be caused by eliminating the strain localization in HAZ soft zones through PWHT.

The FZ and HAZ microstructure and microhardness variations along the vertical direction were resulted by the peak temperatures and thermal cycles variations of the multi-pass GTAW process. Normalization and tempering PWHT is an effective way to ease the welded joint inhomogeneity in microstructure and mechanical properties, if needed.

The Rockwell B hardness values of the weld deposit in the as welded, tempered, and normalized + tempered CNA materials were 108 ± 3.2 HRB, 101 ± 3.9 HRB, and 103 ± 0.3 HRB, respectively. The normalized + tempered deposited material satisfied the material designed specification of 102 ± 2 HRB.

Future Work

Future work of this study includes SEM characterization of the welded joint specimen with and without PWHT, bend testing, and corrosion testing coupon preparation, as well as studies of the 5-ton heat of CNA material after it is received.

Acknowledgements

Research sponsored by the Office of Fusion Energy Sciences, U.S. Department of Energy (DOE), under contract DE-AC05-00OR22725 with UT-Battelle LLC, and additional support by DOE Advanced Research Projects Agency – Energy (ARPA-E) 20/CJ000/08/06. The authors thanks Dr. Yiyu Wang for valuable discussions.

1.5 THE EFFECTS OF MICROSTRUCTURE ON RADIATION RESPONSE IN FERRITIC-MARTENSITIC STEELS—

W. Zhong, L. Tan (Oak Ridge National Laboratory)

OBJECTIVE

Reduced activation ferritic-martensitic (FM) steels were one of the candidates for fusion first wall and blanket structural materials application. The objective of this work is to investigate the neutron irradiation effects on the tensile properties of two FM steels. In this work, the tensile properties of two irradiated FM steels are reported, in addition to the unirradiated materials. Pre-irradiated microstructure of these FM steels was characterized and compared.

SUMMARY

Two FM steels (9Cr-Ta and 9Cr-NbMo) were irradiated in High Flux Isotope Reactor (HFIR), and their post irradiation tensile properties were tested and compared. Irradiation induced hardening at 400°C were observed for both materials, which is common for FM steels at low irradiation temperature (< ~0.45 T_M). For irradiation at 490°C to 7.4 dpa, different tensile behaviors were observed. 9Cr-Ta exhibits irradiation induced softening, whereas 9Cr-NbMo maintains similar strength as unirradiated materials. Microstructure characterization on the pre-irradiated materials exhibits different microstructure. 9Cr-Ta has smaller grain size, whereas 9Cr-NbMo has higher dislocation density and higher number density of precipitates.

PROGRESS AND STATUS

Two 9% Cr FM steels were investigated for the irradiation effects on the tensile properties. The compositions of these two steels are Fe-8.9%Cr-1.9%W-0.47%Mn-0.14%Si-0.2V-0.4%Mo-0.1%Nb-0.1%Ni-0.1%C-0.05%N (designated as 9Cr-NbMo) and Fe-9.0%Cr-1.1%W-0.46%Mn-0.23%Si-0.3%V-0.1%Ta-0.1%C-0.05%N (designed as 9Cr-Ta) respectively. Shown in Figure 1 are the stress–strain curves for the unirradiated and irradiated materials that were tested at room temperature; the solid lines represent 9Cr-NbMo, and dashed lines represent 9Cr-Ta. The irradiation conditions were labeled using the same colors as the stress–strain curves. Before irradiation, the tensile behaviors for 9Cr-NbMo and 9Cr-Ta are similar, as indicated by the black curves. The yield strength of these alloys are ~744 – 773MPa.

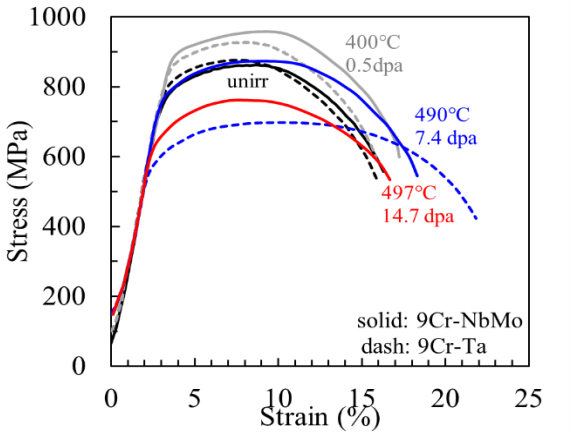

Figure 1. Stress–strain curves of unirradiated and irradiated 9Cr-NbMo (solid curves) and 9Cr-Ta (dashed curves) alloys. Tensile tests were performed at room temperature.

After the irradiation at lower temperature (400°C, 0.5 dpa), both alloys exhibit irradiation-induced hardening by about 50–130 MPa. Such irradiation induced hardening is consistent with the hardening that was commonly observed in FM steels at low irradiation temperature (less than about < ~0.45T_M). At higher irradiation temperature (490°C, 7.4 dpa), 9Cr-Ta exhibited irradiation-induced softening: yield stress decreased by about 27% to 565 MPa. By contrast, under the same irradiation conditions, 9Cr-NbMo maintained yield stress of 761 MPa, like the unirradiated materials (744 MPa). Extended irradiation to 14.7 dpa causes softening to 641 MPa in 9Cr-NbMo.

Microstructure characterizations were performed on the unirradiated materials. Figure 2 shows the inverse pole figure-colored map of these two alloys with the insets showing high-angle boundaries (>15degree). The intercept method was used to examine the grain size. The mean number of intersections per unit length are 0.23 ± 0.03 μm^{-1} and 0.35 ± 0.03 μm^{-1}, corresponding to the average grain size of 4.3 ± 0.5 μm and 2.8 ± 0.3 μm for 9Cr-NbMo and 9Cr-Ta, respectively, indicating smaller grain size for 9Cr-Ta.

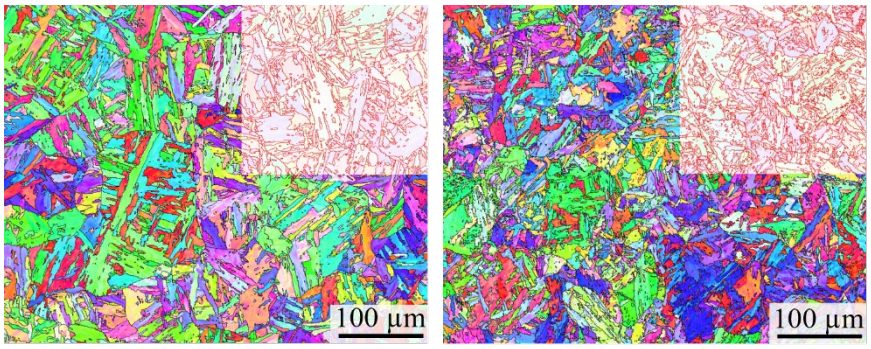

Figure 2. Inverse pole figure for unirradiated (left) 9Cr-NbMo alloy, (right) 9Cr-Ta alloy with the high angle grain boundary distribution shown in the inset.

Transmission electron microscopy (TEM) was used to identify the precipitate and dislocation structure in both alloys. The Cr/V energy dispersive spectroscopy (EDS) maps in Figure 3a and 3b reveal the distribution of $Cr_{23}C_6$ and MX precipitates in 9Cr-NbMo and 9Cr-Ta. The MX precipitates in 9Cr-Ta are (V,Ta)(C,N) that are distributed inside the matrix, while they are VN in 9Cr-NbMo that are distributed at boundaries. Both $Cr_{23}C_6$ and MX precipitates in 9Cr-NbMo are smaller but have higher number density than 9Cr-Ta. In addition to the VN precipitate at boundary in 9Cr-NbMo, platelet VN precipitates were also observed, as shown by a dark field image in Figure 3a. These platelet VN precipitates have higher number density by two orders of magnitude than $Cr_{23}C_6$ and coarser VN precipitates in 9Cr-NbMo. Images of dislocations on both alloys were taken by the on-zone STEM images, as shown in Figure 3c and 3d. The dislocation density of 9Cr-NbMo is higher than 9Cr-Ta.

Although the yield strength of both alloys is similar before irradiation, the microstructures are different: 9Cr-Ta has a smaller grain size, whereas 9Cr-NbMo has a higher dislocation density and higher precipitate number density, indicating different strengthening contributions from these alloys.

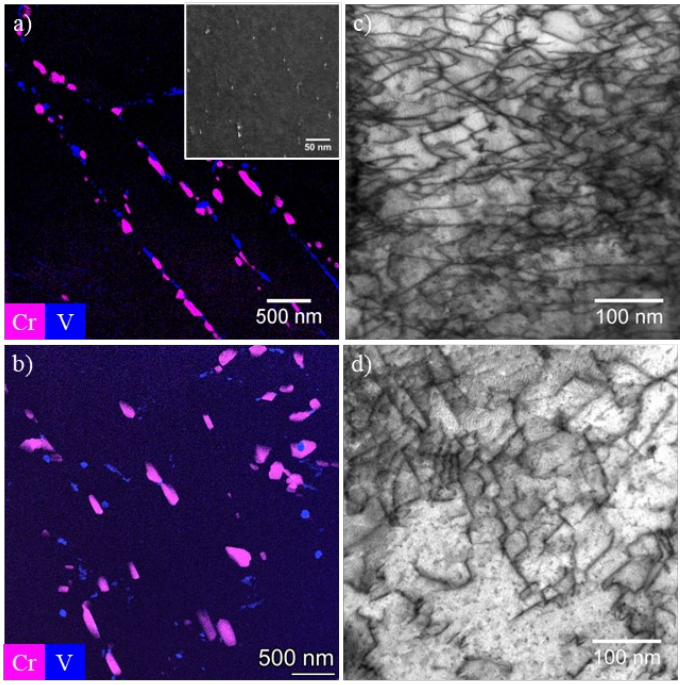

Figure 3. Precipitate and dislocation distribution in unirradiated (a,c) 9Cr-NbMo and (b,d) 9Cr-Ta.

Future Work

Microstructure of the post-irradiated FM steels will be characterized to understand the mechanism of different tensile behaviors after the irradiation at higher temperature.

1.6 MICROSTRUCTURE AND TENSILE PROPERTY OF 0.25-TON SCALE CASTABLE NANOSTRUCTURED ALLOY ROD—W. Zhong, Y. Wang, Y. Yang (Oak Ridge National Laboratory)

OBJECTIVE

To meet the fusion industry needs, efforts to scale up fusion structural materials must be taken. The objective of this project is to demonstrate the scalability of castable nanostructured alloys (CNA) for production and performance for used as fusion first wall and blanket structural materials. A quarter-ton scale CNA rods were fabricated, and the examination on multiple properties are on-going. In addition, fabrication of multi-ton scale CNA plates is on-going.

SUMMARY

The 0.25-ton scale heat of CNA rods were fabricated by Metalwerks Inc. Optimized heat treatment was performed on the CNA rods to ensure the hardness of materials satisfies the desired criteria (102 ± 3 HRB). Microstructural characterization was performed on the CNA to examine grain structure and precipitate distribution. The result of precipitate size and distribution is reported here. $Cr_{23}C_6$ precipitates of 30-150 nm were observed at boundary with the number density on the order of 10^{19} m^{-3}. Both coarse (50-250 nm) TiC precipitates with low number density (~10^{17} m^{-3}) and ultrafine (3-10 nm) TiC precipitates with high number density (~10^{21} m^{-3}) were observed, and they were distributed inside the matrix. Tensile tests were performed at room temperature as well as elevated temperatures up to 700°C with 1–4 tests per temperature following ASTM standards E8 and E21. Comparing to Eurofer 97, CNA demonstrates higher tensile yield strength and ultimate tensile strength, with slightly lower total elongation and area reduction.

PROGRESS AND STATUS

As-received 0.25-ton scale CNA rods (1 inch diameter) from Metalwerks requires additional heat treatment to meet the hardness design specification of 102 ± 3 HRB. An optimized heat treatment (designed as HT7) was selected based on the screening tensile tests using SS-J3 samples. These optimized CNA were normalized at 1180°C for 10 minutes, followed by water quenching. Tempering was then performed at 710°C for 60 minutes with subsequent air cooling.

Scanning transmission electron microscopy (STEM) was used to characterize the precipitate distribution in CNA rods. Figure 1a and 1b show the dark field STEM image and Ti/Cr energy dispersive spectroscopy (EDS) maps of the TEM sample that was prepared at the center of a 1-inch diameter rod. The $Cr_{23}C_6$ precipitates were distributed at boundaries with the size of 30-150 nm and the number density of the order of 10^{19} m^{-3}. A few coarse (50 – 250nm) TiC precipitates were observed, and they have low number density on the order of 10^{17} m^{-3}. The presence of these coarse TiC precipitates is likely attributed to the undissolved TiC precipitates from the normalization step in the additional heat treatment. In addition to these coarse TiC precipitates, ultrafine TiC precipitates (~3-10 nm) were observed, as shown in the dark field STEM image and Ti EDS map in Figure 2. These ultrafine TiC precipitates have a high number density of the order of 10^{21} m^{-3}.

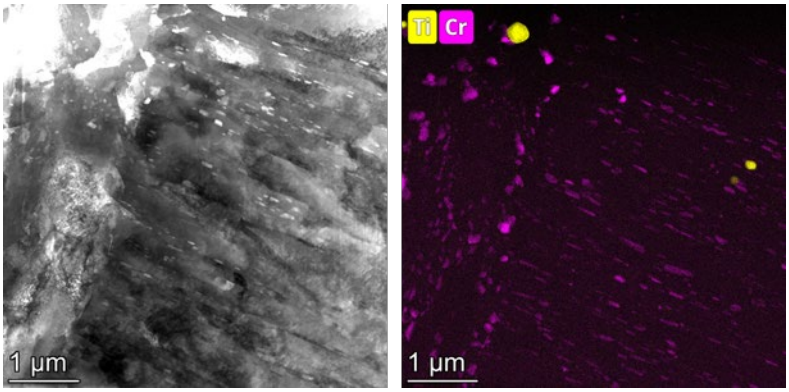

Figure 1. (left) Dark field STEM image and (right) Ti/Cr EDS maps showing the distribution of $Cr_{23}C_6$ and coarse TiC particles in the CNA rods with optimized heat treatment.

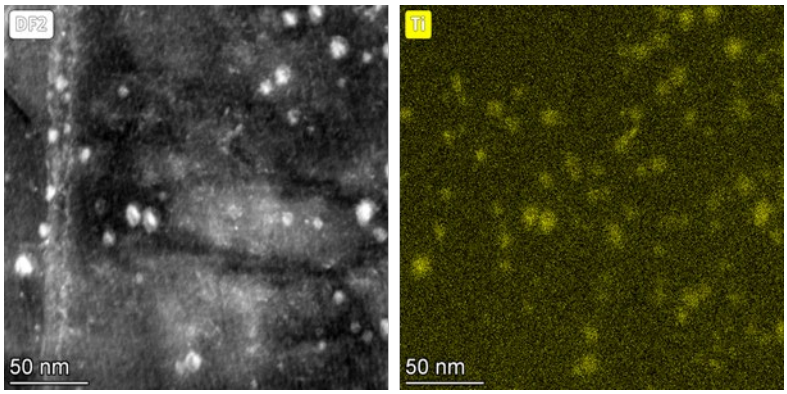

Figure 2. (left) Dark field STEM image and (right) Ti EDS map showing the distribution of ultrafine TiC precipitate in the matrix of CNA rods with optimized heat treatment.

To investigate the tensile properties of CNA rods, ASTM-standard tensile samples with 0.25-inch diameter and nominal gage length of 1.25-inch were machined from the CNA rods with optimized heat treatment. Tensile tests were performed in air. The tensile testing procedure follows ASTM E8 for room temperature and ASTM E21 for elevated temperature. Figure 3 shows the 0.2% offset yield stress, total elongation, and the area reduction of CNAs, in comparison to Eurofer 97 [1]. The CNA rods demonstrate higher yield strength than Eurofer 97 for all investigated temperature, with greater yield strength by ~140 MPa at 23°C, and by ~70 MPa at 700°C. The higher yield strength is accompanied by the reduced elongation and smaller reduction of area for CNA rods.

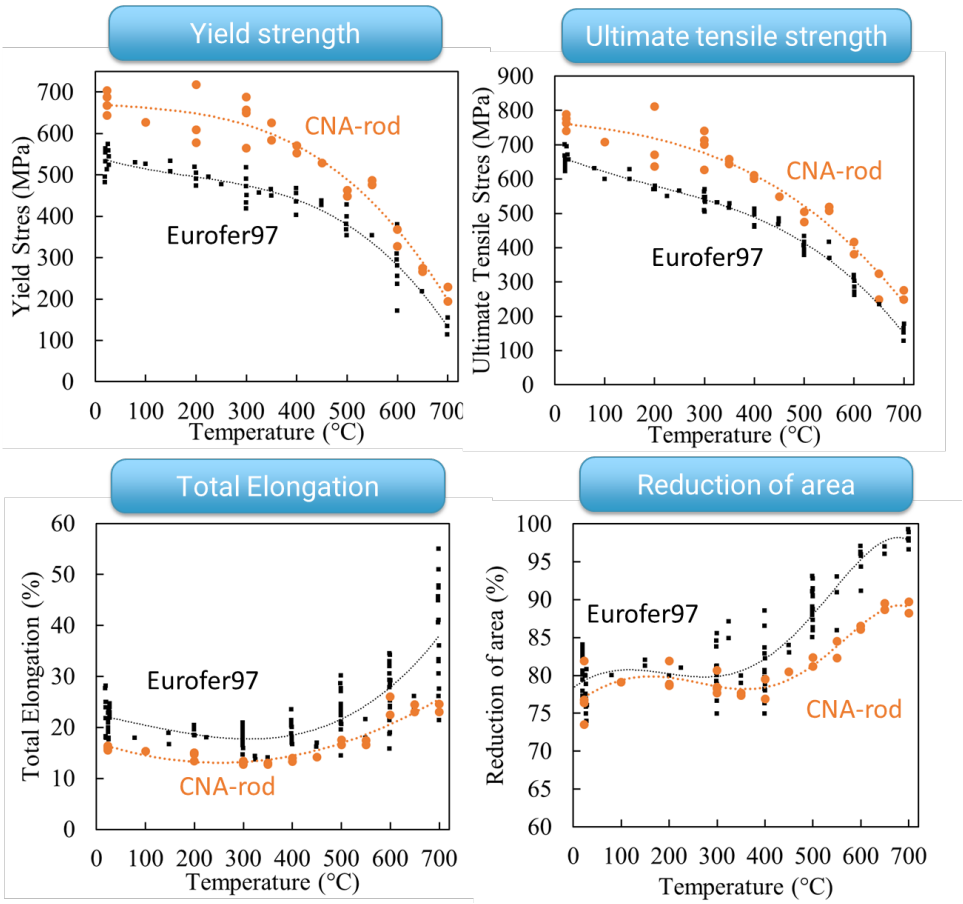

Figure 3. The 0.2% offset yield strength, ultimate tensile strength, total elongation and reduction of area of CNA tensile properties up to 700°C, in comparison to Eurofer97 [1].

Future Work

Other properties of CNA rods are under investigation, such as creep, fracture toughness, low cycle fatigue properties, weldability, and compatibility with the liquid-metal coolants. In addition, fabrication of multi-ton CNA plates are on-going, which will be followed by microstructure characterization and mechanical property testing on the CNA plates.

Reference

[1] Lucon, E., and W. Vandermeulen. Overview and Critical Assessment of the Tensile Properties of unirradiated and irradiated EUROFER97. No. BLG--1042. Belgian Nuclear Research Center SCK-CEN (Belgium), 2007.

2. ODS AND NANOCOMPOSITED ALLOY DEVELOPMENT

2.1 COLD SPRAY AND FRICTION STIR PROCESSING OF GARS ODS STEEL POWDER ON A FERRITIC MARTENSITIC STEEL SUBSTRATE—D. Zhang, X. Wang, K. A. Ross, J. Darsell, L. Li, D. J. Edwards, W. Setyawan (Pacific Northwest National Laboratory)

OBJECTIVE

The objective of this work is to explore alternative route of fabricating oxide dispersion strengthened (ODS) steel plate, including the potential of plating such ODS plate onto a substrate of reduced activation ferritic martensitic (RAFM) steel. We have demonstrated successful cold spray of ODS steel powder onto ferritic martensitic steel (P92) plates. Two large plates, i.e., #1 and #2, were prepared for subsequent development of friction stir processing (FSP) to (a). eliminate pores and defects in cold sprayed deposit and fully densify ODS steel; (b) further disperse Y-(Ti)-O particles with severe plastic deformation in FSP; (c) maintain and possible improve bonding between ODS steel deposit and the substrate. Multiple “single pass” FSP runs were performed on plate #1 to optimize FSP parameters, including FSP tool plunge depth, compression force, and temperature control program. Subsequently, #2 plate was processed with a multi-pass FSP raster to impact an extended area (i.e., ~4’’ long, ~3’’ wide).

SUMMARY

Cold spray was used to successfully deposit ODS steel powder onto ferritic martensitic steel (P92) plate. The feedstock ODS steel powder was provided by collaborators at Ames Laboratory, made with their unique gas atomization reaction synthesis (GARS). The GARS ODS steel powder had the nominal composition of 14YWT (14Cr-0.4Ti-3W-0.35Y-0.1O, wt.%). Meanwhile the largely spherical powder was not ball milled, hence it can be cold sprayed. The P92 steel plate was used as a surrogate for RAFM steel, having nominal composition of 9Cr-2W-Si0.5-Mn0.5-Mo0.4-Ni0.3-V0.2-C0.1, wt.%. The state-of-the-art cold spray system was used with helium carrier gas and robust processing parameters to ensure good deposition quality. Subsequently FSP was successfully used to further process the cold sprayed plates.

PROGRESS AND STATUS

Introduction

The conventional fabrication route [1] of ODS steel plate involves production of powder by gas atomization, ball milling, powder vacuum canning, hot isostatic pressing, hot cross rolling, cold rolling, with annealing steps often required in-between rolling steps. This route is time consuming, expensive, hard to scale up, and also extremely delicate as cracks can develop and the plate can “bend out of shape” during the laborious rolling process. Based on the realistic consideration that conventional route is not capable of producing tons of ODS steel for fusion energy application, some researchers [1] proposed to “plate” a mm-level thickness of ODS steel onto RAFM steel, with the idea that the ODS steel plating would be a critical top layer to handle expected extreme temperature and radiation dose in a fusion environment. This means that on top of the laborious plate fabrication process, additional bonding step (e.g., diffusion bonding) is required to make ODS steel plating. Therefore, it would be highly desirable to directly deposit an ODS steel layer onto a RAFM steel without the abovementioned laborious steps. Unfortunately, melt-based additive methods won’t be suitable as dispersed particles tend to agglomerate in molten metal. Cold spray is a solid-state based method that could offer a potential solution. Yet effective cold spray would require the feedstock powder to be largely spherical for aerodynamic purposes. Namely, the flaky ball milled ODS steel powder won’t work well with cold spray.

The GARS method produces spherical precursor ODS steel powder with an outer shell of Cr-rich oxide, whereas the nano-oxide forming species, i.e., Y and Ti, are at the powder interior in the form of Fe-intermetallics. Upon heating and consolidation (e.g., hot isostatic pressing, [HIP]), oxygen atoms diffuse into the powder interior to react with Y/Ti, forming the Y-Ti-O nano-oxides [2]. Therefore, GARS ODS steel powder offers the geometrical (i.e., spherical) and compositional (i.e., Y/Ti/O species all contained in the powder) requirements for cold spray deposition.

Experimental Procedure

Figure 1(a) shows a cross-section overview in scanning electron microscope (SEM) of the GARS ODS steel powder provided by Ames Laboratory. The powder size ranges between 45 μm and 108 μm. Figure 1(b) is medium magnification SEM image of several powder particles, showing the grain substructure inside. Figure 1(c) is high magnification image inside one powder particle, showing bright spots mainly decorating the grain boundaries. Energy dispersive X-ray spectroscopy (EDS) mapping in Figure 1(d) reveals that these bright spots correspond to Y signals, namely these are Fe-Y intermetallic particles.

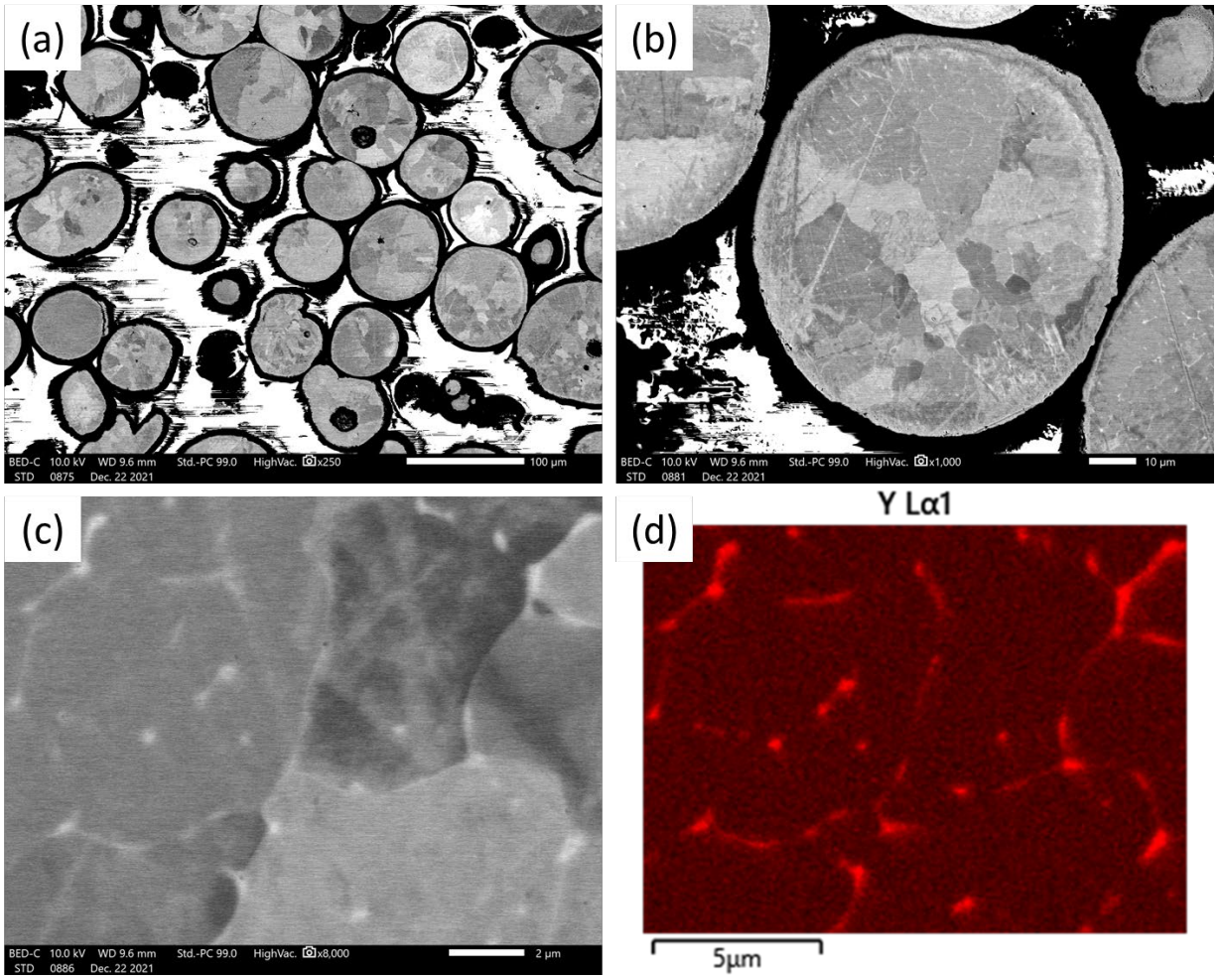

Figure 1. (a) Cross-section SEM overview of the GARS ODS steel powder. (b) Grain substructure inside powder particles. (c) Bright spots decorating the grain boundaries. (d) EDS map showing bright spots are Fe-Y intermetallic particles.

Preliminary Results and Future Work

The P92 steel substrates had as-machined surface which could be beneficial for bonding at the cold spray interface. Based on prior experience with steels and Ni alloys, a set of robust cold spray parameters were chosen to ensure effective deposition and preserve limited GARS powder. For example, helium carrier gas was used at 600 psi, with the gas temperature at 650°C. It is noted that 650°C would still be considered "cold" for ODS steel powder since such a temperature wouldn't alter the powder microstructure. As shown in Figure 2, two large-area ODS steel deposits (#1 and #2) were cold sprayed onto P92 substrates,

respectively. The #1 was used for optimization of the FSP step, where 4 trail FSP passes were performed. First to determine the optimal FSP tool plunge depth where abundant material was getting processed while also ensuring that the tool was not "buried" in the material to the point of damaging the tool itself. Then the compression force on the FSP tool was fine tuned to enable temperature controlled FSP run (at 750°C) through a combination of steady force and tool rotation speed (rotation per minute [RPM]). After these optimizations, a "1.5" pass was performed where after one complete pass along the "X" direction for 4'', the tool traversed in the "Y" direction for 8 mm then travelled back in the "X" direction again for 2''. In this way, cross-section samples can be extracted from the tracks of both the single pass and the "overlapping" 2 passes. Upon examination of the two samples with optical microscopy (OM) and hardness mapping, #2 plate was FSP processed with an 8-pass raster.

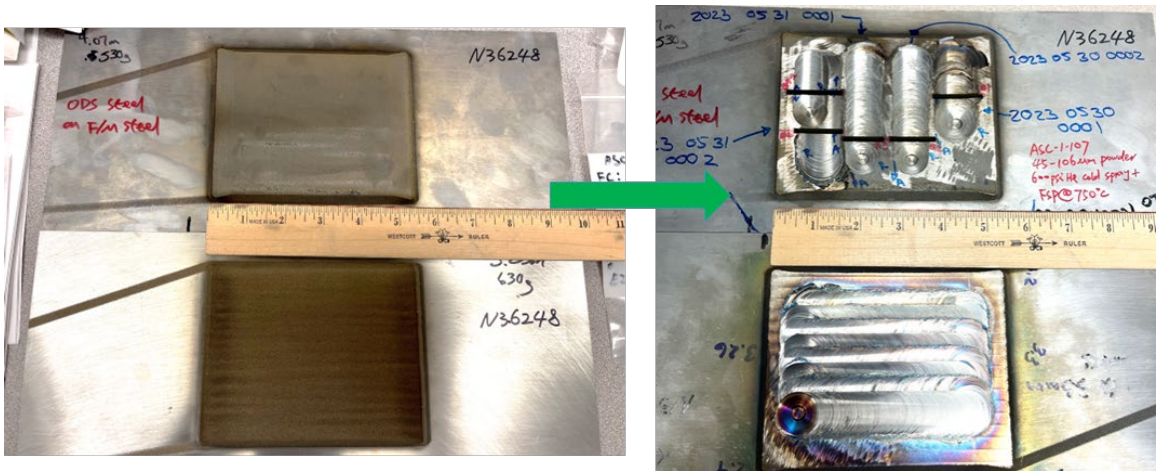

Figure 2. Two large-area ODS steel deposits (#1 and #2) were cold sprayed onto P92 substrates, respectively. The #1 plate was used for optimization of the FSP step. The #2 plate was FSP processed with an 8-pass raster.

Figure 3 is the OM and hardness map of the cross section of the single pass. The top ~3.5 mm thickness is the ODS layer (brighter color), whereas the much thicker bottom part is the P92 substrate. The black dashed line outlines the approximate shape of the FSP zone, namely outside the FSP zone is the as-cold sprayed ODS steel deposit. The OM and hardness map reveals that the as-cold sprayed deposit (e.g., the top-right corner) has non-uniform structure, in that most areas have high hardness due to the plastic deformation from cold spray impact; but due to remaining porosity, some areas have very low hardness. In contract, FSP zone has very uniform hardness (hence microstructure) with ~200 HV hardness value. This means that FSP at 750°C achieved the goal of eliminating cold spray defects and forming full-dense material with likely uniform microstructure.

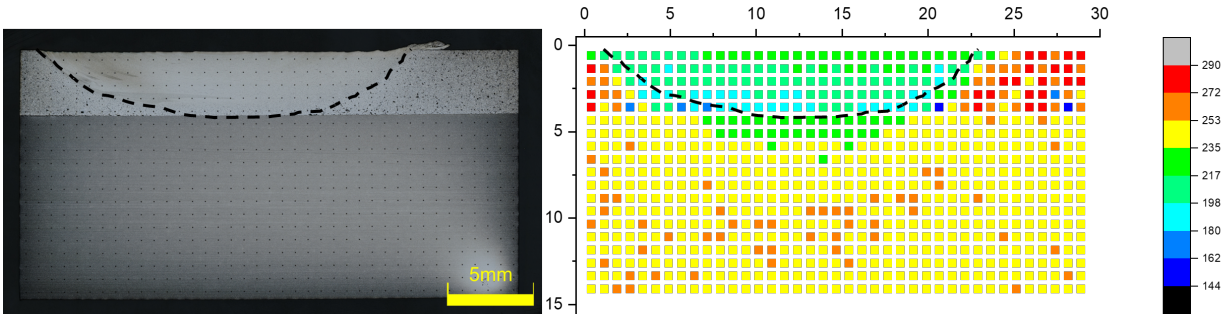

Figure 3. The OM montage image and hardness map of the cross section of the single pass.

Similarly, Figure 4 is the OM and hardness map of the cross section of the overlapping two passes. Even though one might see a slight trace of the second FSP pass as pointed out by the yellow arrow in the OM image, the hardness map shows very uniform hardness distribution in the FSP zone (outlined approximately by the black dashed line). Namely, the two-pass experiment demonstrated that procession of partially overlapping FSP passes (i.e., FSP raster) has the potential of transforming extended area of cold sprayed ODS steel deposit into pore-free uniform bulk material.

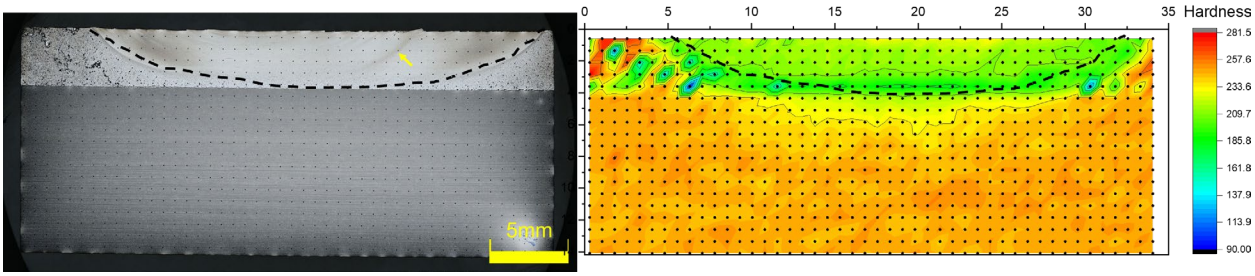

Figure 4. The OM montage image and hardness map of the cross section of the overlapping two passes.

Future work will focus on subsequent characterization and mechanical testing of the #2 large plate after FSP raster to quantify dispersed oxide particles and grain structure, hence their effects on tensile strength, ductility, fracture toughness, and creep behavior at 650°C and above.

Acknowledgements

This research is funded by the U.S. Department of Energy Office of Fusion Energy Sciences under contract DE-AC05-76RL01830. We are grateful to cold spray technical support provided by Chris Smith, Justin Olson, and Mark Rhodes.

References

[1] M. Rieth, M. Dürrschnabel, S. Bonk, G. Pintsuk, G. Aiello, J. Henry, Y. de Carlan, B.E. Ghidersa, H. Neuberger, J. Rey, C. Zeile, N. De Wispelaere, E. Simondon, J. Hoffmann, Impact of materials technology on the breeding blanket design – Recent progress and case studies in materials technology, Fusion Engineering and Design 166 (2021) 112275.

[2] J. Rieken, Gas atomized precursor alloy powder for oxide dispersion strengthened ferritic stainless steel, Ames Laboratory (AMES), Ames, IA (United States), 2011, p. 362.

2.2 BASIC CHARACTERISTICS OF LOW-COST ODS ALLOYS—T.S. Byun, T. Lach, Y. Lin, D. Collins, D. Hoelzer (Oak Ridge National Laboratory)

OBJECTIVE

This research is to develop an economically attractive, technically feasible processing route for oxide dispersion strengthened (ODS) ferritic alloys for fusion reactor structural components. Microstructures and mechanical properties are analyzed to evaluate the newly produced ODS materials.

SUMMARY

Various ODS steels produced via different thermomechanical treatment (TMT) routes, which did not include the traditional mechanical alloying process, were analyzed for microstructure characteristics and key mechanical properties. In production of each ODS alloy, a combination of high-temperature rolling operations is applied to a simple mixture of Fe-14Cr or Fe-10Cr alloy powder and yttrium or iron oxide powder to consolidate the powder mixture, refine the microstructure, and redistribute the alloying elements using thermomechanical activation. Thus far, more than twenty combinations of thermomechanical processes and alloy powder/oxide powder mixtures have been attempted with uniaxial tensile testing to obtain strength and ductility data to down select the ODS materials with desirable properties. For some selected materials, further characterizations have been performed to obtain more detailed property information, such as high-temperature tensile properties, fracture toughness values, grain structures, and particle distributions. This report presents some newly obtained materials characterization data, including a comparison with the reference ODS ferritic alloy (14YWT-PM).

PROGRESS AND STATUS

In the earlier report, the uniaxial tensile ductility and strength data were used to compare the ODS materials produced by different processing routes. Among the thermomechanical processing routes applied in the research, the TMT process consisting of powder consolidation at 900°C and multiple rolling's at relatively low temperature (550−600°C) produced reasonably good tensile properties. A good combination of tensile properties was measured from the 14YWT (HR-2CC) alloy, which was from the 14YWT/Fe_2O_3 mixture processed via HR-2CC (see Table 1). This alloy demonstrated a good combination strength and ductility: a yield strength of ~880 MPa and an ultimate tensile strength of ~1090 MPa; a uniform elongation of ~5% and a total elongation of ~13%.

Further investigation has been performed for the 14YWT alloys produced via a few selected processing routes. Table 1 summarizes the base materials (i.e., powder mixtures) and the TMT processes applied to the powder mixtures. Note that the 14YWT base alloy powder included some yttrium (~0.1%), into which oxide powders were mixed to provide oxygen for an oxide content of 0.3-0.4 wt.% in total. The standard 14YWT alloy produced by mechanical alloying and consolidation is included for comparison. Note that this reference ODS alloy has a very high strength (yield stress ~1500 MPa) but low uniform and total ductility (< 1% and < 3%, respectively), which is one of the most extremely strengthened ODS alloys.

The scanning electron microscope (SEM) Electron Backscatter Diffraction (EBSD)-IPF images showing grain structures and grain orientation distributions are compared in Figure 1. The 14YWT materials without mechanical alloying shown in Figures 1(a)−1(c) demonstrate overall very fine grain structures but their size distributions seem bimodal, and the grain orientations form domains within which both grain orientations and sizes are similar. These grain structures might indicate that the domains are related to the deformation process of alloy powder: during the TMT process imposing heavy deformation, each powder grain might be broken into many grains and subgrains. It is noted that many grain and subgrain boundaries appear not clear, which shows a strong contrast to the grain structure of 14YWT-PM. Along with the nonuniform grain sizes, these rather fuzzy boundaries might indicate that the microstructures in Figures 1(a)−1(c) are partially recovered structures and still under strong residual internal stresses. The grains in 14YWT-PM shows not only clear boundaries but also uniform sizes, and those are overall less texturized. This may indicate that

the structure is in a more annealed state and grains have nucleated and grown from the completely milled powder in near-amorphous state.

Table 1. Summary of base materials, processing steps, and testing status for the selected ODS alloys

Process ID	Base Materials (Alloy and Oxide Powders)	Consolidation Process (Strain)	Continuous TMT (Total Strain)
HR-3A	14YWT base+Y_2O_3	6 x HR at 900°C (80%)	8 x HR at 550 °C (240%)
HR-1CC	14YWT alloy (with Y, O)	6 x HR at 900°C (80%)	8 x HR at 600 °C (220%)
HR-2CC	14YWT base+Fe_2O_3	6 x HR at 900°C (80%)	8 x HR at 600 °C (220%)
14YWT-MA	14YWT base+Y_2O_3	850°C extrusion after high-energy mechanical milling	

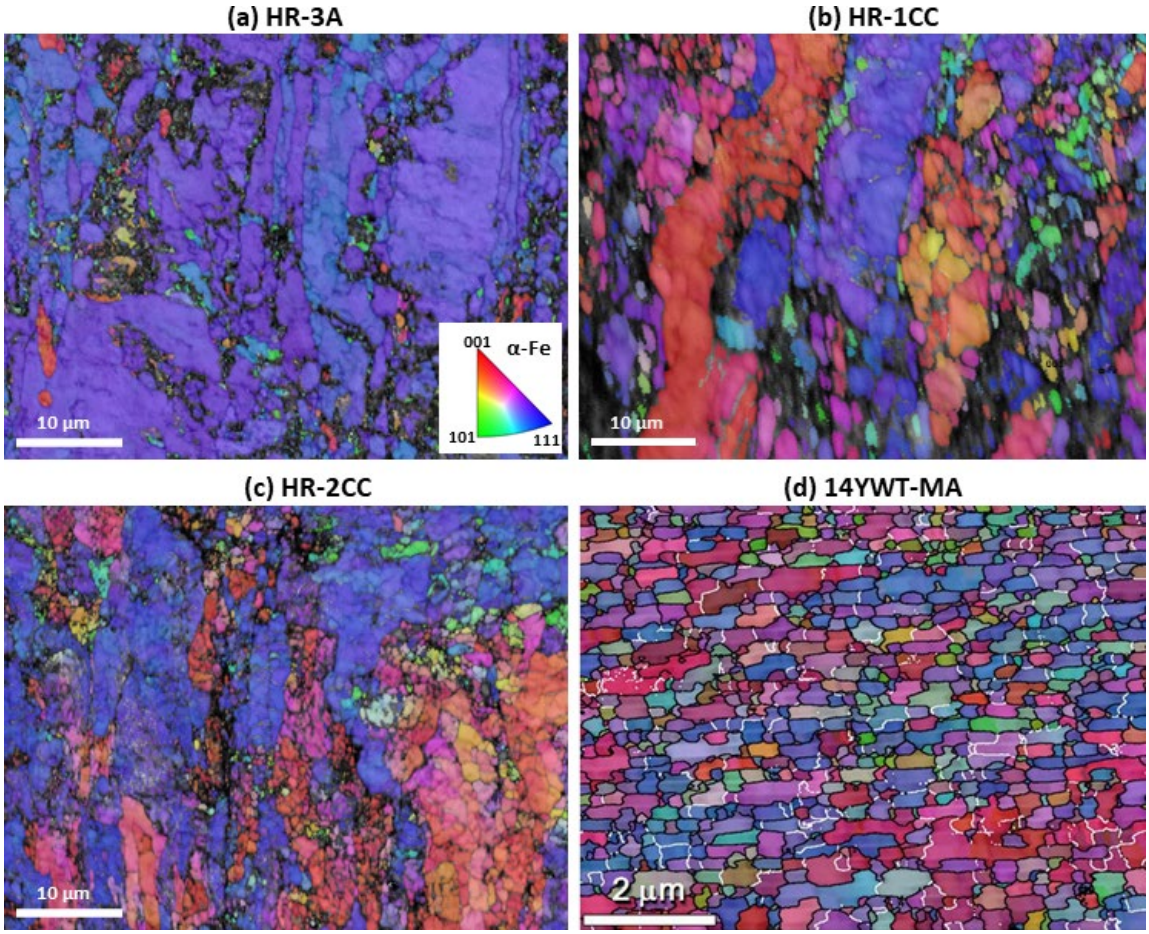

Figure 1. Grain structures of ODS steels: (a) HR-3A from 14YWT based alloy mixed with yttrium oxide, (b) HR-1CC from Y and O containing 14YWT, (c) HR-2CC from 14YWT mixed with iron oxide, and (d) 14YWT-MA from the traditional 14YWT processing.

The room temperature fracture toughness values (K_C, converted from 0.2 mm offset J-integral value) are compared for the ODS alloys from different powder mixtures and processing routes. The first three alloys show fracture toughness values in a very narrow range of 91 – 93 MPa√m, while the HR-3A alloy shows a

relatively higher value of ~130 MPa√m. Considering the low-cost processing, which consisting of a simple powder mixing and a series of TMT steps, fracture toughness is well maintained in the new ODS alloys.

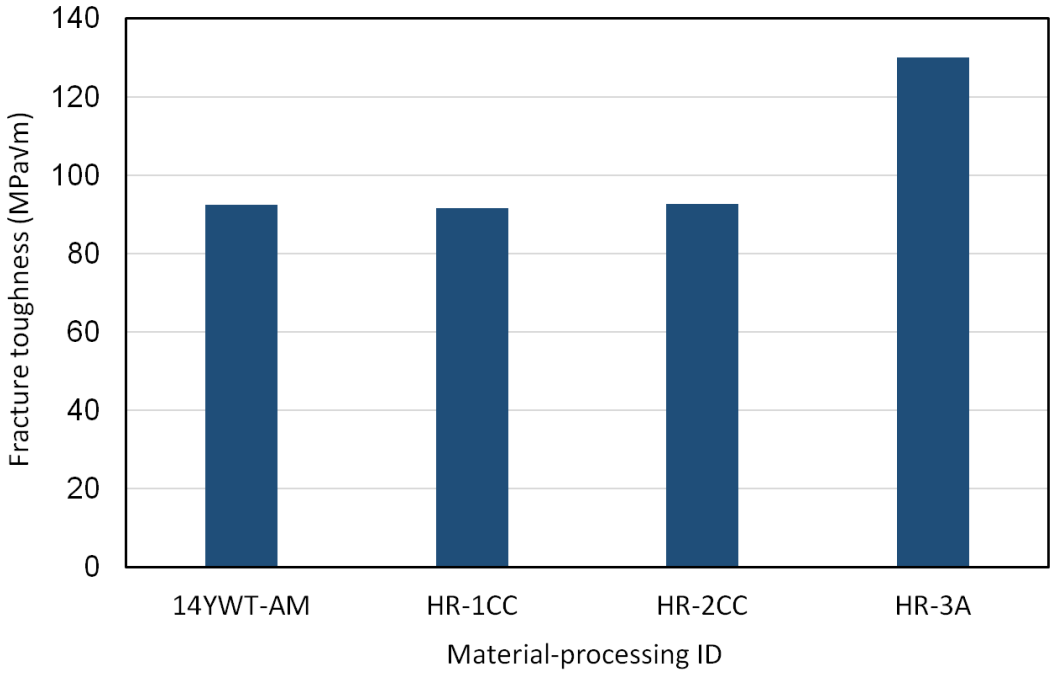

Figure 2. Comparison of room temperature fracture toughness (K_C) data for different 14YWT alloys. Note that the 14YWT-AM is the standard 14YWT ODS alloy (SM10 version).

Future Work

Fracture toughness testing at high temperatures and microscopy for characterizing distribution of oxide particles will be continued for the low-cost ODS alloys. Down selection of the processing route and powder mixture will be completed based on the mechanical properties data and oxide distribution characteristics.

2.3 TENSILE PROPERTIES OF AN OUT-OF-PLANE S-ORIENTED 14YWT NANOSTRUCTURED FERRITIC ALLOY NFA-1—M. Alam, G. Odette (University of California, Santa Barbara), D. Hoelzer (Oak Ridge National Laboratory), S. Maloy (Pacific Northwest National Laboratory)

OBJECTIVES

The main objective of this study is to characterize the tensile properties of a larger heat of 14YWT nanostructured ferritic alloy (NFA)-1, at its short thickness (S) orientation at a wide range of temperatures.

SUMMARY

The Fuel Cycle Research and Development (FCRD) NFA-1 is a 55-kilogram heat of best practice NFA that was synthesized by ball milling argon atomized Fe-14Cr-3W-0.4Ti-0.2Y (wt.%) and FeO powders, followed by hot-extrusion at 850°C, annealing and multi-pass cross-rolling, both at 1000°C, to produce a ≈ 10 mm thick plate. The cross-rolling stage results a large population of {001}<110> cleavage system microcracks (MCs) that run on planes parallel to the plate face and side, which we call here an S direction. The NFA-1 exhibits excellent in-plane (L and T) tensile strengths and ductility (σ_y ≈ 1042 ± 102 MPa, σ_u ≈ 1133 ± 100 MPa, and ε_t ≈ 12.9 ± 1.5% at room temperature [RT]). However, the out-of-plane, S RT tensile properties are quite inferior (σ_y ≈ 708 ± 57 MPa, σ_u ≈ 730 ± 92 MPa, and ε_t ≈ 0.2 ± 0.2%) due to the orientation and presence of pre-existing MCs. The MCs vary in size and density within, and in between the plates. Here, we have performed the tensile test on an S-oriented NFA-1 specimen at a wide range of temperatures (800 to -196°C) to understand the effect of MCs, orientation, and temperature on the tensile properties, and compared it with the L-oriented tensile properties.

PROGRESS AND STATUS

Introduction

Background on the NFA and further details on NFA-1 are reported elsewhere and will not be reviewed here [1-5]. In short, NFAs, a variant of oxide dispersion strengthened (ODS) steels, possesses a unique combination of properties like high strength, excellent irradiation tolerance, outstanding thermal stability up to 900°C and corrosion resistance, and therefore, are considered a promising candidate for the advanced nuclear fission and future fusion reactor applications [5]. The material of interest, NFA-1, is developed in a collaboration among the Oak Ridge National Laboratory (ORNL), Los Alamos National Laboratory (LANL) and the University of California Santa Barbara (UCSB), which was processed by first ball milling Fe-14Cr-0.25Y-3W-0.35Ti (wt.%) gas atomized powder with FeO powder to dissolve the Y and provide a proper balance of Ti and O. The mechanically alloyed powders were then canned, degassed, hot extruded at 850°C, annealed for 1 h and cross-rolled to a ≈ 50% thickness reduction, both at 1000°C, to form a ≈ 15 mm thick can, containing a ≈10 mm NFA-1 plate sandwiched in-between the can.

The orientation of the plane and the specimens for NFA-1 are shown in Figure 1a. The top face (LT) of the plate exhibits nearly equiaxed grain morphology with an average grain size of ≈ 0.64 ± 0.45 μm along with a small fraction of larger 1-10 μm grains. The front (TS) and side (LS) of the plate exhibit pancake-shaped ≈ 0.8 ± 0.6 x 0.3 ± 0.1 μm size grains. Bimodal grains with up to 10 μm length were also observed. The TS and LS plate view also reveal a large number of MCs lying on planes parallel to the plate faces (normal to the thickness direction, see Figure 1b). The average crack mouth opening width is ≈ 250 nm, whereas the average crack separation distance is ≈ 16 μm (Figure 1c and Reference [3]). Figure 1d shows the crack distribution. The average crack length is ≈ 12 ± 9.5 μm, and the observed range is from 2 μm to 105 μm, with an average crack density is ≈ 2.4 x $10^9/m^2$. Note, around 75% of the observed cracks are below 15 μm. Also note, no crack was observed on the LT face view. The details of microstructural observation, the texture, and MC formation mechanisms are reported in [2,3,6].

Due to the presence of MCs, the mechanical properties are highly anisotropic. The tensile test on the in-plane L and T specimens shows very good strength and ductility over a wide range of temperatures. However, the RT tensile properties of the out-of-plane, S specimens are quite inferior and often failed in their elastic loading zone with zero ductility. Here, in this study, we have investigated the tensile properties of S-oriented specimens at a wide range of temperatures from -196°C up to 800°C and compared them to the in-plane L-oriented tensile properties. In most cases, two to four specimens were tested, except for the -100 and -150ºC for the S-tensile specimens, where we tested 15 specimens at each temperature to observe the effect of specimen size (therefore crack length) and the plate variations.

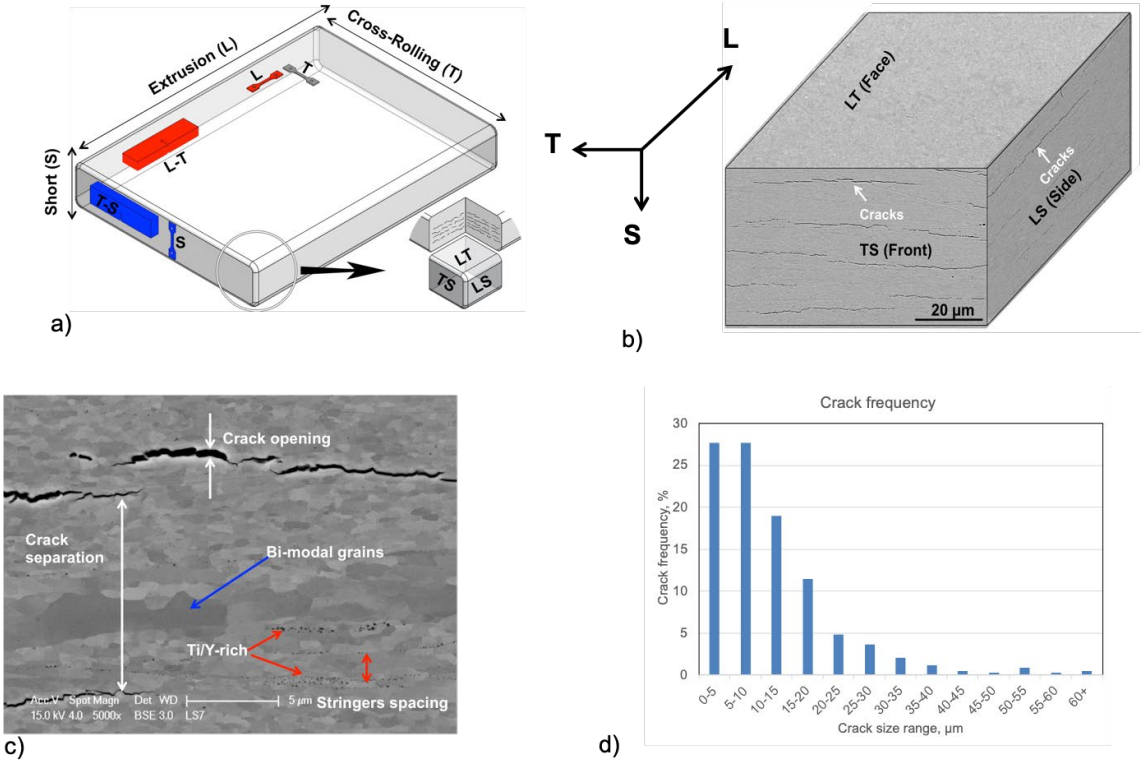

Figure 1. a) NFA-1 specimen orientations labeled with respect to the extrusion, cross-rolling, and plate thickness directions; b) MCs and their orientation; c) high magnification scanning electron microscope (SEM) image showing the grain and MCs; and d) the MCs distribution.

Experimental Procedure

The uniaxial tensile tests, loaded in the S direction, were performed on two different dog-bone-shaped and sub-sized flat specimens that are fabricated by electrical discharge machining (EDM). The SSJ2 type specimens are fabricated from both plate-1 (P1) and plate-2 (P2) with a nominal gage section length, width, and thickness of 5.0x1.2x0.5 mm; see Figure 2a. The µ-SSJ2 type specimens are fabricated only from NFA-1 P2, which is relatively thinner than P1. The nominal gage section dimension of µ-SSJ2 is 2.2x0.86x0.5 mm (Figure 2b). Before testing, all specimens were sanded down to 1500 grit to remove any surface contamination, minor cracks, or residual stresses due to the EDM machining. All the in-plane L-oriented specimens are SSJ2 type and fabricated from P1. The tests were carried out on an 810 MTS servo-hydraulic universal testing machine equipped with both the clam-shell resistance heating furnace and a cooling chamber. The specimens were heated in air to the target temperature and held for 10 min at the target temperature before testing. For the low-temperature test, the specimens were cooled to the target temperature by spraying controlled LN_2 in an atmospheric environment and held for 30 minutes before testing. Testing was carried out at a strain rate of $\approx 10^{-3}$/s. Except for the small size of the specimens, the tensile properties were determined in accordance with ASTM Standard E8M-15 [7].

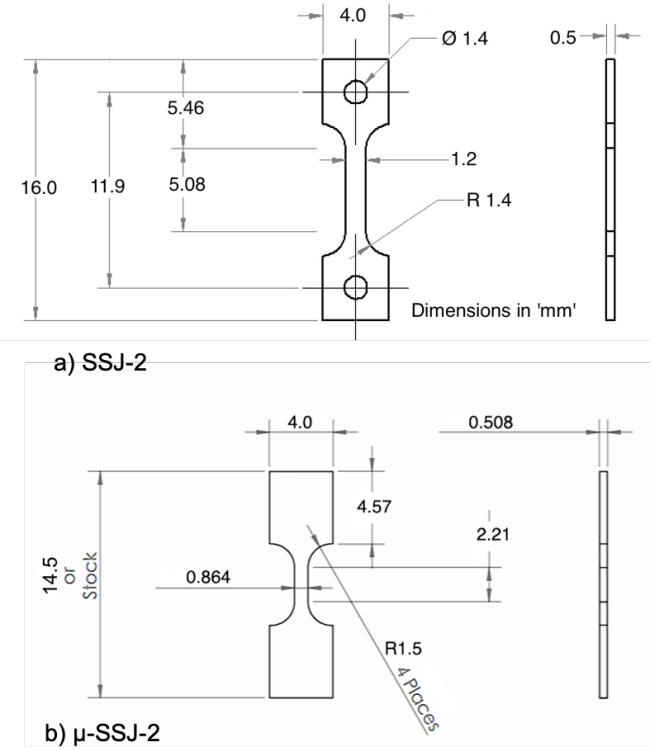

Figure 2. Schematics of tensile specimens: a) SSJ-2; and b) μ-SSJ-2, used in this study.

Materials

Room to low-temperature tensile properties

Table 1 shows the room (≈ 23°C) to low temperature, up to -196°C, tensile properties of the S-oriented NFA-1 specimens. The in-plane L-oriented tensile properties are also summarized in Table 1 for comparison. Note, the in-plane L, and T-oriented tensile specimens show relatively similar properties [2], and therefore only L-oriented tensile tests are mentioned here. Also note, S-oriented specimens are fabricated from two different batches of NFA-1 plates and tested on two different specimen sizes (SSJ2- and μ-SSJ2, see Figure 2) at lower temperatures. However, due to the fair comparison, we have mentioned here only the tests that are performed on SSJ2 specimens and from P1. The effect of specimen size and NFA-1 plate variation on the low-temperature S-loaded tensile properties has been discussed below in a separate sub-section. The representative engineering stress-strain (σ-ε) curves and the low-temperature tensile properties for S- and L- oriented specimens are shown in Figure 3. The RT 0.2% yield (σ_y) and ultimate (σ_u) tensile stress for the S-oriented specimen are 708 ± 57 MPa and 730 ± 92 MPa, respectively, which are quite inferior to the L-oriented specimens (σ_y = 1042 ± 102 MPa, σ_u = 1133 ± 100 MPa). Moreover, the S-tensile specimen mostly failed in its elastic region with ≈ 0% ductility whereas L-tensile shows ≈ 13% total ductility (Table 1). The lower strength and ductility for the S-oriented specimen are primarily due to the presence of MCs that runs normal to the loading directions (Figure 1a,b).

Table 1. Room (23 °C) to liquid nitrogen (-196 °C) temperature tensile properties of S- and L-oriented NFA-1

Test Temp. (ºC)	Specimen orientation	σ_y, MPa	σ_u, MPa	ε_u, %	ε_t, %
23	S	708 ± 57	730 ± 92	0.2 ± 0.3	0.2 ± 0.3
	L	1042 ± 102	1133 ± 100	3.8 ± 3.7	12.9 ± 1.5
-50	S	550 ± 8	550 ± 8	0 ± 0	0 ± 0
	L	1073 ± 65	1183 ± 76	6.9 ± 4	15.7 ± 0.7
-100	S	368 ± 107	368 ± 107	0 ± 0	0 ± 0
	L	1162 ± 54	1293 ± 62	5.7 ± 6	14.8 ± 1.8
-150	S	316 ± 43	316 ± 43	0 ± 0	0 ± 0
	L	1332 ± 69	1453 ± 103	6 ± 6.5	13 ± 5
-196	S	372 ± 23	372 ± 23	0 ± 0	0 ± 0
	L	1555 ± 121	1643 ± 112	1.0 ± 0	7.9 ± 0.7

σ_y = yield stress, σ_u= ultimate tensile stress, ε_u= uniform elongation, ε_t= total elongation

All the S-oriented tensile specimens that are tested at subzero temperature up to -196°C fractured in their elastic loading zone with 0% ductility (Figure 3b,c, and f). Note, the strengths also systematically decrease with decreasing temperature down to -150°C ($\sigma_y \approx \sigma_u \approx 316 \pm 43$ MPa) for the S-tensile specimen. This is due to the combination of microcracks and the cleavage orientation of the plane. However, the -196°C test show slightly higher strengths ($\sigma_y \approx \sigma_u \approx 372 \pm 23$ MPa) than -150°C. This might be due to the presence of various MC sizes. More tests were performed on lower temperatures that showed linearly downward strengths to -196°C which has been discussed later in this section. In contrast to the S-oriented low-temperature results, the in-plane, L-tensile specimens showed an opposite trend due to the Peierls stress, which is expected (see Figure 3d,e). The σ_y and σ_u at -196°C for the L-tensile specimen are 1555 ± 121 MPa and 1643 ± 112 MPa, respectively. Interestingly, both the uniform (ε_u) and total (ε_t) elongation either increased or unaffected up to -150°C ($\varepsilon_u \approx 6\%$, $\varepsilon_t \approx 13\%$), and only slightly reduced at -196°C ($\varepsilon_t \approx 8 \pm 1\%$) for L-tensile specimens (see Table 1 and Figure 3f).

Figure 4 shows the SEM fractographs for the selective S and L-oriented tensile specimens tested from RT (≈ 23°C) down to liquid nitrogen (LN_2 ≈ -196°C) temperature. Due to the high density of MCs whose crack planes are normal to the loading directions, along with bcc {001}<110> cleavage planes, all the S-oriented specimens including the RT test show flat, cleavage facets on their elastic fracture surfaces (Figure 4a-e). In contrast, the L-oriented fractures are dominated by periodic delaminations that split the gage section and form knife-edge type rupture features, full with shallow ductile dimples (Figure 4f-j). Note, for the L-tensile specimens, the microcracks plane is parallel to the loading direction, which gradually splits during the low-temperature test, which helps to reduce the stress concentration, and therefore, stops cleavage fracture to maintain similar ductility at a lower temperature compared to the RT. Also note, whereas the RT (down to LN_2) S-tensile shows flat, cleavage fracture; in contrast, the fully ductile features are observed for L-oriented specimens, even at -196°C (see Figure 4).

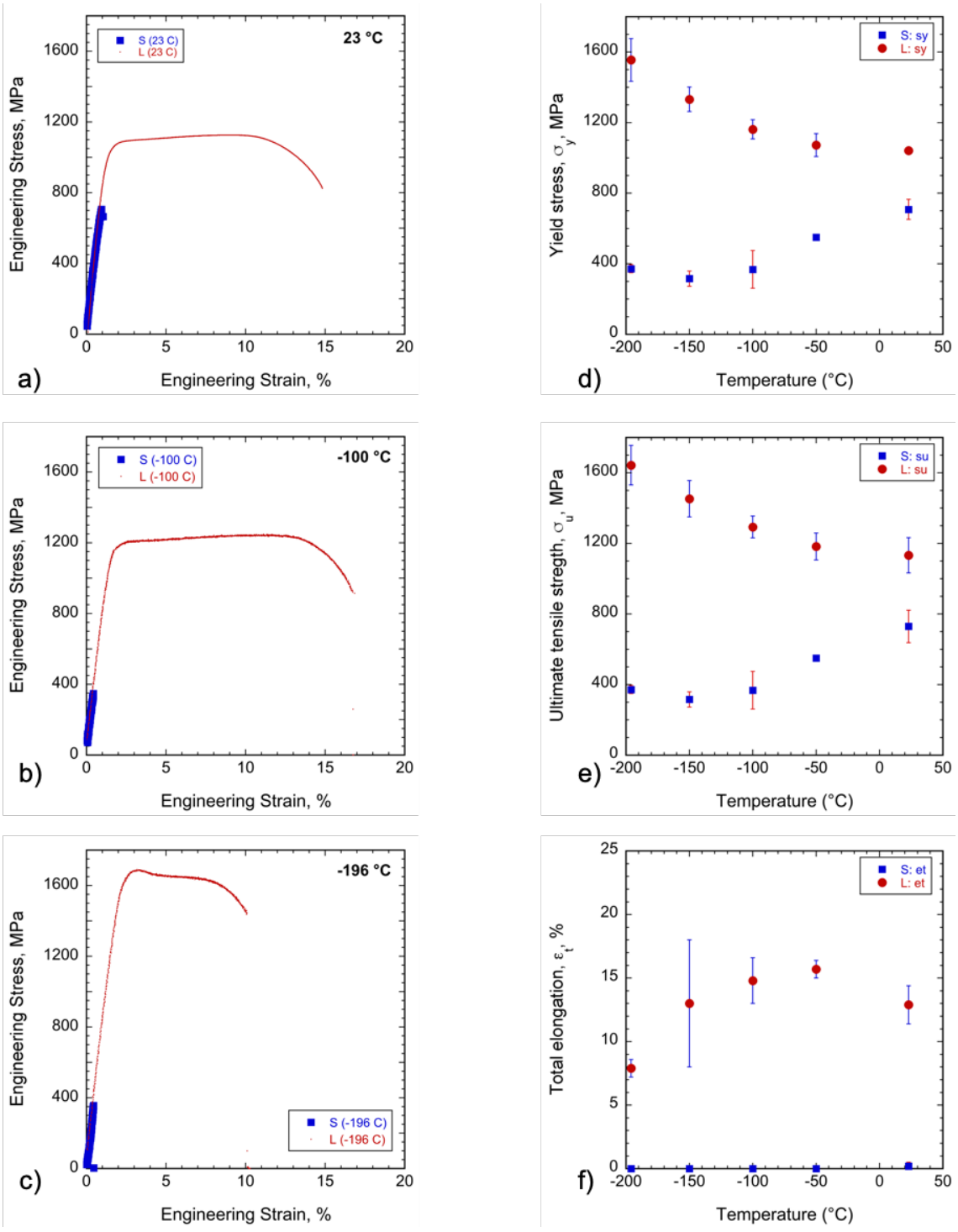

Figure 3. Engineering tensile stress-strain (σ–ε) curves for S and L-oriented NFA-1 specimens at: a) 23 °C; b) -150°C; c) -196°C, and their corresponding tensile properties are shown in: d) σ_y; e) σ_u; and f) ε_t, respectively.

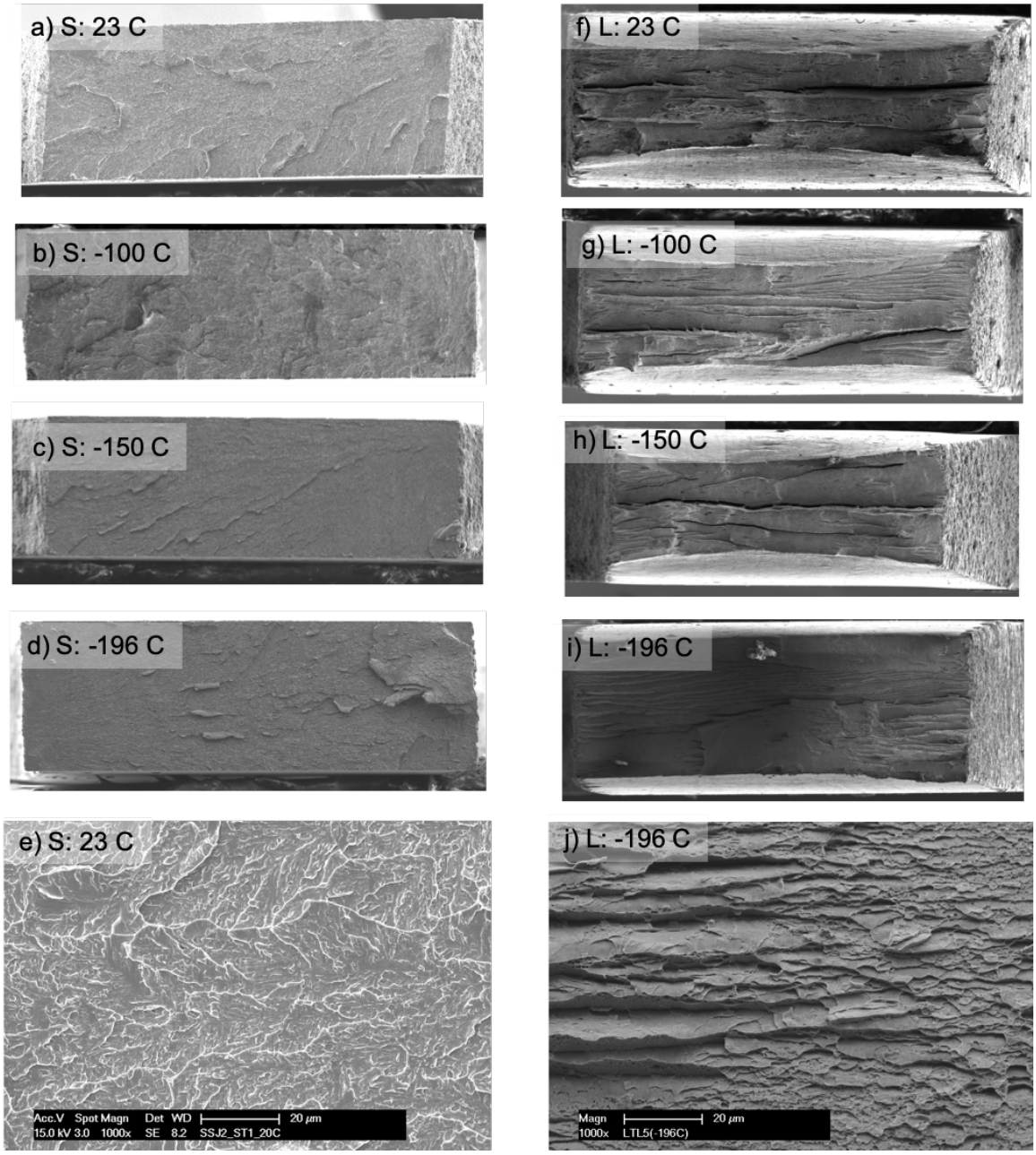

Figure 4. Low magnification SEM fractographs for S-oriented tensile specimens tested at: a) 23°C; b) -100 °C; c) -150°C; and d) -196°C; and for L-oriented specimens tested at: f) 23°C; g) -100°C, h) -150°C; and i) -196°C, respectively. Figure e) shows a high magnification SEM image for S at 23°C test that reveals cleavage fracture, whereas j) shows a high magnification SEM image with shallow ductile dimples for L-oriented specimen tested at -196°C. For low magnification images (a-d, f-i): the nominal specimen width is 1.2 mm, and the thickness is 0.5 mm before deformation.

High-temperature tensile properties

Figure 5a shows room-to-high temperature (up to 800°C) engineering stress-strain (σ–ε) curves for the S-oriented NFA-1 specimens. For comparisons, the σ–ε curves for L-oriented NFA-1 specimens up to 800°C

are also plotted in Figure 5b, and their corresponding σ_y, σ_u, and ε_t are plotted in Figures 5c,d, and e, respectively, and summarized in Table 2 along with ε_u.

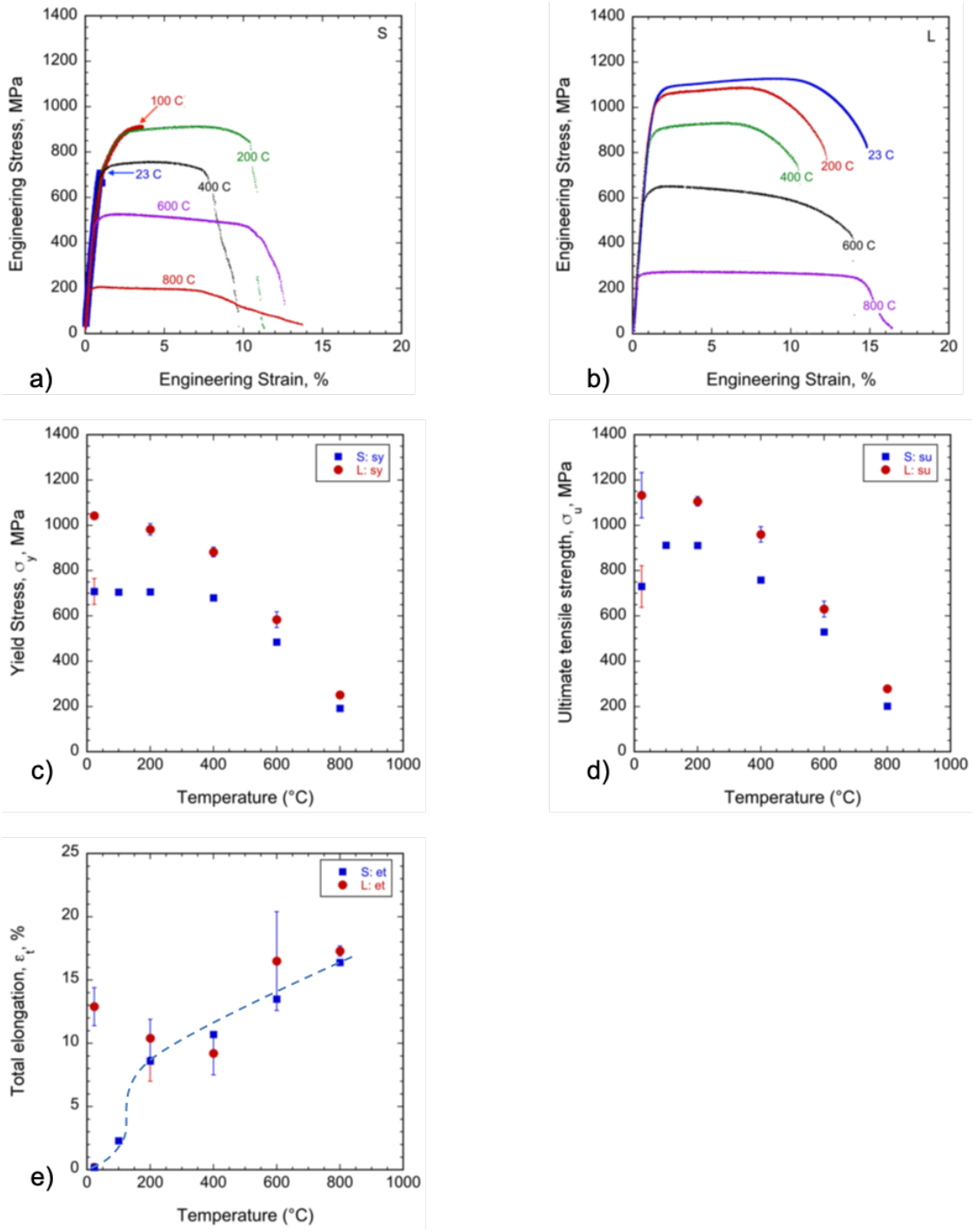

Figure 5. High-temperature engineering tensile stress-strain (σ–ε) curves are shown for: a) S; and b) L-oriented NFA-1 specimens. Their corresponding tensile properties are shown in: c) σ_y; d) σ_u; and e) ε_t, respectively.

While the RT S tensile fracture at the elastic loading zone, the S at 100°C test shows a small amount of yielding and strain hardening, though the fracture is still essentially brittle (Figure 5a). A significant plastic strain occurs at 200°C test for S tensile specimen with an $\varepsilon_t \approx 8.6 \pm 1.6\%$ (Figure 5a, e). Due to the increase in ductility, σ_u increases from 730 ± 92 MPa at RT to 911 ± 8 MPa at 200°C test, though the σ_y remains nearly the same to ≈ 700 MPa up to 400°C, and then both the σ_y and σ_u drop sharply after 400°C due to a variety of thermally activated processes including dislocation bypass mechanisms associated with de-pinning from the $Y_2Ti_2O_7$ nano-oxides (NOs) and coarser TiO_2 particles (Table 2 and Figure 5c,d) [5,8]. Nevertheless, both the σ_y (192 ± 12 MPa) and σ_u (201 ± 12 MPa) are still reasonably high at 800°C for the S-tensile specimen. The ε_t increases in a way that follows the tensile brittle-to-ductile transition (BDT) trend from room temperature ($\varepsilon_t \approx 0\%$) to 200°C ($\varepsilon_t \approx 9\%$), and then increases approximately linearly with temperature to 800°C ($\varepsilon_t \approx 16\%$) (see Table 2 and Figure 5e). Note, the MCs are very unlikely to heal in between 100 and 200°C tests, but we see a huge jump in ductility. We believe the cleavage plane, in combination with the MCs orientation, plays a major role for the lower ductility of S-tensile specimens at temperatures below 200°C. Therefore, the temperature below 200°C for S-tensile specimens can be rationalized by the BDT temperature, which in this case is ≈ 100°C.

In contrast to the S-tensile specimen, the L-tensile shows excellent RT properties as discussed above. Both the strength decreases slowly with increasing temperature up to 400°C, primarily due to the corresponding decrease in the shear modulus [2,5]. Similar to S-tensile, L-tensile specimens also drop strength rapidly after 400°C due to the similar deformation mechanism as mentioned for the S-tensile specimens (Table 2 and Figure 5b,c,d). The deformation is dominated by viscoplastic creep, even at relatively high strain (≈ 10^3/s). Despite the decrease at the higher temperature, the tensile strength for L-oriented specimens remains reasonably high with $\sigma_y \approx 584 \pm 35$ MPa, $\sigma_u \approx 630 \pm 35$ MPa at 600°C, and $\sigma_y \approx 251 \pm 6$ MPa, $\sigma_u \approx 278 \pm 15$ MPa at 800°C (Table 2). Note, the strength gap for S and L-tensile specimens is high up to 400°C and converges to close above 400°C (Figure 5c,d).

Table 2. Room to high (800 °C) temperature tensile properties of S- and L-oriented NFA-1

Test Temp. (ºC)	Specimen orientation	σ_y, MPa	σ_u, MPa	ε_u, %	ε_t, %
23	S	708 ± 57	730 ± 92	0.2 ± 0.3	0.2 ± 0.3
	L	1042 ± 102	1133 ± 100	3.8 ± 3.7	12.9 ± 1.5
100	S	705	912	2.3	2.3
	L	-	-	-	-
200	S	706 ± 9	911 ± 8	5.4 ± 1.2	8.6 ± 1.6
	L	982 ± 25	1106 ± 21	4.8 ± 1.5	10.4 ± 1.5
400	S	680	759	3.2	10.7
	L	882 ± 21	960 ± 34	4.5 ± 1.3	9.2 ± 1.7
600	S	484	529	1.7	13.5
	L	584 ± 35	630 ± 35	2.3 ± 1.0	16.5 ± 3.9
800	S	192 ± 12	201 ± 12	0.7 ± 0.0	16.2 ± 0.3
	L	251 ± 6	278 ±1	3.4 ± 0	17.3 ± 0.4

Low-magnification SEM images of the tensile side and fractured faces for S-oriented high-temperature tests are shown in Figure 6a-d for the side view and Figure 6e-h for the fractured view, respectively. Figure 6i-l shows the low-magnification SEM images of the fractured face for L-oriented specimens for comparison.

Figures 6a and e clearly show that the fractured specimens are very flat without any necking for the 100°C S tensile test. However, noticeable necking can be observed from the side view of the 200°C S-tensile test (Figure 6b) with much wavy-like, full of dimple features in its fractured face, shown in Figure 6f. Similar necking and fractured faces are observed for all high-temperature tests for S-tensile specimens (Figure 6). While the room or lower temperature L tensile fracture surfaces are dominated by periodic delaminations that splits gage sections (see Figure 4f-i), these delaminations diminish at higher temperature tests and are completely absent ≥ 400°C (Figure 6i-l).

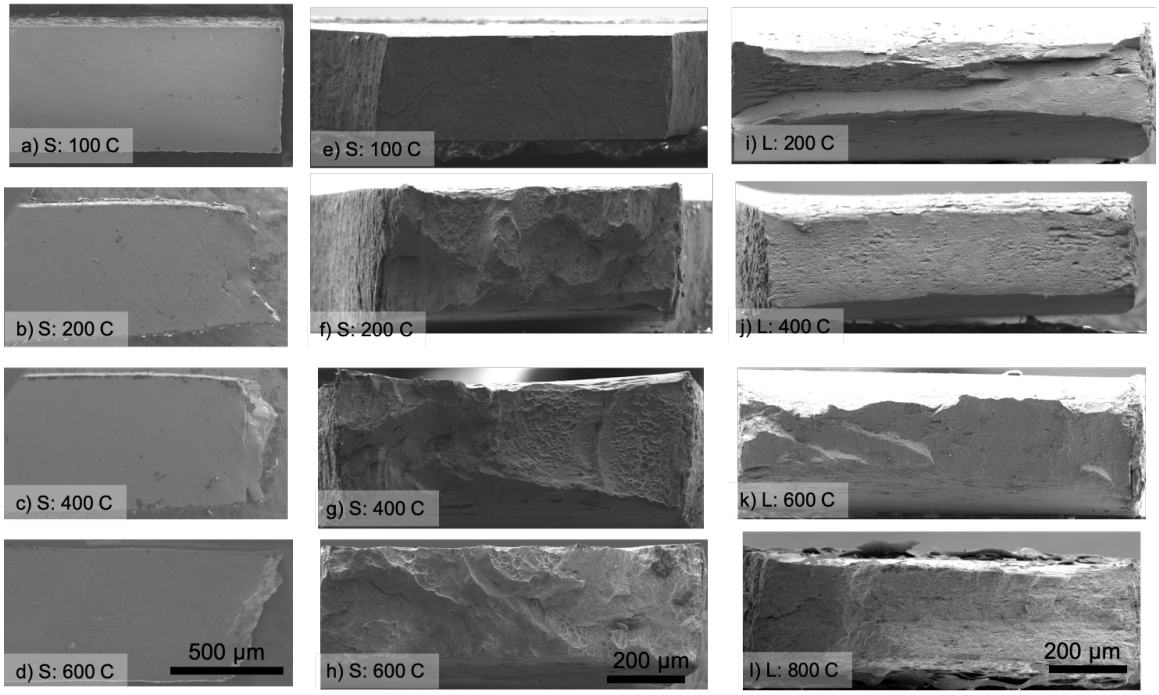

Figure 6. Low magnification SEM fractographs probed on the side (a-d) and fractured faces (e-h) for S-oriented tensile specimens tested at: a,e) 100°C; b,f) 200°C; c,g) 400°C; and d,h) 600°C; and fractured faces for L-oriented specimens at: i) 200°C; j) 400°C, k) 600°C; and l) 800°C, respectively. The scale bars are shown at the bottom of each column.

High-magnification SEM images of the tensile fractured surfaces for high-temperature tests are shown in Figure 7. Figure 7a shows the fractured surface for the 100°C S-tensile test that exhibits slight yielding before fracture. The cleavage features are dominated all over the fractured face, except for some random local areas where dimple features are observed (black box in top right of Figure 7a, and higher magnification view in Figure 7b). The TiO_2 coarse particles were found in the pocket of these dimples [2,4]. Figure 7c-e shows the high magnification SEM images for 200, 400, and 600°C S tensile tests, respectively, and reveals full of dimple features all over the surface. Note, some oxide layers are seen for the 600°C and above test, both for S and L-oriented specimens, since the test is performed in air. Figure 7f-h shows the shallow ductile dimples for the 200 and 400°C and deep dimples with coarser particles in pockets for 600°C tensile tests for L-oriented specimens. In general, the S and L-oriented fracture surfaces look very similar at or above 600°C.

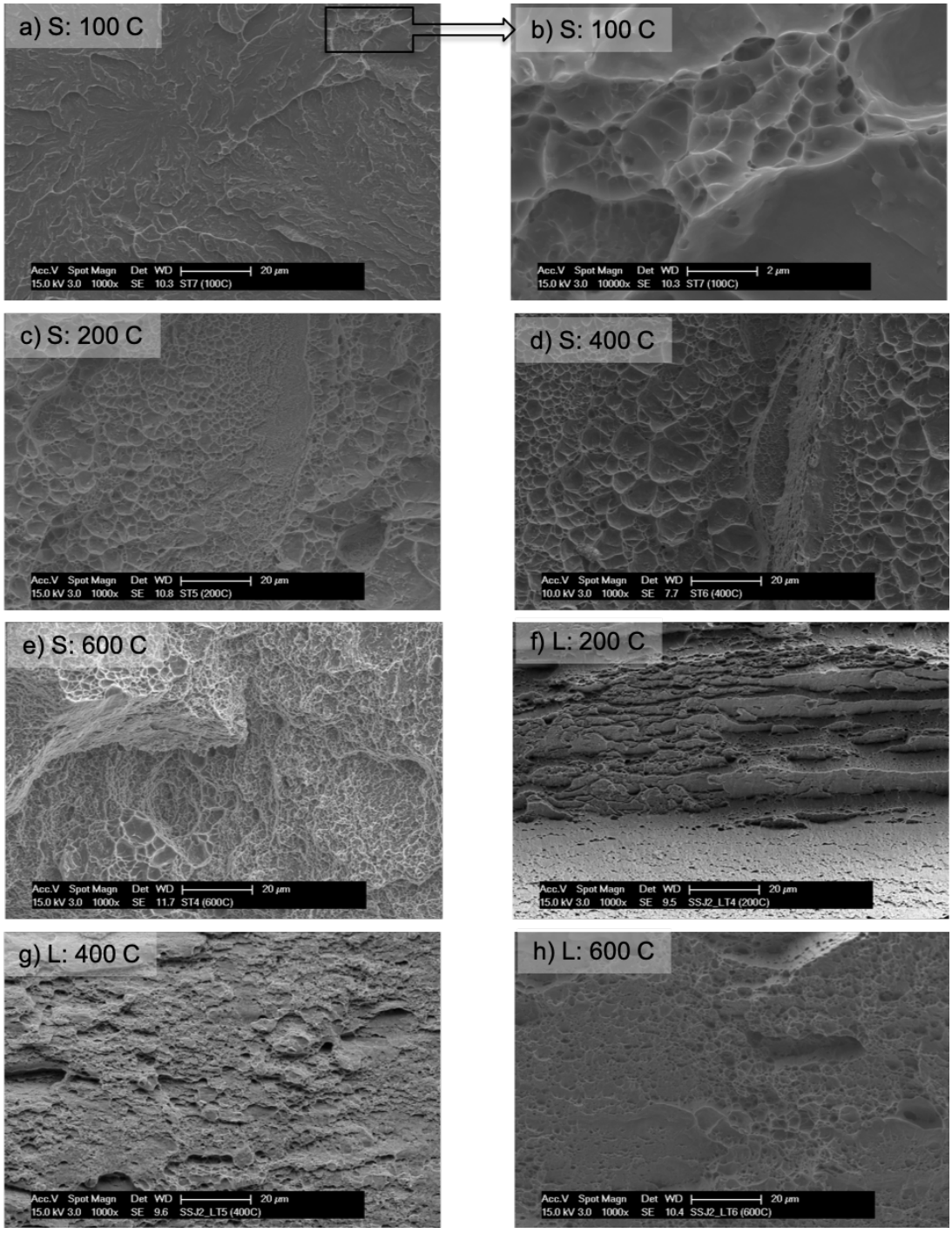

Figure 7. High magnification SEM images probed on tensile fractured faces for: a,b) S at 100°C; c) S at 200°C; d) S at 400°C; e) S at 600°C; f) L at 200°C; g) L at 400°C; and h) L at 600°C test, respectively.

Specimen size and NFA-1 plate variation for S-tensile test

The color-coded Table 3 shows the room (≈ 23°C) to liquid nitrogen temperature (-196°C) tensile properties as a function of NFA-1 plate and specimen size variation and are plotted in Figure 8. Note, S-oriented specimens are fabricated from two different batches of NFA-1 plate and tested on two different specimen

sizes (SSJ2-and μ-SSJ2, see Figure 2) at lower temperatures. The NFA-1 plate-2 (P2) follows the same synthetization procedures as plate-1 (P1), however, P2 somewhat found much lower MC density than P1. The black and red color codes are for SSJ2 specimens fabricated from the P1 and P2 of NFA-1, respectively. The blue color code is for the μ-SSJ2 specimens fabricated from P2. Since all of the specimens (except two out of 41 tests) failed in their elastic loading zone with zero ductility, therefore, we have considered only the σ_y ($\approx \sigma_u$) for analysis. The $\sigma_y \approx \sigma_u$ strength of all the RT to -196°C S-tensile results are plotted in Figure 8a. Again, all the room to low-temperature test S-tensile fractographs shows flat, cleavage fracture (as seen in Figure 4a-e), except those that show up to 3% ductility with very minimal localized ductile dimples (similar to Figure 7a,b). The average tensile strengths are much better for S when P2 test results are included with P1 ($\sigma_y \approx \sigma_u \approx$ 846 ± 192 MPa at RT and 562 ± 141 MPa at -100°C, Table 3) over only for P1 plate ($\sigma_y \approx \sigma_u \approx$ 708 ± 57 MPa at RT and 368 ± 107 MPa at -100°C, Table 1).

Figure 8b shows the effect of specimen size variation on the low-temperature S-tensile strength. Note, both the SSJ2 and μ-SSJ2 specimens are fabricated from P2. The SSJ2 shows lower σ_y than the μ-SSJ2 specimen at 23°C, however, the σ_u for that particular SSJ2 specimen is higher (1020 MPa) than σ_y (777 MPa) and nearly similar $\sigma_y \approx \sigma_u$ of the μ-SSJ2 specimen (1087 ± 18 MPa), see Table 3. The -100°C and -150°C results are inconclusive and very similar considering the standard deviation. Therefore, the effect of specimen size variation on strength is minimal or negligible, at least for the P2 which has a lower MCs density. Note, μ-SSJ2 specimens are not tested at -50°C and -196°C. Figure 8c again shows the specimen size variation effect. However, in this case, SSJ2 specimens' results are both from P1 and P2 whereas μ-SSJ2 specimens are only from P2. By adding the P1 SSJ2 with P2 SSJ2 results, the μ-SSJ2 shows better strength up to -100°C, though the -150°C test shows the opposite. However, considering the spreading, which is quite large in all cases, the effect of specimen size variation on the strength of S-tensile in low temperatures is minimal. Figure 8d shows strength variation as a function of NFA-1 plates. It is clear from Figure 8d that P2 is much stronger than P1 for S-oriented tensile specimens tested at a lower temperature. This is primarily due to the lower MC density of P2 than P1. Though both the NFA-1 plates are fabricated by following fairly similar procedures, the reasons for such plate-to-plate property variation are not clear at this moment. Specimen mapping from the plate location might help.

Table 3. Room to liquid nitrogen temperature tensile properties of S-oriented NFA-1 as a function of specimen type and plates

Test Temp. (°C)	NFA-1 Plate	Specimen type	Specimen ID	σ_y, MPa	σ_u, MPa	ε_t, %
23	P1	SSJ2	ST-01	765	832	0.5
		SSJ2	ST-02	707	707	0
		SSJ2	ST-13	652	652	0
	P2	SSJ2	ST-14	777	1020	3.6
		μ-SSJ2	ST-15	1074	1074	0
		μ-SSJ2	ST-16	1100	1100	0
Average				846 ± 192	898 ± 194	0.7 ± 1.4
-50	P1	SSJ2	ST-L1	544	544	0
		SSJ2	ST-L8	555	555	0
	P2	μ-SSJ2	ST-L38	717	717	0
Average				605 ± 97	605 ± 97	0 ± 0
-100	P1	SSJ2	ST-L2	443	443	0
		SSJ2	ST-L9	292	292	0

	P2	SSJ2	ST-L11	551	551	0
		SSJ2	ST-L12	749	749	0
		SSJ2	ST-L13	538	538	0
		SSJ2	ST-L14	428	428	0
		SSJ2	ST-L15	686	686	0
		SSJ2	ST-L16	625	625	0
		SSJ2	ST-L17	586	586	0
		SSJ2	ST-L18	423	423	0
		μ-SSJ2	ST-L20	781	781	0
		μ-SSJ2	ST-L21	605	605	0
		μ-SSJ2	ST-L22	734	898	3.2
		μ-SSJ2	ST-L23	658	658	0
		μ-SSJ2	ST-L24	486	486	0
Average				562 ± 141	562 ± 141	0.2 ± 0.8
-150	P1	SSJ2	ST-L3	285	285	0
		SSJ2	ST-L10	346	346	0
	P2	SSJ2	ST-L5	458	458	0
		SSJ2	ST-L6	410	410	0
		SSJ2	ST-L19	524	524	0
		μ-SSJ2	ST-L25	553	553	0
		μ-SSJ2	ST-L26	249	249	0
		μ-SSJ2	ST-L27	393	393	0
		μ-SSJ2	ST-L29	342	342	0
		μ-SSJ2	ST-L30	414	414	0
		μ-SSJ2	ST-L3	335	335	0
		μ-SSJ2	ST-L32	474	474	0
		μ-SSJ2	ST-L33	298	298	0
		μ-SSJ2	ST-L34	277	277	0
		μ-SSJ2	ST-L35	365	365	0
Average				382 ± 91	382 ± 91	0 ± 0
-196	P1	SSJ2	ST-L4	388	388	0
		SSJ2	ST-L7	356	356	0
Average				372 ± 23	372 ± 23	0 ± 0

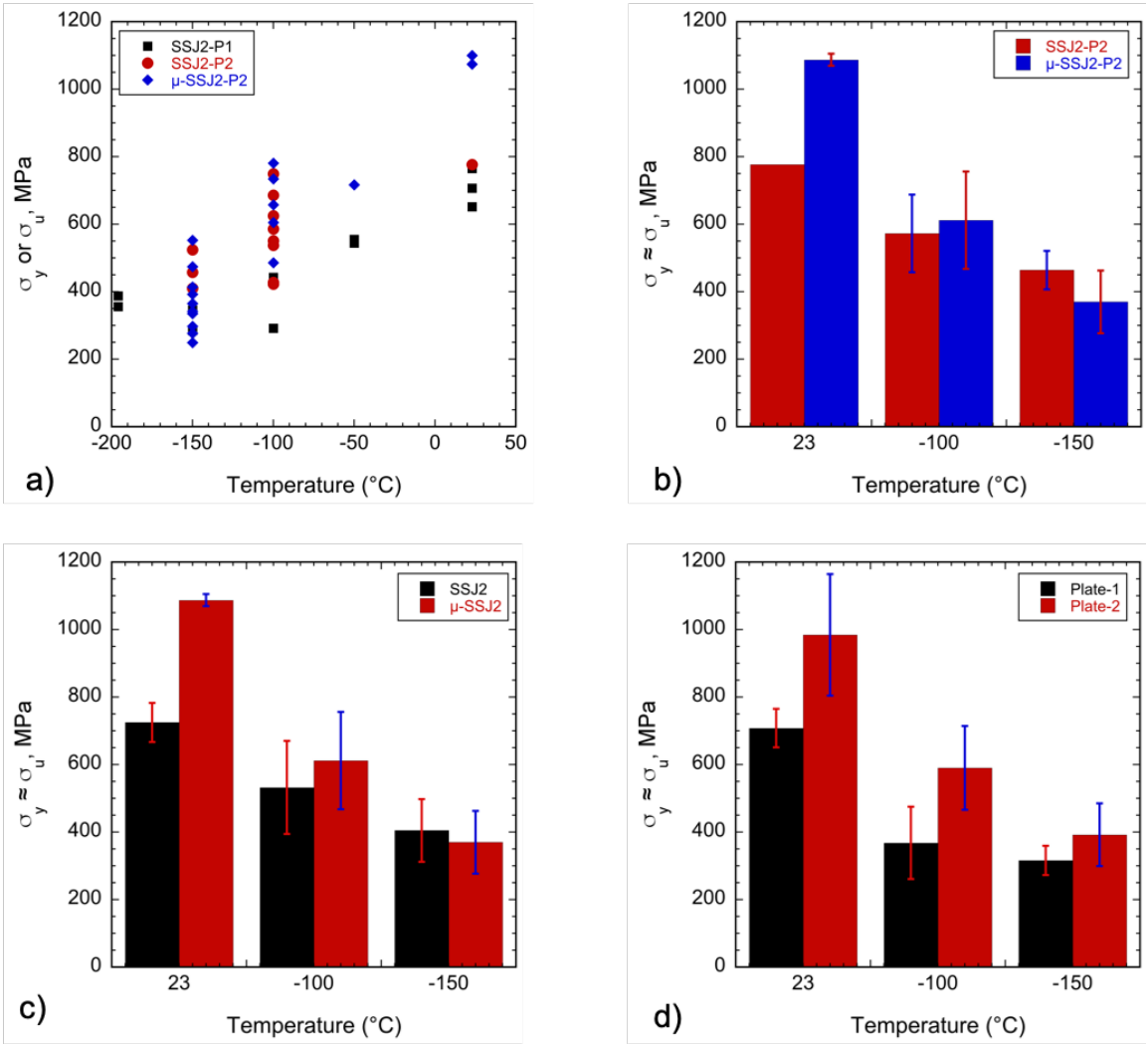

Figure 8. $\sigma_y \approx \sigma_u$ for S-oriented tensile specimens and the effect of specimen size and plates: a) all S-tensile tests from room to -196°C; b) SSJ2 vs. μ-SSJ2 specimen size variation for P2 NFA-1; c) SSJ2 (P1+P2) vs. μ-SSJ2 (P2) specimen size variation; and d) P1 vs. P2.

Results

We have performed tensile tests on a wide range of temperatures (-196°C to 800°C) for the out-of-plane, S-oriented FCRD NFA-1 material. All the room to -196°C test specimens fractured in their elastic loading zone with zero plasticity. The strength also gradually reduced with decreasing temperature ($\sigma_y \approx 708 \pm 57$ MPa at RT and 372 ± 23 MPa at -196°C). All the fractured surfaces were very flat, full of cleavage-dominated features. In contrast, the in-plane L tensile results showed an increase in strength with the decrease in temperature ($\sigma_y \approx 1042 \pm 102$ MPa at RT and 1555 ± 121 MPa at -196°C). The L-oriented specimens also showed ductility up to ≈ 8%, even at -196°C. The texture and microcrack plane orientation with respect to the specimen orientation and loading might be the main reason for such contrasting behavior. The higher temperature test for S-tensile specimens showed that the σ_y remained the same, while σ_u increased with increasing temperature up to 400°C and then dropped sharply till 800°C. The increase in σ_u is attributed to the increase in ductility beyond the BDT which was ≈ 100°C for this NFA-1 P1 material. The ductility continued to increase till 800°C with $\varepsilon_t \approx 16.2 \pm 0.2\%$ for S-tensile. For comparison, the strength

of L-oriented specimens was slightly reduced till 400°C, and then sharply reduced at higher temperatures due to the various thermally activated mechanisms including viscoplastic creep. In contrast to low-temperature results where the strengths diverged, both the strengths and ductility converged for L and S tensile specimens at or above 600°C. Specimen size effect on the S-tensile strength was minimal whereas a noticeable plate-to-plate variation effect was observed.

Acknowledgments

This work is part of a multi-laboratory collaboration between LANL, UCSB, and ORNL. We thank our UCSB colleagues David Gragg, and Kirk Fields for their important contributions to this work. We also acknowledge the support provided by the U.S. Department of Energy through the Office of Fusion Energy Sciences (DE-FG02-94ER54275). The U.S. National Science Foundation supported the California Nanoscience Institute (CNSI) which provided the facilities critical to the success of this research.

References

[1] N.J. Cunningham, Y. Wu, G.R. Odette, D.T. Hoelzer, S.A. Maloy, Characterization of a larger best practice heat of 14YWT in annealed powder, HIP consolidated and extruded forms, DOE Fusion React. Mater. Progr. Semiannu. Prog. Rep. DOE0313/54 (2013) 15–26.

[2] M.E. Alam, S. Pal, K. Fields, S.A. Maloy, D.T. Hoelzer, G.R. Odette, Tensile deformation and fracture properties of a 14YWT nanostructured ferritic alloy, Mater. Sci. Eng. A. 675 (2016) 437–448.

[3] M.E. Alam, S. Pal, S.A. Maloy, G.R. Odette, On delamination toughening of a 14YWT nanostructured ferritic alloy, Acta Mater. 136 (2017) 61–73.

[4] M.E. Alam, S. Pal, N.J. Cunningham, G.R. Odette, On a new Ti-carbooxinitride redistribution driven microcrack healing mechanism in an annealed 14YWT nanostuctured ferritic alloy, Acta Mater. 210 (2021) 116842.

[5] G.R. Odette, Recent Progress in Developing and Qualifying Nanostructured Ferritic Alloys for Advanced Fission and Fusion Applications, JOM. 66 (2014) 2427–2441.

[6] S. Pal, M.E. Alam, S.A. Maloy, D.T. Hoelzer, G.R. Odette, Texture evolution and microcracking mechanisms in as-extruded and cross-rolled conditions of a 14YWT nanostructured ferritic alloy, Acta Mater. 152 (2018) 338–357.

[7] ASTM E8M-15a, ASTM E8/E8M - 15a: Standard test methods for tension testing of metallic materials, in: Annu. B. ASTM Stand., ASTM International, 100 Barr Harbor Drive, PO Box C700, West Conshohocken, PA 19428-2959, United States, 2015.

[8] S. Pal, M.E. Alam, G.R. Odette, S.A. Maloy, D.T. Hoelzer, J.J. Lewandowski, Microstructure, texture and mechanical properties of the 14YWT nanostructured ferritic alloy NFA-1, in: Miner. Met. Mater. Ser., Springer International Publishing, 2017: pp. 43–54.

3. CERAMIC COMPOSITE STRUCTURAL MATERIAL DEVELOPMENT

3.1 CORROSION CHARACTERISTICS OF MONOLITHIC SiC MATERIALS IN BERYLLIUM-BEARING MOLTEN FLUORIDE SALT—T. Koyanagi, J. J. Lee, J. Keiser, H. Gietl, Y. Katoh (Oak Ridge National Laboratory)

Abstract of a manuscript in Corrosion Science Volume 220 (2023) 111301

Chemical vapor deposited SiC single crystal and polycrystals were exposed to a static beryllium-bearing molten fluoride salt, 2LiF–BeF_2 for 500 and 1000 h at 750 °C. Overall, the single crystal and polycrystalline SiC materials experienced slight weight loss and nominal surface etching regardless of the material type. Localized pitting and nonuniform Si removal from surface regions were associated with trace metal impurities and oxygen. Cross-sectional observation revealed minimal subsurface changes in the microstructure. The corrosion damage processes were similar to those reported for molten LiF–KF–NaF salt with trace impurities, indicating that the impurities significantly affect SiC corrosion.

3.2 DIMENSIONAL STABILITY OF NEUTRON-IRRADIATED BORON-11 ENRICHED ZIRCONIUM DIBORIDE—Y. Lin, T. Koyanagi, C. Petrie, Y. Katoh (Oak Ridge National Laboratory), D. Sprouster, L. Snead (Stony Brook University)

OBJECTIVE

To develop ultra-high temperature ceramics for potential plasma facing component material, the principal factor behind the volumetric expansion of neutron-irradiated ZrB_2 materials was investigated. This volumetric expansion can arise from various sources, including point defect lattice expansion, cavity swelling, or grain boundary microcracks.

SUMMARY

Cavity swelling and dimensional changes resulting from grain boundary cracks in ^{11}B-enriched (99.37 wt.%) ZrB_2, subjected to mixed-spectrum neutron irradiation at High Flux Isotope Reactor (HFIR) (220°C and 620°C, neutron fluence: 2.2×10^{25} neutron/m^2, E > 0.1 MeV), are evaluated based on their dimensions and densities as observed in transmission electron microscopy (TEM) and scanning electron microscope (SEM) images. Furthermore, synchrotron X-ray diffraction (XRD) was employed to examine the changes in the lattice parameters. Post-irradiation XRD analysis revealed an expansion along the *a*-axis and a contraction along the *c*-axis. By comparing volumetric swelling data from diverse sources, our findings elucidate that the primary dimensional change is attributed from grain boundary microcracks.

PROGRESS AND STATUS

In our previous report [1], we observed prevalence of prism dislocation loops and dislocation networks in ZrB_2 samples irradiated at 220°C and 620°C. In addition, only the 620°C samples had cavities, likely due to increased temperatures from neutron-absorbed residual ^{10}B and He production through ^{10}B transmutation in matrix and grain boundaries. To investigate the principal factor behind the macroscopic volumetric expansion of neutron-irradiated ZrB_2, we used SEM to study the surface cracks and synchrotron XRD to study the lattice parameter changes along "a" and "c" axes.

Figure 1 shows surface cracks on ZrB_2 samples subjected to irradiation at temperatures of 220°C (ZB02) and 620°C (ZB04). With the Electron Backscatter Diffraction (EBSD) findings, we selected the ZB02 and ZB04 samples with a comparable average grain size of approximately 7 μm for further detailed examination. In ZB02 and ZB04, the intergranular surface cracking per unit volume was 0.27 and 0.05 1/μm, respectively. Additionally, trans-granular surface cracking per unit volume was 0.28 and 0.06 1/μm in ZB02 and ZB04, respectively.

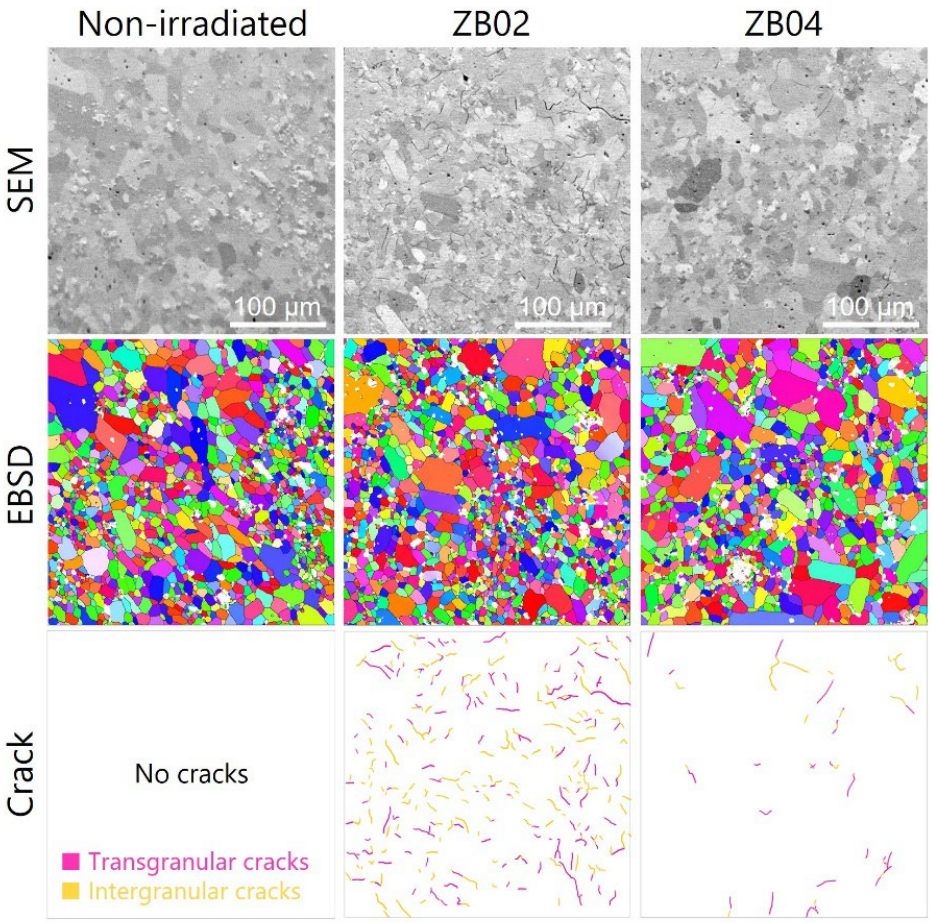

Figure 1. The SEM and EBSD IPF images of non-irradiated and neutron irradiated ZrB2: ZB02 (220°C) and ZB04 (620°C).

The XRD measurements were conducted at the National Synchrotron Light Source-II (NSLS-II) using the high-energy X-rays provided by The Pair Distribution Function (PDF) beamline. Figure 2 presents a summary of the XRD pattern analysis conducted on both unirradiated and neutron-irradiated ZrB_2 samples. The samples, namely ZB05, ZB06, and ZB02, were irradiated at 220°C, while ZB04, ZB08, and ZB01 were irradiated at a higher temperature of 620°C. The background-subtracted XRD patterns underwent rigorous Rietveld refinement using the TOPAS software package from Bruker.

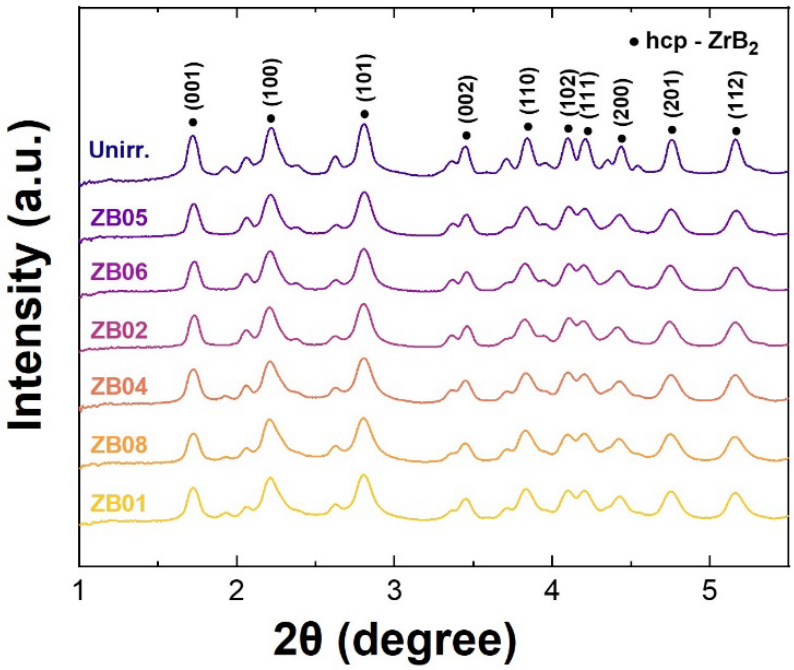

Figure 2. The XRD patterns comparing unirradiated and neutron irradiated ZrB2 samples. ZB05, ZB06, and ZB02 were irradiated at 220°C, while ZB04, ZB08, and ZB01 underwent irradiation at 620°C.

In the case of the unirradiated sample illustrated in Figure 3, phase identification was executed using the Match! 3 software (Crystal Impact, Bonn, Germany). Among the ZrB_2 samples investigated, only the hexagonal ZrB_2 phase was indexable; the cubic ZrB_2 phase was not observed. Alongside the ZrB_2 matrix, other phases containing Zr-O inclusions were detected (including monoclinic ZrO_2, orthorhombic ZrO_2, and cubic ZrO). These inclusions raise concerns about potential trans-granular cracking. In addition, no discernible presence of free metallic boron or zirconium phases was observed in the XRD patterns.

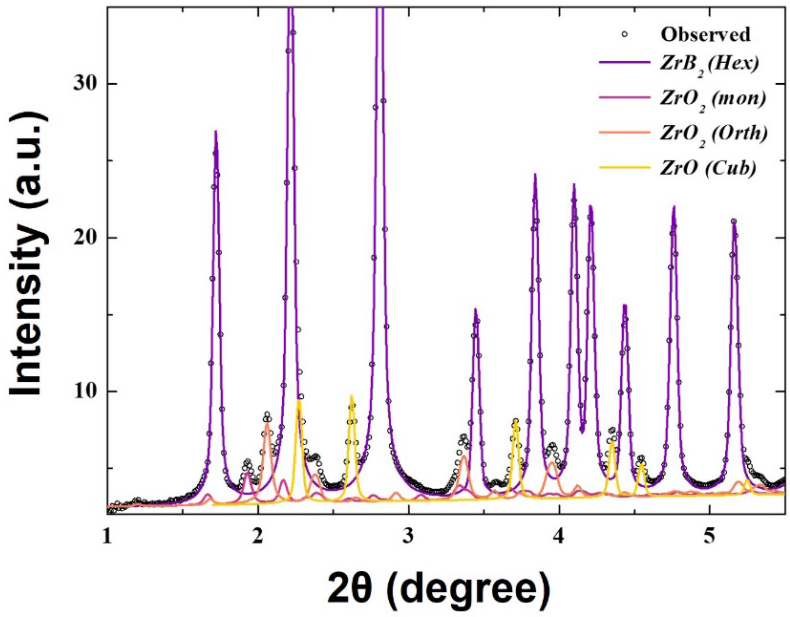

Figure 3. The XRD pattern and phase identification of the unirradiated ZrB_2 sample. (Hex: hexagonal, Mon: monoclinic, Orth: orthorhombic, and Cub: cubic).

Figure 4 clearly displays peak shifts indicating lattice expansion along the "a" parameter and contraction along the "c" axis in ZrB_2 after irradiation at 220°C (ZB02) and 620°C (ZB04). The "a" lattice expanded by 0.41% (ZB02) and 0.14% (ZB04), while "c" lattice contracted by -0.39% (ZB02) and -0.11% (ZB04). These changes align with our previous TEM study on dislocation loops [1], showing decreased loop density at higher temperature. Furthermore, irradiation induced notable changes in micro-strain (MS) and coherent grain size (CGS), as evidenced by the data in Table 1. These changes were substantial and resembled trends observed in other hexagonal ceramics, such as graphite, Mo_2C, and BeO. Additionally, the XRD analysis captured subtle changes in minor oxide phases. Specifically, FCC ZrO exhibited lattice contraction, while orthorhombic ZrO displayed expansions in the "a" and "c" axes and a contraction in the "b" axis. The overarching result of irradiation was an increase in overall volume, accompanied by corresponding changes in CGS.

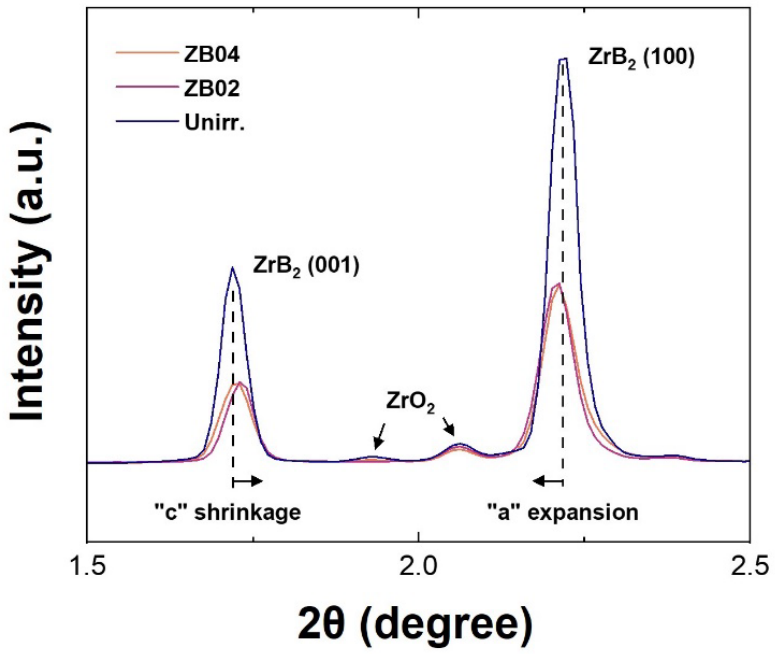

Figure 4. The XRD peak shifts observed at various irradiation temperatures: ZB02 (220°C), ZB04 (620°C), and Unirr. (unirradiated).

Table 1. Summary of phase, coherent grain size (CGS), and micro-strain (MS) analysis from XRD data

Sample	Phase	CGS (nm)	MS (arb units)
Non-irradiated ZrB_2	ZrB_2 (P6/mmm)	169.4 ± 9.6	0.24 ± 0.01
	ZrO_2_mon (P2_1/c)	23.2 ± 7.3	
	ZrO_2_Orth (Pbc21)	25.9 ± 4.5	
	ZrO_Cub (Fm-3m)	89.2 ± 18.7	
ZB02 (220°C)	ZrB_2 (P6/mmm)	57.7 ± 2.7	1.33 ± 0.01
	ZrO_2_mon (P2_1/c)	11.6 ± 10.6	
	ZrO_2_Orth (Pbc21)	35.9 ± 6.6	
	ZrO_Cub (Fm-3m)	14.0 ± 1.4	
ZB04 (620°C)	ZrB_2 (P6/mmm)	38.5 ± 1.0	1.26 ±0.01
	ZrO_2_mon (P2_1/c)	21.2 ± 7.4	
	ZrO_2_Orth (Pbc21)	32.7 ± 4.9	
	ZrO_Cub (Fm-3m)	14.2 ± 1.0	

Figure 5 provides an overview of the volumetric swelling resulting from different mechanisms. Macroscopic swelling is gauged through dimensional alterations in the bulk irradiation samples. In this study, we quantified the total crack volume by considering both their density and the gap size (~100 nm, as measured in TEM images). Lattice expansion and cavity swelling were derived from synchrotron XRD and TEM analyses, respectively. Upon thorough comparison of volumetric swelling data from these mechanisms, our investigation reveals that grain boundary microcracks dominate the volumetric swelling observed in neutron-irradiated ZrB_2. These findings significantly enhance our understanding of the impact of neutron irradiation on ultra-high temperature ceramics (UHTCs) and their potential applications.

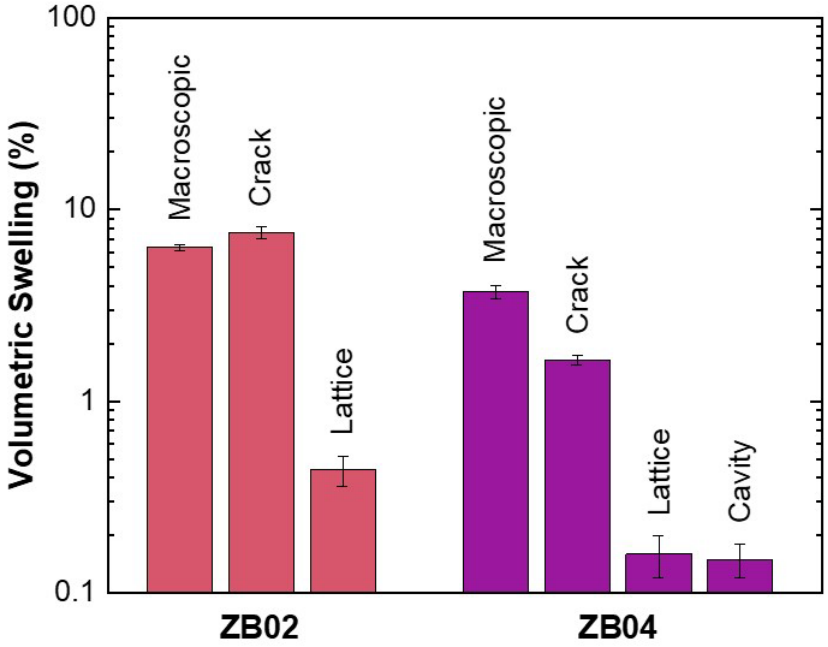

Figure 5. Volumetric swelling contributions from various sources in neutron-irradiated ZrB_2 at 220°C (ZB02) and 620°C (ZB04).

Future Work

The findings on the response of ZrB_2 to neutron irradiation will be submitted to a peer-reviewed journal.

Reference

[1] Y. Lin, T. Koyanagi, C.M. Petrie, M.G. Burke, Y. Katoh, “Microstructure of neutron-irradiated Boron-11 enriched Zirconium diboride at elevated temperatures”, U.S. DOE Office of Fusion Energy Science, Fusion Materials, Semiannual Progress Report, DOE/ER-0313/73 (2022).

4. PLASMA-FACING AND HIGH HEAT FLUX MATERIALS AND COMPONENT TESTING

4.1 BORON-DOPED TUNGSTEN FOR FUSION PFCS—X.-Y. Yu, T. Graening, G. Yang, Y. Katoh (Oak Ridge National Laboratory)

OBJECTIVE

The objective of this project is to determine: 1) if boron is doped into the tungsten plates via the usual route of powder metallurgy and hot rolling and 2) if boron is doped at the desired quantity.

SUMMARY

The ALMT prepared boron (B) doped tungsten (W) plates were characterized using microscale spectroscopy and microscopy including scanning electron microscopy (SEM), Raman spectroscopy and imaging, and depth profiling of time-of-flight secondary ion mass spectrometry (ToF-SIMS). The B was detected at the surface of the doped W plates using Raman and SIMS.

PROGRESS AND STATUS

Introduction

Doping a small amount of B can deter recrystallization of W effectively [1, 2]. B-doping ductilizes W and it is beneficial for additive manufacturing (AM) build of W [3]. The B-doping can potentially offer benefits to PFC performance. Therefore, understanding basic properties of B-doped W is useful for developing materials for fusion applications. The ALMT prepared two B-doped W plates via powder metallurgy and hot rolling, which nominally have 0.1 at% B and 0.01 at% B, respectively. A reference W plate without B doping was also provided as the reference material.

Materials

Pieces from all three rolled plates were sectioned and the top surface of the rolled plates was polished to a 0.5 *μm* finish, followed by a chemical polishing step. The SEM was performed using a MIRA 3 SEM (TESCAN USA, Inc.) equipped with an Oxford Symmetry electron backscatter diffraction (EBSD) detector. The probe current was around 6 nA. All EBSD data were collected using a 20 kV accelerating voltage with a 6 nA beam current. Appropriate step sizes of 0.2 were used for all scans. Two maps with different magnifications were recorded for each sample.

The Raman mapping was collected on a confocal Raman spectrometer (Horiba, 405 nm edge, objective = 50×, a grating with 2400 grooves/ mm, numerical aperture (N.A.) = 0.42, local power <500 μW). The laser spot diameter was estimated to be 1 *μm*. The scan region was set 17.31 μm × 18.96 μm, with the step size of 0.4 μm × 0.5 μm/pixel. The integration time was set to 8 s for each point. Autofocus mode was applied at each step to assure consistent focus on the sample surface. All Raman mappings were analyzed using Horiba Labspec 6 imaging and spectroscopy software and the K-means clustering algorithm integrated into the Scikit-learn platform with a previously reported similar method [4, 5].

Results

SEM findings

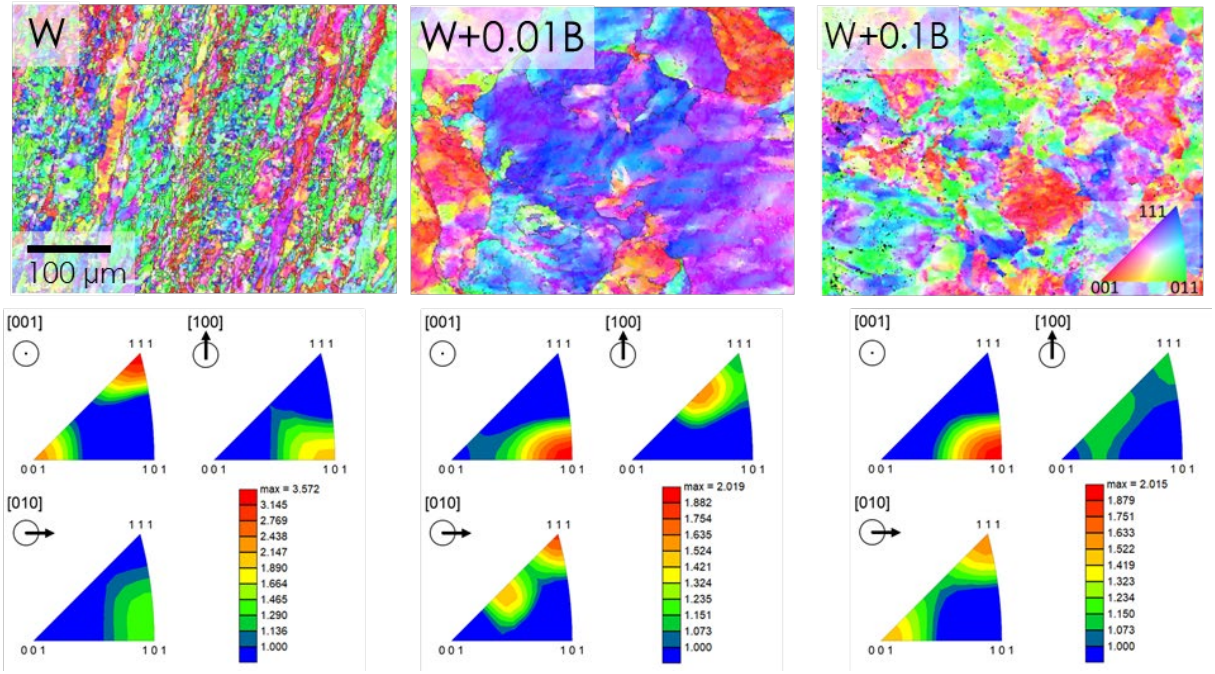

Figure 1. Inverse pole figure (IPF) maps, evaluated in the rolling direction from top to bottom, of W and B-doped W using the same magnification clearly showing a grain size difference. Pole figures on the bottom correspond to the IPF above.

Figure 1 shows the microstructure of the pure W sheets next to the two doped variants using IPF maps. The rolling direction (RD) of the sheets is from bottom to top. A clear change in grain size and shape is visible with the addition of B for both sheets (middle and right). The typical elongated grains in the rolling direction were observed in the reference material. They exhibit the expected (001) and (101) texture in normal direction to the rolling direction, with the (101) orientation being preferred in RD [6]. The texture is relatively weak for a rolled W plate, suggesting a low rolling reduction. The texture changes to a lower texture anisotropy within the doped W sheets, with a preferred (101) orientation in normal direction to the rolling direction. The grain shape appears more spherical which aligns well with current findings of doped-W [7]. Those findings support the speculation that the boron supports the formation of new grains during the thermomechanical treatment process.

Raman spectral and imaging characterization

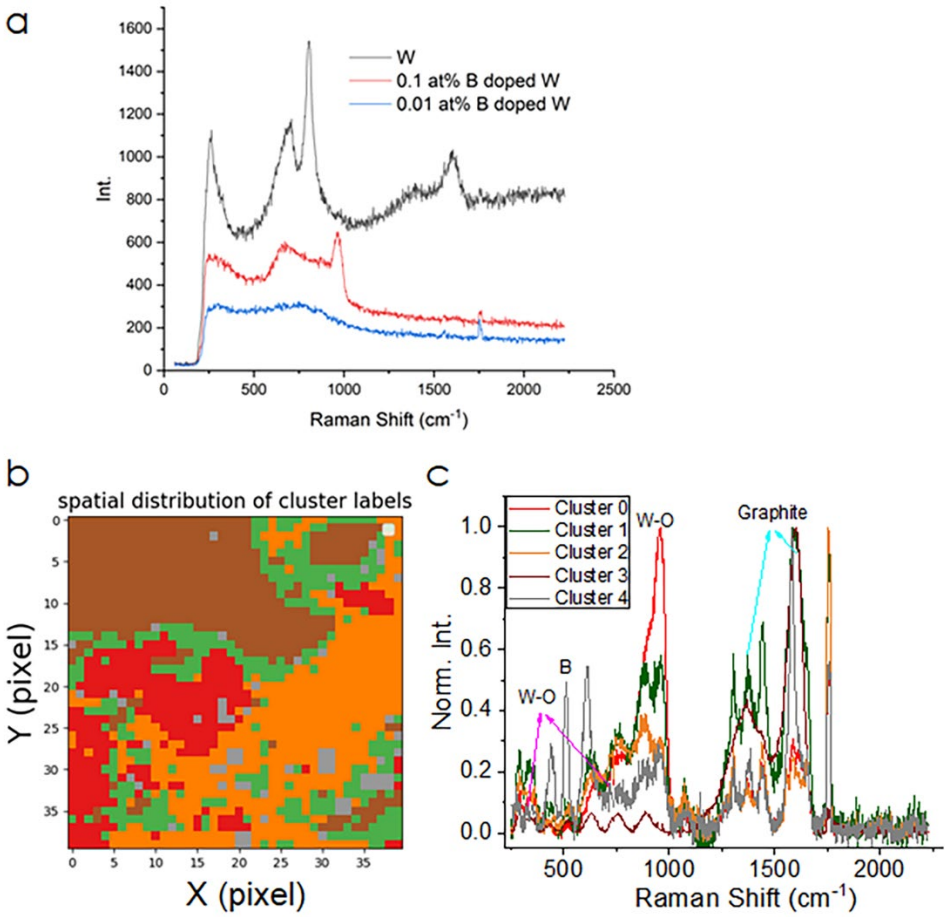

Figure 2. a) Raman spectral comparison of AM prepared W, 0.1 at% B doped W, and 0.01 at% B doped W coupons; b) 2D Raman surface mapping of 0.1 at%B doped W coupon; and c) Cluster analysis of surface composition of (b).

Figure 2 depicts initial Raman characterization results of the B doped W coupons. Raman surface spectral comparison in Figure 2a shows that surface compositions are quite different among the three types of metals. The W oxide (WO_3) is present at room temperature as a mixture of the monoclinic (γ-phase) and triclinic (δ-phase) phases, often revealed by the presence of peaks at 183, 207, 275, 718 and 810 cm^{-1} [8]. Two-dimensional (2D) Raman imaging was also performed. Figure 2b shows the reconstructed surface map of the 0.1 at% B doped W coupon based on the principal component analysis or cluster analysis. Five components or clusters were identified as the main contributors of the spectral features observed in the 2D mapping shown in Figure 2c.

The band in the range of 100–500 cm^{-1} is associated to O–W–O bending modes, and the band in the range 600–1000 cm^{-1} is associated to W–O stretching modes [8]. Raman peaks at 143, 308, 645, 678 cm^{-1} are associated with the monoclinic ε-phase of WO_3. The band at around 960 cm^{-1} is assigned to the terminal W-O stretching mode, possibly on the surface of the cluster and in micro-void structures in the plate. The band at around 950 cm^{-1} is ascribed to W trioxide hydrate(WO_3, xH_2O), corresponding to the W=O stretching mode [9]. The hydrates may have more bands in the lower-frequency region of under 400 cm^{-1}. These peaks are the main contributor to clusters 0, 1, and 2.

The Raman spectrum also has characteristics of an amorphous W oxide (*a*-WO_3) [10]. The Raman peak at 713.7 cm^{-1} is attributed to *v*(O-W-O) modes of m-WO_3. The broad band centered at ca. 760 cm^{-1} can be deconvoluted into several Raman peaks, including the strongest peaks at 715 and 807 cm^{-1} of the monoclinic WO_3. Other known vibrational shifts from W-O and O-W-O characteristic of W oxides are also visible from all materials, for example 328.1, 268.5 cm^{-1} indicative of *δ*(O-W-O) [11]. Raman peaks at 318, 645, and 813 cm^{-1} are attributed *h*-WO_3. The spectrum has also characteristic bands of the crystalline W oxide, namely weak bands around 430 and 450 cm^{-1} are visible [9]. These peaks contribute to the loadings of clusters 0, 1, and 2, suggesting surface oxidation of these plates.

The band at 882 cm^{-1} is typical of ethanol [12]. The appearance of bands at ~1368 and ~1590 cm^{-1} indicates existence of disordered graphitic carbon. They are contributors to clusters 3 and 4. Surface contamination is evident in all main components of the map. Among them, cluster 3 mainly represents surface contamination components like graphite. The other clusters are mixtures of WO_3 with different degree of surface contaminations or solvent used to clean the surface.

There is not a report about B doped W in Raman to the best of our knowledge. Using Raman spectra acquired from B, B doped graphite, or B doped 2D materials, we evaluated the cluster components. The Raman peak wave numbers shift to higher values due to doping. The peaks of 500 cm^{-1} and 1230 cm^{-1} were determined previously as a result of B doping into the diamond lattice [13]. We postulate peaks at 514 cm^{-1}, 1308 cm^{-1}, 1387 cm^{-1}, and 1443 cm^{-1} may reflect the effect of B doping on the diamond lattice, which are represented in cluster 4. The peaks appearing at 611 cm^{-1}, 717 cm^{-1}, 763 cm^{-1}, and 763 cm^{-1} can be related to β-B. The peaks occurring at ~ 850 cm^{-1}, 880 cm^{-1}, and 948 cm^{-1} can be related to γ-B [14]. Thus, cluster 4 likely represents the contributions from B Raman spectral peaks. The distribution of cluster 4 is depicted in gray in Figure 2b. These findings suggest that that B is incorporated into the W matrix.

Additional analysis and peak identification of the Raman observations are currently ongoing. Results from other spectroscopy and microscopy analysis like SIMS will be incorporated in the determination of the B distribution and quantification in future reports.

References

[1] C. Fan, X. Hu, Recovery and recrystallization of warm-rolled tungsten during helium thermal desorption spectroscopy annealing, Journal of Nuclear Materials 569 (2022) 153914.
[2] A. Hasegawa, T. Miyazawa, D. Itou, T. Hattori, K. Yohida, S. Nogami, Helium effects on recovery and recrystallization of powder metallurgically processed tungsten, Physica Scripta 2020(T171) (2020) 014016.
[3] Y. Liu, X. Liu, C. Lai, J. Ma, X. Meng, L. Zhang, G. Xu, Y. Lu, H. Li, J. Wang, S. Chen, Boriding of tungsten by the powder-pack process: Phase formation, growth kinetics and enhanced neutron shielding, International Journal of Refractory Metals and Hard Materials 110 (2023) 106049.
[4] F. Pedregosa, G. Varoquaux, A. Gramfort, V. Michel, B. Thirion, O. Grisel, M. Blondel, P. Prettenhofer, R. Weiss, V. Dubourg, J. Vanderplas, A. Passos, D. Cournapeau, M. Brucher, M. Perrot, É. Duchesnay, Scikit-learn: Machine Learning in Python, J. Mach. Learn. Res. 12(null) (2011) 2825–2830.
[5] G. Yang, R. Tao, C.J. Jafta, C. Shen, S. Zhao, L. He, I. Belharouak, J. Nanda, Investigating Multiscale Spatial Distribution of Sulfur in a CNT Scaffold and Its Impact on Li–S Cell Performance, The Journal of Physical Chemistry C 125(24) (2021) 13146-13157.
[6] C. Bonnekoh, P. Lied, S. Zaefferer, U. Jäntsch, A. Hoffmann, J. Reiser, M. Rieth, The brittle-to-ductile transition in cold-rolled tungsten sheets: Contributions of grain and subgrain boundaries to the enhanced ductility after pre-deformation, Nuclear Materials and Energy 25 (2020) 100769.
[7] X. Li, L. Zhang, G. Wang, Y. Long, J. Yang, M. Qin, X. Qu, K.P. So, Microstructure evolution of hot-rolled pure and doped tungsten under various rolling reductions, Journal of Nuclear Materials 533 (2020) 152074.
[8] A. Baserga, V. Russo, F. Di Fonzo, A. Bailini, D. Cattaneo, C.S. Casari, A. Li Bassi, C.E. Bottani, Nanostructured tungsten oxide with controlled properties: Synthesis and Raman characterization, Thin Solid Films 515(16) (2007) 6465-6469.

[9] A.T. Miyakawa, Raman Study on Sol-Gel Derived Tungsten Oxides from Tungsten Ethoxide, Japanese Journal of Applied Physics 30(8B) (1991) L1508.
[10] C. Santato, M. Odziemkowski, M. Ulmann, J. Augustynski, Crystallographically Oriented Mesoporous WO3 Films: Synthesis, Characterization, and Applications, Journal of the American Chemical Society 123(43) (2001) 10639-10649.
[11] Y. Djaoued, S. Balaji, R. Brüning, Electrochromic Devices Based on Porous Tungsten Oxide Thin Films, Journal of Nanomaterials 2012 (2012) 674168.
[12] S. Corsetti, D. McGloin, J. Kiefer, Comparison of Raman and IR spectroscopy for quantitative analysis of gasoline/ethanol blends, Fuel 166 (2016) 488-494.
[13] B. Dec, M. Ficek, M. Rycewicz, Ł. Macewicz, M. Gnyba, M. Sawczak, M. Sobaszek, R. Bogdanowicz, Gas Composition Influence on the Properties of Boron-Doped Diamond Films Deposited on the Fused Silica, Materials Science-Poland 36(2) (3918) 288-296.
[14] G. Parakhonskiy, N. Dubrovinskaia, E. Bykova, R. Wirth, L. Dubrovinsky, Experimental pressure-temperature phase diagram of boron: resolving the long-standing enigma, Scientific Reports 1(1) (2011) 96.

4.2 ON THE CRACK SELF-HEALING BY HIGH-TEMPERATURE ANNEALING OF 90-97WNiFe TUNGSTEN HEAVY ALLOYS

—M. Alam, G. Odette (University of California, Santa Barbara)

OBJECTIVE

The aim of this study is to achieve self-healing of cracks in a series of WNiFe tungsten heavy alloys (WHAs) by annealing at a temperature close to their operating condition for the nuclear fusion reactor application.

SUMMARY

The high and cyclic thermal loads in the fusion environment often result in the formation of many sharp surface cracks in the W and W-alloy divertors that might eventually cause failure. The WNiFe WHAs are the most promising candidates for the plasma-facing component as divertor due to their balance of thermal, physical, and mechanical properties, and most likely to be used at a temperature ≈ 1300°C due to various limiting factors. Here, we have fatigue pre-cracked (PC) three-point bend (3PB) bars of a series of 90 to 97W WHAs and annealed them at 1300°C for 24 h to investigate the crack self-healing at their intended operating temperature. Results show annealing heals cracks with up to ≈ 5mm deep with a mouth opening of 1.8 μm. Self-healing is confirmed by loading these healed specimens in the 3PB bar fixtures at room temperature (RT). Diffusion might play a vital role but the healing mechanism is not completely known yet.

PROGRESS AND STATUS

Introduction

The W is well known for its remarkable combination of high melting temperature, thermal conductivity, strength, and low sputtering rate which makes it a leading candidate for the plasma-facing divertor material in a nuclear fusion environment. Unfortunately, high brittle to ductile transition temperature (BDTT, ≈ 300 °C), low RT tensile and fracture toughness, which are further degraded by neutron exposure, limit the use of monolithic W as divertor tiles [1-5]. The ductile phase (DP) toughened, and liquid-phase sintered (LPS) WHAs possess a balance of thermal and mechanical properties and recently attracts the scientific community as an alternative to monolithic W or W-alloys for divertor materials [3,6-10]. Despite the superior maximum load fracture toughness (K_{Jm} ≈ 70 to 120 MPa√m) of 90W to 97W-NiFe WHAs compared to the monolithic W (≈ 8 MPa√m), the intense and repeated thermal loads in the fusion environment can lead to the formation of numerous sharp surface cracks, posing a potential risk of divertor failure [11-15]. Open literature does not show any evidence of systematic study on the crack formation or healing for WHAs, except Neu et al. [7,8] who reported the use of monolithic W and 97W-2Ni-1Fe WHA as divertor tiles for the mid-size tokamak ASDEX Upgrade facilities that experienced cyclic plasma heat flux up to 20 MW/m^2 and surface temperatures up to 2200°C. They reported that while the surface cracks were found in monolithic W tiles, these cracks were not observed in the 97WNiFe WHA tiles.

In recent times, much research has been focused on increasing the reliability and integrity of engineering materials in service by introducing the self-healing concept; however, they are performed mostly on polymeric, concrete, and ceramic materials [16-24]. While there have been far fewer studies, self-healing of damage in metallic materials is a topic of rapidly increasing interest [25-35]. In the case of bulk metallic materials autonomous self-healing of creep cavities without any additional external stimulus has been reported [32,35]. Non-autonomous crack healing by the application of external triggers, like electro pulsing [30,31], heat-treatment [25,26,28,29], diffusion and precipitation [36,37], and a bridging mechanism in shape memory alloys [33] are reported.

In this study, we have explored the possibility of macro through-thickness crack healing of a series of 90W to 97W-NiFe WHAs by annealing (AN) at the higher end of the operating temperature range. Fatigue PC 3PB bars were annealed under vacuum at 1300°C for 24 h. Scanning electron microscopy (SEM) before and after AN, shows partial to full crack healing, depending on the initial crack-mouth opening. To further confirm healing, the 3PB specimens were loaded, and in-situ images of the healed crack were observed

using a telescopic optical microscope. Post-test SEM was also used to image the healed cracks. The healing mechanism is consistent with the self-diffusion of atoms at the PC tip, which follows a DP path. The corresponding maximum load fracture toughness, K_{Jm}, was measured following ASTM E1921 [38].

Experimental Procedure

The materials acquisition, 3PB specimen fabrication, microstructural observation, PC, and mechanical testing procedures can be found in detail in [11,13,14]. Briefly, four commercially available 90, 92.5, 95, and 97 wt.% W liquid phase sintered plates were acquired from Mi-Tech Metals, Indianapolis, Indiana, United States of America [11]. The fcc DP is 50Ni, 20Fe, and 30W (by wt.%), where the latter dissolves into the 7Ni-3Fe binder powders during sintering.

The 3PB bar specimens with nominal length/width/thickness dimensions of 16/3.3/1.65 mm (1x), and 50/10/5 mm (3x), were fatigue PC to a final crack length (a) to specimen width (w), a/w ≈ 0.42 to 0.446, from a a/w = 0.15 to 0.3 notch [13]. The PC procedure is described in [11,13]. The fatigue crack length varied between 0.9 and 1.33 mm, corresponding to depths from 1.65 to 5.0 mm. The PCs are sharp at the tip (< 0.2 μm) and much wider at the notch (up to 4 μm), and generally follow a DP path. The fatigue PC specimens were ultrasonically cleaned for 15 minutes in acetone and annealed on an acetone-cleaned molybdenum sheet (purity > 99.95%) on an alumina tray (purity > 99.8%). Vacuum AN (3x 10^{-8} torr) was carried out in a resistance furnace at 1300°C for 24 h with a 5°C/min heating and cooling rates [14].

Optical, and SEM, were used to characterize the crack in all conditions. Energy dispersive spectroscopy (EDS) was used to measure the elemental compositions of the W and DP at all conditions.

The RT fracture toughness tests on an MTS 810 servo-hydraulic universal testing machine on the 3PB bar fixtures. A long-distance (telescopic) optical microscope was used to capture the in-situ images while loading the specimens. Loading was almost immediately stopped just after reaching maximum load for the smaller 1x specimens to compare the PC and post-test crack length after healing. The ASTM E1921 standard [38] was used to analyze the RT fracture toughness of these healed specimens. Reasons for using some ASTM E1921 K_{Jm} procedures are explained in [13]. Note, the evaluated K_{Jm} value for the healed specimens might not follow all the ASTM E1921 standards as the a/w is much smaller for relatively blunted and healed cracks, and smaller 1x specimen dimensions.

Results

Crack healing of 1x 90 to 97W WHAs

The SEM images shown in Figures 1 to 4 reveal the stages from PC to test after AN for crack healing in the 3PB bars for the 90W, 92.5W, 95W, and 97W WHAs, respectively. Note, these are small 1x bend bars with nominal length/width/thickness dimensions of 16/3.3/1.65 mm. Here, Figures 1a) to 4a) show the specimens after they are fatigue PC (indicated by black arrow) to the final crack length-to-width ratio (a/W) of ≈ 0.4313 to 0.446, including the notch-length/width ratio ≈ 0.15 - 0.16. The PC length for the 1x specimens averaged ≈ 0.9 mm with a depth of 1.65 mm, and the crack mouth width was from ≈ 4 μm to 0.2 μm at the crack tip. Figures 1b-4b show the SEM images of the PC and 1300°C/24h AN specimens (PC+AN). It can be seen from the images that these specimens are at least healed partially (red arrow in Figure b) that started from the PC tip. Interestingly, 90W to 95W WHA are healed partially from the crack tip up to the crack width of ≈ 1.3 μm, whereas the 97W healed completely, even though the average crack width at the notch is 1.84 μm and has a relatively lower DP fraction (≈ 6%). Note, our observation is solely based on one specimen per composition or size.

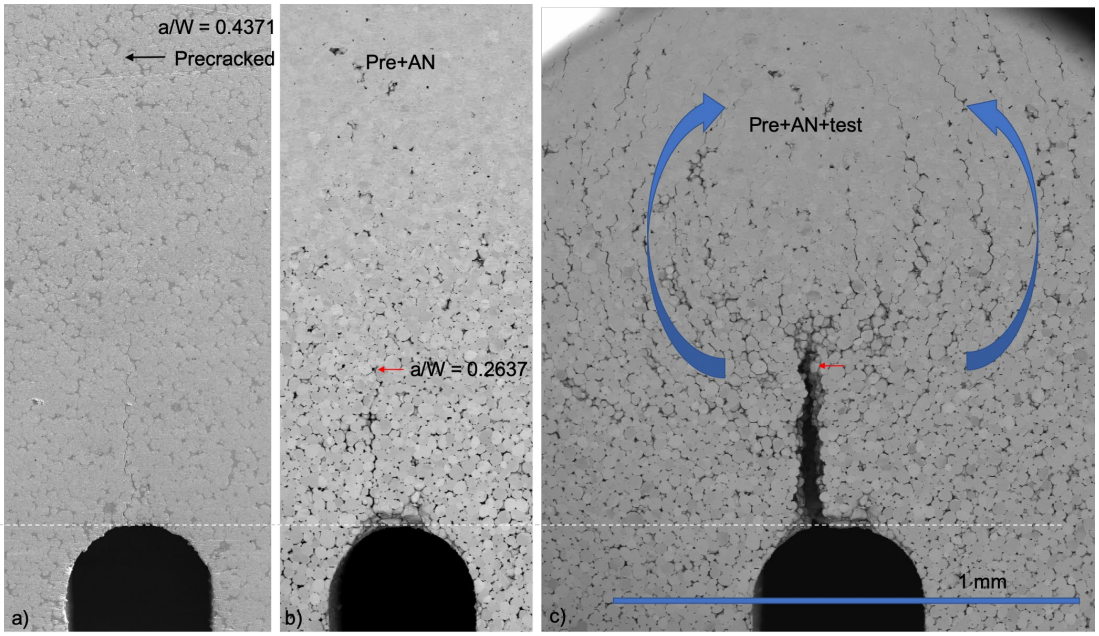

Figure 1. The SEM images for 90W showing: a) the PC length; b) the partially healed crack after 1300°C/24h AN; and c) the healed specimen that was loaded in a 3PB fixture at RT.

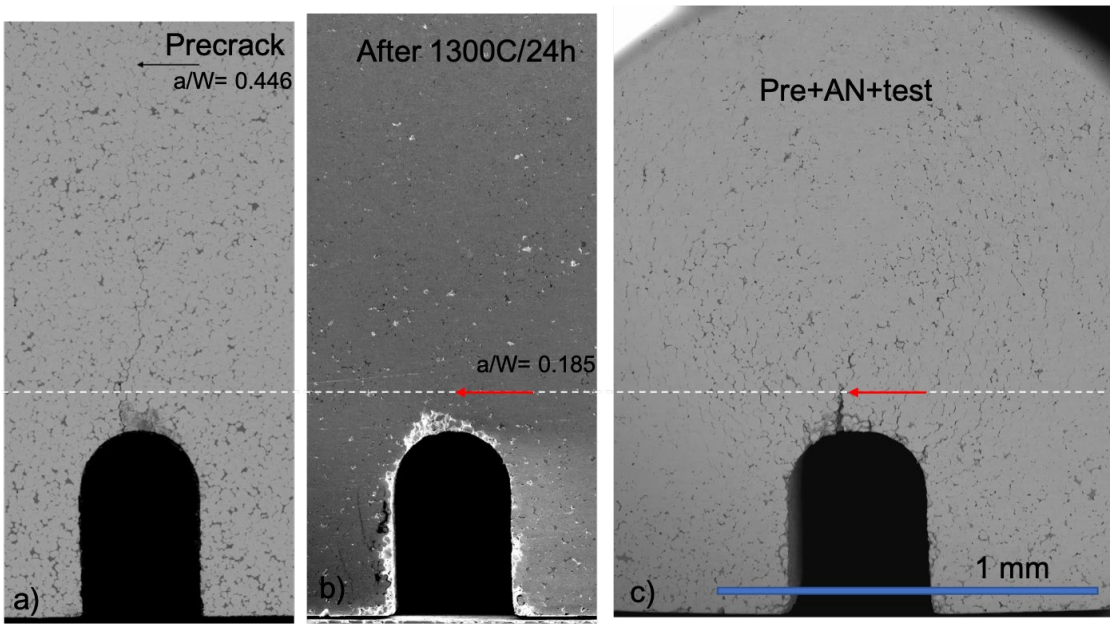

Figure 2. The SEM images for 92.5W showing: a) the PC length; b) the partially healed crack after 1300°C/24h AN; and c) the healed specimen that was loaded in a 3PB fixture at RT.

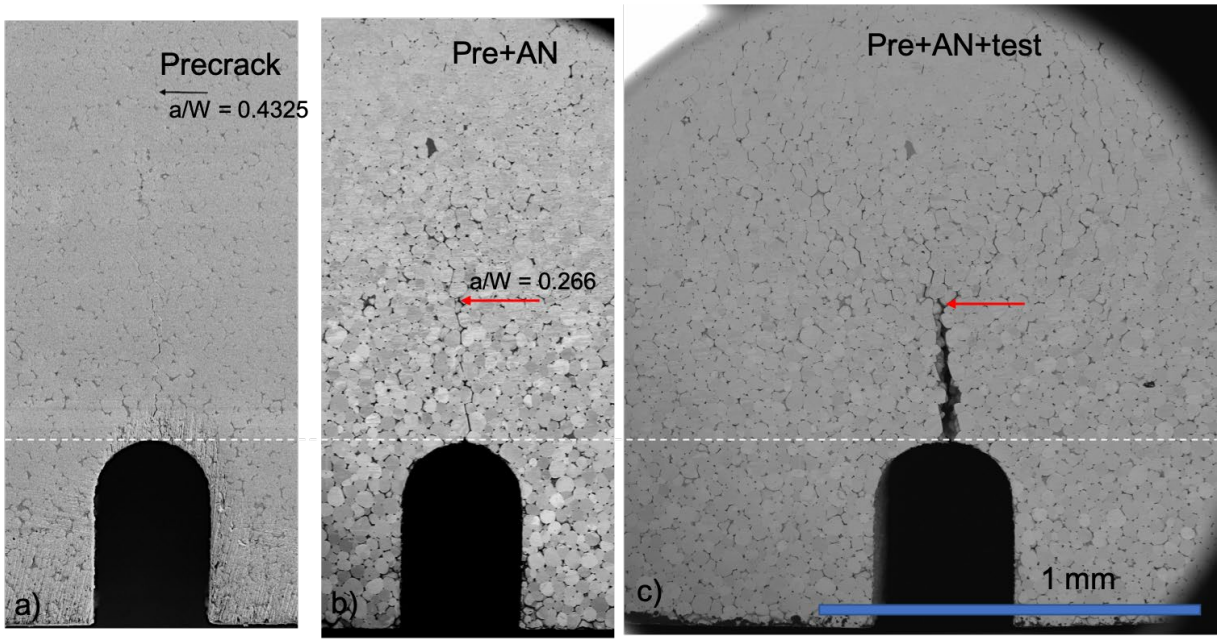

Figure 3. The SEM images for 95W showing a) the PC length; b) the partially healed crack after 1300°C/24h AN; and c) the healed specimen that was loaded in a 3PB fixture at RT.

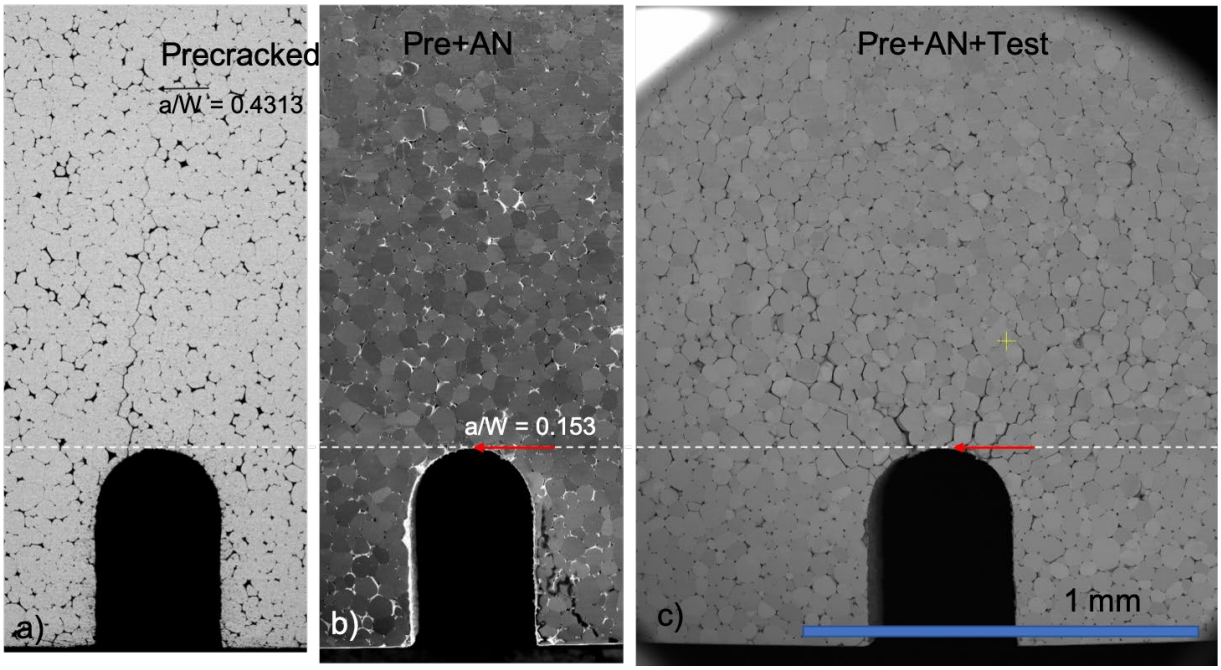

Figure 4. The SEM images for 97W showing: a) the PC length; b) healed crack after 1300°C/24h AN; and c) the healed specimen that was loaded in a 3PB fixture at RT.

We have loaded all the PC + AN specimens that seem partially or fully healed after AN on the 3PB bar fixture at RT to understand if the healing occurred only at the skin (outer surface) or thoroughly of the specimen. It also helped to measure the length of the healed cracks. Note, we stopped loading just after reaching the maximum load which helped us to measure the healed crack length. The in-situ images obtained by a long-distance optical microscope and their corresponding load points at the load (P)-

displacement (d) curves for all four 1x 90W to 97W WHAs are shown in Figure 5a-d. Here, point-1 is at the elastic loading zone, point-2 is at the maximum load and point-3 is close to the post-maximum load point. The black lobes (due to the lateral contraction causing them to out of focus) at the crack tip in point-3 of Figure 5 indicate the start of the plastic process zone that is much shorter and closer to the notch than the initial crack tip, which further confirms the crack healing of WHAs at the mentioned condition. The SEM images shown in Figures 1c) - 4c) that are taken after the test again confirm the new crack tip after healing. Note, the 92.5W WHA almost healed, while 97W healed completely as the plastic process zone starts beyond the notch tip in both cases (Figures 2c and 4c).

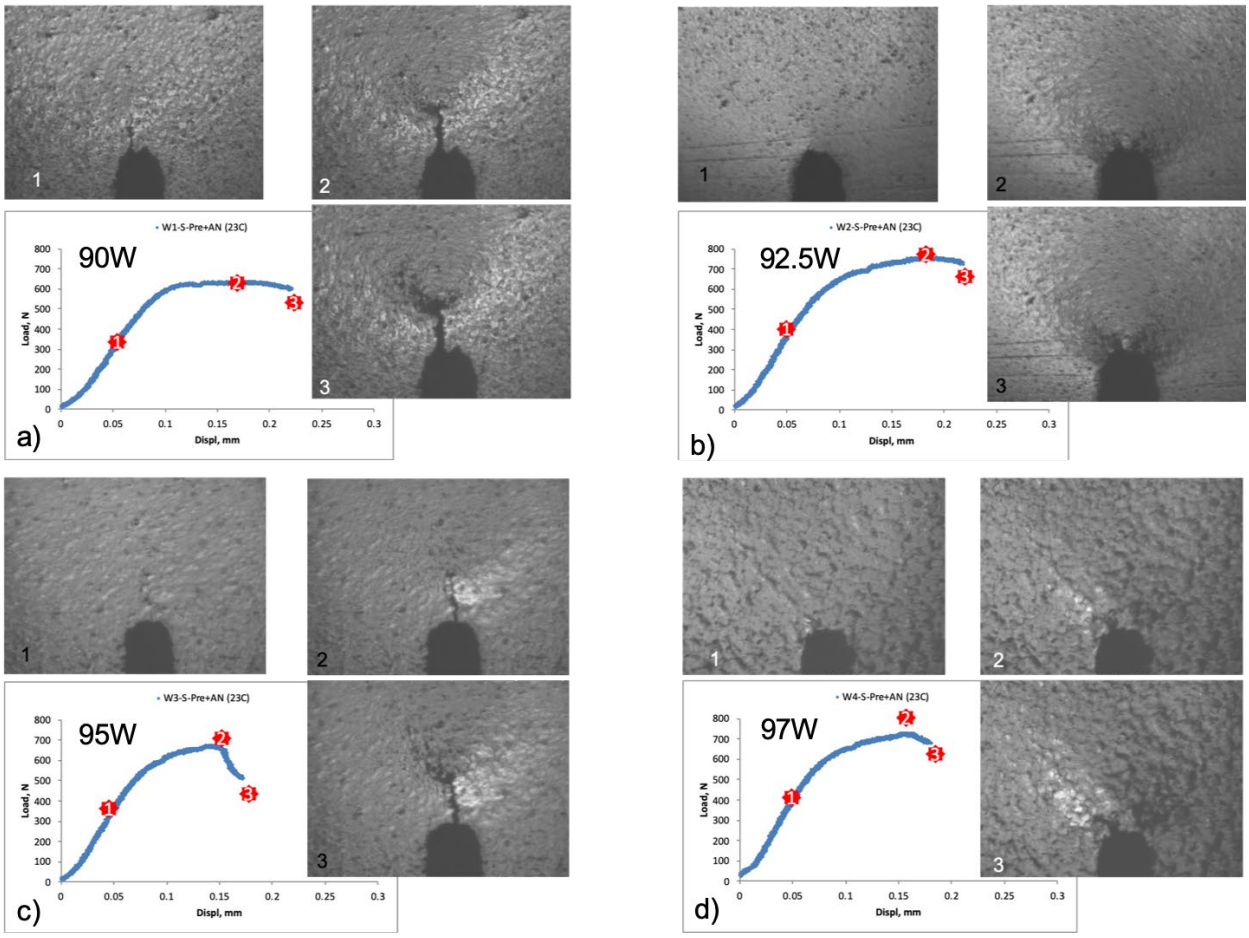

Figure 5. The RT load-displacement (P-d) curves with in-situ optical images show different loading points: 1 at the elastic part, 2 at maximum load, and 3 at close to the post-maximum load for the a-d) 90 - 97W WHAs, respectively.

Crack healing of 3x 90W WHA

We have PC and AN two 3x 90W WHA at 1300°C/24 h. In this case, two different approaches were taken. One specimen was PC to a/W ≈ 0.428 as shown in Figure 6a. Note, the fatigue PC length from the notch to crack tip is 1.329 mm, which goes beyond the top of the image shown in Figure 6a. A higher magnification image of the PC specimen close to the notch is shown in Figure 6b. The average PC width close to the notch is ≈ 1.65 µm with a maximum width of up to 1.8 µm, and <0.2 µm at the crack tip. The PC 3x 90W specimen was AN at 1300°C/24h, similar to the 1x specimens as mentioned above. The SEM images probed on both sides of the AN specimen do not show any visible crack (Figure 6c,d).

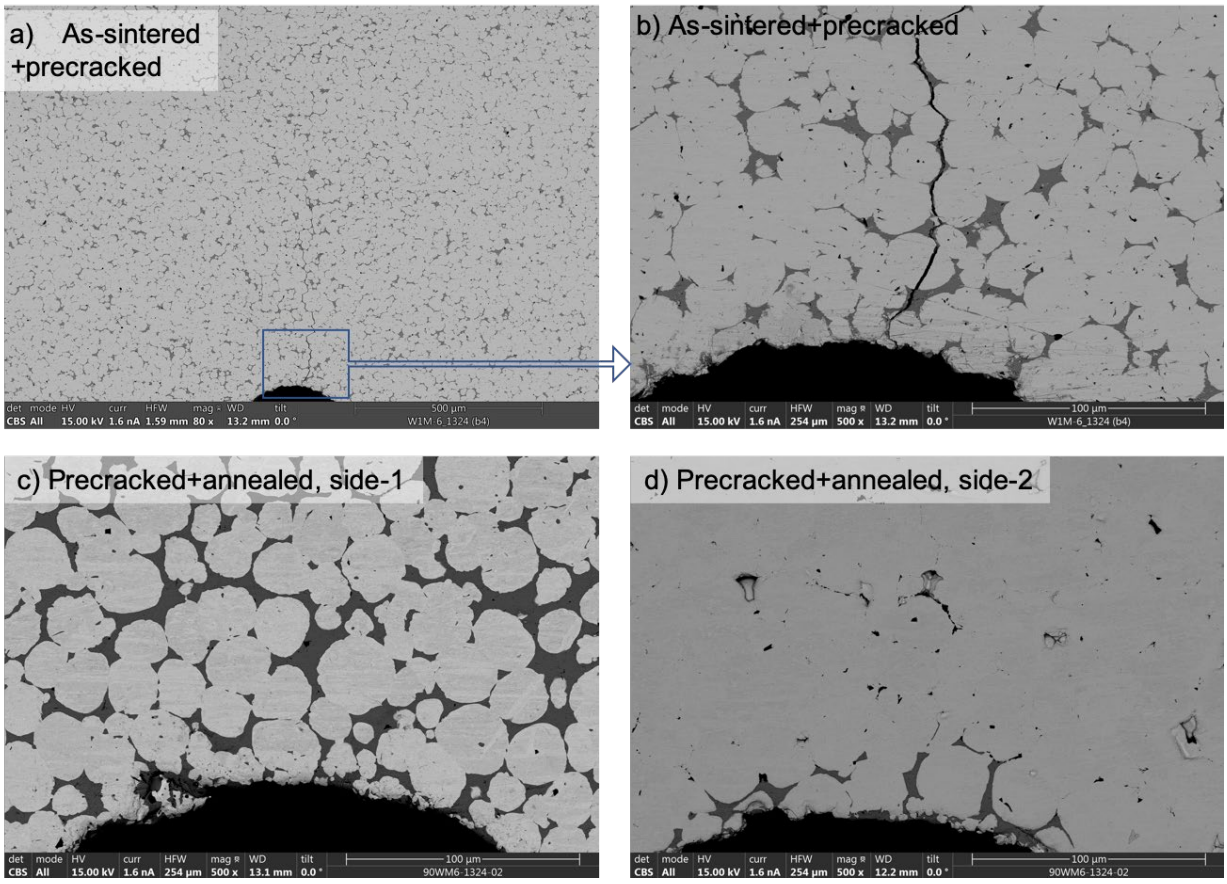

Figure 6. The SEM images of the 3x 90W WHA: a) PC; b) higher magnification image showing PC width close to the notch; c) and d) show both sides of the AN specimen close to the notch with no visible crack.

We have loaded the PC and AN 3x 90W specimen in a 3PB bar fixture to verify whether the same 1300°C/24h condition can heal partially or fully a 4.922 mm deep, through-thickness, and 1.33 mm long crack. Again, we used an in-situ telescopic optical microscope during the test and the images associated with the load points at the P-d curve are shown in Figure 7a. The image-3 of Figure 7a is associated with the maximum load (P_m) and the image reveals that process-zone plasticity starts from the notch of the specimen, rather than the initial crack tip. Further images at points 4 and 5 also support that evidence. Note the white dash line on image-5 of Figure 7a is the crack propagation line after the specimen is loaded to $0.65P_m$. Figure 7b shows the SEM image of the specimen after the test. Again, the non-linear crack propagation path along with the process-zone damage around it confirms the start of the crack from the notch at loading. Moreover, even after loading to $0.65P_m$ beyond post maximum load, the propagated crack length is 706 μm (Figure 7b), whereas the total PC length from the notch is 1329 μm before AN. The higher magnification SEM image of Figure 7b shown in Figure 7c reveals the process-zone damage mechanism which is mostly W-W and W-DP decohesion, indicated by red arrows. All this evidence confirms that the 1300°C/24 h AN can completely heal a 1.329 mm large, 4.922 mm through-thickness, and up to 1.8 μm wide crack of 90W WHA. We dubbed this specimen as PC +healed (PC+H).

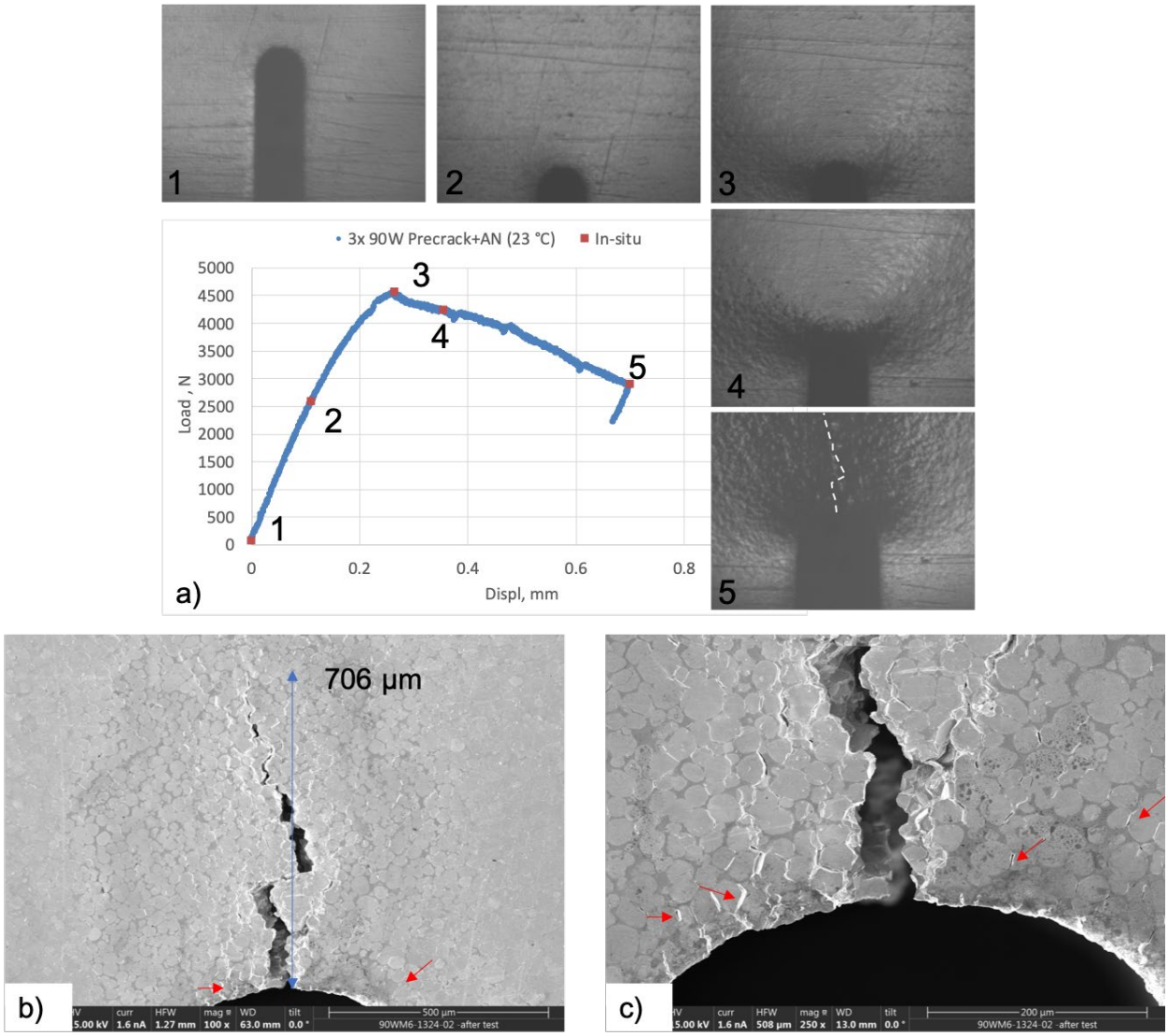

Figure 7. a) The RT P-d curves with the in-situ optical images for the PC+ AN 3x 90W specimen. The white dash line in point-5 image shows the crack propagation path at the test; b) the SEM image of the 3x 90W after the test; and c) a higher magnification SEM image close to the notch showing the process-zone damage around the notch.

The second 3x 90W WHA was PC to a/W ≈ 0.413 with a notch tip to PC tip length of 1.129 mm, shown in Figure 8. The PC width close to the notch tip averaged ≈ 0.871 ± 0.153 µm (Figure 8b), and that at the crack tip averaged ≈ 0.152 ± 0.064 µm (Figure 8c). The thickness of this specimen is 4.902 mm, which is eventually the PC depth. The specimen was then AN as the other specimens at 1300°C for 24 h in a vacuum. Similar to the previous one, extensive SEM image analysis did not show any visible crack along the PC zone (Figure 8d). Here, we again PC the healed specimen, slightly larger than the previous length, to a/W ≈ 0.4322 to compare: a) the fatigue cycle counts (61K vs. 56K at 20 Hz with $\Delta K \approx$ 18-20 MPa$\sqrt{m}$); b) the microstructure close to the notch for PC+H vs. PC+H+re-PC (PC+H+RPC) specimens; and c) RT toughness for the PC+H vs. PC+H+RPC (otherwise, AN) specimens. The microstructure and the RT fracture toughness will be discussed later in this report.

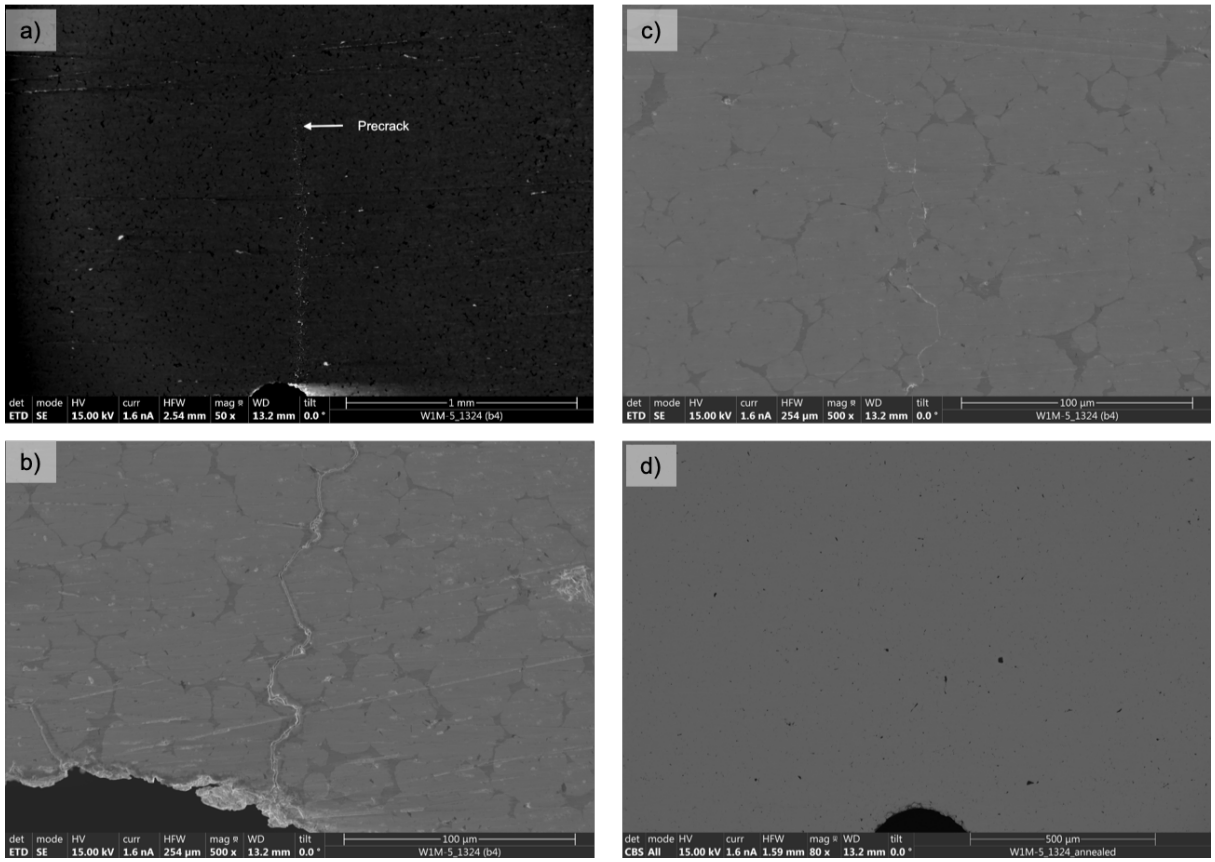

Figure 8. The SEM images of the 3x 90W WHA: a) PC; b,c) higher magnification image showing PC width close to the notch (b) and at the crack tip in (c), respectively. Image d) shows no visible crack after AN at 1300°C/24h in a vacuum.

Figure 9a shows the in-situ P-d curves with associated load-point optical images for the PC +AN+re-PC (PC+H+RPC) specimen. Note, due to the re-PC to a/W = 0.4322 of PC+H+RPC specimen, the maximum load is much lower (2815 N) than the PC+H 3x 90W WHA (4551 N) with an effective a/W ≈ 0.295 due to the healed PC (see Figure 7a), although the other dimensions are nominally the same. Figures 9a and b also show the crack initiation and propagation along with the plastic damaged zone which is far away from the notch tip. Figure 9c shows the damage mechanism at the crack tip after loading to deformation. Figure 9d compares the side view of the PC+H 3x 90W specimen to the PC+H+RPC specimen shown in Figure 9b and reveals much narrower and shorter propagated crack width and length, and the initiation of the damaged zone which starts around the notch tip for the first one. Note, even though the PC length and depth for the 3x 90W are larger (≈1.3 mm) and deeper (≈ 5.0 mm) compared to the 1x 90W (≈ 0.9 mm and 1.65 mm, respectively), both the 3x 90W PC healed completely while the 1x 90W healed partially (see Figures 1, 7, and 9). These results indicate that the larger and deeper cracks can be healed at 1300°C/24h AN, but the cracks wider than 2 μm may not be healed completely. The maximum width of the cracks for the two 3x 90W are 1.8 and 1.13 μm and that for 1x 90W is near 4.0 μm at the notch. Note, the 1x 90W crack healed up to the width of 1.3 μm.

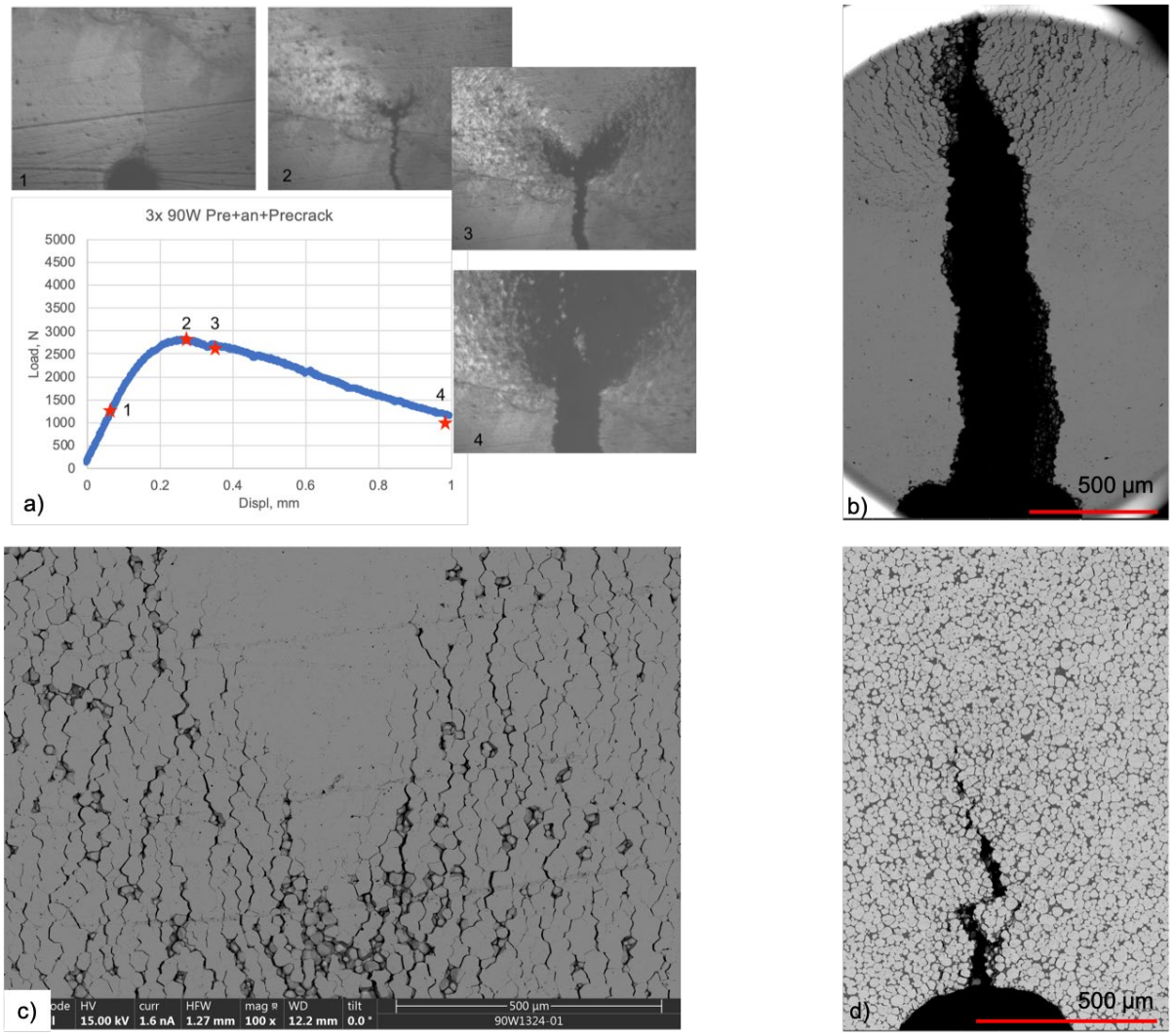

Figure 9. a) The RT P-d curves with the in-situ optical images for the PC+H+RPC to a/W ≈ 0.4322, 3x 90W specimen; b) SEM image of the same specimen after the test; c) higher magnification SEM image at the crack tip after deformation; and d) low magnification SEM image of the PC+H 3x 90W after loading to deformation. Note, the crack propagation starts far away from the notch for the PC+H+RPC specimen in Figure b whereas that starts at the notch for the PC+H specimen, shown in Figure d.

Microstructure

Basic microstructural characterizations for the W-particle size, DP area fraction, DP thickness, DP constituents, W-W contiguity, and texture for the as-sintered (AS), and the 1300°C/24h AN specimens has been reported previously [14] and are not different to these crack-healed specimens, at least outside of the healed zone. The W-particles are nearly 100% pure, irrespective of alloy compositions or AN conditions. The size of the W-particles varies between 17 ± 7 µm for the 90W and that increases with increasing W% to 38 ± 15 µm for the 97W, both for the AS and AN specimens. The Ni-rich DP is also unaffected which remains ≈ 50%Ni-30%W-20%Fe (by wt.%) for all the alloys and AN conditions. The DP ligament thickness averaged ≈ 5 ± 4.5 µm for all, though the DP area fraction reduced from 16% for 90W to ≈ 6% for 97W, remaining unchanged after annealing. Both the W and DP textures are random for all alloys and at pre-and post- AN conditions. In short, the 1300°C/24 h AN has a very negligible effect on the observed microstructures on the various as-sintered 90W-97W WHAs.

Our preliminary study shows that the microstructure around the healed zone is nearly the same as the outside of the healed zone or the other AN specimens reported previously in [14], except for one 3x 90W shown in Figure 10. Figure 10a shows the SEM image of the healed zone, marked by a red rectangle, for a 3x 90W WHA and reveals some speckles in the W-particles. The higher magnification SEM image of this healed zone is shown in Figure 10b which clearly shows the speckles are Ni-rich DP, confirmed by EDS (not shown here). These speckles are not visible in the far-from-healed zone area as shown in Figure 10c.

Figure 11 shows the SEM fractographs of the two 3x 90W PC+H, and PC+H+RPC specimens, both after loading. Figure 11a shows the low magnification SEM image of the notch and deformed zone that starts just after the notch. Reasonably a good amount of DP rupture can be seen around the deformed zone. Figure 11b shows the higher magnification secondary electron (SE) SEM image of the deformed zone and reveals the DP rupture more clearly, along with the presence of DP in W-particles, which aligns with the speckles observed in the cracked healed zone (see Figure 10a,b). Figure 11c shows the BSE image of the same area revealing some defragmented W-particles in the DP-rich zone. The mix-up of DP in W-particles and vice versa might help to close up the crack at the 1300°C high AN temperature. Figure 11d-f shows the SEM fractographs of the PC+H+RPC specimens that are loaded to deform. The notch re-PC and the deformed zone under the test are shown in the low magnification SEM image in Figure 11d. Figure 11e shows the fatigue PC zone, close to the notch, and reveals striation-like features in the DP. Both images in Figure 11b and 11e are captured close to the notch of the PR+H and PC+H+RPC 3x 90W, respectively, but the differences between the features again prove the crack healing. Figure 11f shows the SEM image probed on the deformed zone for the PC+H+RPC specimen. Here the W-particles are relatively flat and clean with less DP infusion compared to the PC+H specimen shown in Figure 11b. The DP rupture is also relatively lower in this case.

The crack healing mechanism is not clear, and not thoroughly studied in this study. However, here, the self-healing of WHAs may occur by the sintering (diffusion) mechanism which is effective for ceramic-like materials at a temperature, $T > 0.7T_m$ [24]. Our AN temperature (1300°C) is much higher than the $0.7T_m$ of Ni (T_m = 1455 °C) and Fe (T_m = 1538°C). The classical Gibb-Thomson sintering mechanism might play a role here too. From Figures 10 and 11, it has been observed that the DP diffused into W-particles from surroundings, and some defragmented W particles into DP phases which might also help to heal the crack by diffusion mechanism. Some metastable intermetallics like Fe_2W, FeW, Ni_4W, NIW, NiW_2, $Fe_3Ni_2W_5$ form in between 800 to 1090°C for the W-Ni-Fe WHA [39], which might be dissolved at 1300°C AN and reprecipitate at the crack face which might also help to close the crack. However, these are just a few assumptions, and more studies will be performed in the future to understand the crack-healing mechanism of WHAs.

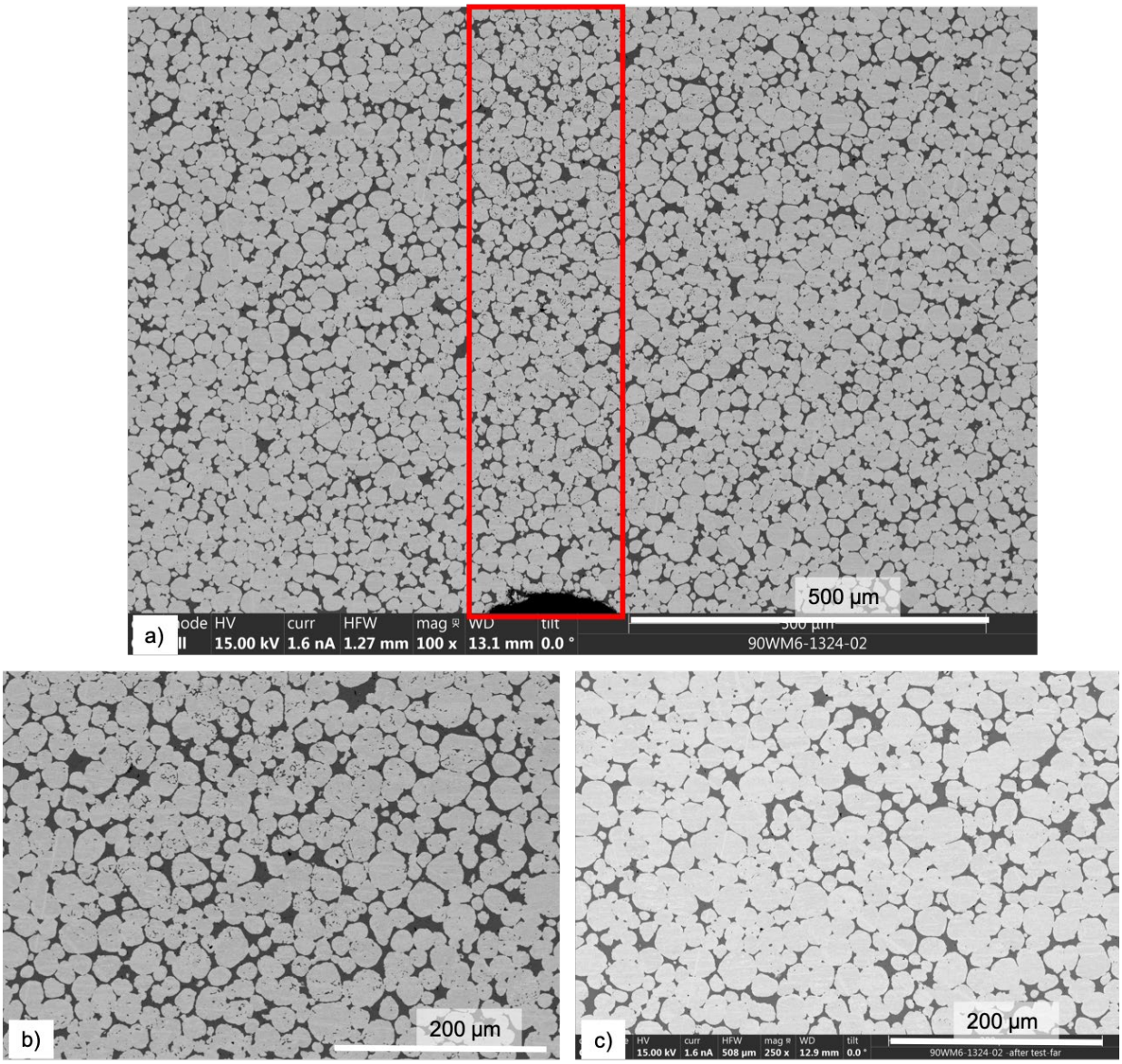

Figure 10. The SEM images showing the microstructure of a 3x 90W PC+H specimen: a) healed PC zone, marked by a red rectangle; b) higher magnification image at the healed zone shows some DP speckles in the W-particles; and c) missing of these DP speckles on W far from the healed zone.

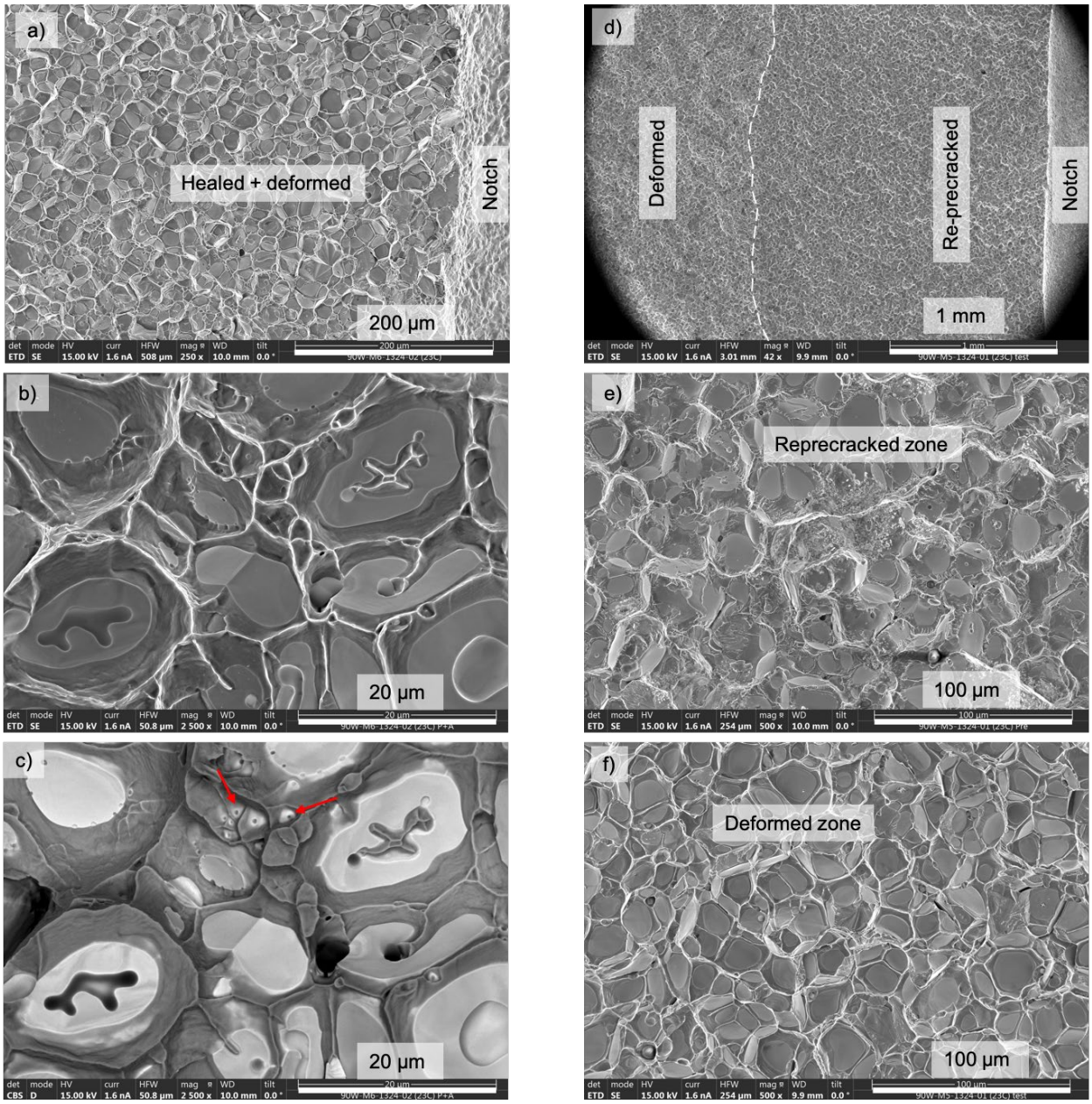

Figure 11. The SEM images showing the fractographs of two 3x 90W PC+H in a-c); and PC+H+RPC specimens in d-f), respectively, as: a) the low magnification SEM image of the notch and deformed zone due to loading; b) higher magnification SE SEM image of the deformed zone showing DP rupture and the presence of DP in W-particles; c) BSE image of the same area showing some defragmented W-particles in the DP rich zone; d) low magnification SEM image of the notch, re-PC zone; and f) high magnification SEM image of the deformed zone.

RT fracture toughness

The RT elastic (K_{Im}) and elastic-plastic (K_{Jm}) fracture toughness at maximum load is also measured by following the ASTM E1921 standard, though the required a/W ratio due to the crack healing, and the specimen size have not been followed strictly. The toughness results are shown in Table 1. Note, the toughness measurement was not the primary focus of this study. Nevertheless, this assessment will help us to understand the strength of the healed material. The RT K_{Im} for the 1x 90W to 97W WHAs are nearly the same for the AS [11], 1300°C/24h AN [14] and the PC+healed (PC+H) specimens that vary between 31 to 41 MPa√m. This shows that the 1300°C/24h AN does not affect the elastic fracture toughness of the AS specimens. More importantly, the elastic fracture toughness of the PC+H specimens is the same as that of AS or AN specimens. The elastic fracture toughness of the 3x 90W is also similar for the AS (52 ± 2 MPa√m), PC+H (56.1 MPa√m), and PC+H+RPC (50.2 MPa√m) specimens. Note, due to the larger re-PC to a/W = 0.4322 of the healed than the initial PC ratio of a/W = 0.413, we can consider this 3x 90W WHA as a 1300°C/ 24h AN specimen.

The RT K_{Jm} is also shown in Table 1 for the 1x and 3x specimens for various conditions and compositions. The K_{Jm} for 1x healed specimens varies from 95.1 to 121.1 MPa√m, which is very close to the AN 1x specimens that vary from 98 to 128 MPa√m. Again, this proves that the cracks are healed completely without sacrificing the materials' elastic-plastic toughness. Indeed, a substantial toughness improvement can be seen if we compare the K_{Jm} of the 1x PC+H specimens to the AS specimens, especially for the 97W that improves up to 45%. The RT K_{Jm} for the 3x 90W of the PC+H specimen (122 MPa√m) is also closer to the 3x AN specimen (117 MPa√m) but much higher than the AS 3x 90W WHA (92 ± 6 MPa√m). Therefore, it can be expected from this study that the cracks that will develop by the thermal cyclic load of 90W to 97W will self-heal if the materials are operated at 1300ºC for 24h. The toughening mechanism of the healed 1x and 3x 90-97W WHAs are similar to that of AN specimens discussed previously (see Figures 1-4, 9 and [14]). Again, the toughness and its mechanism are not the main focus of this study.

Table 1. The RT maximum load fracture toughness (K_{Im} and K_{Jm}, in MPa√m) of as-sintered [11,13], AN [14], and healed WHAs

Conditions	90W		92.5W		95W		97W	
	K_{Im} MPa√m	K_{Jm} MPa√m	K_{Im} MPa√m	K_{Jm} MPa√m	K_{Im} MPa√m	K_{Jm} MPa√m	K_{Im} MPa√m	K_{Jm} MPa√m
1x PC+H	39	109.4	37.8	121.1	41.2	95.1	31.9	100.5
3x PC+H	56.1	122.0						
3x PC+H+RPC	50.2	116.8						
1x AS [11]	36 ± 4	97 ± 18	39 ± 4	96 ± 12	42 ± 6	107± 14	36 ± 5	69 ± 12
1x AN-1323 [14]	37 ± 0	127±11	37 ± 1	100 ± 7	38 ± 1	117 ± 2	35 ± 1	98 ± 17
3x AS [13]	52 ± 2	92 ± 6	50 ± 3	83 ± 11	49 ± 1	75 ± 4	38 ± 4	38 ± 4

PC = precracked; H= healed; RPC = repre-cracked; AS= as-sintered; AN = annealed.

Future Work

This study clearly shows that up to 1.3 mm long, 5 mm deep, and 1.8 µm wide macrocrack can be self-healed if the 90W-97W WHAs are operated at 1300°C. The toughness of the healed WHAs is similar to the AN WHAs and higher than the as-sintered WHAs. Though the diffusion is assumed to be the primary healing mechanism, however, more study will be explored in the future with the following questions in mind:

a) Does the intermix of DP and W-particle diffusion help to close the crack at a higher temperature?

b) What is the time-temperature kinematics of the WHA healing mechanism? Are they different for different WHA and crack dimensions?
c) The PC more generally proceeds through the DP. However, W particles are also cracked in some cases. How does a 1300°C temperature heal the cracked/cleaved W-particle? Does DP diffuse in between the cracked W particles to heal these cleaved W-particles?
d) Do the W, Ni, and Fe metastable intermetallics have any role in WHA crack healing? The XRD study might be helpful to understand.
e) Is the result repeatable? What is the maximum dimension or width of the crack that can be healed?
f) Any change of W-particles or DP area fraction around the healed zone?
g) Any change of texture around the healed zone?

Acknowledgments

We thank our University of California, Santa Barbara colleagues David Gragg, Dano Pagenkopf, and Kirk Fields for their important contributions to this work. We also acknowledge the support provided by the U.S. Department of Energy through the Office of Fusion Energy Sciences (DE-FG02-94ER54275). The U.S. National Science Foundation supported the California Nanoscience Institute (CNSI) which provided facilities critical to the success of this research.

References

[1] P. Norajitra, R. Giniyatulin, W. Krauss, V. Kuznetsov, I. Mazul, I. Ovchinnikov, J. Reiser, M. Rieth, V. Widak, Current status of He-cooled divertor development for DEMO, Fusion Eng. Des. 84 (2009) 1429–1433.

[2] E. Gaganidze, A. Chauhan, H.C. Schneider, D. Terentyev, G. Borghmans, J. Aktaa, Fracture-mechanical properties of neutron irradiated ITER specification tungsten, J. Nucl. Mater. 547 (2021) 152761.

[3] C. Henager Jr, W. Setyawan, T. Roosendaal, N. Overman, B. Borlaug, E. Stevens, K. Wagner, R. Kurtz, G.R. Odette, B. Nguyen, K. Cunningham, Ductile-phase toughened tungsten for plasma-facing materials in fusion reactors, Int. J. Powder Metall. 53 (2017) 53–69.

[4] J. Reiser, J. Hoffmann, U. Jäntsch, M. Klimenkov, S. Bonk, C. Bonnekoh, M. Rieth, A. Hoffmann, T. Mrotzek, Ductilisation of tungsten (W): On the shift of the brittle-to-ductile transition (BDT) to lower temperatures through cold rolling, Int. J. Refract. Met. Hard Mater. 54 (2016) 351–369.

[5] B. Gludovatz, S. Wurster, A. Hoffmann, R. Pippan, Fracture toughness of polycrystalline tungsten alloys, Int. J. Refract. Met. Hard Mater. 28 (2010) 674–678.

[6] M. Scapin, Mechanical characterization and modeling of the heavy tungsten alloy IT180, Int. J. Refract. Met. Hard Mater. 50 (2015) 258–268.

[7] R. Neu, H. Maier, M. Balden, S. Elgeti, H. Gietl, H. Greuner, A. Herrmann, A. Houben, V. Rohde, B. Sieglin, I. Zammuto, Investigations on tungsten heavy alloys for use as plasma facing material, Fusion Eng. Des. 124 (2017) 450–454.

[8] R. Neu, H. Maier, M. Balden, R. Dux, S. Elgeti, H. Gietl, H. Greuner, A. Herrmann, T. Höschen, M. Li, V. Rohde, D. Ruprecht, B. Sieglin, I. Zammuto, Results on the use of tungsten heavy alloys in the divertor of ASDEX Upgrade, J. Nucl. Mater. 511 (2018) 567–573.

[9] H. Sattar, S. Jielin, H. Ran, M. Imran, W. Ding, P. Das Gupta, H. Ding, Impact of microstructural properties on hardness of tungsten heavy alloy evaluated by stand-off LIBS after PSI plasma irradiation, J. Nucl. Mater. 540 (2020) 152389.

[10] Q. An, A. Elshafiey, L. Huang, D.A. Hammer, M. Hassani, Plasma and X-ray radiation-induced damage mechanisms in a tungsten heavy alloy, J. Nucl. Mater. 539 (2020) 152325.

[11] M.E. Alam, G.R. Odette, On the remarkable fracture toughness of 90 to 97W-NiFe alloys revealing powerful new ductile phase toughening mechanisms, Acta Mater. 186 (2020) 324–340.

[12] M.E. Alam, J. Wang, C.H. Henager, W. Setyawan, G.R. Odette, The effect of hot rolling on the strength and fracture toughness of 90W–7Ni3Fe tungsten heavy metal alloys, Mater. Sci. Eng. A. 824 (2021) 141738.

[13] M.E. Alam, G.R. Odette, On the Influence of Specimen Size and Geometry on the Fracture Toughness of Tungsten Heavy Metal Alloys, J. Nucl. Mater. 571 (2022) 154025.
[14] M.E. Alam, G.R. Odette, Improving the Fracture Toughness and Ductility of Liquid Phase Sintered WNiFe Tungsten Heavy Alloys by High-Temperature Annealing, Materials (Basel). 16 (2023) 916.
[15] M.E. Alam, G.R. Odette, The comparative strength and fracture toughness properties of commercial 95W-3.5Ni1.5Fe and 95W-3.5Ni1.5Cu tungsten heavy alloys, Nucl. Mater. Energy. 36 (2023) 101467.
[16] S.R. White, N.R. Sottos, P.H. Geubelle, J.S. Moore, M.R. Kessler, S.R. Sriram, E.N. Brown, S. Viswanathan, Autonomic healing of polymer composites, Nature. 409 (2001) 794–797.
[17] J.D. Rule, N.R. Sottos, S.R. White, Effect of microcapsule size on the performance of self-healing polymers, Polymer (Guildf). 48 (2007) 3520–3529.
[18] T. Yin, M.Z. Rong, M.Q. Zhang, G.C. Yang, Self-healing epoxy composites - Preparation and effect of the healant consisting of microencapsulated epoxy and latent curing agent, Compos. Sci. Technol. 67 (2007) 201–212.
[19] R.S. Trask, I.P. Bond, Biomimetic self-healing of advanced composite structures using hollow glass fibres, Smart Mater. Struct. 15 (2006) 704–710.
[20] K.S. Toohey, N.R. Sottos, J.A. Lewis, J.S. Moore, S.R. White, Self-healing materials with microvascular networks, Nat. Mater. 6 (2007) 581–585.
[21] T.K. Gupta, Crack Healing and Strengthening of Thermally Shocked Alumina, J. Am. Ceram. Soc. 59 (1976) 259–262.
[22] G. Bandyopadhyay, J.T.A. Roberts, Crack healing and strength recovery in UO2, J. Am. Ceram. Soc. 59 (1976) 415–419.
[23] S. K. Ghosh, Self-healing materials: fundamentals, design strategies, and applications, John Wiley & Sons, Verlag GmbH & Co. KGaA, Weinheim, 2009.
[24] F. Tavangarian, D. Hui, G. Li, Crack-healing in ceramics, Compos. Part B Eng. 144 (2018) 56–87.
[25] K.W. Gao, L.J. Qiao, W.Y. Chu, In situ TEM observation of crack healing in α-Fe, Scr. Mater. 44 (2001) 1055–1059.
[26] D. Wei, J. Han, Z.Y. Jiang, C. Lu, A.K. Tieu, A study on crack healing in 1045 steel, J. Mater. Process. Technol. 177 (2006) 233–237.
[27] M.E. Alam, S. Pal, N.J. Cunningham, G.R. Odette, On a new Ti-carbooxinitride redistribution driven microcrack healing mechanism in an annealed 14YWT nanostuctured ferritic alloy, Acta Mater. 210 (2021) 116842.
[28] J. Han, G. Zhao, Q. Cao, Internal crack recovery of 20MnMo steel, Sci. China Ser. E Technol. Sci. 40 (1997) 164–169.
[29] R.S. Xin, J. Kang, Q.X. Ma, S. Ren, H.L. An, J.T. Yao, J. Pan, L. Sun, Evolution Behaviors and Mechanisms of Internal Crack Healing in Steels at Elevated Temperatures, Metall. Mater. Trans. A. 49A (2018) 4906–4917.
[30] Y. Zhou, J. Guo, M. Gao, G. He, Crack healing in a steel by using electropulsing technique, Mater. Lett. 58 (2004) 1732–1736.
[31] H. Song, Z.J. Wang, X.D. He, J. Duan, Self-healing of damage inside metals triggered by electropulsing stimuli, Sci. Rep. 7 (2017) 1–11.
[32] K. Laha, J. Kyono, T. Sasaki, S. Kishimoto, N. Shinya, Improved creep strength and creep ductility of type 347 austenitic stainless steel through the self-healing effect of boron for creep cavitation, Metall. Mater. Trans. A. 36 (2005) 399–409.
[33] G.S. Firstov, J. Van Humbeeck, Y.N. Koval, High-temperature shape memory alloys Some recent developments, Mater. Sci. Eng. A. 378 (2004) 2–10.
[34] D. Wei, J. Han, A.K. Tieu, Z. Jiang, Simulation of crack healing in BCC Fe, Scr. Mater. 51 (2004) 583–587.
[35] N. Shinya, J. Kyono, K. Laha, C. Masuda, Self-healing of creep damage through autonomous boron segregation and boron nitride precipitation during high temperature use of austenitic stainless steels, in: Proc. First Int. Conf. Self-Heal. Mater., The Netherlands, 2007: pp. 1–9.

[36] R.N. Lumley, G.B. Schaffer, Precipitation induced densification in a sintered Al-Zn-Mg-Cu alloy, Scr. Mater. 55 (2006) 207–210.
[37] R.N. Lumley, R.G. O'Donnell, I.J. Polmear, J.R. Griffiths., Enhanced fatigue resistance by underageing an Al-Cu-Mg-Ag alloy, Mater. Forum. 29 (2005) 256–261.
[38] ASTM E1921-20, Standard Test Method for Determination of Reference Temperature , To , for Ferritic Steels in the Transition Range, in: Annu. B. ASTM Stand., ASTM International, 100 Barr Harbor Drive, PO Box C700, West Conshohocken, PA 19428-2959, United States, 2020: pp. 1–25.
[39] R.M. German, Tungsten Heavy Alloy Handbook, Metal Powder Industries Federation, East Princeton, New Jersey, USA, 2021.

4.3 CRACKING IN HIGH-HEAT-FLUX TESTED TUNGSTEN—C. Parish, R. Juneja, J. Rapp, T. Gray, A. Hussain (Oak Ridge National Laboratory)

OBJECTIVE

Determine an experimental methodology for tracking crack paths and other defects in high-heat-flux tested tungsten.

SUMMARY

A large polycrystalline tungsten test piece was exposed to high-heat-flux in vacuum at the Applied Research Laboratory (ARL) at Pennsylvania State University. Cracking and melting were observed. The specimen (~80 mm tall, ~2.2 kg) was examined in plan-view using the large-chamber Tescan Mira3 GMH scanning electron microscopy (SEM) in Oak Ridge National Laboratory (ORNL) Low Activation Materials Development and Analysis (LAMDA) laboratory. Imaging and X-ray spectroscopy were used to study the cracks and melt regions. The sample was then sectioned by electro-discharge machining and one cracked section prepared by diamond saw and metallography for cross-sectional electron backscatter diffraction (EBSD) in SEM. The crack path was observed and related to grain structures.

RESULTS

In plain-view, the structure was seen to contain thin, long cracks and some debris or dirt on the surface (Figure 1 left). The cracks contained dark electrically insulating material that showed carbon by X-ray spectroscopy. Leaf- or flower-like structures were observed (Figure 1, right) which might have been melt structures. Low-energy X-ray mapping found no carbon or oxygen concentration in the leaf structures, so they were probably either pure tungsten or a very thin surface layer of oxide or oxycarbide.

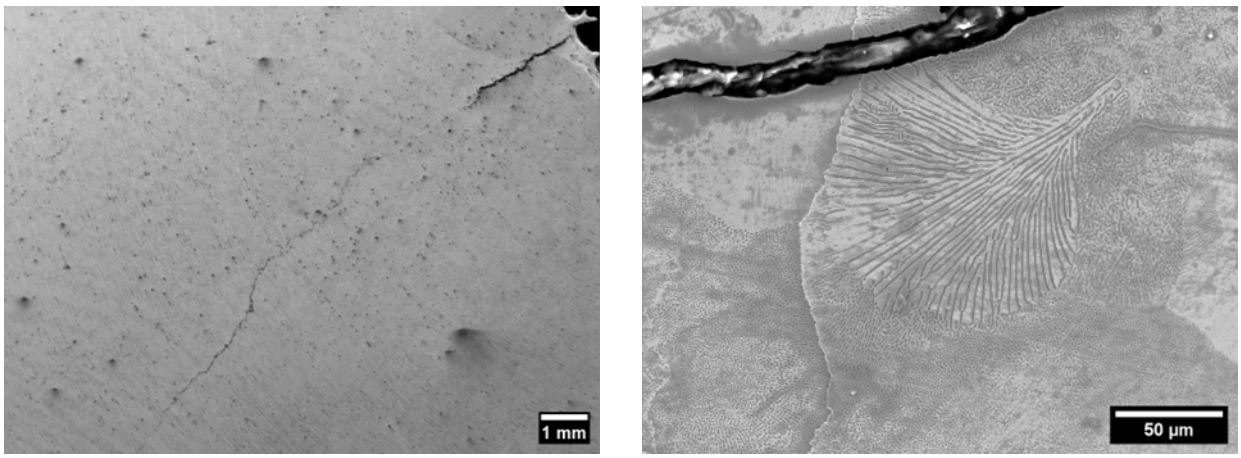

Figure 1. Plan-view SEM images at low and high magnification of cracking and melt structures.

In cross-section, large grains consistent with aggressive recrystallization from high temperature were observed (Figure 2). Further, the crack was seen to be entirely intergranular, moving down grain boundaries and not cutting through grains. (i.e., crystallographic orientations on either side of the crack were not similar.) Whether the crack occurred down the grain boundaries or the crack occurred and then grain growth occurred that was arrested by the free surface cannot be determined from post-mortem EBSD.

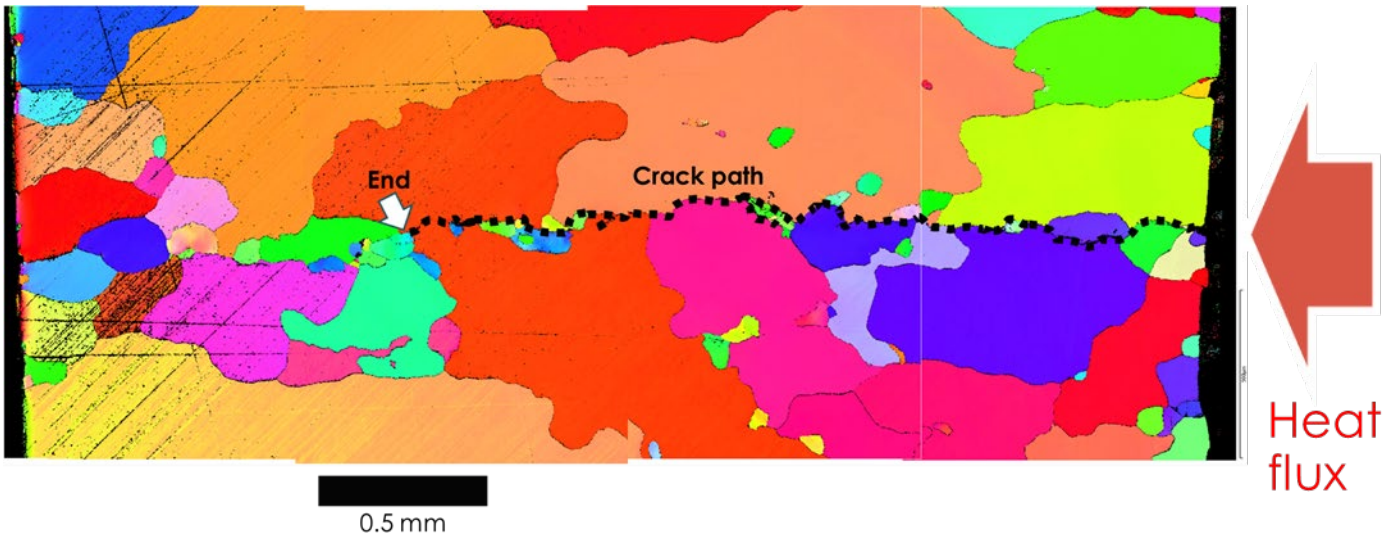

Figure 2. Cross-sectional EBSD montage showing the intergranular cracking.

Future Work

An ORNL Laboratory Directed Research and Development (LDRD) is under review to perform multiscale modeling of these and similar results.

4.4 IN-SITU MICROMECHANICAL TESTING ON W/NiFe DUCTILE-PHASE TOUGHENED TUNGSTEN—A. V. Garcia Caraveo, T. Chen (Oregon State University), W. Setyawan (Pacific Northwest National Laboratory)

OBJECTIVE

The objective of this project is to evaluate the changes in radiation-induced properties of ductile phase toughened (DPT) W-NiFe alloys. The aim is to use this evaluation to inform computational models for predicting performance and manipulating microstructure. Specifically, the project focuses on simulating the conditions of irradiation and helium embrittlement that occur in fusion reactors through ion irradiation. Small-scale mechanical testing techniques are used to characterize the mechanical response due to radiation damage in the shallow radiation damage region (on the order of micrometers). It is proposed that small-scale mechanical testing will provide input to low-dimension computational models, which will generate material parameters for an engineering-scale model to predict the material's performance under service conditions.

SUMMARY

In the first year of the project (October 2022 to July 2023), micromechanical testing methods were assessed and demonstrated to obtain microstructure-specific mechanical properties of DPT W-NiFe alloys. The testing techniques used included notched microcantilever bending, microbeam deflection, and micropillar compression. The obtained microstructure-specific properties include microscopic fracture toughness, stress-strain constitutive relationship, and the critical resolved shear stress (CRSS).

The applicability of these testing methods to the material of interest was validated by showing that the micromechanical properties obtained from the W particles in DPT W-NiFe alloys matched those obtained from bulk W samples in existing literature. In notched microcantilever bending test, the continuous stiffness measurement (CSM) technique was extended to enable the quantification of crack length changes. This allowed for determining both crack initiation and propagation toughness in tungsten (W). The crack initiation toughness in W was determined to be 12.7 $MPa - m^{1/2}$, and during propagation, an R-curve behavior was observed. Through microbeam bending, the elastic modulus and flexural yield strength of W were determined to be 397 GPa and 2.95 GPa, respectively. Taking advantage of the microbeam size effect, which allows for ductility even in relatively brittle materials like W at ambient temperature, strain hardening can also be characterized through microbeam bending. Furthermore, micropillar compression tests were employed to characterize the CRSS of the{110}<111> slip systems in W, which was found to be approximately 434 MPa for a 3 x 3 x 6 μm^3 micropillar. The potential of micropillar compression testing in revealing dislocation nucleation, multiplication, and interaction mechanisms in irradiated materials was discussed to guide future research efforts.

In the following year of the project, these testing techniques will be applied to characterize the mechanical response of DPT W-NiFe alloys to ion radiation, aiming to gain a mechanistic understanding of the microstructure-property relationship with the help of theoretical models.

Through this project, a graduate student from under-represented group was recruited. The student has demonstrated satisfactory academic performance and finished several essential trainings to be successful in graduate school and in conducting research for this project. The trainings include scanning and transmission electron microscopy (TEM), focused ion beam, and micromechanical testing techniques. This effort promotes the Department of Energy's (DOE's) education mission and the future workforce pipeline for United States (US) energy sectors.

PROGRESS AND STATUS

Introduction

The DPT W-NiFe alloys have significantly improved fracture toughness compared to W, mitigating the brittle challenge of W-based plasma-facing materials. With the strong interface between the hard and the ductile phases, microcracks imitate in the hard W phase are arrested and blunted by the ductile NiFeW phase, which also bridges co-planar microcracks [1, 2]. However, after ion irradiation (which emulates helium accumulation and radiation damage effects of 14 MeV neutrons), helium cavities were observed at the W/NiFeW interface [3], raising concerns about possible interfacial debonding, which impairs the above toughening mechanisms. Further development, evaluation, and qualification of DPT alloys for fusion applications require answering the following questions. (1) To what extent does the radiation evolution of the W/NiFeW interface affect the interfacial mechanical properties, microcrack initiation, and propagation? (2) Should we expect new toughening mechanisms to emerge due to the local mechanical property changes? And (3) Can we tailor the microstructure of the DPT alloys for better performance in radiation environments? One critical step to answering these questions and understanding the mechanisms is quantifying the microstructure-specific properties, which will also provide input to computational models for performance prediction and microstructure optimization. Yet, probing the mechanical responses to irradiation damage at specific microstructural features is challenging, especially in ion-irradiated samples with shallow irradiated zones.

Small-scale mechanical testing has demonstrated success in characterizing mechanical responses to ion irradiation. Prior studies mainly applied hardness, stress relaxation, and nanoindentation creep tests to understand irradiation hardening effects [4, 5]. Recent studies showed the promise of obtaining fracture properties of ion-irradiated samples using nanomechanical bending tests [6, 7]. Yet, the specimen size effect has been recognized as one of the challenges in the quantitative assessment of fracture properties at micro scales [8]. First, the plastic zone usually extends beyond the vicinity of the crack tip, the so-called K-dominated zone, invalidating the small-scale yielding condition for the application of linear elastic fracture mechanics (LEFM) even in relatively brittle materials [9]. Thus, J-integral must be employed to describe crack propagation. Second, the sample size dependence of the fracture resistance is hard to eliminate because of the small sample dimensions relative to the plastic zone and the characteristic microstructural length scales governing certain fracture resistance mechanisms [8, 10, 11]. Besides, micropillar compression testing is proposed to understand the local deformation behavior of an individual microstructure / phase under uniaxial compression [12]. When analyzing the data, crystal orientation has to be taken into consideration, as well as the activation of slip systems and the building up of dislocations [13]. Bending of an unnotched microcantilever (microbeam deflection) has also been proposed to characterize the elastic modulus, yield strength, and potentially hardening property of a material [14].

In this report, we demonstrated the applications of notched microcantilever bending, microbeam deflection, and micropillar compression for the evaluation of fracture toughness, flexural stress strain relationship, and CRSS for slip activation, respectively. The investigations primarily focus on the W phase, which is the major component of this composition material, and has sufficient literature data to validate the proposed techniques.

Experimental Procedure

The DPT alloy used for this research is W-NiFe alloy sample W90, which contains 90W-7Ni3Fe (by wt%) supplied and mechanically polished by Pacific Northwest National Laboratory (PNNL). The microstructure and crystal orientation relationships of the W and NiFe phases were characterized by electron

backscattered diffraction (EBSD), Figure 1. This practice allows for crystal orientation-dependent studies. For fracture studies, microcantilevers can be orientated to fracture on dedicated crystal planes.

Guided by the EBSD survey shown in Figure 1, microcantilevers and micropillars were fabricated with controlled crystal orientations. Particularly, single-crystal W and Ni microcantilevers were prepared with the {011} and {001} crack planes, respectively, being close normal with respect to the beam longitudinal direction. For micropillars, the EBSD-recorded axial direction will be the direction of the uniaxial loading, which will be used to analyze the activation of slip planes.

Free-standing notched microcantilevers were employed to test microstructure-specific fracture toughness. A straight-trough notch (STN) geometry with a house-shaped cross section was employed for the easiness of fabrication and the existence of reference protocols in the literature. The microcantilever geometry and dimensions are defined by the following ratios ($\frac{a}{b}, \frac{w}{b}, \frac{L_0}{b}, \frac{L_1}{b}$) where b = 2 μm, a = 0.4 μm, L_0 = 0.2 μm, L_1 = 10 μm and w = 2 μm, as shown in Figure 2 [15] and Figure 3a.

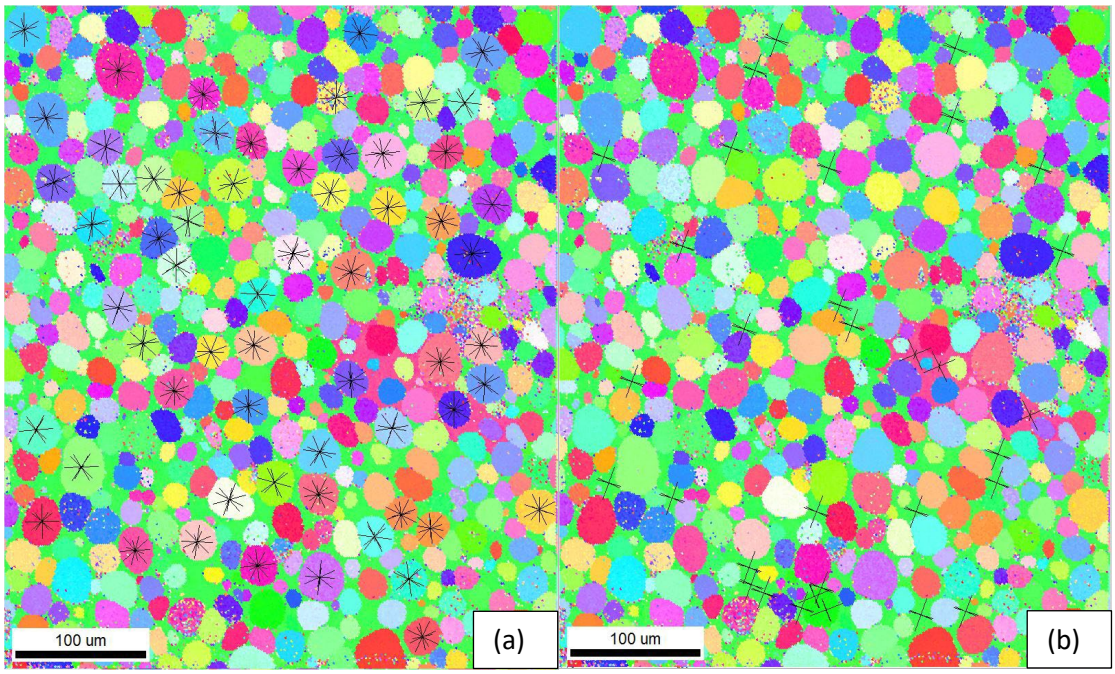

Figure 1. The EBSD analysis with the W [011] and Ni [001] orientations marked in (a) and (b), respectively.

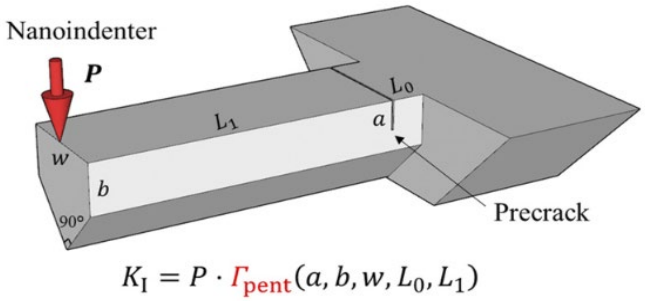

Figure 2. Free-standing notched microcantilever dimension diagram reference. [15]

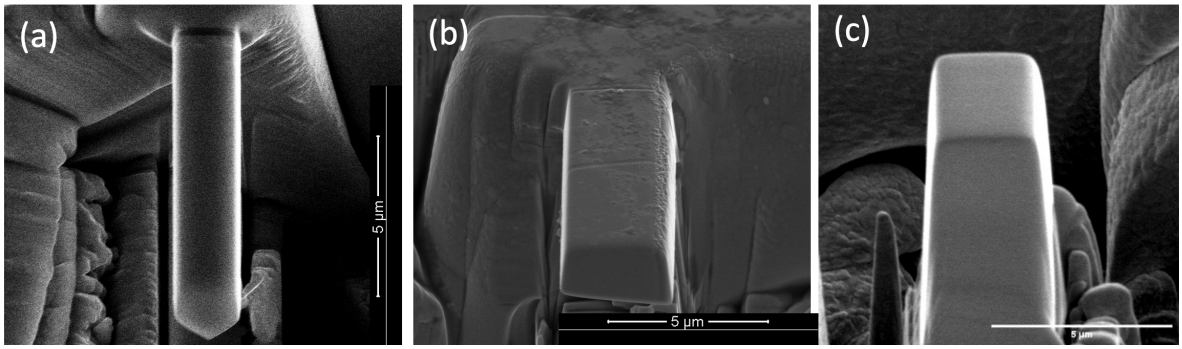

Figure 3. Examples of micro-milled microcantilevers with (a) house-shaped cross section and (b) rectangular cross section, and (c) rectangular micropillar.

For microbeam deflection, a microcantilever geometry similar to the notched microcantilevers discussed above was selected, with an exception that the cross section is rectangular rather than the house shape, Figure 3b. The width (w) and height (b) of the microcantilever are both 2 µm, and the distance between the free and the fix ends is 10µm.

For micropillar compression, rectangular pillars with cross section areas of 3 x 3 μm^2 and heights of 6 µm were fabricated, Figure 3c. All the micromechanical specimens were fabricated using a Quanta 3D scanning electron microscopy (SEM) / focused ion beam (FIB) system. The micro-milling was done using gallium ions of 30 keV. Initial milling employs high beam current of 15 nA for faster process. The ion beam current gradually reduces to 0.5 nA to finish the specimen preparation. The lower beam current was employed to achieve a fine finish of the specimen surface.

In-situ SEM bending experiments were performed with a Femto Tools (FT)-NMT04 nano indenter. The in-situ data allows the analysis of the cantilever displacement, fracture propagation, plastic deformation, and slip activation and development. A conical tip with a diameter of 2 µm and flat-punch tips with diameters of 5 and 10 µm were used to apply the loading under different testing conditions. Displacement control mode was employed for both microcantilever bending and micropillar compression tests. For microcantilever bending, the displacement rate was 5 nm/s. For micropillar compression, a nominal strain rate of 3 x $10^{-3}/s$ was achieved by setting the displacement rate to be 18 nm/s. During microscopic fracture toughness testing, CSM technique was employed to obtain the stiffness evolution for crack length estimation. The CSM frequency and oscillation amplitude were chosen to be 200 Hz and 2 nm, respectively.

Results

Microscopic fracture toughness

Figure 4 a-c and d-f show fracture initiation and propagation in the W microcantilever and slip band development without fracture initiation in the Ni microcantilever, respectively. The fractography of the W microcantilever, Figure 4c, indicates plastic-energy dissipation during fracture. Slip band development was observed at quite early stage in the bent Ni microcantilever. Plastic deformation continued until the end of the test when the displacement reached around 4 µm, corresponding to a strain of ~0.4. Both the number density and the step depths of the slip bands were observed to increase during the test. Fracture initiation in the Ni microcantilever was not observed.

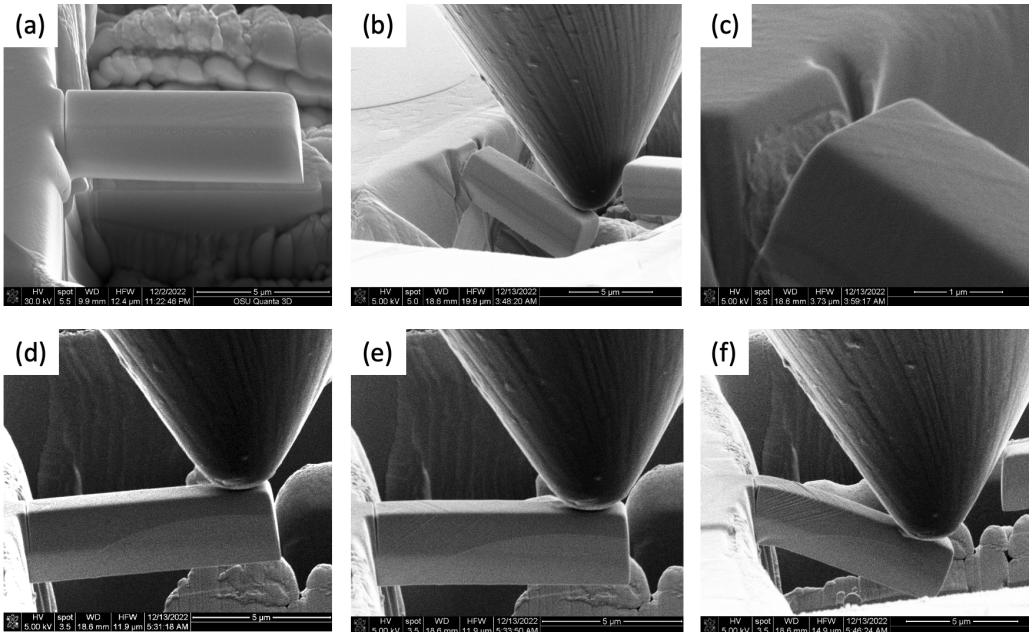

Figure 4. Snapshots during the in-situ bending tests of notched microcantilevers of W (a-c) and Ni (d-f).

Figure 5a and b present the load and stiffness curves with increasing displacement for the W and Ni cantilevers. In Figure 5a., the single-phase W microcantilever shows linear elastic and plastic behavior, whereas the single-phase Ni microcantilever shows almost flat load in the plastic regime with load drops due to slip bursts. In Figure 5b., the initial rapid increase in stiffness happened as the indenter came in full contact with the micro-cantiler. A flat stiffness curve, as shown by the Ni microcantilever, corresponds to a constant notch depth through the test. On the other hand, stiffness decreases with the decreasing length of *(b-a)* in Figure 2, corresponding to fracture growth. The initial drop of stiffness in the W curve marks the fracture initiation.

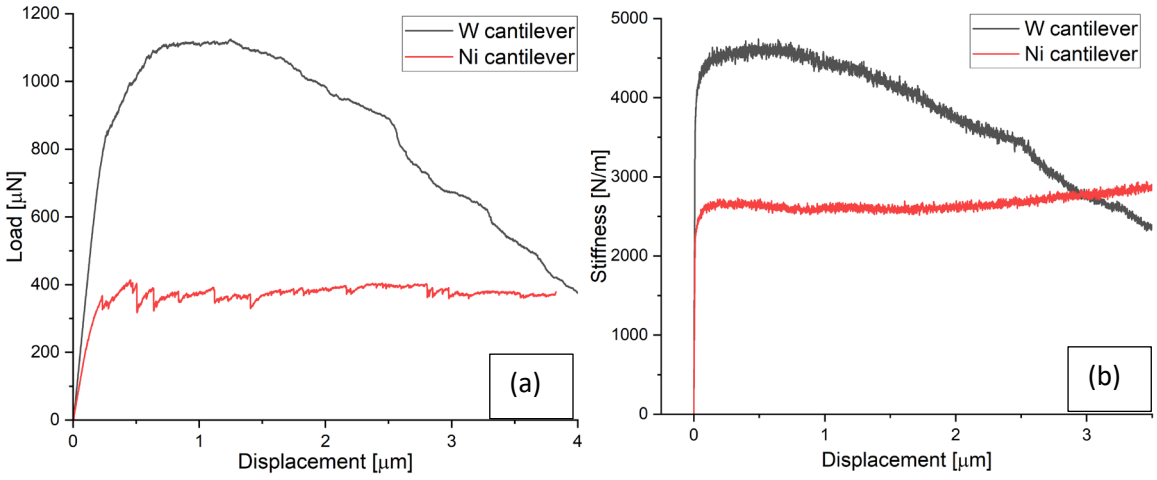

Figure 5. Single-phase W microcantilever (black) and single-phase Ni microcantilever (red) raw data load-displacement curves (a), and the stiffness-displacement curves (b) .

The J-integral-based crack resistance was evaluated with the input of the raw data of load (P), displacement (u), time (s) and stiffness (k) according to elastic plastic fracture mechanics (EPFM) and using the iterative method described in ASTM 1820 [14]:

$$J(a) = J^{el}(a) + J^{pl}(a) \tag{1}$$

$$J_n^{el} = \frac{K_{q,n}^2(1-v^2)}{E} \tag{2}$$

$$J_n^{pl} = \left\{J_{n-1}^{pl} + \frac{\eta_n}{b-a_n}\frac{A_n^{pl}-A_{n-1}^{pl}}{w}\right\}\left\{1-\gamma_n\frac{a_n-a_{n-1}}{b-a_n}\right\} \tag{3}$$

where $J^{el}(a)$ and $J^{pl}(a)$ are the elastic and plastic J-integral values at specific crack lengths a. For W, the $J^{el}(a)$ was evaluated using the values of E = 410 GPa and v = 0.28. The number of iteration steps is n and the stress intensity factor K_q was evaluated following ASTM 399 [15]:

$$K_{q,n} = \frac{P_n L_1}{wb^{1.5}} f\left(\frac{a_n}{b}\right) \tag{4}$$

Here b, w and L_1 are geometric dimensions as shown in Figure 2, P is the Force and $f(a/b)$ is a geometry factor specified for the cantilever geometry. For this study $f(a/b)$ employs a polynomial function proposed by Alfreider *et al.* [16] in which the crack length a_n was found by the following correlation:

$$\left(\frac{a_n}{b}\right) = 1 - 2.897\left(\frac{k_n}{k_{max}}\right) + 10.618\left(\frac{k_n}{k_{max}}\right)^2 - 23.620\left(\frac{k_n}{k_{max}}\right)^3 + 24.497\left(\frac{k_n}{k_{max}}\right)^4 9.600\left(\frac{k_n}{k_{max}}\right)^5 \tag{5}$$

where a_n is the crack length, k_n is stiffness and k_{max} is the maximum value of stiffness obtained during the bending test.

The plastic part of the J-integral was calculated using geometry independent pre-factors η = 1.9 and γ = 0.9 as proposed for straight-trough notch bend specimen in ASTM 1820 [14]. The plastic work A^{pl} was computed numerically from the load-displacement curve for each point n where u_n, P_n and k_n are the respective displacement, load and stiffness shown in the following equation:

$$A_n^{pl} = A_n - A_n^{el} = \int_0^{u_n} P du - \frac{P_n^2}{2k_n} \tag{6}$$

Since J-integral is a function of the crack length a, using equation 5, the crack extension during the bending test was calculated using the measured stiffness k. Figure 6, shows the calculated crack length compared with the load-displacement curve for the single-phase W microcantilever, as well as a snapshot of W microcantilever cross-section after the bending test.

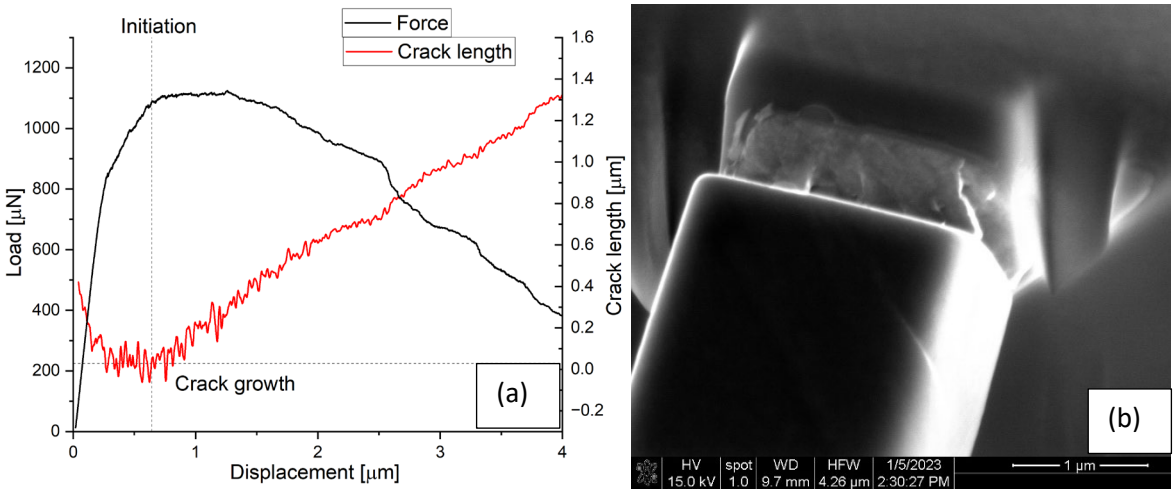

Figure 6. Load-displacement curve (black) and crack length curve (red) show crack initiation and growth (a); and snapshot of W cantilever cross-section after bending test (b).

J-Integral curve was generated from Equation 1, where the J elastic component was calculated using Equation 2, and the J plastic component was calculated from Equation 3. Figure 7 shows the plot of the result and the J initiation obtained from the crack initiation value.

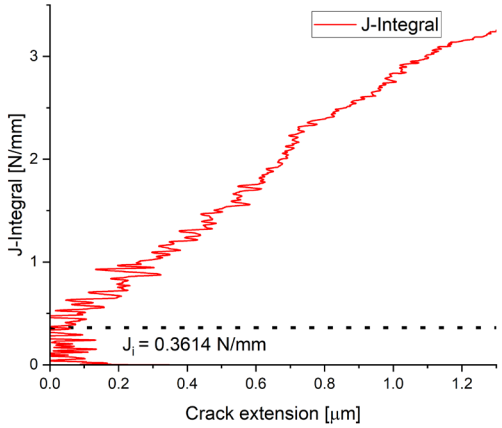

Figure 7. J-integral results for single-phase W microcantilever, where J_i is the initiation J value.

The K toughness for fracture initiation was determined to be 12.7 *MPa – m*$^{1/2}$ using the following equation:

$$K_i = \sqrt{\frac{EJ_i}{(1-\nu^2)}} \tag{7}$$

Fracture initiation and stable growth were observed in the W microcantilever along the {011} crack plane. However, in the single-phase Ni microcantilever, slip-band development without cracking was observed because of its ductile characteristics. The high surface-volume ratio favors the escape of dislocations without dislocation piling up. As a result, plastic deposition of energy prevails over the formation of new fracture surfaces. This sample-size effect has led to the absence of fracture in the Ni microcantilever and the high J-integral in W as shown in Figure 7, although the fracture initiation toughness of W obtained by the microcantilever bending test is in good agreement with literature [16].

The preliminary examination proved the concept of J-integral- based crack resistance approach using microcantilever bending tests. Crack evolution can be derived from the measured stiffness from the CSM nanoindentation measurement. The results are in good agreement with that of Bohnert *et al.* [16] who took into consideration the house-shape geometry for the J-integral-based crack resistance calculation and used similar a/b and w/b ratios, which are the predominant factors influencing the fracture behavior in straight-trough notch microcantilevers [15].

Microbeam deflection

The load (P) and displacement (u) data were monitored during the in-situ microbeam deflection at constant displacement rate, Figure 8ab. The stress and strain, Figure 8c, are obtained from the load-displacement curves using the following formulas [17]:

$$I = \frac{wb^3}{12} \tag{8}$$

$$\sigma = \frac{PL_1 b}{2I} \tag{9}$$

$$\varepsilon = \frac{3bu}{2L_1^2} \tag{10}$$

where I is the moment of inertia for a rectangular cross-section beam, L_1, w, and b are the microcantilever geometric dimensions; L_1 is the distance from the notch to the applied load, b is the cantilever height, w the cantilever width. The resultant flexural stress-strain curve obtained is presented in Figure 8c.

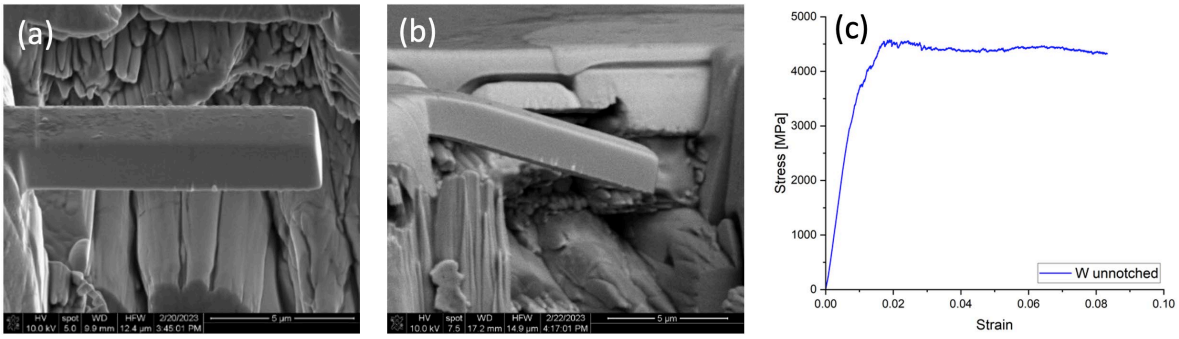

Figure 8. Single crystal W microbeam before (a) and after deflection (b), and the flexural stress-strain data obtained from the microbeam deflection (c).

Using the stress-strain curve, the flexural yield strength was determined to be 2.95 GPa. The Young's modulus was estimated to be 397 GPa using the following formula [7]:

$$E = \frac{L_1^3}{3I}\frac{dP}{du} \tag{11}$$

Both the flexural yield strength and the modulus data are well in the range of reported literature values yield strength 1.6 – 2.8 GPa [10, 18] and Young's modulus of 380-420 GPa [13]. At room temperature, W samples tend to break in the elastic regimen under macroscopic flexural testing [18]. However, as shown in Figure 8c and Reference [10], W microbeams show ductility even at room temperature. This, on the one hand, is attributed to the reduced specimen size without any defects, such as grain boundaries, as stress raisers to cause catastrophic failure; on the other hand, allows for the observation of the hardening behavior

and the characterization of the flow stress using the microscopic flexural stress-strain relationship, Figure 8c. Future studies on the irradiated samples can leverage this small-scale method, which extends the characterizable regime beyond elastic region, to compare multiple material properties, including the elastic modulus, flexural yield strength and flow stress, single-crystal ductility, and the hardening behavior [14].

Micropillar compression

In-situ micropillar compression tests were performed on two pillars along the uniaxial loading directions of [1931] and [18112] respectively. Figure 9 presents the stress-strain curves obtained from these two tests, as well as the morphologies of the two microcantilevers after the testing. The stress is estimated by the load (P) divided by the pillar cross-sectional areas. The strain is estimated by the displacement (u) divided by the original heights of the pillars. Based on Figure 9a, the yield strength of the two pillars are 970 and 950 MPa, respectively, as marked by the arrows. Consider their maximum Schmid factors being 0.46 and 0.48 for {110}<111> slip systems, the two tests reach to a fairly close CRSS values around 434 MPa.

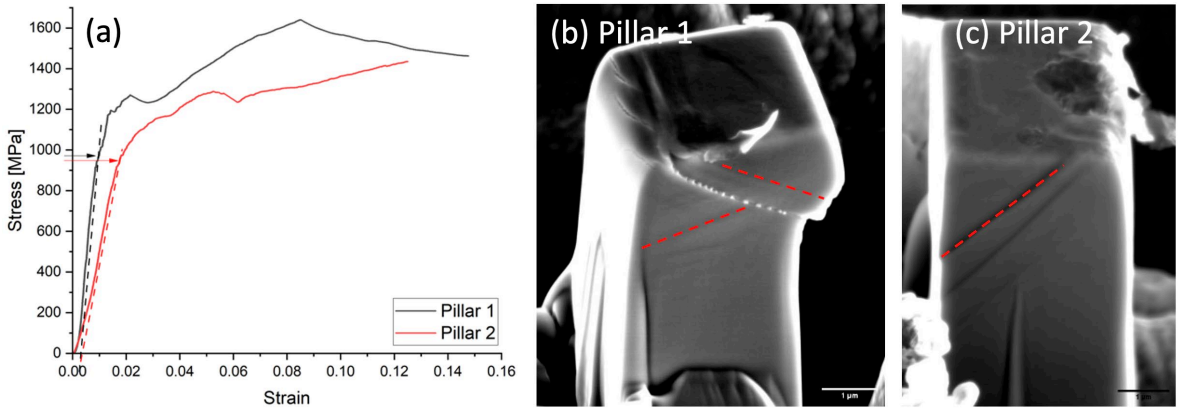

Figure 9. Micropillar compression stress-strain curves (a) and the pillars after compression in (b) and (c).

Figure 9 b and c show that two and one slip systems were activated under the uniaxial stress along [1931] and [18112] directions, respectively. This can be explained by the Schmid factors in Table 1. For [1931] indentation, the primary and secondary slip systems have Schmid factors that are close to each other, favoring the activation of both systems. On the other hand, the Schmid factor for the primary slip system is considerably greater than the secondary slip system under [18112] compression. As a result, only the primary slip system was activated till the emergence of the shear bands, Figure 9c.

Table 1. Schmid factor analysis for micropillar compression

Loading direction	Slip systems		Schmid factor
[1931]	Primary	[111] (101)	0.462
	Secondary	[111] (101)	0.456
[18112]	Primary	[111] (110)	0.480
	Secondary	[111] (110)	0.459

We demonstrated that the micropillar compression technique is self-consistent in determining the CRSS values. Yet, it is essential to note that the CRSS values obtained through micropillar compression are influenced by the sample size effect – smaller specimens yield higher CRSS [19]. Thus, a size effect study will benefit data extrapolation as well as the identification of deformation mechanism in the future [20]. On the other hand, the elastic modulus are derived from the stress-strain curves, using the slopes of the elastic

regime, to be 98 and 54 GPa, respectively. These values are considerably lower than the bulk values around 400 GPa. This observation aligns with the systematic trend of lower elastic moduli determined by microcantilever bending tests compared to bulk values, as previously observed in various materials [21].

Considering our primary objective of integrating models with experimental data, micropillar compression tests are best suited for measuring CRSS. The intrinsic frictional resistance of the slip systems, which can be determined by analyzing the CRSS data, serves as valuable input for mesoscale models. These mesoscale models, in turn, are instrumental in linking microscale behavior to macroscale performance predictions [22].

Future Work

The current study has successfully demonstrated that a combination of notched microcantilever bending, microbeam deflection, and micropillar compression techniques can systematically investigate microstructure-specific mechanical properties, including fracture initiation and propagation toughness, elastic modulus, flexural yield strength, and CRSS for slip deformation activation. These data are valuable for inputting into mechanistic models to establish constitutive laws for engineering-scale models that can predict the service performance of materials [14, 22].

The future work will focus on two key areas:

Correlating Mechanical Response to Irradiation and Understanding Microstructural Correlations

In this phase, the demonstrated micromechanical testing methods will be applied to ion-irradiated samples. Specifically, the research will evaluate the fracture toughness change of W and the W-Ni interface through notched microcantilever bending tests, the phase-specific elastic modulus, flow stress, and hardening behavior through microbeam deflection, and the effects of irradiation on slip systems through micropillar compression. By doing so, the research aims to establish a clear correlation between the mechanical response and radiation damage from a micromechanical perspective. This will contribute to a deeper understanding of how irradiation affects the mechanical properties of DPT W-NiFe alloys.

Integrating Small-Scale Experiments with Physics-Based Models

Another significant aspect of future work is the integration of small-scale experimental data with physics-based models. The research will focus on developing analytical methods to extract material parameters from the small-scale mechanical testing results. Specifically, the strain hardening laws will be parameterized using microbeam deflection data, and the micropillar compression data will be analyzed to gain insights into dislocation nucleation, multiplication, and interaction mechanisms. This step will serve as the initial foundation for integrating experimental data with computational models. Our goal is to provide a strategy for obtaining engineering-scale constitutive laws and model parameters from small-scale mechanical testing and low-dimensional modeling to enabling reliable predictions of material behavior under various conditions.

Publication Plan

The research aims to prepare two manuscripts for journal publication. One manuscript will focus on the application of small-scale mechanical testing to obtain local mechanical properties, demonstrating how the combination of notched microcantilever bending, microbeam deflection, and micropillar compression can be utilized effectively. The other manuscript will be dedicated to exploring the mechanical response of W-

NiFe alloys to ion irradiation, presenting the findings from the correlation between mechanical response and radiation damage.

Other Progress

This project has enabled the recruitment and training of Ana Garcia, a first-year Ph.D. student in the materials science program. With the project's support, Ana has finished her training on SEM, FIB, and nanomechanical testing and can work independently. Ana also received TEM training in June 2023. This preparation will allow Ana to perform in-depth studies of the irradiated samples and investigate and understand the microstructure – mechanical property correlations.

Acknowledgements

The research was supported by the Office of Fusion Energy Science, US DOE and performed under the Contract DE-AC05-76RL01830. The authors acknowledge Ramprashad Prabhakaran for providing the samples and James V. Haag IV and Weilin Jiang for meaningful discussion.

References

[1.] Alam ME, Odette GR (2020) On the remarkable fracture toughness of 90 to 97W-NiFe alloys revealing powerful new ductile phase toughening mechanisms. *Acta Materialia*, 186:324–340. https://doi.org/10.1016/j.actamat.2020.01.012.

[2.] Haag JV, Edwards DJ, Henager CH, Setyawan W, Wang J, Murayama M (2021) Characterization of ductile phase toughening mechanisms in a hot-rolled tungsten heavy alloy. *Acta Materialia*, 204:116523. https://doi.org/10.1016/j.actamat.2020.116523.

[3.] Jiang W, Zhang D, Li D, Heo J, Wang Z, Zhang L, Overman N, Varga T, Hu Z, Wang X, Shao L, Setyawan W (2022) Behavior of helium cavities in ion-irradiated W-Ni-Fe ductile-phase toughened tungsten. *Journal of Nuclear Materials*, 561:153565. https://doi.org/10.1016/j.jnucmat.2022.153565.

[4.] Hosemann P (2018) Small-scale mechanical testing on nuclear materials: bridging the experimental length-scale gap. *Scripta Materialia*, 143:161–168. https://doi.org/10.1016/j.scriptamat.2017.04.026.

[5.] Chen T, He L, Cullison MH, Hay C, Burns J, Wu Y, Tan L (2020) The correlation between microstructure and nanoindentation property of neutron-irradiated austenitic alloy D9. *Acta Materialia*, 195:433–445. https://doi.org/10.1016/j.actamat.2020.05.020.

[6.] Armstrong DEJ, Hardie CD, Gibson JSKL, Bushby AJ, Edmondson PD, Roberts SG (2015) Small-scale characterisation of irradiated nuclear materials: Part II nanoindentation and micro-cantilever testing of ion irradiated nuclear materials. *Journal of Nuclear Materials*, 462:374–381. https://doi.org/10.1016/j.jnucmat.2015.01.053.

[7.] Chen T, Frazer D, Cullison M, Teng F, Lian J, Mo K, Cappia F (2023) The effects of radiation-induced grain subdivision and dislocations on the fracture properties of uranium dioxide. *Journal of Nuclear Materials*, 577:154297. https://doi.org/10.1016/j.jnucmat.2023.154297.

[8.] Pippan R, Wurster S, Kiener D (2018) Fracture mechanics of micro samples: Fundamental considerations. *Materials & Design*, 159:252–267. https://doi.org/10.1016/j.matdes.2018.09.004.

[9.] Jaya BN, Jayaram V (2016) Fracture Testing at Small-Length Scales: From Plasticity in Si to Brittleness in Pt. *JOM*, 68(1):94–108. https://doi.org/10.1007/s11837-015-1489-2.

[10.] Ast J, Göken M, Durst K (2017) Size-dependent fracture toughness of tungsten. *Acta Materialia*, 138:198–211. https://doi.org/10.1016/j.actamat.2017.07.030.

[11.] Ast J, Schwiedrzik JJ, Wehrs J, Frey D, Polyakov MN, Michler J, Maeder X (2018) The brittle-ductile transition of tungsten single crystals at the micro-scale. *Materials & Design*, 152:168–180. https://doi.org/10.1016/j.matdes.2018.04.009.

[12.] Fei H, Abraham A, Chawla N, Jiang H (2012) Evaluation of Micro-Pillar Compression Tests for Accurate Determination of Elastic-Plastic Constitutive Relations. *Journal of Applied Mechanics*, 79(6):061011. https://doi.org/10.1115/1.4006767.

[13.] Kiener D, Fritz R, Alfreider M, Leitner A, Pippan R, Maier-Kiener V (2019) Rate limiting deformation mechanisms of bcc metals in confined volumes. *Acta Materialia*, 166:687–701. https://doi.org/10.1016/j.actamat.2019.01.020.

[14.] Weihs TP, Hong S, Bravman JC, Nix WD (1988) Mechanical deflection of cantilever microbeams: A new technique for testing the mechanical properties of thin films. *Journal of Materials Research*, 3(5):931–942. https://doi.org/10.1557/JMR.1988.0931.

[15.] Liu X, Athanasiou CE, Padture NP, Sheldon BW, Gao H (2021) Knowledge extraction and transfer in data-driven fracture mechanics. *Proceedings of the National Academy of Sciences*, 118(23):e2104765118. https://doi.org/10.1073/pnas.2104765118.

[16.] Bohnert C, Schmitt NJ, Weygand SM, Kraft O, Schwaiger R (2016) Fracture toughness characterization of single-crystalline tungsten using notched micro-cantilever specimens. *International Journal of Plasticity*, 81:1–17. https://doi.org/10.1016/j.ijplas.2016.01.014.

[17.] Tarleton E, Balint DS, Gong J, Wilkinson AJ (2015) A discrete dislocation plasticity study of the micro-cantilever size effect. *Acta Materialia*, 88:271–282. https://doi.org/10.1016/j.actamat.2015.01.030.

[18.] Levin ZS, Hartwig KT (2017) Strong ductile bulk tungsten. *Materials Science and Engineering: A*, 707:602–611. https://doi.org/10.1016/j.msea.2017.09.100.

[19.] Dou R, Derby B (2009) A universal scaling law for the strength of metal micropillars and nanowires. *Scripta Materialia*, 61(5):524–527. https://doi.org/10.1016/j.scriptamat.2009.05.012

[20.] Bei H, Gao YF, Shim S, George EP, Pharr GM (2008) Strength differences arising from homogeneous versus heterogeneous dislocation nucleation. *Physical Review B*, 77(6):060103. https://doi.org/10.1103/PhysRevB.77.060103.

[21.] Konstantinidis AA, Michos K, Aifantis EC (2016) On the correct interpretation of compression experiments of micropillars produced by a focused ion beam. *Journal of the Mechanical Behavior of Materials*, 25(3–4):83–87. https://doi.org/10.1515/jmbm-2016-0009.

[22.] Gong M, Xie D, Sun T, Zhang X, Shao L, Wang J (2023) Bridging microscale to macroscale mechanical property measurements of FeCrAl alloys by crystal plasticity modeling. *International Journal of Plasticity*, 165:103608. https://doi.org/10.1016/j.ijplas.2023.103608.

4.5 EFFECT OF HOT-ROLLING ON ION IRRADIATION DAMAGE IN W/NiFe DUCTILE PHASE TOUGHENED TUNGSTEN—J. V. Haag IV, M. Olszta, W. Jiang, D. Edwards, W. Setyawan (Pacific Northwest National Laboratory)

OBJECTIVE

This report provides an update on the implementation of transmission electron microscope tilt-series in ion irradiated tungsten heavy alloy specimens to yield defect densities in bulk and at interfaces.

SUMMARY

This work is centered on providing experimentally derived density values for irradiation damage quantification in tungsten heavy alloy (WHA) specimens subjected to the simulated fusion environment. This is done with the intention of using said values to inform ongoing modelling thrusts within Pacific Northwest National Laboratory (PNNL). These datasets are being collected for a WHA specimen both in its as-sintered state as well as post hot-rolling. To generate this data, regions of interest have been imaged using a transmission electron microscope (TEM) at a series of projection angles and stacked into a tilt-series for extrapolation of defect densities. This has been done for the bulk W and γ-phase domains as well as at interfaces to understand the nature of damage manifestation in these materials. As TEM specimens represent vanishingly small volumes, especially with the limited peak damage regions from ion irradiation, site specificity and careful characterization is necessary for accurate damage tracking.

PROGRESS AND STATUS

In this reporting period, a dual phase 90W-7Ni-3Fe (wt.%) WHA has been quantitatively studied after exposure to the simulated fusion environment in its as-sintered state as well as post-thermomechanical processing. Both processing conditions were selected for this analysis as the effects of thermomechanical treatment upon the irradiation behavior of these alloys must be thoroughly understood in the selection and optimization of WHAs in fusion. Prior reporting periods have focused on the establishment of thermal and irradiation conditions to simulate the fusion environment and on the preliminary identification of features in samples exposed to the high temperature ion implantation steps [1-3] but have not focused on quantification between the processing conditions. Notably, during this reporting period, two journal articles detailing these analyses were published, one focusing on advancements in imaging of cavities post irradiation [4] and one on the formation of brittle boundary carbides at W-γ interfaces under heavy ion irradiation [5].

This collective work is now being expanded upon within PNNL by applying a multi-projection TEM and scanning TEM (STEM) approach to yield a more directly interpretable view of the irradiation damage present in specimen foils. Datasets have been generated through the collection of multiple S/TEM images from a single region of interest (ROI) across a large angular range, then compiling and aligning the image series into a ‘tilt-series’. This produces a video of the ROI which is more directly interpretable in resolving the complex contrast present within irradiated materials. While the benefits of a more three-dimensional approach in the analysis of irradiation damage is difficult to visually convey in a static format, this multi-projection approach is particularly powerful in the analysis of defects in thicker TEM foils as well as at materials interfaces. When coupled with thickness mapping via electron energy loss spectroscopy (EELS), the desired ROI can then be considered as a volume for numerical quantification of damage. Combining the volume derived from EELS and the 3D structure representation of the region from tilt-series acquisition then allows for the joining of these datasets to reconstruct a 3D defect density within the TEM foil thickness.

This information can then be used for quantification of those defects within the ROI. It should be noted that the application of EELS thickness mapping in the derivation of volumetric densities of He cavities in bulk grains of irradiated materials is not novel and does not necessitate the collection of tilt-series; but this combined methodology is particularly advantageous in the analysis of grain boundaries and phase boundaries under irradiation. If a boundary is oriented to be edge-on with respect to the incident electron beam for the collection of the thickness map, the apparent area of the physical boundary plane through the

thickness of the specimen can be mapped, assuming the boundary is straight in the thickness dimension of the TEM foil. It is then possible to track the dispersion of defects along interfaces through tilt-series acquisition and derive areal defect densities along the boundary plane. The workflow to collect these datasets has been provided in Figure 1.

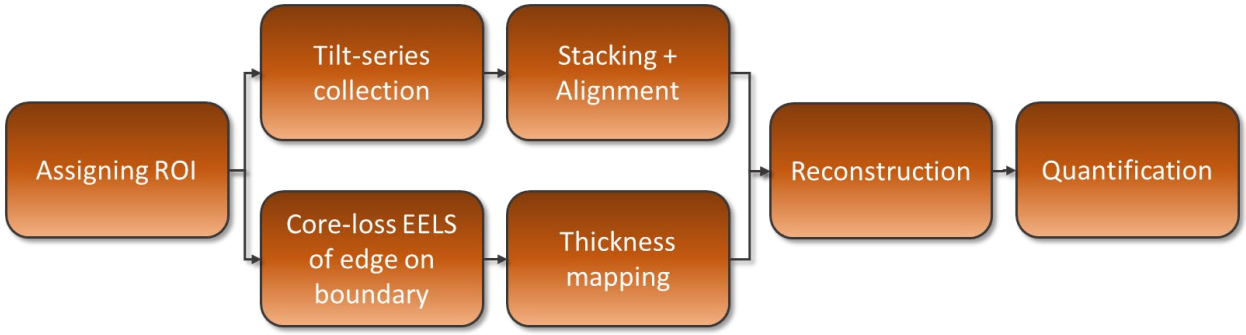

Figure 1. Workflow for the collection of 3D datasets for the visualization and quantification of irradiation damage features in WHA specimens.

The inherent benefits of this approach in the characterization of ion-irradiated specimens lie in the direct interpretability of these datasets. A detailed understanding of the complex nature of TEM image contrast and projection effects is not necessary in the numerical quantification of defect densities in this way. Overlapping features and defect morphologies are easily resolved making the quantification of volumetric defect densities in bulk and areal defect densities at interfaces trivial. The microscope's acquisition parameters and selected tilt conditions for the generation of a tilt series can be varied to utilize parameters which magnify or minimize the contributions of diffraction contrast in the specimens. For instance, a high angle annular dark field (HAADF) tilt series can be collected with a minimal camera length (CL) over a series of tilt conditions which avoids any strong diffraction condition. This will maximize the relative contrast of He cavities within the material, Figure 2a; whereas a tilt-series of the same ROI can be collected utilizing a different series of tilt conditions which maintains a strong diffraction condition throughout, in this case the FCC {100}, to retain sharp and consistent dislocation contrast, Figure 2b. While the collection of this data requires that the operating microscopist have a detailed knowledge of data collection utilizing the most advantageous imaging parameters, the interpretation and quantification of said datasets does not necessitate the same applied crystallographic knowledge. This has been stated as an upcoming thrust for the next reporting period will be the application of this method for 3D defect analysis across all interface types (W-W, γ-γ, and W-γ) for the as-sintered and thermo-mechanically processed WHA specimens' post-exposure to identical irradiation conditions, and the production/analysis of these datasets is time consuming. The time required for the compilation of results from all conditions may be greatly reduced through quantification of acquired datasets via technical staff not trained in TEM analysis or the potential implementation of processes for automated image segmentation and quantification.

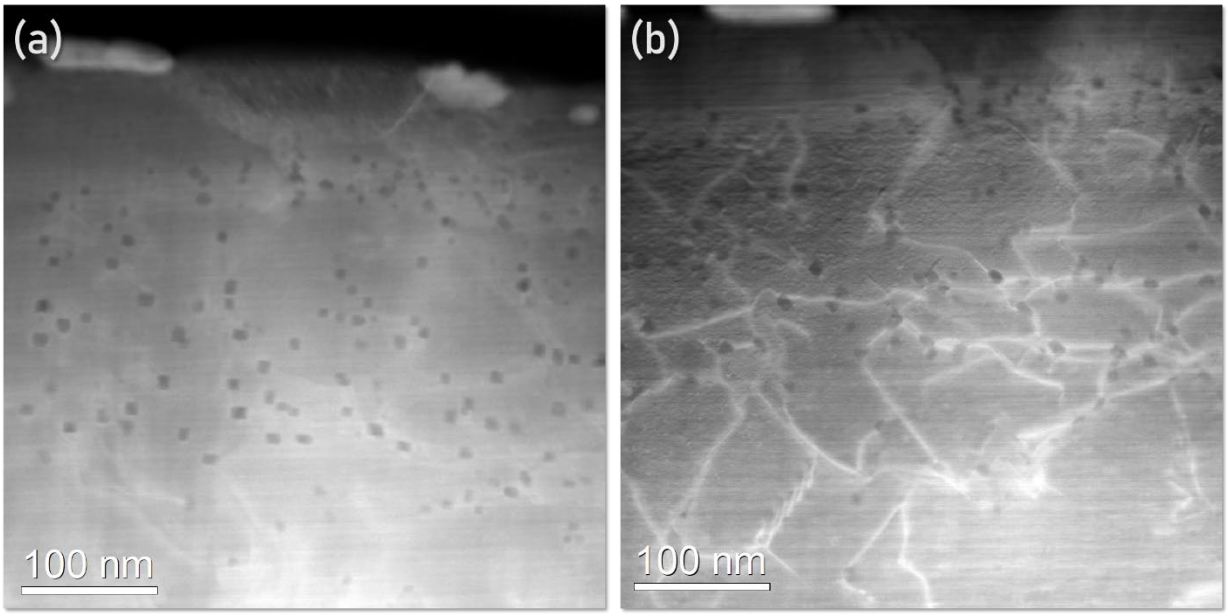

Figure 2. Single frames from tilt series of an irradiated FCC γ-phase grain. (a) HAADF STEM image acquired away from a strong diffraction condition maximizing contrast from He cavities. (b) HAADF STEM image acquired from the same region, this time utilizing a strong diffraction condition to maintain sharp dislocation contrast.

While this technique is powerful in its application to the characterization of irradiated materials, it does possess some distinct drawbacks. One of the largest criticisms of this approach is in the time necessary to collect the data. A trained microscopist may set up and collect a single tilt-series over a ±35° range with a 2° increment in approximately 2 hours. The data must then be compiled, stacked, aligned, and exported for analysis. Analysis and quantification of the results is largely subjective but adds significant additional processing time which altogether makes this technique extremely time consuming. Added to this is the need to collect a correlative EELS thickness map of the ROI. While TEM instruments equipped with EELS detectors are present at most national laboratories and many research institutions, these systems are by no means ubiquitous. There are alternative methods for the calculation of specimen foil thickness via convergent beam techniques or geometric tilting to measure boundary overlap at different tilt conditions, but these approaches are uncommon and difficult. Finally, a major drawback to quantifying projected bulk damage from TEM foils of heavy ion irradiated materials is the vanishingly small volumes for analysis. Even comparatively large and thick TEM liftout specimens possess dimensions of approximately 5.0 × 5.0 × 0.2 μm (~5 μm^3). With ion irradiation, the peak damage region represents only a small fraction of this total volume and can be on the order of 200nm or less in some cases, leaving a total quantifiable volume across the same dimensioned liftout specimen to something more akin to ~0.2 μm^3 and even less for select interfaces. This is clearly an infinitesimal volume for extrapolation of projected damage in bulk materials and must therefore be stated alongside the measured density values to weigh the ultimate practicality of this approach. With that being said, this approach naturally pairs with the ongoing atomistic simulation of materials interfaces under the simulated fusion environment within PNNL, and the collected results will be used to inform the ongoing modelling thrusts on these materials.

In the upcoming reporting period, this established technique will be applied in the analysis of grain boundaries and phase boundaries within both the as-sintered WHA and the 87% rolling reduction WHA specimens. Both processing conditions are of direct interest as it is theorized that thermomechanical processing of WHAs may introduce a higher degree of interfaces per unit volume which may act as more desirable sink sites for irradiation damage over the W-γ interfaces which are responsible for the high balance of strength and toughness these alloys exhibit. Preliminary findings suggest that the high degree

of annealing twins found in the γ-phase post hot-rolling may help reduce the high degree of He cavity segregation at W-γ interphase boundaries, potentially leading to a greater retention of toughness through prolonged irradiation as compared to the as-sintered material.

Acknowledgements

This research was supported by the U.S. Department of Energy (US DOE), Office of Science, Office of Fusion Energy Sciences, through Contract No. AT2030110-13784 and was performed at PNNL, which is operated by Battelle for the US DOE under Contract No. DE-AC05-76RL0-1830.

References

[1] W. Jiang, D. Zhang, D. Li, J. Heo, Z. Wang, L. Zhang, N. Overman, T. Varga, W. Setyawan, Z. Hu, X. Wang, L. Shao, “BEHAVIOR OF HELIUM CAVITIES IN ION-IRRADIATED W-Ni-Fe DUCTILEPHASE TOUGHENED TUNGSTEN” DOE0313/72, pp. 64-65.

[2] W. Jiang, L. Kovarik, K. Kruska, W. Setyawan, “CONVERGENT-BEAM STEM AND STEM-EELS MAPPING OF HELIUM CAVITIES IN 87R DPT TUNGSTEN IRRADIATED WITH He+ IONS AT 973 K” DOE0313/72, pp. 66-72.

[3] J. V. Haag IV, M. J. Olszta, W. Jiang, W. Setyawan, “PROGRESS ON THE CHARACTERIZATION OF IRRADIATION DEFECTS IN TUNGSTEN HEAVY ALLOYS, THE ANALYSIS OF INTERPHASE BOUNDARY STRUCTURES, AND THE SYNTHESIS OF ROLLED TUNGSTEN HEAVY ALLOYS” DOE0313/72, pp. 57-63.

[4] W. Jiang et al., “Behavior and properties of helium cavities in ductile-phase-toughened tungsten irradiated with He+ ions at an elevated temperature,” Materialia, vol. 29, p. 101789, Jun. 2023, doi: 10.1016/j.mtla.2023.101789.

[5] J. V. Haag, M. J. Olszta, D. J. Edwards, W. Jiang, and W. Setyawan, “Characterization of boundary precipitation in a heavy ion irradiated tungsten heavy alloy under the simulated fusion environment,” Acta Materialia, p. 119059, Jun. 2023, doi: 10.1016/j.actamat.2023.119059.

4.6 ION IRRADIATION OF DUCTILE-PHASE-TOUGHENED TUNGSTEN FOR MICROSTRUCTURAL EXAMINATION AND MECHANICAL TEST—W. Jiang, J. V. Haag IV, W. Setyawan (Pacific Northwest National Laboratory), T. Chen (Oregon State University)

OBJECTIVE

The aim of this work is to correlate the mechanical properties with irradiation defects in ductile-phase-toughened (DPT) tungsten (W) alloys. The irradiation is intended to emulate exposure of the material in a fusion reactor environment.

SUMMARY

Compared to brittle tungsten, DPT W alloys possess significantly improved mechanical properties. The materials have been investigated for potential applications in the plasma-facing components (PFCs) of fusion reactors. The DPT W in this study consists of W particles embedded in a DP NiFeW matrix. Our previous studies show that He cavities form in DPT W irradiated with Ni^+ and He^+ ions at 700°C. Larger cavities are observed in the NiFeW than W phase. There is also a preferential distribution of cavities along the interphase boundaries. It is crucial to study degradation of the mechanical properties as a function of dose and gas concentration, and understand how the presence of irradiation defects dictates the properties, including the He cavities and dislocation loops in DPT W. In this report, we describe the design and performance of an ion irradiation experiment for both microstructural examination and mechanical tests of a DPT W alloy sample.

PROGRESS AND STATUS

Introduction

The DPT W alloys exhibit significantly higher fracture toughness than pure W [1-5], while still being able to largely retain the favored thermomechanical properties of W for application in the PFCs of fusion reactors. Irradiation of DPT W with 14.1 MeV fusion neutrons not only produces atomic displacements, resulting in generation of lattice defects, but also induces elemental transmutation from Ni, Fe and W [6,7], creating gas species, including He. We have employed ion irradiation to emulate a fusion environment to study the microstructural response of DPT W [8,9]. The results from the study show that He cavities form in NiFeW and W, and aggregate preferentially along the NiFeW/W boundaries during ion irradiation at elevated temperatures. In general, the presence of He cavities in metals has considerable concerns because it could substantially deteriorate the mechanical properties, including dramatic embrittlement. This embrittlement results mainly from He cavity formation at grain boundaries and may occur even at low He concentrations [10,11]. Therefore, it is crucial to study the relationship between the mechanical property and irradiation defects in DPT W. This study focuses on the development of the mechanisms responsible for the property degradation in DPT W dictated by the irradiation defects, including He cavities and dislocation loops.

Experimental Procedure

Stopping and Range of Ions in Matter (SRIM) Simulation

The composition of the DPT W (90W-7Ni-3Fe) alloy used in this study was determined [8] to be 88 wt.% W and 12 wt.% NiFeW that contains 54.68 wt.% Ni, 22.57 wt.% Fe and 22.75 wt.% W, corresponding to 63.83 at.% Ni, 27.69 at.% Fe and 8.48 at.% W. El-Guebaly *et al*. [12] calculated the dpa dose and gas concentration in DPT W alloys in the front of the divertor in a conceptual ARIES-ACT2 fusion reactor. The total dose after 10 years of operation (8.65 full power years) was reported to be 91.7 dpa in NiFeW of WHA-2 (94.1 wt.% W, 4.1 wt.% Ni and 1.8 wt.% Fe) with the DP composition of 62 at.% Ni, 26 at.% Fe and 12 at.% W. For the same exposure, the He concentration in the DP was calculated to be 1,174 appm based on the reported data of 1620 appm He from Ni, 645 appm He from Fe and 16.2 appm He from W [12]. Therefore, the ratio of the He concentration to the dose is 12.8 appm/dpa in NiFeW. Although this ratio is

obtained from the total dose and accumulated gas concentration over 10 years of operation, it also provides a good estimate at any point of time during operation as the ratio is expected to remain largely unchanged over time.

Table 1. Parameters for sequential Ni^+ and He^+ ion irradiations of DPT W

No.	Ion & Energy (MeV)	Al Foil (μm)	Sample Rotation (°)	Ion Fluence (ions/cm^2)
1a	5.0 MeV Ni^+	0	0	3.2E16
2a	2.5 MeV Ni^+	0	0	1.0E16
3a	1.0 MeV Ni^+	0	0	7.0E15
1b	1.8 MeV He^+	3.0	0	5.3E14
2b	1.8 MeV He^+	3.0	25	5.8E14
3b	1.8 MeV He^+	3.0	40	5.8E14
4b	1.8 MeV He^+	3.0	47	4.9E14
5b	1.8 MeV He^+	3.0	54	4.9E14
6b	1.8 MeV He^+	3.0	61	4.9E14
7b	1.8 MeV He^+	3.0	68	4.9E14
8b	1.8 MeV He^+	3.0	74	4.9E14
9b	1.8 MeV He^+	3.0	79	5.8E14
10b	1.8 MeV He^+	3.0	84	5.8E14

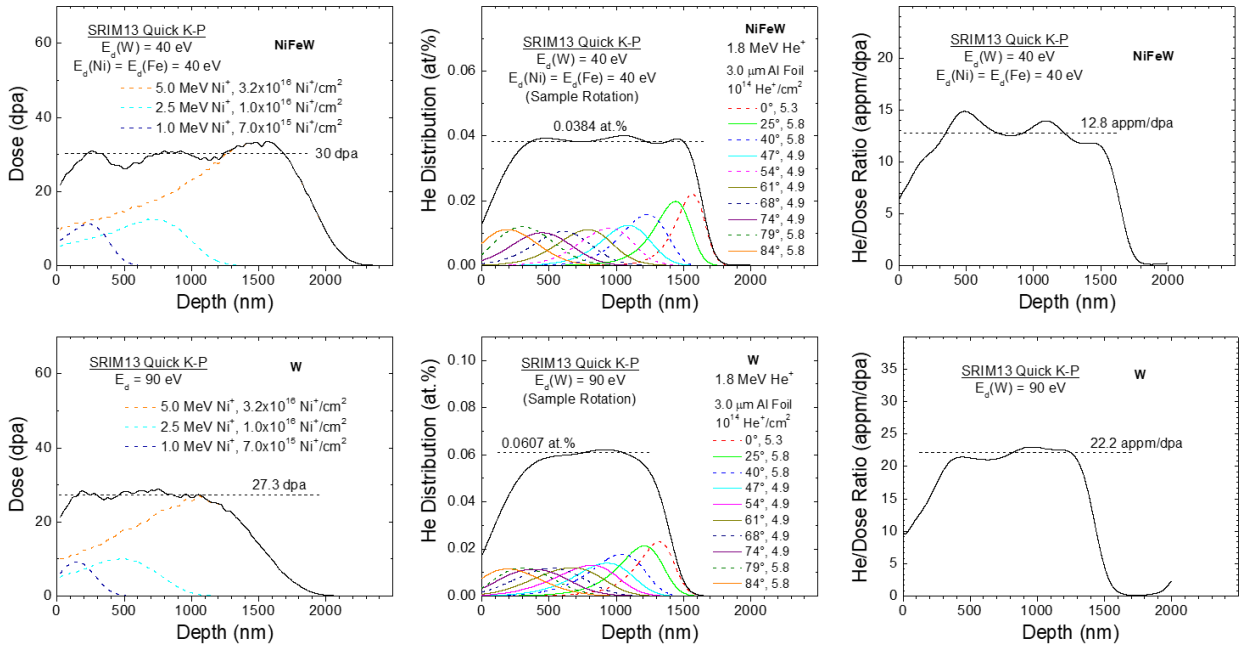

Figure 1. Depth profiles of the dose, He concentration, and appm/dpa ratio from quick Kinchin-Pease SRIM13 simulations of Ni^+ and He^+ irradiations in NiFeW and W.

In order to estimate dose and He atomic distributions in the body-centered cubic W and face-centered cubic NiFeW phases, quick Kinchin-Pease (K-P) SRIM13 (Stopping and Range of Ions in Matter, version 2013 [13]) simulations were carried out for Ni^+ and He^+ ion irradiations in NiFeW and W, where the threshold displacement energies of E_d(W)=90 eV in W and E_d(Ni)=E_d(Fe)=40 eV in NiFeW were adopted [14]. As W

serves as a minor element in NiFeW, its threshold displacement energy is chosen the same as that for Ni or Fe, i.e., E_d(W)=40 eV in NiFeW. The theoretical densities were assumed to be 19.25 g/cm^3 (or 6.3×10^{22} at./cm^3) and 9.50 g/cm^3 (or 8.3×10^{22} at./cm^3) for W and NiFeW, respectively. For convenience of mechanical tests, two sequences of irradiation with Ni^+ and He^+ ions were applied to produce a broad damage plateau over a depth region in the material. The first sequence of self-ion irradiations is intended to emulate high-energy neutron irradiation without introducing impurities. The irradiation employs 5.0, 2.5 and 1.0 MeV Ni^+ ions to fluences of 3.2×10^{16}, 2.5×10^{16} and 7.0×10^{15} Ni^+/cm^2, respectively. These irradiation parameters are listed in Table 1. The second sequence is to implant He^+ ions to allow them to migrate and interact with the Ni^+ ion irradiation induced damage. The implantation applies 1.8 MeV He^+ ions with a 3.0 μm Al foil in front of the DPT W sample; the sample was first implanted at normal incidence to a fluence of 5.3×10^{14} He^+/cm^2, and then was rotated to 25° and implanted to 5.8×10^{14} He^+/cm^2 over the same area, followed by repeating the step for further sample rotations and additions to the ion fluence until the last rotation to 84° and fluence to 5.8×10^{14} He^+/cm^2 were completed. Table 1 provides the specific combinations of rotation angles and ion fluences.

The results from SRIM13 simulations under the irradiation conditions are shown in Figure 1. From the figure, the dose in NiFeW is ~30 dpa over a depth region from 300 to 1,800 nm and the He concentration is ~0.0384 at.% or ~384 appm from 400 to 1,500 nm. The ratio of the He concentration to dose is ~12.8 appm/dpa from 300 to 1,500 nm in NiFeW. This region emulates exposure of the NiFeW in DPT W in the front of the divertor in the conceptual ARIES-ACT2 fusion reactor. Under the irradiation conditions, there is also a plateau of the appm/dpa ratio produced in W, which is at the level of 22.2 appm/dpa over the depths from 400 to 1,300 nm. This ratio is, however, much higher than the expected one of 0.6 appm/dpa in the front of divertor in the conceptual ARIES-ACT2 fusion reactor based on the reported data [12]. While irradiation effects in pure W have been extensively investigated, this work focuses on the study of irradiation behavior of NiFeW in DPT W. Note that SRIM simulations are performed at the temperature of 0 K. The actual He depth profiles are expected to be broader in W and NiFeW due to diffusion during He^+ ion irradiation at an elevated temperature. In addition to the interaction of He atoms and vacancies to form He cavities, a fraction of the implanted He atoms is expected to diffuse to the surface and escape from the sample.

Ion Irradiation

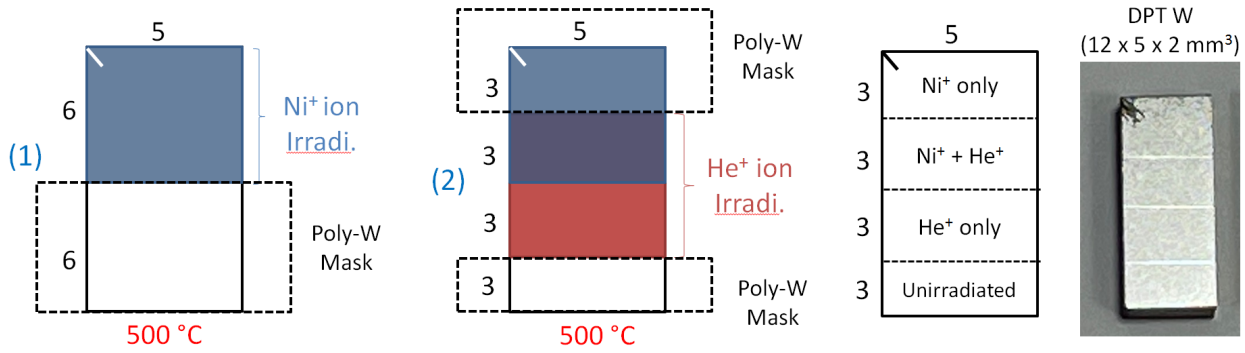

Figure 2. An illustration of a DPT W sample sequentially irradiated with Ni^+ and He^+ ions at 500°C to produce three different irradiation regions with an additional unirradiated area.

Similar to what has been described in [15], sequential ion irradiation with Ni^+ and He^+ ions was performed in different areas of a DPT W alloy at 500°C, as shown in Figure 2. The DPT W sample in this study has a dimension of 12 mm long × 5 mm wide × 2 mm thick. An area of 6 mm × 5 mm was irradiated sequentially with 5.0, 2.5 and 1.0 MeV Ni^+ ions to fluences of 3.2×10^{16}, 2.5×10^{16} and 7.0×10^{15} Ni^+/cm^2, respectively. Subsequently, an area of 6 mm × 5 mm shifted downward by 3 mm was irradiated with 1.8 MeV He^+ ions to various combinations of sample rotation angles and ion fluences as given in Table 1; a 3.0 μm thick Al

foil was used to degrade the He^+ ion energy and put the implants in the depth region of the Ni^+ ion damage. There is an overlapping area of 3 mm × 5 mm between the Ni^+ and He^+ ion irradiations, as shown in Figure 2, thus creating three 3 mm × 5 mm irradiation regions of Ni^+ ions only, Ni^+ and He^+ ions, and He^+ ions only, in addition to an unirradiated area of 3 mm × 5 mm. The irradiations were performed with a rastering system to achieve a uniform irradiation over the intended areas in each case. The average ion flux was 4.0×10^{12} (Ni^+/cm^2)/s and 3.6×10^{12} (He^{2+}/cm^2)/s. Figure 2 also shows the irradiated sample with engraved line markers to identify the four different regions. There is no visible coloring in the irradiated areas. The irradiation temperature of 500°C is selected based on the consideration that the irradiation condition is expected to produce He cavities in DPT W but could greatly suppress or potentially inhibit precipitation of other-phase particles that were observed at the interphase boundaries in DPT W irradiated at 700°C due to inward diffusion of C impurities [16].

Figure 3 shows how the DPT W sample was mounted in the ion irradiation experiments. Polycrystalline W plates were used as masks that were clamped to hold the sample on a copper backing. A resistance heater was located behind the backing. The sample temperature of 500°C was monitored using a thermocouple on the copper backing to an accuracy of ±5°C or better.

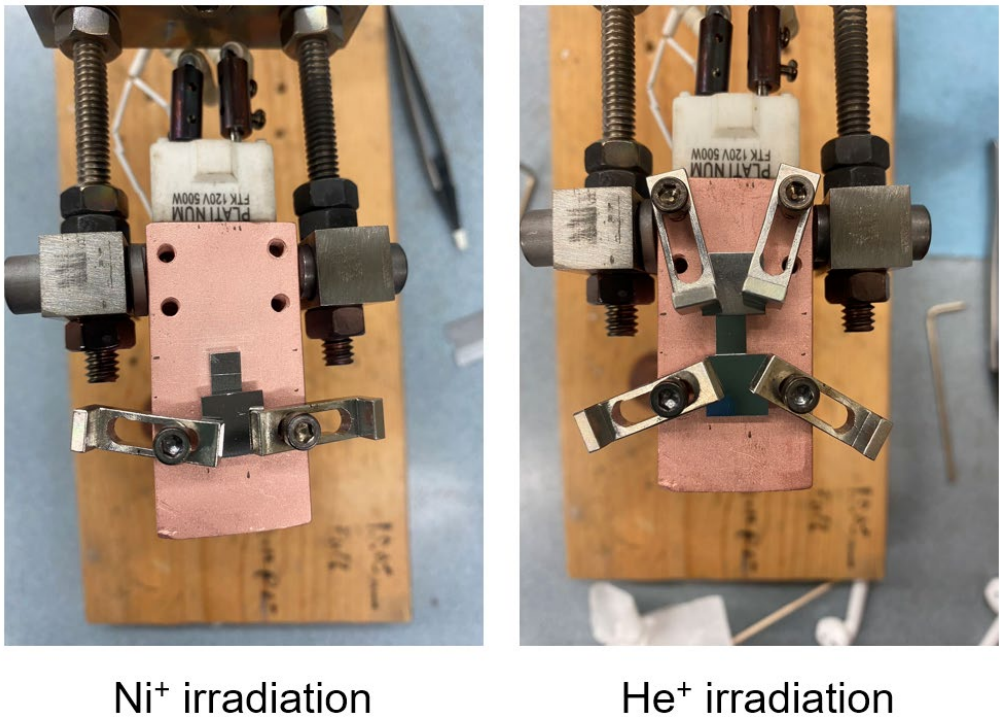

Figure 3. Experimental setup for mounting a DPT W sample for sequential ion irradiation at 500°C.

Results

The three irradiated regions and unirradiated area on the DPT W sample are being used for microstructural examination and mechanical tests to isolate different types of defects to some extent, such as He cavities and dislocation loops, to study individual and combined effects of the irradiation defects on material's mechanical properties. The on-going efforts include (1) characterizing He cavities, (2) imaging dislocation loops, and (3) testing mechanical properties. The microstructures in the damage band will be examined by Transmission electron microscopy (TEM) to reveal He cavity distributions, followed by a quantitative analysis of the cavity size and number densities in NiFeW and W as well as along the interphase boundaries. High-resolution TEM/Scanning TEM (STEM) will be performed to image ion irradiation induced

dislocation loops in NiFeW and W. To avoid focused ion beam (FIB) damage, TEM specimens will be prepared using dimple thinning and low-energy plasma polishing. The FIB samples will be prepared for mechanical tests under a SEM, including measurements of the strain-stress curves to study the effects of the high-density He cavities located at the interphase boundaries and the low-density large He cavities in NiFeW on the mechanical properties of DPT W.

Acknowledgements

This research was supported by the Office of Fusion Energy Sciences, U.S. Department of Energy and performed at Pacific Northwest National Laboratory (PNNL) under Contract DE-AC05-76RL01830. The TEM/STEM will be performed at PNNL. Mechanical testing experiments will be performed at Oregon State University. We are grateful to Zhihan Hu, Xuemei Wang, and Lin Shao at Texas A&M University (TAMU) for performing and supporting the ion irradiation experiments for this study.

References

[1] C.H. Henager, Jr., W. Setyawan, T.J. Roosendaal, N.R. Overman, B.A. Borlaug, E.L. Stevens *et al*., Int. J. Powder Metall. 53 (2017) 53.
[2] R. Neu, H. Maier, M. Balden, R. Dux, S. Elgeti, H. Gietl *et al*., J. Nucl. Mater. 511 (2018) 567.
[3] M.E. Alam, G.R. Odette, Acta Mater. 186 (2020) 324.
[4] J.V. Haag IV, D.J. Edwards, C.H. Henager Jr., W. Setyawan, J. Wang, M. Murayama, Acta Mater. 204 (2021) 116523.
[5] J.V. Haag IV, J. Wang, K. Kruska, M.J. Olszta, C.H. Henager Jr., D.J. Edwards, W. Setyawan, M. Murayama, Sci. Rep. 13 (2023) 1.
[6] M.R. Gilbert, J.-Ch. Sublet, Nucl. Fusion 51 (2011) 043005.
[7] Fusion Evaluated Nuclear Data Library Ver.3.1d (FENDL-3.1d) at https://www-nds.iaea.org/fendl/.
[8] W. Jiang, D. Zhang , D. Li, J. Heo, Z. Wang, L.M. Zhang, N. Overman, T. Varga, Z. Hu, X. Wang, L. Shao, W. Setyawan, J. Nucl. Mater. 561 (2022) 153565.
[9] W. Jiang, L. Kovarik, K. Kruska, Y. Fu, Z. Hu, L. Shao, W. Setyawan, Materialia 29 (2023) 101789.
[10] R. Neu, H. Maier, M. Balden, R. Dux, S. Elgeti, H. Gietl *et al*., J. Nucl. Mater. 511 (2018) 567.
[11] M.E. Alam, G.R. Odette, Acta Mater. 186 (2020) 324.
[12] L.A. El-Guebaly, W. Setyawan, C.H. Henager Jr., R.J. Kurtz, G.R. Odette, Nucl. Mater. Energy 29 (2021) 101092.
[13] J.F. Ziegler, J.P. Biearsack, U. Littmark, *The stopping and Range of Ions in Solids* (Pergamon Press, New York, 1985); available at: http://www.SRIM.org/.
[14] ASTM, ASTM Standard E521-96 (2009), *Standard Practice for Neutron Radiation Damage Simulation by Charged-Particle Irradiation,* ASTM International, West Conshohocken, PA (2009).
[15] W. Jiang, W. Setyawan, K. Kruska, L. Kovarik, D. Zhang, Fusion Materials Semiannual Progress Report for Period Ending June 30, 2020, DOE/ER-0313/68, U.S. Department of Energy, 96.
[16] J.V. Haag IV, M.J. Olszta, D.J. Edwards, W. Jiang, W. Setyawan, Acta Mater. (2023), in press.

4.7 TEMPERATURE EFFECTS ON THE HELIUM CAVITY DISTRIBUTIONS IN DUCTILE-PHASE-TOUGHENED TUNGSTEN—W. Jiang, J. V. Haag IV, W. Setyawan (Pacific Northwest National Laboratory), D. Chen (University of Houston)

OBJECTIVE

The aim of this work is to study the effects of irradiation temperature on the distributions of the helium cavity size and number density in ductile-phase-toughened tungsten (DPT W) alloys.

SUMMARY

The DPT W alloys exhibit significantly higher fracture toughness as compared to pure W. They have been investigated as candidate materials for application in the plasma-facing components (PFCs) of fusion reactors. The DPT W in this study consists of W particles embedded in a ductile-phase NiFeW matrix. Our previous studies indicate that He cavities form in DPT W irradiated with Ni^+ and He^+ ions at 700°C. Larger cavities are observed in the NiFeW than W phase. There is also a preferential distribution of cavities along the interphase boundaries. It is important to study temperature effects on the He cavity behavior in DPT W and understand how the cavity size and number density change as a function of temperature. In this progress report, we describe an ion irradiation experiment and present preliminary results for DPT W irradiated at room temperature (RT) and 1000°C while further investigations are still being performed.

PROGRESS AND STATUS

Introduction

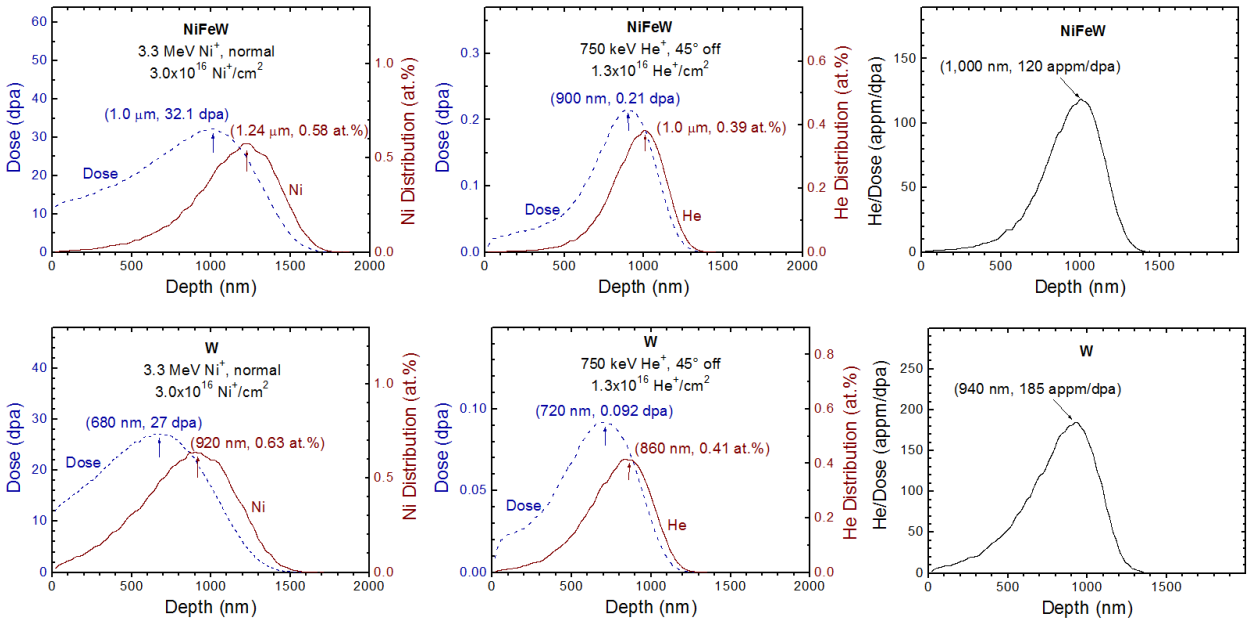

Figure 1. Depth profiles of the dpa dose, He concentration and the ratio of the He concentration to the total dose from Kinchin-Pease Stopping and Range of Ions in Matter (SRIM)13 simulations of Ni and He ion irradiations in NiFeW and W.

The composition of the DPT W (90W-7Ni-3Fe) alloy used in this study was determined [1] to be 88 wt.% W and 12 wt.% NiFeW that consist of 54.68 wt.% Ni, 22.57 wt.% Fe and 22.75 wt.% W, corresponding to 63.83 at.% Ni, 27.69 at.% Fe and 8.48 at.% W. As described in [1,2], calculations by Gilbert *et al*. [3] show that after 5-year operation in a conceptual fusion power plant at a neutron flux of 1.04×10^{15}

Table 1. The SRIM13 simulation results for Ni and He ion irradiations in NiFeW and W

Ion	Material	Damage Peak Depth (nm)	Peak Dose (dpa)	Ni or He Peak Depth (nm)	Ni or He Peak Concentration (at.%)	Max. He to Dose Ratio (appm/dpa)
3.3 MeV Ni^{2+} 3.0×10^{16} Ni^{2+}/cm^2	W	680	27	920	0.63	---
750 keV He^+, 45° 1.3×10^{16} He^+/cm^2	W	720	0.092	860	0.41	185
3.3 MeV Ni^{2+} 3.0×10^{16} Ni^{2+}/cm^2	NiFeW	1000	32.1	1240	0.58	---
750 keV He^+, 45° 1.3×10^{16} He^+/cm^2	NiFeW	900	0.21	1000	0.39	120

$(n/cm^2)/s$, He concentration through elemental transmutation is 1,090 appm produced from Fe and 33.6 appm from W. The He production from Ni is 2,442 appm, which is estimated based on the cross-sections of Ni (99.9 mb) and Fe (44.6 mb) reactions with 14 MeV neutrons [4]. Thus, the total He concentration in NiFeW is 1,863 appm or ~0.19 at.% in NiFeW. The dose in W as the first-wall material after 5-year irradiation in the conceptual fusion power plant has been estimated to be 27.4 displacements per atom (dpa) based on the data reported in [5] with a proper adjustment in the neutron flux [3].

In order to estimate the dose and He distributions in the body-centered cubic W and face-centered cubic NiFeW phases, Kinchin-Pease (K-P) SRIM13 (Stopping and Range of Ions in Matter, version 2013 [6]) simulations were carried out for Ni and He ion irradiations in NiFeW and W, where the threshold displacement energies of $E_d(W)=90$ eV and $E_d(Ni)=E_d(Fe)=40$ eV were adopted [7]. The theoretical densities were assumed to be 19.25 g/cm^3 (or 6.3×10^{22} $at./cm^3$) and 9.50 g/cm^3 (or 8.3×10^{22} $at./cm^3$) for W and NiFeW, respectively. The self-ion (Ni) irradiation is used to emulate high-energy neutron irradiation without introducing impurities. The results from the SIRM13 simulations are shown in Figure 1 and summarized in Table 1. For 3.3 MeV Ni ion irradiation at normal incidence to 3.0×10^{16} Ni/cm^2 in W, the peak dose is 27 dpa at 680 nm, equivalent to the dose in W for 5-year irradiation in a fusion power plant [3,5]; for the same ion fluence, the peak dose in NiFeW is 32.1 dpa at 1000 nm. For 750 keV He ion irradiation at 45° off surface normal to 1.3×10^{16} He/cm^2 in NiFeW, the maximum He concentration is 0.39 at.% at 1000 nm. The He concentration peak is spatially overlapped with the Ni ion damage peak, as intended. The ratio of the He concentration to the dpa dose at the peak is 120 appm/dpa in NiFeW at 1000 nm and 185 appm/dpa in W at 940 nm. It should be noted that the He concentration of 0.39 at.% and the appm/dpa ratio of 120 appm/dpa are doubled on purpose compared to those produced in NiFeW during neutron irradiation in a fusion reactor for 5 years because a significant amount (assumed to be ~50%) of the implanted He atoms is expected to be released during He ion irradiation at elevated temperatures.

Ion Irradiation

Similar to what has been described in [1], sequential irradiation with Ni^{2+} and He^+ ions was performed in different areas of two DPT W alloy samples at RT and 1000°C, respectively, as shown in Figure 2. The DPT W sample in this study has a dimension of 16 mm long × 3 mm wide × 1 mm thick. An area of 8 mm × 3 mm was irradiated uniformly with 3.3 MeV Ni^{2+} ions to an ion fluence of 3.0×10^{16} Ni^{2+}/cm^2. Subsequently, an area of 8 mm × 3 mm shifted downward by 4 mm was irradiated with 750 keV He^+ ions at 45° off normal to an ion fluence of 1.3×10^{16} He^+/cm^2, as given in Table 1. There is an overlapping area of 4 mm × 3 mm

between the Ni^{2+} and He^{+} ion irradiations, as illustrated in Figure 2, thus creating three 4 mm × 3 mm irradiation regions of Ni^{2+} ions only, Ni^{2+} and He^{+} ions, and He^{+} ions only, in addition to an unirradiated area of 4 mm × 3 mm. The irradiations were performed with a defocused 3.3 MeV Ni^{2+} beam and a rastered 750 keV He^{+} beam to achieve uniform irradiation over the intended area of 8 mm × 3 mm. The average ion flux was 2.5×10^{12} (Ni^{2+}/cm^2)/s and 7.2×10^{11} (He^{+}/cm^2)/s. Figure 2 also shows the two irradiated samples with engraved line markers to identify the four different regions. There is no visible coloring in the irradiated areas.

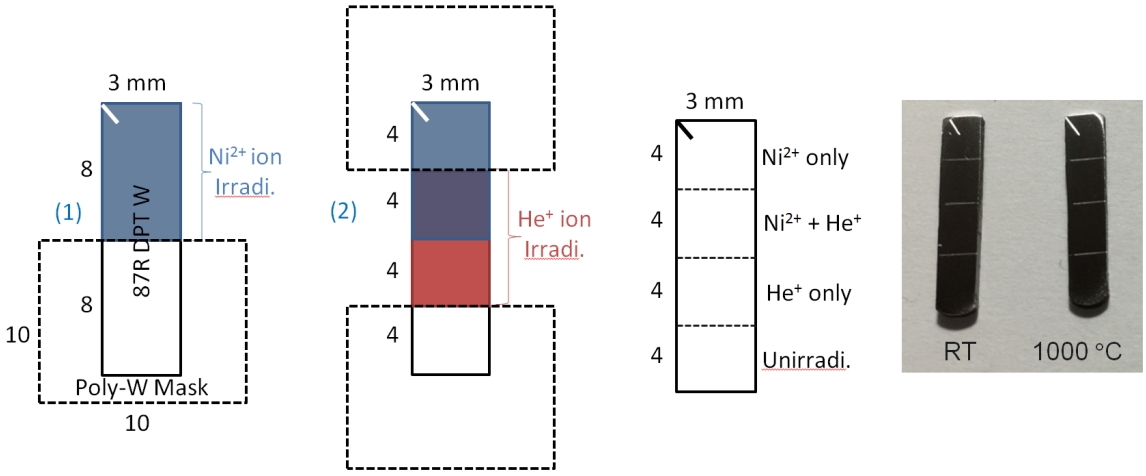

Figure 2. An illustration of two DPT W samples sequentially irradiated with Ni^{2+} and He^{+} ions at RT and 1000°C, respectively, to produce three different irradiation regions with an additional unirradiated area. A picture of the two real samples irradiated at RT and 1000°C, respectively, is also shown.

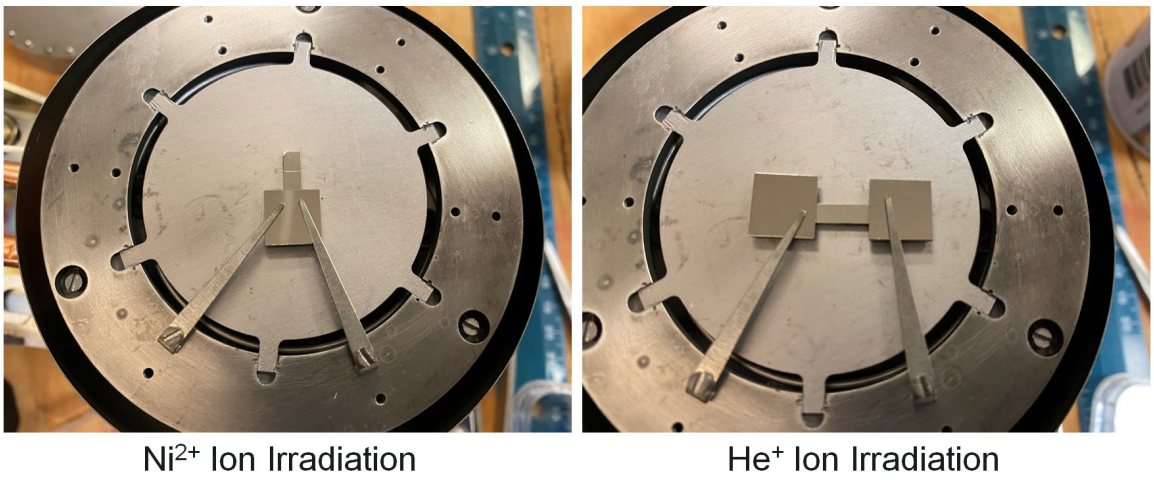

Figure 3. A DPT W sample mounted on a heating stage for a sequential irradiation with 3.3 MeV Ni^{2+} and 750 keV He^{+} ions at the University of Houston.

Figure 3 shows how a DPT W sample was mounted for ion irradiation. Polycrystalline W plates were used as masks that were clamped to hold the sample on a specially designed high-temperature heating stage (up to 1600°C) with a water-cooling system at the University of Houston. The sample temperature was monitored using a thermocouple inside the heating stage.

Results

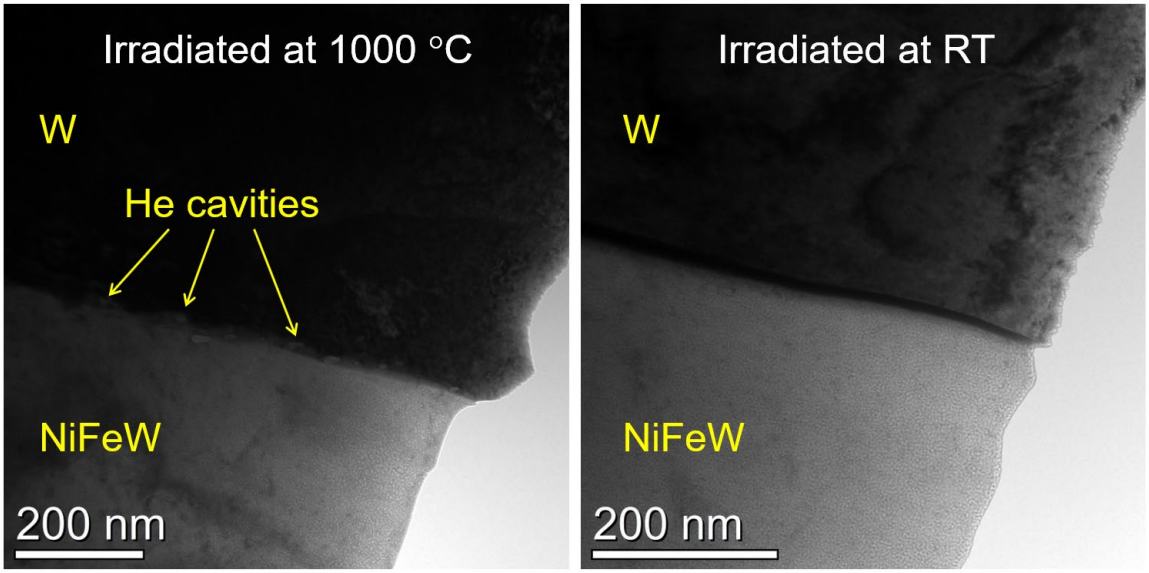

Figure 4. Defocus transmission electron microscopy (TEM) images for two DPT W samples irradiated to combined fluences of 3.0×10^{16} Ni^{2+}/cm^2 and 1.3×10^{16} He^{+}/cm^2 at 1000°C (left image) and RT (right image), respectively.

Similar to our previous reports for DPT irradiated at 700°C [1,8], He cavities are also observed on the interphase boundary between W and NiFeW in the DPT W sample irradiated to combined fluences of 3.0×10^{16} Ni^{2+}/cm^2 and 1.3×10^{16} He^{+}/cm^2 at 1000 °C, as shown in the left image of Figure 4. The average size of the He cavities at 1000°C appears to be significantly larger and the number density lower than at 700°C. In contrast to the 700°C case, no apparent cavities in NiFeW phase are observed at 1000°C. It is expected that He cavities are present in W phase irradiated at 1000°C, but they are not visible probably due to large foil thickness and focused ion beam (FIB) damage. New FIB samples will be prepared and flash electropolishing will be followed to study the He cavities in W phase. Cavities in the sample irradiated at RT have not been observed, as shown in the right image of Figure 4. They might be too small to be visible because mono-vacancies in either NiFeW or W are not mobile at RT. This will need to be carefully confirmed using a better FIB sample to be prepared for higher-resolution TEM examination.

Future Work

As noted above, further examination of the He cavity distributions in DPT W irradiated at 1000°C will be performed. Defocus beams will be used to image He cavities at different magnifications. Depth profiles of the cavities in both NiFeW and W phases will be determined. The behavior of the He cavities along the NiFeW/W interphase boundary and W/W grain boundary, if existing, will also be investigated. For the sample irradiated at RT, evidence will be obtained regarding whether He cavities are visible in W and NiFeW as well as along the interphase boundary. Two methods for the reduction or removal of Ga^{+} ion damage in the FIB foils will be investigated, i.e., low kV Ar^{+} ion milling and flash electropolishing. It is expected that both methods will improve the sample quality for high-resolution TEM examination of the He cavities in the irradiated DPT W samples.

Acknowledgements

This research was supported by the Office of Fusion Energy Sciences, U.S. Department of Energy and performed at Pacific Northwest National Laboratory (PNNL) under Contract DE-AC05-76RL01830. Ion irradiation experiment was performed at the University of Houston.

References

[1] W. Jiang, D. Zhang , D. Li, J. Heo, Z. Wang, L.M. Zhang, N. Overman, T. Varga, Z. Hu, X. Wang, L. Shao, W. Setyawan, J. Nucl. Mater. 561 (2022) 153565.
[2] W. Jiang, W. Setyawan, K. Kruska, L. Kovarik, D. Zhang, Fusion Materials Semiannual Progress Report for Period Ending June 30, 2020, DOE/ER-0313/68, U.S. Department of Energy, 96.
[3] M.R. Gilbert, J.-Ch. Sublet, Neutron-induced transmutation effects in W and W-alloys in a fusion environment, Nucl. Fusion 51 (2011) 043005.
[4] Fusion Evaluated Nuclear Data Library Ver.3.1d (FENDL-3.1d) at https://www-nds.iaea.org/fendl/.
[5] M.R. Gilbert, S.L. Dudarev, S. Zheng, L.W. Packer, J.-Ch. Sublet, An integrated model for materials in a fusion power plant: transmutation, gas production, and helium embrittlement under neutron irradiation, Nucl. Fusion 52 (2012) 083019.
[6] J.F. Ziegler, J.P. Biearsack, U. Littmark, *The stopping and Range of Ions in Solids* (Pergamon Press, New York, 1985); available at: http://www.SRIM.org/.
[7] ASTM, ASTM Standard E521-96 (2009), *Standard Practice for Neutron Radiation Damage Simulation by Charged-Particle Irradiation,* ASTM International, West Conshohocken, PA (2009).
[8] W. Jiang, L. Kovarik, K. Kruska, Y. Fu, Z. Hu, L. Shao, W. Setyawan, Materialia 29 (2023) 101789.

4.8 HIGH-TEMPERATURE MECHANICAL TESTING OF W/NiFe DUCTILE-PHASE TOUGHENED W COMPOSITES

—R. Prabhakaran, J. V. Haag IV, W. Setyawan (Pacific Northwest National Laboratory)

OBJECTIVE

The objective of this task is to investigate the high-temperature operating limit of W/NiFe ductile-phase toughened tungsten (W) composites and to explore how hot-rolling may improve the high-temperature tensile and fracture toughness.

SUMMARY

This report summarizes the status of the elevated temperature mechanical test facility setup, annealing studies, and hot rolling operations to fabricate a new batch of ductile phase-toughened (DPT) W-NiFe mechanical test specimens for obtaining room and elevated temperature mechanical properties.

PROGRESS AND STATUS

Introduction

The (W) is a promising candidate material for plasma-facing components (PFCs) due to its excellent high-temperature strength, low sputtering rate, good thermal conductivity, and high melting temperature. [1-2] However, the potential application of W, as a structural material in PFCs is limited due to its low ductility which will further degrade after irradiation. [3] Therefore, introducing a DP to develop a W composite could serve as an alternative route to overcome its limitations. The DPT is a fracture toughness improvement concept that is being utilized to develop W-based composites for fusion reactor divertor and plasma-facing materials. Liquid-phase sintered tungsten heavy metal alloys (WHAs), due to their balance of strength, ductility and toughness, are being considered to be a suitable alternative to monolithic polycrystalline W for fusion applications.

The low melting point of the alloying elements Fe and Ni being 1538°C and 1455°C, respectively, could restrict the operational space. However, in order to avoid recrystallisation of W to preserve its original mechanical properties, the temperature should be kept anyway below 1300°C, which means that the improvement in ductility and toughness by using Fe and Ni remains expected, though to a lesser extent compared to room temperature mechanical property improvement [4]. Determining the mechanical properties of DPT W at elevated temperatures is indeed an important aim of this research.

As per the literature, the maximum service temperature for divertors is likely 1200-1300°C [4-6], and hence it is critical to obtain the elevated temperature mechanical properties of WHA. The issue of W fuzz has not been fully resolved and, if significant, it might lower the maximum temperature to about 700°C. [7-9] The melting temperature of the DP phase (near Ni:Fe weight ratio of 7:3) is ~1440°C.

Different thermomechanical plastic deformation processing routes, such as hot-rolling (HR), extrusion and swaging, can increase the strength of WHAs [10-16]. Researchers at Pacific Northwest National Laboratory (PNNL) have characterized the effects of the composite architecture on deep notch bend bar toughness for a 90 wt.% W–Fe–Ni WHA, hot rolled to different thickness reductions of 62, 74 and 87% [17]. As per our previous study, the deformed W and DP phases that form a ‘brick-and-mortar (BAM)’ like microstructure could improve strength by hot working, while enhancing the ductility and toughness, by creating a more distributed damage zone under deep notch bar loading [17,18].

In the past, researchers have performed heat treatment on WHA to improve the mechanical properties, especially the ductility and fracture toughness [19-21]. Hence, efforts are ongoing at PNNL to conduct a systematic annealing study for various durations to evaluate its effect on the mechanical properties and microstructure.

Previous mechanical tests have been performed at room temperature using an Instron 5582 servomechanical test frame equipped with an Epsilon ONE optical extensometer, and the results could be found in our previous reports [21-24]. Recently, room temperature tensile testing was conducted using an Instron 8801 servo hydraulic test frame on as sintered 90W, 95W and 97W samples, along with hot rolled 90W samples with various rolling reductions (57R, 78R and 86R), and the results can be found in our previous report [25]. Currently, efforts are ongoing to understand the mechanical behavior of DPT W-NiFe alloys at elevated temperatures (590°C, 880°C and ~1200°C) and this report is focused in documenting the status of the elevated temperature mechanical test facility setup, hot rolling operations to fabricate a new batch of tensile specimens to obtain elevated temperature mechanical properties, annealing studies, and tensile testing at PNNL.

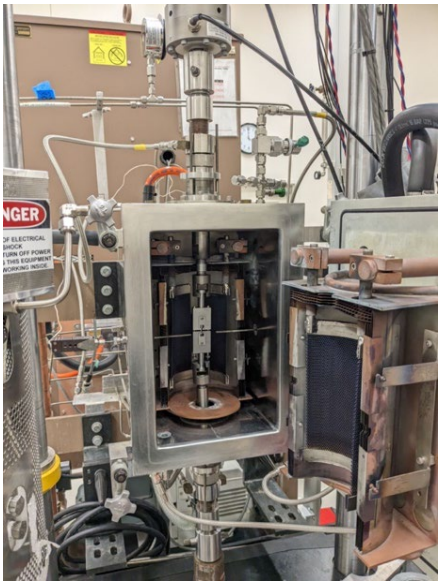

Figure 1. Materials Research Furnaces, Inc (MRF) furnace (1600°C) along with Instron 8801 mechanical test frame and tensile test fixture.

Experimental Procedure

Elevated Temperature Mechanical Test Facility Setup

1. Instron 8801 servo hydraulic mechanical test system

   Instron 8801 is a compact servo hydraulic fatigue testing system that could be employed to perform static and dynamic mechanical tests at ambient and elevated temperatures. Additional information on this test frame can be found in the previous report [25,26].

2. Elevated temperature tensile test fixture

   Currently, efforts are also ongoing to perform tensile testing of DPT W-NiFe (as-sintered and rolled) at 590°C (~1/2 Tm, where Tm is the melting temperature of the ductile phase), 880°C (~2/3 Tm of the ductile phase) and slightly higher (1000-1200°C). The MRF furnace has a usable work zone of 3.5" dia. x 4.0" high. It has water-cooled pull rods (17-4 PH stainless steel) on either side of the furnace, and a tensile fixture that can withstand elevated temperatures without any water cooling is required. Based upon material availability, machinability, cost, and mechanical properties at elevated temperatures, 'titanium-zirconium-molybdenum' (TZM) was chosen as the fixture material. The TZM is a molybdenum alloy containing 0.5% titanium, 0.08% zirconium, 0.02% carbon and the

balance molybdenum. The TZM material was procured, and the tensile fixture fabrication was performed at PNNL. The fabricated TZM tensile fixture (shown in Figure 3) is available for use. Additional information about TZM can be found in the previous report [25].

Figure 2. Shoulder-loaded TZM tensile fixture.

3. The MRF model M-4x6-M-1600-V&G furnace

   The PNNL has an MRF Model M-4x6-M-1600-V&G front-loading furnace with a usable work zone of 3.5" diameter x 4.0" high, and a maximum operating temperature of 1600°C. The hot zone is a 180° split design with tungsten mesh heating elements for operation in vacuum (50-100 mTorr) and inert gas (Ar, N2 or Ar/O2 gas mixture). Additional information about this furnace can be found in previous reports [26,27]. Figure 1 shows the photo of the MRF furnace along with the Instron 8801 mechanical test frame.

   Annealing studies on DPT W-NiFe (as-sintered and rolled) at 1300°C (under 10-15 mTorr vacuum) was performed using this furnace recently (see section E). Tensile testing was also recently performed at 600°C for another project at about 10 mTorr vacuum. Recently, the furnace developed a vacuum leak issue and currently efforts are ongoing to fix the leak. Once the vacuum leak is fixed, efforts will be made to test DPT W-NiFe samples at 590°C and other temperatures.

Procurement of 90 wt.% W–Fe–Ni Alloys

Sintered 90 wt.% alloy was procured from MiTech to fabricate mechanical test samples for room and elevated temperature mechanical testing. Table 1 shows the lot information of the WHA alloy.

Table 1. Sintered W–Fe–Ni alloys procured from MiTech

Material	Vendor	Vendor Code	Lot Number	Lot Chemistry (wt.%)
90W	MiTech	HD 17D	36124	90.37 W; 6.82 Ni and 2.81 Fe

Hot Rolling of 90 wt.% W–Fe–Ni WHA

During 2022, hot rolling was performed on the sintered 90 wt.% W–Fe–Ni alloy procured from MiTech (HD 17D; Lot # 36124). In order to perform hot rolling, the material (approximately 2” thick x 2” wide x 4” long)

was sectioned into approximately 1” thick x 1” wide x 2.25” long pieces. At that time, a 10% reduction was utilized for each pass, and hot rolled samples with different thickness reductions (57R, 78R and 86R) were successfully fabricated. Hot rolling was performed at 1150°C during the first two passes (from about 1.0” to 0.8”) and then it was performed at 900°C (from 0.80” to 0.14”). Figure 4 shows hot rolled (with different thickness reductions: 57R, 78R and 86R) and annealed 90 wt.% W–Fe–Ni plates/foils. All rolled plates were degassed to remove hydrogen. Additional information about 2022 hot rolling operations can be found in the previous report [25]. Tensile test samples were obtained from these hot rolled plates and results can also be found in the previous report [25]. Elevated temperature (1300°C) annealing studies for different durations were performed on tensile samples obtained from as sintered and 86R plates. See section E for additional information on annealing studies.

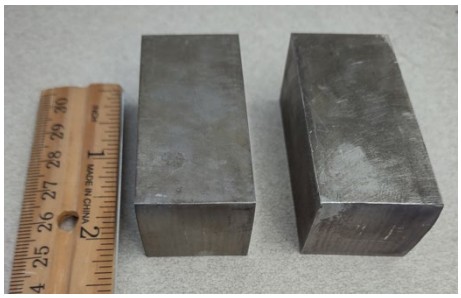

(a) Before hot rolling

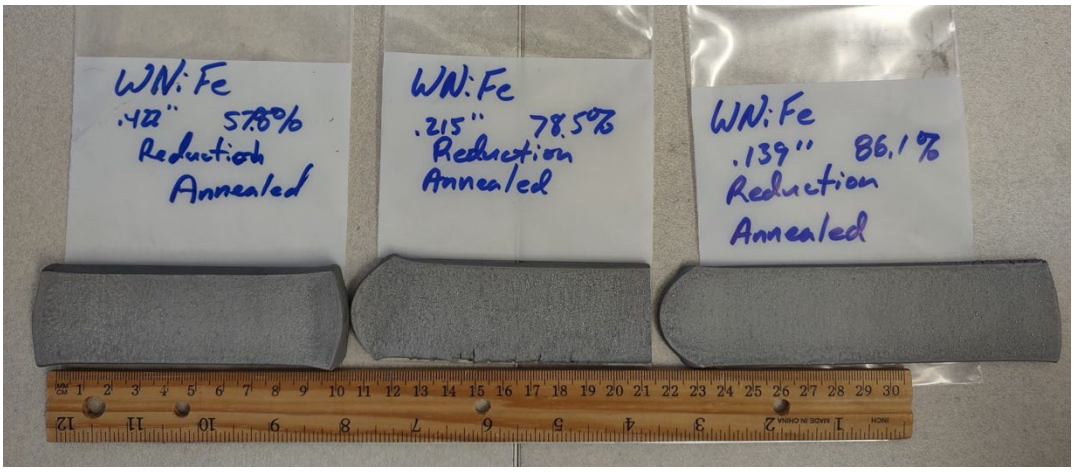

(b) After hot rolling and annealing

Figure 3. Hot rolled (thickness reductions: 57R, 78R and 86R) and annealed 90W–Fe–Ni plates/foils.

During 2023, efforts were made to perform hot rolling on sintered 90 wt.% W–Fe–Ni alloy procured from MiTech (HD 17D; Lot # 36124) with a larger starting thickness, to obtain much thicker rolled plate (around 0.5 in thick) so that mechanical test samples can also be obtained in the thickness direction. Hence, the initial material (approximately 2” thick x 2” wide x 4” long) was sectioned into approximately two 2” thick x 2” wide x 2” long pieces. Sectioning was performed to obtain a material of a suitable mass that can be handled safely using tongs during hot rolling.

During the 2023 hot rolling study #1, a 2-inch cube was employed, and a 5% reduction was utilized for the first three passes (from 2.2” to 1.9”) since the starting thickness was double (2” vs 1”) compared to 2022 rolling studies. The sample was preheated in a Lucifer model 7GT-M48 furnace (see Figure 4) at 1150°C for about 20 minutes. Hot rolling was performed at 1150°C employing a Waterbury Farrell Two High/Four High 755 Rolling Mill (see Figure 4) using a 5% reduction for the first three passes and then switched to 10% reduction from the fourth pass (from 1.9” to 1.4”) as shown in Table 2.

Table 2. Hot rolling schedule of sintered 90 wt.% W–Fe–Ni alloy (Study#1: 5% reduction for initial three passes and then 10% reduction at different rolling temperatures)

Pass #	Thickness (Inches)		Buck (Inches)		Mill Set	Reduction %		Notes
	Desired	Actual	Estimate	Actual	(inches)	Pass	Total	
Start		2.180						Started with 1 piece, a 2" cube, June, 16 2023
1	2.071	2.090	0.015	0.034	2.056	4.13%	4.13%	1150C 20 min preheat 5% target reduction
2	1.986	1.999	0.020	0.033	1.966	4.35%	8.30%	1150C 15 min preheat
3	1.900	1.900	0.030	0.030	1.870	4.95%	12.84%	1150C 10 min preheat
4	1.710	1.705	0.035	0.030	1.675	10.26%	21.79%	1150C 20 min preheat 10% target reduction
5	1.535	1.551	0.030	0.046	1.505	9.03%	28.85%	1150C 20 min preheat 10% target reduction
Annealed 3 hours 1200C, Ar Purge then 100% H2					6/21/23			
		1.524						Post anneal cold measurement
6	1.372	1.407	0.020	0.055	1.352	7.68%	35.46%	10% reduction target, 900°C 20 minute min. soak time
7								Material split horizontally during pass 6

Figure 4. Preheating Lucifer Furnace and Waterbury Farrell Rolling Mill.

During the hot rolling process, the rolled material was annealed (purged with argon for 70 minutes, followed by hydrogen purge and heating cycle; ramp up @5°C/min; dwell at 1200°C for 3 hours; ramp down via natural cooling @ 3-5°C/min; hydrogen purge continued until the furnace reached under 100°C while cooling down; followed by 70 minutes of argon purge) using a CM model 1516GSH2FL furnace (see Figure 6) after the fifth pass of the rolling process, as shown in the Table 2. During the sixth pass (when thickness was 1.5”), hot rolling was performed at 900°C and a 10% reduction was employed. The material got split horizontally during the sixth pass, as shown in Figure 7. Lower hot rolling temperature (900°C vs. 1150°C) could have played a role and additional rolling studies focused on parameters may be required to obtain more detailed information.

Figure 5. Left: CM Furnace utilized for 1200°C annealing during hot rolling process. Right: Thermal Technologies/Brew Furnace for degassing hydrogen.

(a) Before hot rolling

(b) After 5th pass (28.85% reduction); Left: pre anneal; Right: post anneal

(c) After 6th pass; Left: pre anneal (rotated 90° before taking a photo); Right: Post anneal
NOTE: The sample split during the 6th pass.

Figure 6. Hot rolled (study#1) and annealed 90W–Fe–Ni plates/foils.

During the 2023 hot rolling, study #2 was conducted on another 2" cube and 1150°C was chosen as the hot rolling temperature for all the passes (unlike 2023 study #1). A 5% reduction was employed for the initial stages (similar to study #1) since the thickness was double (2" vs 1") compared to 2022 rolling studies. However, the 5% reduction was employed for a much longer time, i.e., utilized for the first eighteen passes (from 2.2" to 0.87" and then switched to 10% reduction per pass when there were indications (such as overhang/cracking) that suggested that reduction per pass was not being aggressive enough. In the future studies, 10% reduction could be employed at a much earlier stage (when the thickness is around 1-75"-1.50"). Table 3 shows the schedule for the 2023 hot rolling study #2. Hot rolling and annealing were performed using the same equipment (Figure 4 and 5) as mentioned earlier. Figure 7 shows the photos of hot rolled and annealed 90W–Fe–Ni plate during various stages. The rolled plate will soon be degassed (to remove hydrogen) using a Thermal Technologies/Brew furnace (model 121224MMS; see Figure 5) at 908°C for 60 minutes (vacuum level before heating around 0.2 mTorr; ramp up rate @ 3-4°C/min and ramp down via natural cooling @ ~4°C/min).

Table 3. Hot rolling schedule of sintered 90 wt.% W–Fe–Ni alloy (Study #2: Performed at 1150°C and 5% reduction for several passes and then 10% reduction)

Pass #	Thickness (Inches)		Buck (Inches)		Mill Set	Reduction %		Notes
	Desired	Actual	Estimate	Actual	(inches)	Pass	Total	
Start		2.190						Started with 1 piece, a 2" cube, July 11, 2023
1	2.080	2.084	0.020	0.024	2.060	4.84%	4.84%	1150C 20 min preheat
2	1.976	1.977	0.020	0.021	1.956	5.13%	9.73%	1150C 20 min preheat
3	1.878	1.882	0.020	0.024	1.858	4.81%	14.06%	1150C 20 min preheat
4	1.788	1.792	0.020	0.024	1.768	4.78%	18.17%	1150C 20 min preheat
								Pass 2-4 measurements performed with hot sample after rolling pass
Annealed 4 hours 1200C, Ar Purge then 100% H2					7/12/23			
		1.786						Post anneal cold measurement
5	1.697	1.706	0.022	0.031	1.675	4.48%	22.10%	1150C 20 min preheat
6	1.621	1.621	0.025	0.025	1.596	4.98%	25.98%	1150C 20 min preheat
7	1.540	1.549	0.025	0.034	1.515	4.44%	29.27%	1150C 15 min preheat
8	1.472	1.470	0.030	0.028	1.442	5.10%	32.88%	1150C 15 min preheat
Annealed 4 hours 1200C, Ar Purge then 100% H2					7/25/23			
		1.455						Post anneal cold measurement
9	1.382	1.382	0.025	0.025	1.357	5.02%	36.89%	1150C 20 min preheat
10	1.313	1.317	0.025	0.029	1.288	4.70%	39.86%	1150C 20 min preheat
11	1.251	1.266	0.025	0.040	1.226	3.87%	42.19%	1150C 20 min preheat
12	1.203	1.209	0.030	0.036	1.173	4.50%	44.79%	1150C 20 min preheat
								Edge cracking has begun, noticed post anneal
Annealed 4 hours 1200C, Ar Purge then 100% H2					7/26/23			
		1.191						Post anneal cold measurement
13	1.131	1.135	0.025	0.029	1.106	4.70%	48.17%	1150C 25 min preheat
14	1.078	1.086	0.025	0.033	1.053	4.32%	50.41%	1150C 20 min preheat
15	1.032	1.029	0.030	0.027	1.002	5.25%	53.01%	1150C 20 min preheat
16	0.978	0.973	0.030	0.025	0.948	5.44%	55.57%	1150C 20 min preheat
Annealed 4 hours 1200C, Ar Purge then 100% H2					7/28/23			
		0.960						Post anneal cold measurement
17	0.912	0.912	0.025	0.025	0.887	5.00%	58.36%	1150C 25 min preheat
18	0.866	0.870	0.025	0.029	0.841	4.61%	60.27%	1150C 20 min preheat
19	0.783	0.785	0.030	0.032	0.753	9.77%	64.16%	1150C 25 min preheat/Increased to 10% target
20	0.706	0.710	0.030	0.034	0.676	9.55%	67.58%	1150C 25 min preheat/Increased to 10% target
	.							
Annealed 4 hours 1200C in Ar Purge then 100% H2					8/1/23			

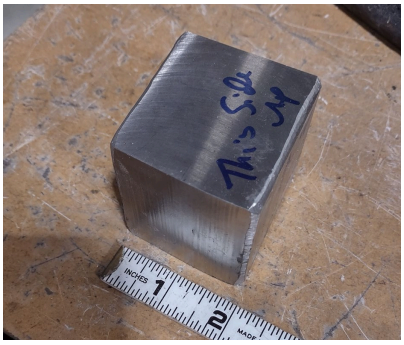

(a) Before hot rolling

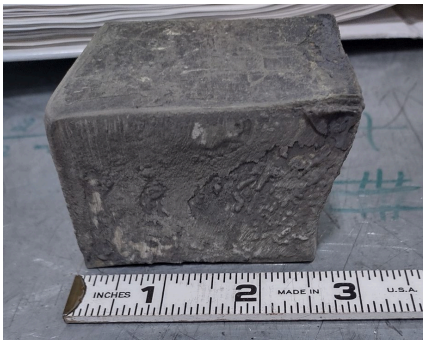

(b) After 4th pass (18.17% reduction; pre anneal)

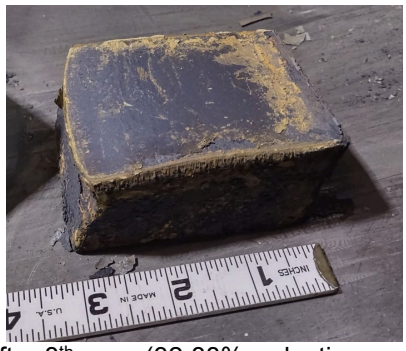

c) After 8th pass (32.88% reduction pre anneal)

(d) After 8th pass (32.88% reduction post anneal)

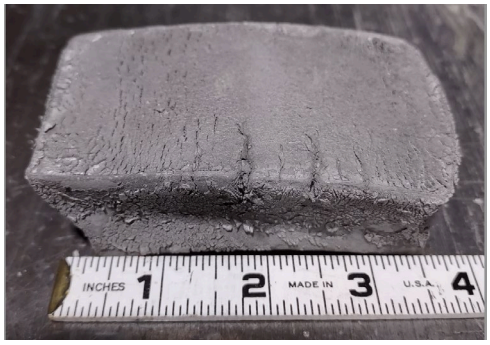

(e) After 12th pass (44.79% reduction post anneal)
Left photo: Top of the sample; Right photo: Bottom – edge cracking begun; noticed post anneal

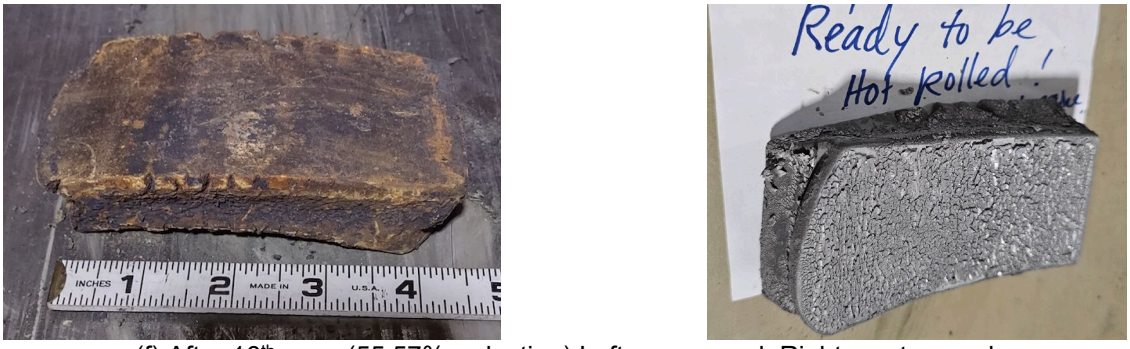

(f) After 16th pass (55.57% reduction) Left: pre anneal; Right: post anneal

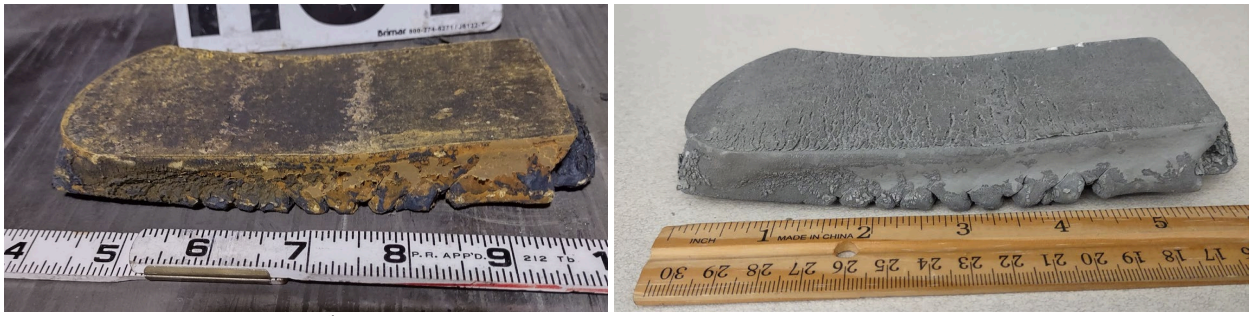

(g) After 20th pass (67.58% reduction): Left: pre anneal; Right: post anneal

Figure 7. Hot rolled and annealed 90W–Fe–Ni plates/foils (study #2).

Tensile Specimen Fabrication

Sub-size tensile specimens, as shown in Figure 7, were machined (single orientation) using an electrical discharge machining (EDM) from as sintered 90W, 95W and 97W samples. Tensile specimens (multiple orientations, as shown in Figure 9) were also fabricated from hot rolled (57R, 78R and 86R), annealed and degassed 90 wt.% W–Fe–Ni plates (see Figure 3) obtained from the 2022 hot rolling study.

Tensile specimens were fabricated to perform testing at room and elevated temperatures (590°C, 880°C and higher). The nominal gage width, gage thickness and reduced length of a sub-size tensile specimen are 1.684 mm, 0.762 mm and 5.029 mm, respectively. The total length and shoulder width of the sub-size tensile specimen are 16.104 mm and 4.013 mm, respectively.

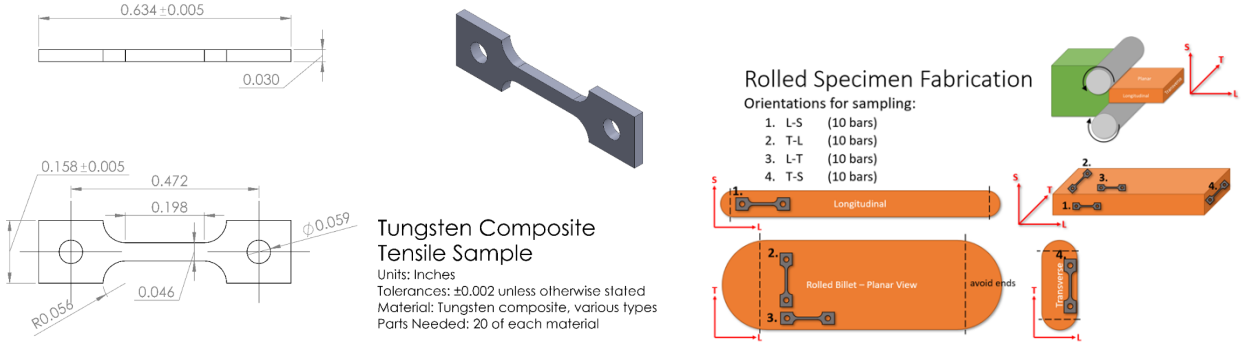

Figure 8. Left: Subsize tensile specimen design; Right: Specimen orientations for rolled specimens.

Annealing Studies (1300°C) on 0R and 86R Tensile Samples

The MRF furnace was utilized for performing elevated temperature annealing studies on DPT W-NiFe (as-sintered and hot rolled - 86R) tensile samples at 1300°C (under 5-10 mTorr vacuum) for three different annealing times (6 hours; 12 hours; 24 hours). The hot rolled (86R) samples from the 2022 rolling study was utilized for the annealing study, along with as-sintered tensile samples. The melting temperatures of W, Ni and Fe are 3422°C, 1455°C and 1535°C, respectively and it is essential to consider the vapor pressure chart for various metals.

Two alumina crucibles were utilized for the annealing study. The alumina crucibles were positioned in such a way that it is at the center of the heat zone, as shown in Figure 9. Tensile specimens from each condition (as sintered and 86R) were placed inside alumina crucibles. Once the samples were placed inside, the furnace door was closed, and the roughing pump was turned on until the vacuum levels reached 5-10 mTorr. The temperature of the MRF furnace was gradually increased at a ramp rate of 3-5°C/min until it reached 1300°C. The samples were then annealed for a particular annealing time and then the furnace hot zone was shut down so that the samples can cool down via natural cooling. The furnace does not have any other cooling system. The vacuum level was maintained until the samples reached the ambient temperature. Figure 10 shows the typical condition of the tensile samples after 1300°C annealing.

Figure 9. Tensile samples were annealed at 1300°C (under 5-10 mTorr vacuum) for different durations (6 h, 12 h and 24 h).

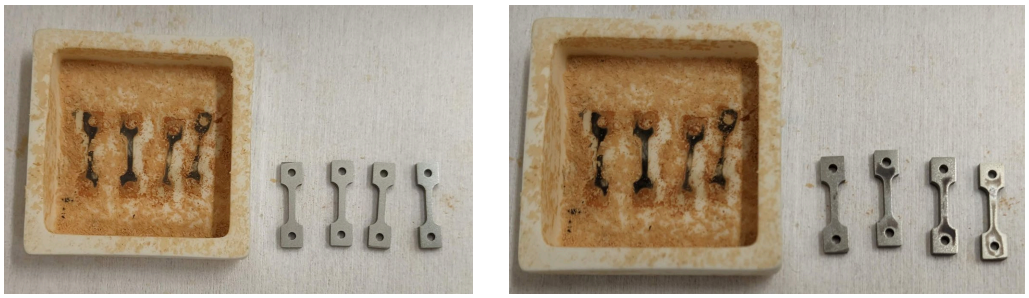

Figure 10. Tensile samples after 1300°C annealing; two sides (as-sintered 90W–Fe–Ni; 12 hours).

Room Temperature Tensile Testing of 1300°C Annealed 0R and 86R Samples

An Instron 8801 servo-hydraulic mechanical testing system was utilized for conducting tensile testing in the displacement control mode. The specimen gage width and thickness were measured using calipers prior to tensile testing. The displacement rate during tensile testing was constant at a crosshead speed of 0.06 mm/min (1 *μm/s*), which can be converted to an estimated strain rate of 1.99x10^-4/s for specimens with a

5.029 mm reduced length. Subsize tensile specimens were shoulder loaded instead of pin loaded to avoid tear out at the pin hole and warping of the pins.

During 2022, polishing (to at least 1200 grit condition) was only performed on the top and bottom wide faces (not on the thickness direction) of the tensile specimens obtained from as-sintered (90W, 95W, 97W) and hot-rolled (2022 batch of 86R, 78R and 57R) materials to remove minor cracks and local residual stresses due to EDM. Tensile test results and analysis of these samples can be found in the previous report [25].

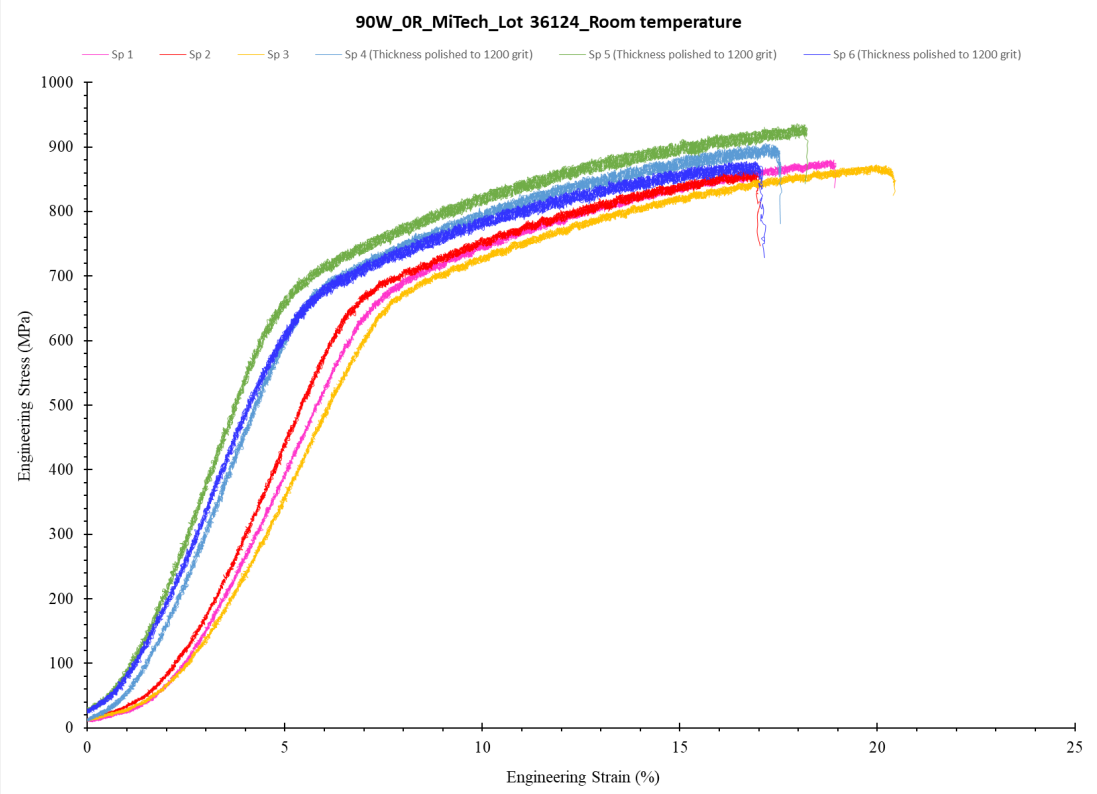

Figure 11. Ambient temperature engineering stress strain curves of as sintered 90W-7Ni-3Fe samples - with and without the thickness sides polished (NOTE: Flat sides were polished for both cases).

During Spring 2023, trial polishing (to at least 1200 grit condition) was performed on the thickness direction also (gage section only) besides the top and bottom faces of the as sintered 90W tensile specimens to determine if there is any change in the tensile properties. The EDM fabricates tensile specimens with good geometrical accuracy. Generally, polishing the flat sides (top and bottom wide faces) are easier (since specimens can be glued to a base/holder and polishing can be performed using sample preparation equipment) and can produce polished surfaces without a major change in tensile specimen thickness across the length. However, polishing the thickness sides (gage section) are little trickier (since specimens cannot be glued; instead, specimens are held using one hand and polished manually to produce the desired finish). The goal is to polish the gage section thickness sides in such a way that the width of tensile specimen doesn't change significantly across the gage length. Figure 11 showed that polishing the thickness sides did not have any detrimental effect.

During Summer 2023, all sides (top and bottom wide faces; gage section thickness direction also) of the tensile samples that were utilized for the 1300°C annealing study were polished to at least 1-*μm* condition. The ASTM Standard E8/E8M was utilized for performing tensile testing and data analysis [28]. Load,

displacement and time were recorded during tensile testing. The displacement was measured from the crosshead movement. The load data was obtained from the load cell. Engineering stress-strain curves were generated by using load-displacement data recorded during testing along with initial specimen gage width, thickness, and reduced length. These curves were used to determine 0.2% offset yield strength (YS), ultimate tensile strength (UTS), uniform elongation (UE), and total elongation (TE).

Table 4 shows the room temperature tensile properties of as-sintered 90W–7Fe–3Ni samples before and after 1300°C annealing at various times. Representative engineering stress vs strain curves are shown in Figure 12. The 0.2% offset YS values were similar for samples annealed for 6 and 12 hours but it increased by about 11% when the duration was 24 hours. The UTS values increased slightly for all durations, and it was the highest (11% increase) for the 24-hour condition. Annealing increased both UE and TE irrespective of the duration. The 1300°C annealing for 12 hours resulted in the highest UE (118% increase) and TE (197% increase) values when compared to un-annealed samples (see Table 6). Efforts will be made to test another specimen annealed for 6 hours, since two tested specimens showed a slightly larger scatter in UE and TE values when compared to other durations. The 1300°C/24-hour annealed samples showed a slightly larger scatter in YS and UTS values. The 1300°C/12-hour annealed samples showed the least scatter for all tensile properties. Based upon the available information, it appears that annealing at 1300°C for 12 hours is optimal for as sintered 90W-7Ni-3Fe samples. Annealing could help to homogenize the microstructure and heal processing damage, which is also an issue for the toughness properties of material in the as sintered condition [20,29].

Table 4. Room temperature tensile properties of as sintered 90W-7Ni-3Fe samples (before and after 1300°C annealing)

Sample Information	Specimen ID	0.2% offset Yield Strength (MPa)	UTS (MPa)	Uniform Elongation (%)	Total Elongation (%)
90W-0R_MiTech_Lot 36124	Sp 1	650	875	10.10	10.15
	Sp 2	650	855	8.65	9.00
	Sp 3	650	865	10.90	11.37
	AVERAGE	**650**	**865**	**9.88**	**10.17**
	SD	0	8	0.93	0.97
90W-0R_MiTech_Lot 36124_1300C_24 h annealed	Sp 1	708	950	14.70	22.08
	Sp 2	740	978	13.50	20.10
	AVERAGE	**724**	**964**	**14.10**	**21.09**
	SD	16	14	0.60	0.99
90W-0R_MiTech_Lot 36124_1300C_12 h annealed	Sp 1	645	931	21.43	29.99
	Sp 2	645	928	21.68	30.48
	AVERAGE	**645**	**930**	**21.56**	**30.24**
	SD	0	2	0.13	0.25
90W-0R_MiTech_Lot 36124_1300C_6 h annealed	Sp 1	655	939	21.70	30.00
	Sp 2	645	949	15.97	23.15
	AVERAGE	**650**	**944**	**18.84**	**26.58**
	SD	5	5	2.87	3.43

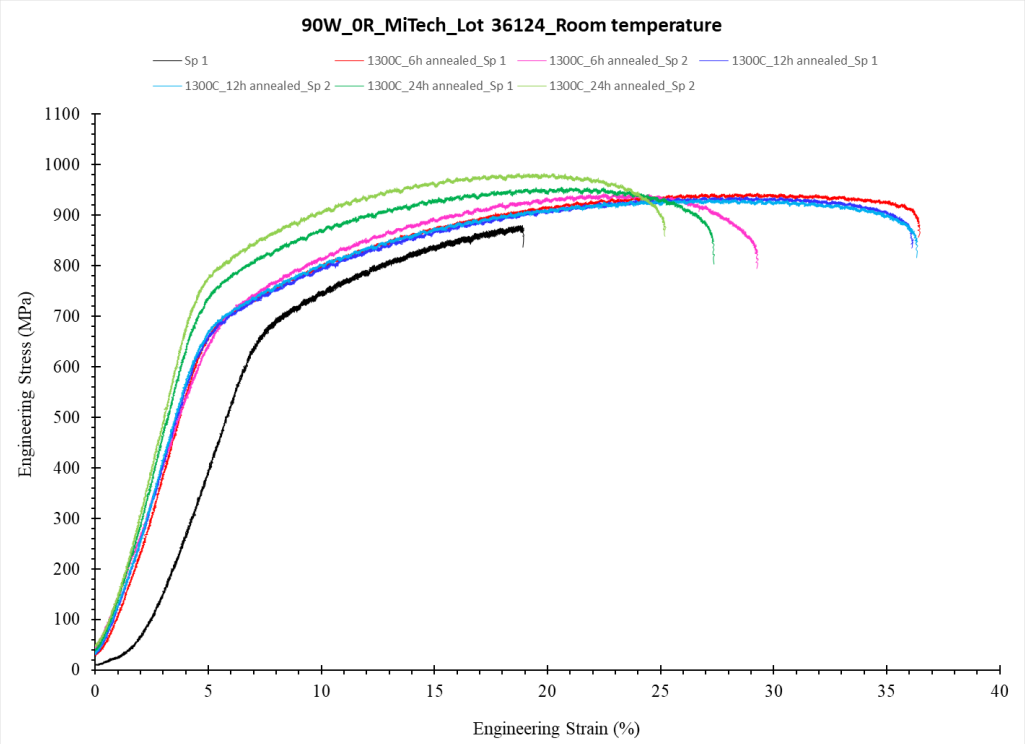

Figure 12. Room temperature engineering stress strain curves of as sintered 90W-7Ni-3Fe samples (before and after 1300°C annealing).

Table 5 shows the room temperature tensile properties of hot rolled (86R) 90W–7Fe–3Ni samples before and after 1300°C annealing at various times. Representative engineering stress vs strain curves are shown in Figure 13. The 1300°C annealing reduced the 0.2% offset YS and UTS irrespective of the durations and the lowest YS (19% decrease) and UTS (9% decrease) was observed for 12 hours. Annealing increased the UE irrespective of the durations and the highest UE (27% increase) was observed for 6 hours (see Table 6). Annealing reduced the TE slightly (5% decrease) for a 24-hour duration, however, the TE increased as the annealing duration was reduced, and the 6-hour duration resulted in the highest TE (39% increase). Efforts will be made to test another specimen annealed for twelve hours, since specimen availability was an issue at that time. In general, annealed samples did not exhibit much scatter in the YS, UTS, UE and TE values (except the 24-hour duration that showed some scatter in TE values). Based upon the available information, it appears that annealing at 1300°C for six hours is optimal for hot rolled (86R) 90W-7Ni-3Fe samples.

Table 5. Room temperature tensile properties of hot rolled (86R) 90W-7Ni-3Fe samples (before and after 1300°C annealing)

Sample Information	Specimen ID	0.2% offset Yield Strength (MPa)	UTS (MPa)	Uniform Elongation (%)	Total Elongation (%)
90W-86R_MiTech_Lot 36124_Orientation 2	Sp 1	860	1050	14.82	19.72
	Sp 2	865	1055	14.40	17.00
	AVERAGE	**863**	**1053**	**14.61**	**18.36**
	SD	3	3	0.21	1.36
90W-86R_MiTech_Lot 36124_Orientation 3	Sp 1	825	1011	16.00	20.72
	Sp 2	852	1013	15.85	22.55
	Sp 3	810	995	15.40	22.57
	AVERAGE	**829**	**1006**	**15.75**	**21.95**
	SD	17	8	0.25	0.87
90W-86R_MiTech_Lot 36124_Orientation 3_1300C_24 h annealed	Sp 1	680	977	15.43	18.77
	Sp 2	690	975	16.74	23.09
	AVERAGE	**685**	**976**	**16.09**	**20.93**
	SD	5	1	0.65	2.16
90W-86R_MiTech_Lot 36124_Orientation 3_1300C_12 h annealed	Sp 1	670	917	19.00	23.85
	AVERAGE	**670**	**917**	**19.00**	**23.85**
	SD	0	0	0	0
90W-86R_MiTech_Lot 36124_Orientation 3_1300C_6 h annealed	Sp 1	700	947	20.12	30.92
	Sp 2	698	945	19.90	30.10
	AVERAGE	**699**	**946**	**20.01**	**30.51**
	SD	1	1	0.11	0.41

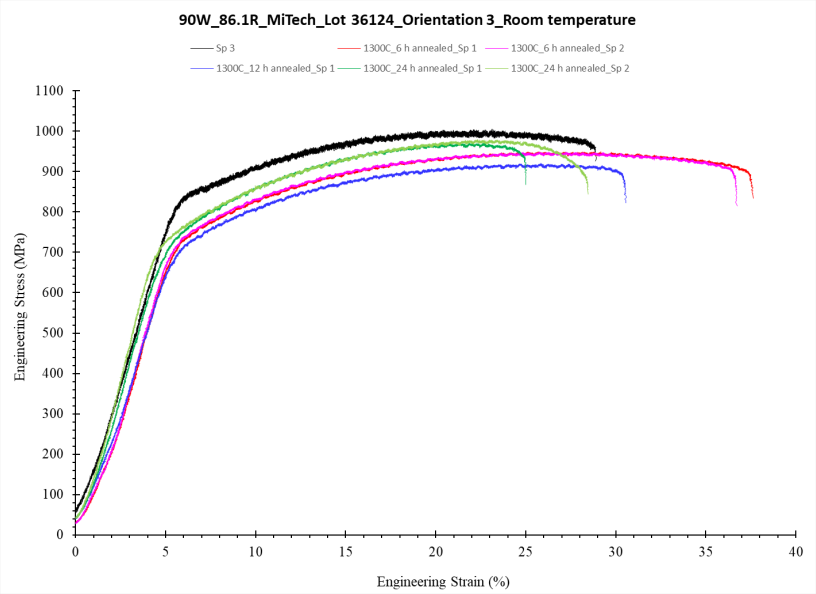

Figure 13. Room temperature engineering stress strain curves of 86R 90W-7Ni-3Fe samples. (before and after 1300°C annealing).

Table 6 and Figure 14 summarizes the effect of 1300°C annealing (with different durations) on the mechanical properties (YS, UTS, UE and TE) of as sintered and hot rolled (86R) 86R 90W-7Ni-3Fe samples. These are all preliminary results and additional testing (such as increasing the number of tensile specimens per condition), and analysis will soon be completed. Fractographic evaluations of the tested annealed samples need to be performed to understand the morphology of the failure.

Table 6. Effect of 1300°C annealing on the mechanical properties of 90W-7Ni-3Fe samples

Sample Information	1300C Annealing Duration (hours)	Difference in YS (MPa)	Difference in UTS (MPa)	Difference in UE (%)	Difference in TE (%)
90W-0R_MiTech_Lot 36124	0	N/A	N/A	N/A	N/A
	6	0	9	91	161
	12	-1	7	118	197
	24	11	11	43	107

Sample Information	1300C Annealing Duration (hours)	Difference in YS (MPa)	Difference in UTS (MPa)	Difference in UE (%)	Difference in TE (%)
90W-86R_MiTech_Lot 36124_Orientation 3	0	N/A	N/A	N/A	N/A
	6	-16	-6	27	39
	12	-19	-9	21	9
	24	-17	-3	2	-5

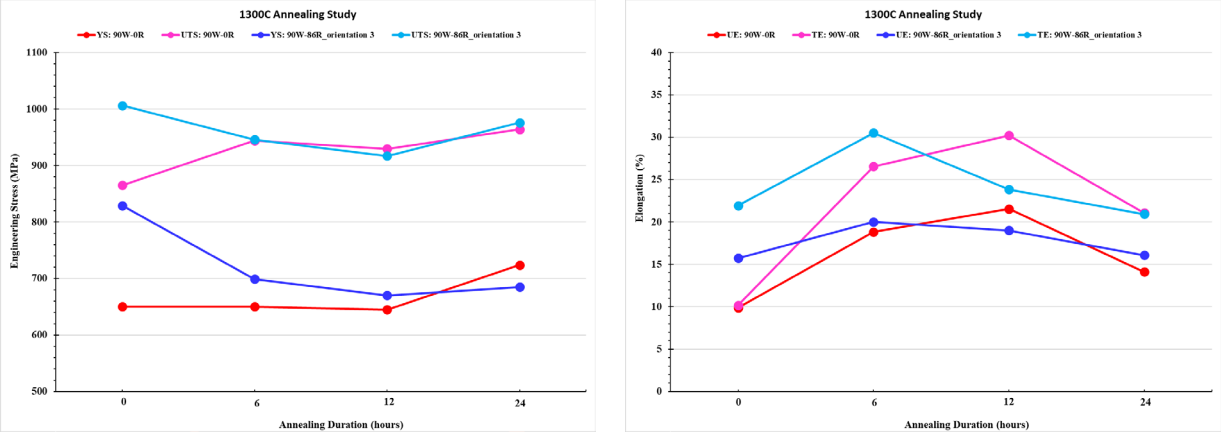

Figure 14. Effect of 1300°C annealing (with different durations) on the mechanical properties of as sintered and hot rolled (86R) 90W-7Ni-3Fe samples.

Electron Backscattered Diffraction (EBSD) Studies on 1300°C Annealed 0R and 86R Samples

Micro-tensile specimens of the 0R and 86R as-fabricated and annealed specimens were examined via low magnification scanning electron microscope (SEM) imaging and EBSD mapping prior to mechanical testing. This was done to determine the extent of annealing required to fully recover pre-existing damage and quantify any changes in microstructure resulting from the annealing. For this analysis, both the 0R and 86R specimens were observed in their as-fabricated state as well as at annealing time steps of 6, 12, and 24 hours.

Prior to observation, the face of one specimen from each condition was prepared for SEM and EBSD via conventional grinding and polishing to 1200 grit, and then finished with a combination etch/polish step using a mixture of colloidal silica and hydrogen peroxide. The 86R specimens were all prepared for imaging on their normal planar view orientation (RD-TD plane). The resulting surfaces were deemed appropriate for EBSD mapping, although secondary electron imaging revealed slight topographic differences between the hard W phase and the soft NiFe phase. The instrument employed for SEM imaging and EBSD mapping was a JEOL 7600 scanning electron microscope operated at 5 kV for backscattered electron imaging (BSE) to reveal the elemental dispersion across the surface, and 20 kV for EBSD mapping to observe the crystallographic orientations of each grain.

Representative BSE micrographs from the 0R annealing conditions have been provided in Figure 15. The hard W phase is bright and the soft NiFe phase is dark. It is clear from these images that there are no significant changes in phase dispersion for annealing trials with the 0R specimens. This is not surprising as the production process for these materials is liquid phase sintering (LPS) for an extended period of time at temperatures in excess of the applied annealing conditions. The 86R specimens appear to exhibit a

similar trend during BSE imaging, with very little apparent differences between domain morphologies under each annealing condition, Figure 16. It is noted that the 86R unannealed specimen possesses mottled BSE contrast within the W domains which is noted to steadily disappear with the applied annealing. This likely equates to existing damage in the W grain interiors but must be confirmed via EBSD mapping. The rolling process also drastically refines the grain size of the NiFe phase, although this is difficult to discern from the low magnification BSE images of Figure 16.

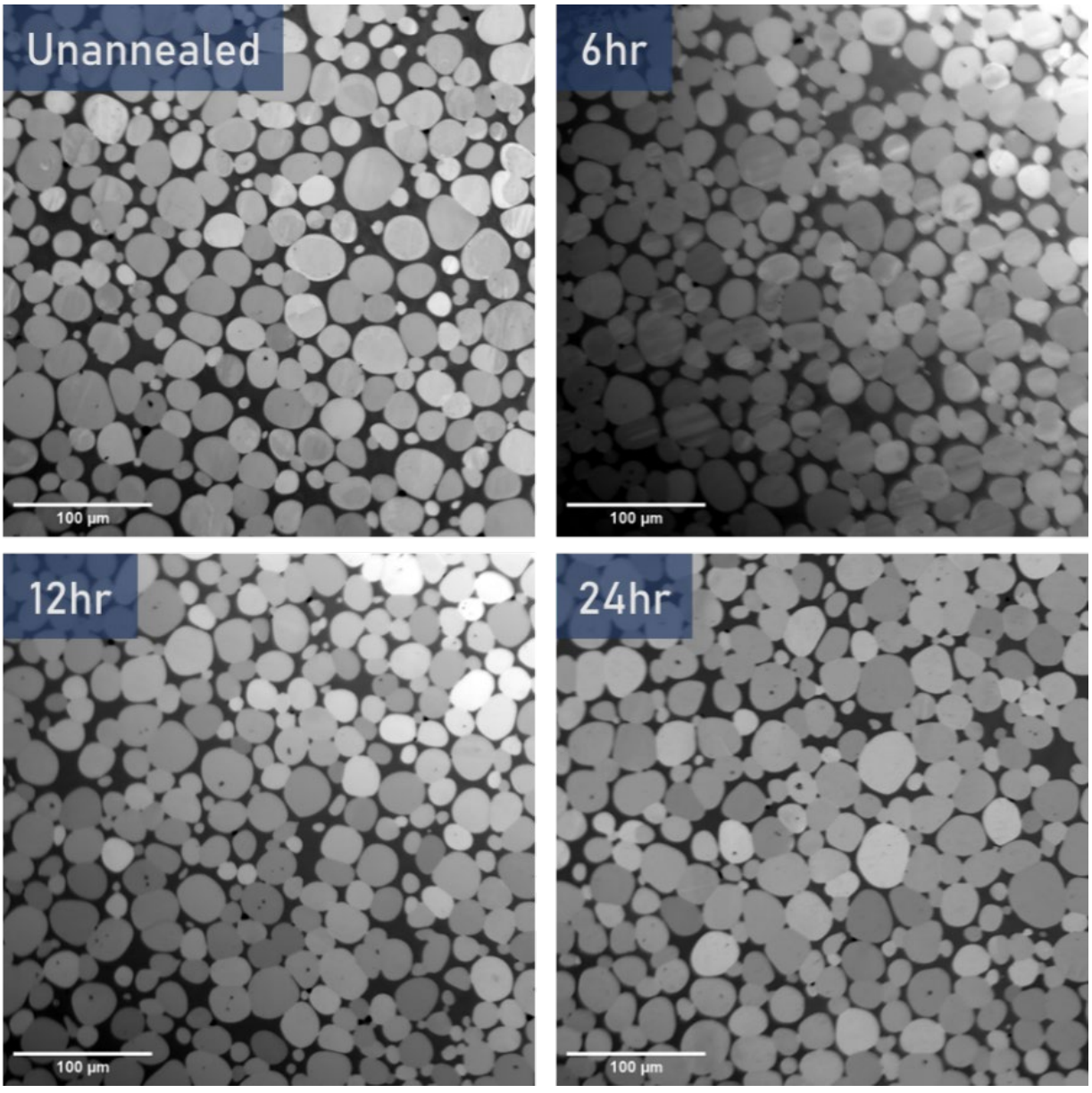

Figure 15. BSE SEM images of all 90W-0R annealing conditions.

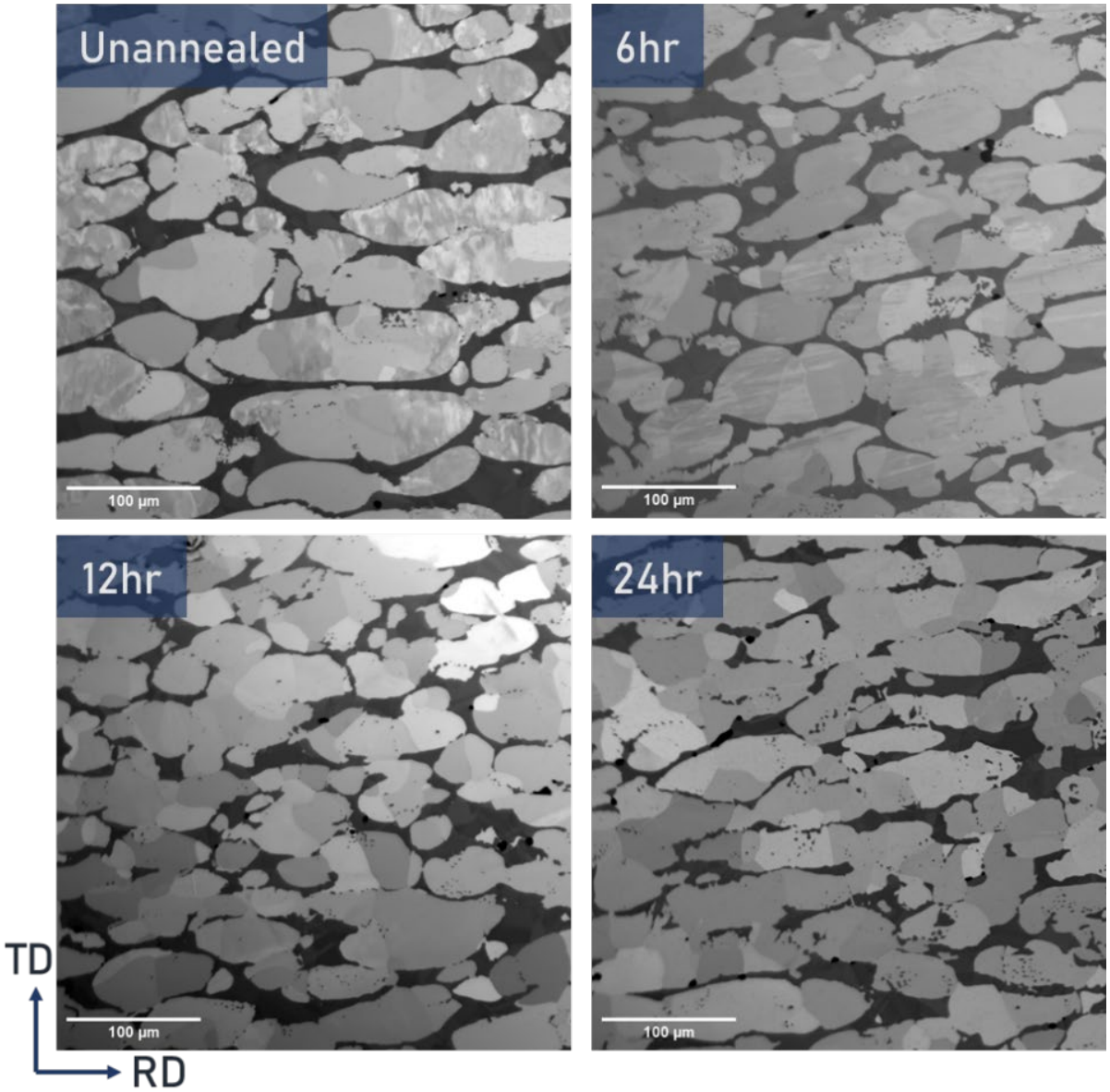

Figure 16. The BSE SEM images of all 90W-86R annealing conditions.

The EBSD mapping of the 0R conditions suggests there is no significant damage present in the 0R unannealed state, and that the applied annealing conditions do not lead to a discernable rearrangement of the W domains. Figure 17 displays the kernel average misorientation (KAM) maps, a measure of the localized misorientation between points. It is noted that the NiFe grains are massive in size, even in the unannealed condition, and therefore no claims can be made on the modification of these grains without massive area EBSD montaging (>1 mm^2). It is thought that the applied annealing conditions may lead to a slight coarsening of the W domains, but the effective W domain size has yet to be measured across all conditions. It should also be noted that additional maps need to be collected from the 0R unannealed and 6-hour annealed specimens during the upcoming reporting period as there exists concern that the incident electron beam for EBSD mapping was improperly aligned prior to mapping, giving an inaccurate sense of the point-to-point misorientation.

The KAM maps of the 86R conditions, Figure 18, indicates that the unannealed state contains significant misorientation within single grains of the W phase, while the NiFe phase appears to be fully recovered and recrystallized. This result suggests that the final hot-rolling and annealing steps applied in the initial production the 86R samples was insufficient in fully recovering the W phase. The 6-hour annealing step significantly reduces the apparent damage with W grains, but still exhibits a limited number of W domains with a high degree of intragranular misorientation. The 12 and 24-hour annealing steps appear to have recovered from all the existing damage within W and NiFe, indicating a post-processing annealing of at least 12 hours at 1300°C is necessary to fully recover the rolled WHA specimens. At present, these results are preliminary in nature, and a full investigation of the effects of grain size, domain shape, and quantification of intragranular misorientation and their bearing upon the mechanical performance of these alloys will be the focus of this upcoming reporting period.

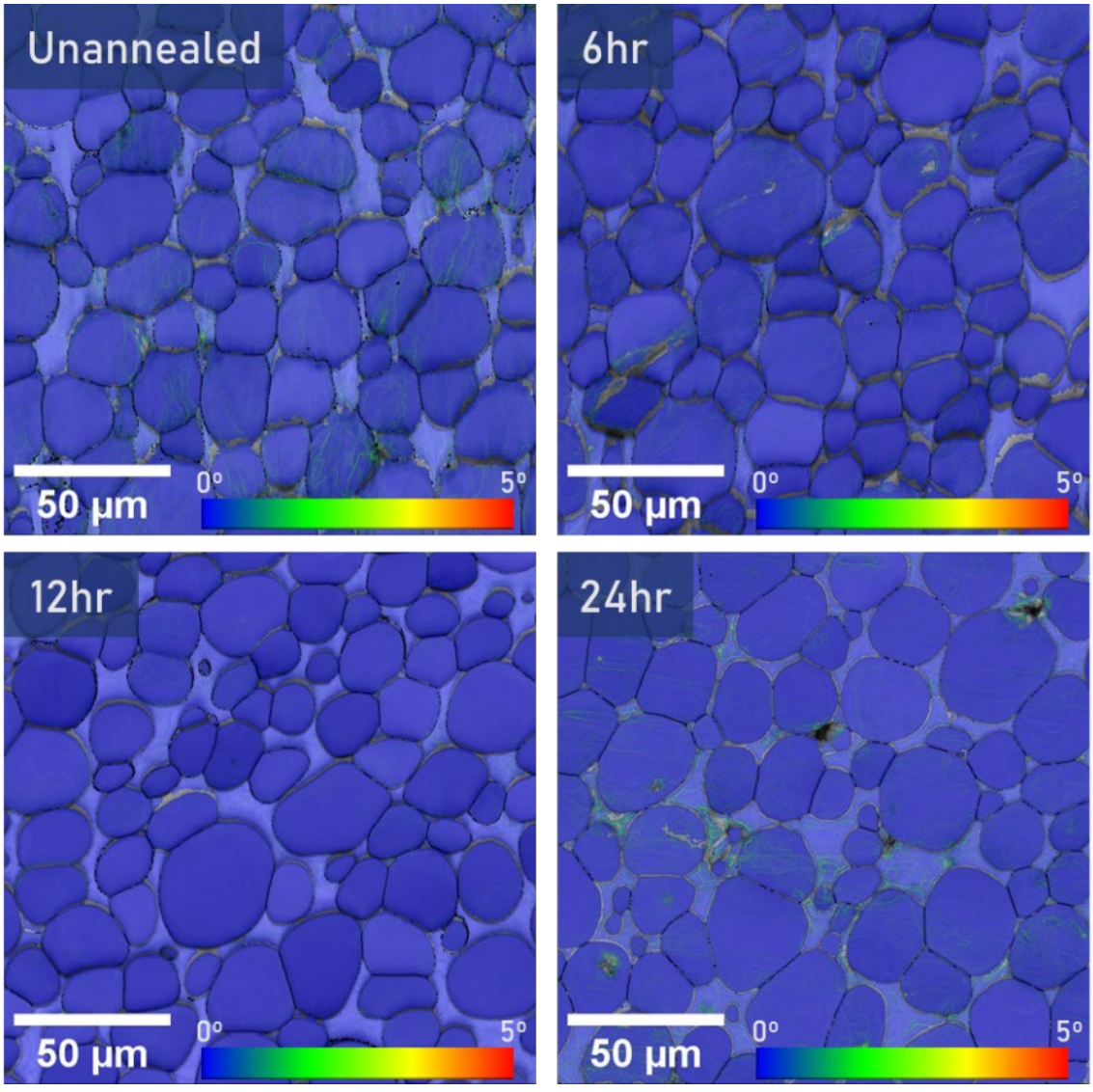

Figure 17. The KAM maps of all 90W-0R annealing conditions.

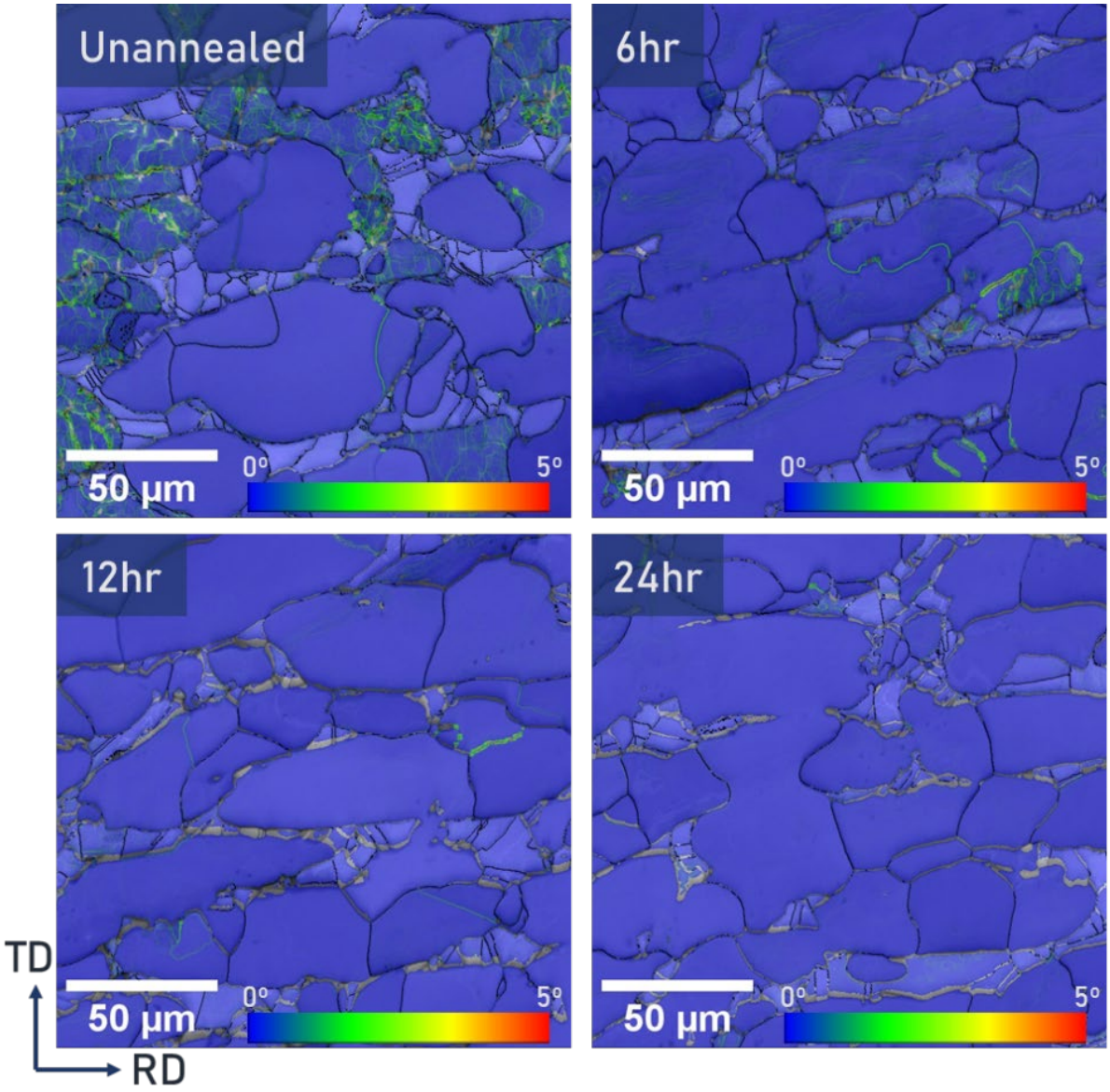

Figure 18. The KAM maps of all 90W-86R annealing conditions.

Future Work

The following activities are being planned to be performed:

- Perform additional tensile testing of 1300°C annealed samples for the 90W-0R 6 hr. and 90W-86R 12 hr. to get better statistics and determine the final optimum annealing time.
- Perform elevated temperature (590°C, 880°C and higher) tensile testing on annealed (as sintered and hot rolled) samples.
- Perform additional hot rolling to fabricate fracture toughness samples.
- Perform room and elevated temperature toughness testing of annealed (as sintered and hot rolled) samples.

Acknowledgments

The authors would like to acknowledge the support of Mark Rhodes for performing hot rolling of 90W WHA samples and coordinating the annealing and degassing operations. This research was supported by the U.S. Department of Energy (US DOE), Office of Science, Office of Fusion Energy Sciences, through Contract No. AT2030110-13784 and was performed at the PNNL, which is operated by Battelle for the US DOE under Contract No. DE-AC05-76RL0-1830.

References

[1.] S. Wurster, et al., *Recent progress in R&D on tungsten alloys for divertor structural and plasma facing materials.* Journal of Nuclear Materials, 442 (1-3): p. S181-S189, 2013.

[2.] D. Stork, et al., *Developing structural, high-heat flux and plasma facing materials for a near-term DEMO fusion power plant: the EU assessment.* Journal of Nuclear Materials, 455(1-3): p. 277-291, 2014.

[3.] A. Hasegawa, et al., *Neutron irradiation effects on the microstructural development of tungsten and tungsten alloys.* Journal of Nuclear Materials, 471: p. 175-183, 2016.

[4.] R. Neu, et al., *Investigations on tungsten heavy alloys for use as plasma facing material,* Fusion Eng. Des. 124 (2017) 450–454.

[5.] R. Neu, et al., *Results on the use of tungsten heavy alloys in the divertor of ASDEX Upgrade*, J. Nucl. Mater. 511 (2018) 567–573.

[6.] M. Alam, et al., *The effect of hot rolling on the strength and fracture toughness of 90W-7Ni3Fe tungsten heavy metal alloys*, Materials Science & Engineering A 824, 141738, 2021.

[7.] G.M. Wright, et al., *Comparison of tungsten nano-tendrils grown in Alcator C-Mod and linear plasma devices*, J. Nucl. Mater. 438 (2013) S84–S89.

[8.] D. Dasgupta, et al., *Prediction of temperature range for the onset of fuzz formation in helium-plasma-implanted tungsten*, Surf. Sci. 698 (2020) 121614.

[9.] Q. Yang, et al., *Nanostructured fuzz growth on tungsten under low-energy and high-flux He irradiation*, Sci. Rep. 5 (2015) 1–9.

[10.] X. Gong, et al., *Effect of tungsten content on microstructure and quasi-static tensile fracture characteristics of rapidly hot extruded W-Ni-Fe alloys*, Int. J. Refract. Metals Hard Mater. 30 (2012) 71–77.

[11.] X. Gong, et al., *Microstructure and highly enhanced mechanical properties of fine-grained tungsten heavy alloy after one-pass rapid hot extrusion,* Mater. Sci. Eng. 528 (2011) 3646–3652.

[12.] Z.S. Levin, K. Ted Hartwig, *Hardness and microstructure of tungsten heavy alloy subjected to severe plastic deformation and post-processing heat treatment*, Mater. Sci. Eng. 635 (2015) 94–101.

[13.] Y. Yang, et al., *Microstructure and mechanical properties of a hothydrostatically extruded 93W-4.9Ni-2.1Fe alloy*, Mater. Sci. Eng. 435–436 (2006) 620–624.

[14.] Y. Yu, H. Hu, et al., *Microstructure evolution and recrystallization after annealing of tungsten heavy alloy subjected to severe plastic deformation*, J. Alloys Compd. 685 (2016) 971–977.

[15.] Y. Yu, et al., *Effect of heat treatment on microstructure and mechanical properties of hot-hydrostatically extruded 93W-4.9Ni-2.1Fe alloy*, J. Alloys Compd. 622 (2015) 880–884.

[16.] Z.H. Zhang, et al., *Deformation characteristics of the 93W-4.9Ni-2.1Fe tungsten heavy alloy deformed by hydrostatic extrusion*, Mater. Sci. Eng. 435–436 (2006) 632–637.

[17.] C. Henager Jr., et al., *Ductile-phase toughened tungsten for plasma-facing materials in fusion reactors*, Int. J. Powder Metall. 53 (2017) 53–69.

[18.] B.N. Nguyen, et al., *Tailoring ductile-phase toughened tungsten hierarchical microstructures for plasma-facing materials*, J. Nucl. Mater. 540 (2020) 152382.

[19.] R.M. German, L.L. Bourguignon, Powder Met. Def. Technol., 6 (1984), pp. 117-131

[20.] M. Li, et al., *Impact of heat treatment on tensile properties of 97W-2Ni-1Fe heavy alloy*, *Journal of Nuclear Materials*, Volume 512, 15 December 2018, Pages 1-7.

[21.] M.E. Alam, G.R. Odette, *Improving the fracture toughness and ductility of liquid-phase sintered WNiFe tungsten heavy alloys by high-temperature annealing*. Materials (Basel). 2023 Jan 18;16(3):916.

[22.] J. Wang, et al., *Tensile testing and microstructural characterization of ductile phase toughened W-NiFe alloys*, in Fusion materials Semiannual Progress Report for the Period Ending June 30, 2020. 2020.
[23.] J. Wang, et al., *Microstructural characterization and mechanical testing of ductile-phase toughened tungsten*, in Fusion materials Semiannual Progress Report for the Period Ending December 31, 2019. 2019.
[24.] J. Wang, et al., *Microstructure-Mechanical Property Correlation in Ductile Phase Toughened W-NiFe Heavy Alloy*, in Fusion Materials Semiannual Progress Report for the Period Ending December 31 2020, D. Clark, Editor. 2020.
[25.] R. Prabhakaran, et al., S*tatus of the elevated temperature mechanical test faciity, hot rolling and tensile testing at PNNL*, PNNL-SA-181771, Vol 73, Chapter 4, in Fusion Materials Semiannual Progress Report for Period Ending December 31, 2022, DOE/ER-0313/73, U.S. Department of Energy, 2023.
[26.] R. Prabhakaran, et al., *Status of the elevated temperature mechanical test facility setup at PNNL*, PNNL-SA-170069, In Fusion Materials Semiannual Progress Report for period ending December 31, 2021, DOE/ER-0313/71, US Department of Energy, 2022.
[27.] R. Prabhakaran, et al., "*Status of the elevated temperature mechanical test facility setup at PNNL*", PNNL-SA-176100, In Fusion Materials Semiannual Progress Report for Period Ending June 30, 2022, DOE/ER-0313/72, U.S. Department of Energy, 2022.
[28.] ASTM E8/E8M-21, Standard Test Methods for Tension Testing of Metallic Materials, ASTM International, West Conshohocken, PA, 2021.
[29.] M.E. Alam, G.R. Odette, *On the influence of specimen size and geometry on the fracture toughness of tungsten heavy metal alloys*. J. Nucl. Mater. 2022;571:154025.

4.9 PRECIPITATE FORMATION IN K-DOPED TUNGSTEN UNDER HFIR IRRADIATION—W. Zhong, T. Koyanagi (Oak Ridge National Laboratory)

OBJECTIVE

K-doped tungsten (W) was irradiated in High Flux Isotope Reactor (HFIR). The objective of this work is to investigate the neutron irradiation effects on the microstructure of K-doped W. The characterization on the irradiation induced precipitates is presented in this report. The results of this work will be used to identify the hydrogen trapping sites in irradiated K-doped W.

SUMMARY

K-doped W was irradiated in HFIR to 0.47 dpa at the nominal temperature of 1100°C. The transmutation elements (primarily Re and Os) form clusters and precipitates. Scanning transmission electron microscopy (STEM)/energy dispersive spectroscopy (EDS) and the high-resolution transmission electron microscopy (TEM) were used to identify the composition and the phase of Re/Os-rich precipitates. Such precipitate exhibits Re-cloud and Os-core morphology, which were identified as χ phase. Two orientation relationships of the χ phase precipitates with W matrix were observed: $[110]_W||[110]_\chi$, $(002)_W||(006)_\chi$ and $[110]_W||[110]_\chi, (002)_W||(\bar{4}4\bar{2})_\chi$.

PROGRESS AND STATUS

K-doped W has demonstrated greater resistance against recrystallization than pure W. In this report, we present the characterization results on the irradiation induced precipitates in K-doped W, which was irradiated at the nominal temperature of 1100°C to 0.47 dpa in HFIR. The W under neutron irradiation transmutes to Re and Os, which often form clusters and precipitates at the concentrations below their equilibrium solubility.

Figure 1 shows the STEM high angle annular dark field (HAADF) image and Re and Os EDS maps of the same region in the irradiated K-doped W. A grain boundary is captured in this TEM foil, which shows Re and Os segregation. In addition, precipitates were observed, and they have Os-core and Re-cloud morphology.

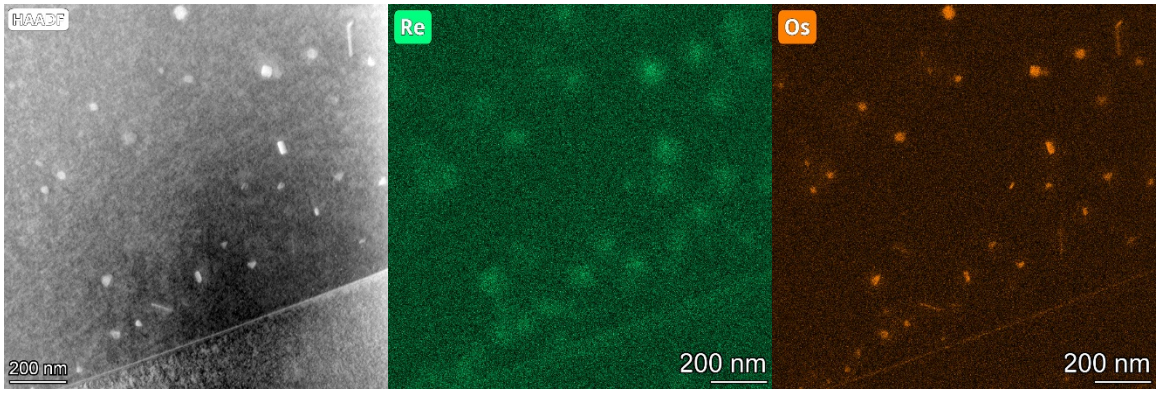

Figure 1. (Left) HAADF images and (middle) Re and (right) Os EDS maps of K-doped W irraidated at 1100°C to 0.47 dpa.

To identify the phase of these principates, the TEM sample was tilted to the W [110] zone, and the diffraction pattern is shown in Figure 2a. Other than the strong diffraction from the W matrix, weak satellite diffraction

spots were observed. Dark field images shown in Figure 2b show that these weak diffraction spots are from the Re/Os-rich precipitates.

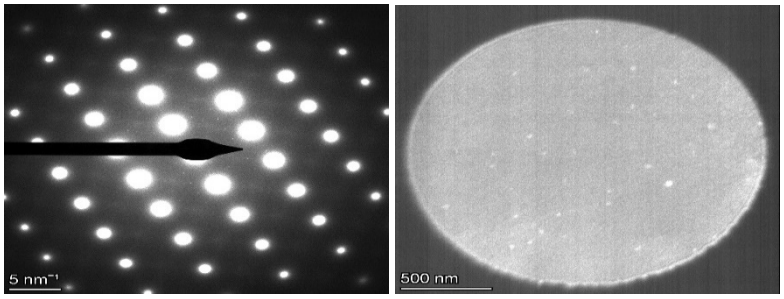

Figure 2. (Left) diffraction pattern of W on the [110] zone, and (right) the dark filed TEM image showing the Re/Os-rich precipitates.

High resolution (HR) TEM images were taken on these Re/Os precipitates under the [110] zone of W matrix. Examples of precipitate HRTEM images are shown in Figure 3a and 3d. The results reveal that these Re/Os-rich precipitates are of the same phase but with different orientation. Fast Fourier Transform (FFT) images of these two HRTEM images are shown in Figure 3b and 3e respectively, and both of them match the pattern of χ phase under the [110] zone. These precipitates have a different orientation relationship with the matrix: $[110]_W||[110]_\chi$, $(002)_W||(006)_\chi$ and $[110]_W||[110]_\chi, (002)_W||(\bar{4}4\bar{2})_\chi$ for precipitates in Figure 3a and 3d respectively. Simulated patterns of such an orientation relationship for precipitates and the matrix are shown in Figure 3c and 3f.

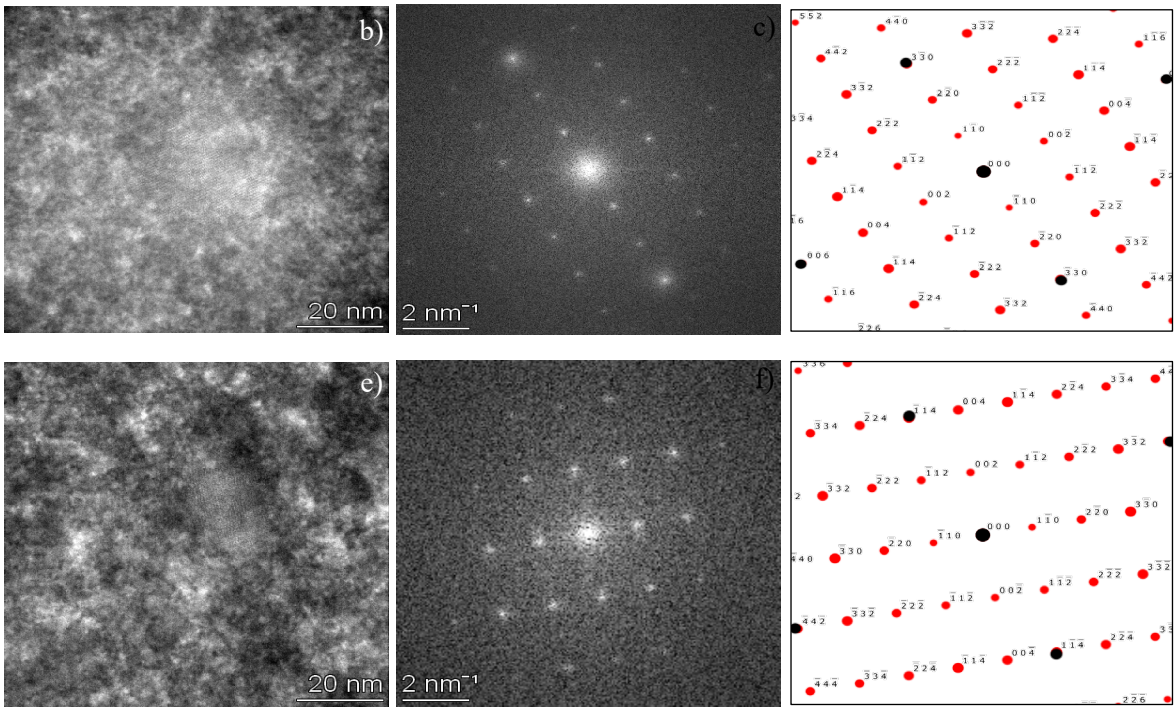

Figure 3. (a,d) High resolution TEM image on two Re/Os-rich precipitates. The FFT of a) and d) are shown in b) and e) respectively, which indicates the orientation relationship as $[110]_W||[110]_\chi$, $(002)_W||(006)_\chi$ and $[110]_W||[110]_\chi, (002)_W||(\bar{4}4\bar{2})_\chi$ for W matrix and χ phase precipitates. Simulated patterns of such relationship are shown in c) and f).

Future Work

Hydrogen retention and desorption experiments will be performed on irradiated W, and the results of TEM will be used to identify hydrogen trapping sites.

5. ADVANCED MANUFACTURING

No contributions this reporting period.

6. EFFECTS OF IRRADIATION

6.1 INVESTIGATION OF HIGH TEMPERATURE HELIUM EMBRITTLEMENT (HTHE) EFFECTS IN NICKEL-BASED AND IRON-BASED ALLOYS—

Z. Qi, S. Zinkle (University of Tennessee)

OBJECTIVE

The objective of this project is to study how tensile stress, He implantation rate, He concentration and different matrix microstructures affect high temperature helium embrittlement (HTHE) behaviour by characterizing cavity size and number density in the matrix and at grain boundaries (GBs) in nickel-based and iron-based alloys after different He implantation conditions.

SUMMARY

An innovative specimen fixture was designed to provide tensile stress 0-200 MPa during He implantations. Transmission electron microscopy/scanning transmission electron microscopy (TEM/STEM) images were obtained to characterize cavity size and density in matrix and at GBs after 4.5 MeV He^{2+} irradiations to 200 appm and 1800 appm peak implanted He concentrations at 750°C with zero and 100MPa stress in Haynes 244 SHT (solution annealed), Haynes 244 STD (standard aging), 316L stainless steel (SS) and Fe-9%Cr. Most matrix cavities were observed at matrix-defect interfaces. High matrix sink strength of Haynes 244 STD enhanced cavity nucleation and trapped He from diffusion to GBs. Fe-9%Cr was more HTHE resistant than 316L SS. No obvious implantation rate and stress effects were observed, which might be because no He-vacancy clusters diffused to GBs. Larger cavities were observed while density remained unchanged for 1800 appm He compared to 200 appm He. No voids were observed in all the alloys.

PROGRESS AND STATUS

Among the five main radiation effects in materials, HTHE is dominant when the temperature exceeds $0.5T_m$, where T_m is the melting point of the materials, and when the He concentration exceeds 10-100 appm. For fusion and Gen IV reactor concepts operating at high temperatures and doses, HTHE can cause loss of ductility and reduced creep rupture lifetime, which might be the lifetime limiting mechanism for structural materials at elevated temperatures. The HTHE is attributed to accelerated intergranular fracture associated with formation of large grain boundary cavities when stress is applied during, He generation. However, only limited understanding exists on HTHE mechanisms.

In this context, an innovative specimen fixture was designed to passively provide tensile stress from zero to ~200 MPa during 4.5 MeV He irradiations on 316L SS, Fe-9Cr, Haynes 244_SHT and Haynes 244_STD at 750°C or five different conditions of different stresses, He implantation rate and He concentrations. The detailed information of the specimen fixture could be found in [1]. The five He implantation conditions are shown in Table 1. The dose and He concentration profile calculated by Stopping and Range of Ions in Matter (SRIM) full cascades using damage energy method are shown in Figure 1. The detailed information about the four alloys used is shown in Table 2. The size and number density of cavities (matrix and grain boundary) were characterized by TEM to study cavity behaviour versus different implantation conditions and different matrix microstructures.

Table 1. Irradiation matrix of the alloys

Target holder	Material	Ion Species	Initial stress (MPa)	Fluence (ions/cm^2)	Flux (ions/cm^{2}s)	Temp. °C
#1	Haynes 244_SHT, Haynes 244_STD, Fe-9%Cr, and 316L SS	4.5 MeV He	0	6.8×10^{14} (200 appm)	2.36×10^{10} (25 appm/h)	750
#2			100			
#3			100		2.36×10^{11} (250 appm/h)	
#4			0	6.12×10^{15} (1800 appm)	9.44×10^{10} (100 appm/h)	
#5			100			

Table 2. Detailed information about the alloys

Material	Crystal structure	Grain size (μm)	Main chemical composition	Matrix			GB ppts
				Dislocations	Precipitates	Sink strength	
Haynes 244_SHT	FCC	150	Ni-22.5% Mo, 8% Cr, 6% W	/	/	~0	Carbides (~150 nm)
Haynes 244_STD	FCC	40		High density (~3e10/cm^2)	High density Ni_2(Mo,Cr) ppts (~3e15/cm^3, ~40 nm)	~1e15 /m^2	Carbides (~250 nm)
316L SS	FCC	40	Fe-17% Cr, 10% Ni, 2% Mo	Low density (~3e9/cm^2)	Low density ppts (~2e13/cm^3, ~60 nm)	~4e13 /m^2	/
Fe-9%Cr	BCC	100	Fe-9% Cr, 0.1% Mn	Low density (~6e9/cm^2)	Low density ppts (~4e13/cm^3, ~40 nm)	~7e13 /m^2	/

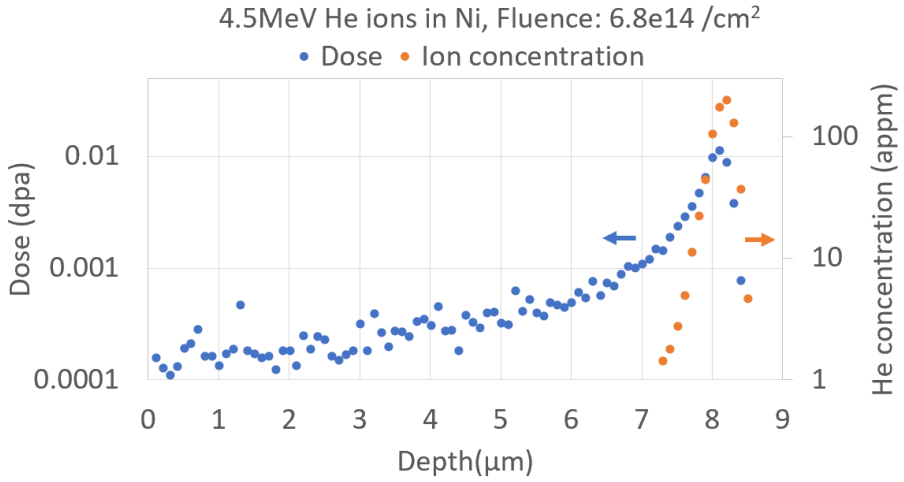

Figure 1. Dose and He concentration profile calculated by SRIM for 4.5 MeV He ions in Ni with the fluence of 6.8×10^{14}/cm^2.

During He implantation, stress relaxation from thermal and irradiation creep can take place due to the strain constraint effect from the substrate under the irradiated layer. The stress evolution versus time is shown in Figure 2. The initial tensile stress could relax by ~45% for He implantations #1 and #2, ~20% for He implantation #3, and ~55% for He implantations #4 and #5 over the course of the implantations, where thermal creep dominates the stress relaxation compared to irradiation creep. The average stresses were calculated to be 65 MPa for #1 and #2, 88 MPa for #3, and 56.5 MPa for #4 and #5.

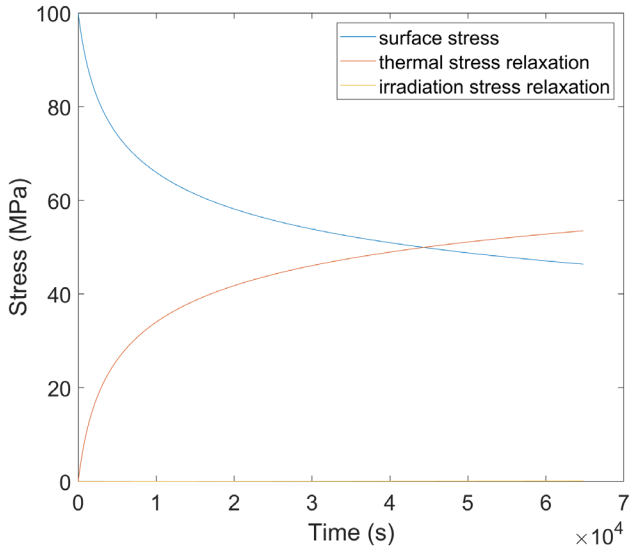

Figure 2. Residual surface stress and stress relaxation by thermal and irradiation creep versus time at 750°C.

The TEM/STEM images for cavities in matrix and at grain boundaries in the four alloys in the He-implanted region for five different He implantation conditions are shown in Figure 3 and Figure 4. Most matrix cavities were observed to be at matrix-defect interfaces, such as at dislocation lines for Haynes 244 STD, and at precipitates for 316L SS and Fe-9%Cr. The corresponding average cavity size and number density values are shown in Figure 5 (a-d) and Figure 6. Comparing four different alloys, Haynes 244 STD had highest number density and lowest size of matrix cavities, while it had low number density and low size of GB cavities. This indicates that the high matrix sink strength of Haynes 244 STD enhanced matrix cavity nucleation and trapped He, thereby inhibiting He-vacancy cluster diffusion to GBs. Comparing 316L SS and Fe-9%Cr, Fe-9%Cr had higher number density and smaller size of cavities for both matrix and GB than 316L SS, revealing that BCC is more resistant against HTHE than FCC, which might be due to the differences in vacancy self-diffusion energies or other possible reasons.

For implantation conditions #1-#3, there was no obvious difference for cavity size and number density in matrix and at GBs for all four alloys, showing that the cavity behavior is not sensitive to He implantation rate and stress, which is contradictory to the literature results that higher He production rate and lower stress should result in higher creep rupture time and strain [2, 3]. The contradiction might be because no He-vacancy clusters diffused to GBs in our experimental conditions, which might also be the case for #4 and #5. Comparing implantation conditions #1/#2 and #4/#5, the cavity sizes were about three times larger, however, there was no obvious change for cavity number density in matrix and at GBs.

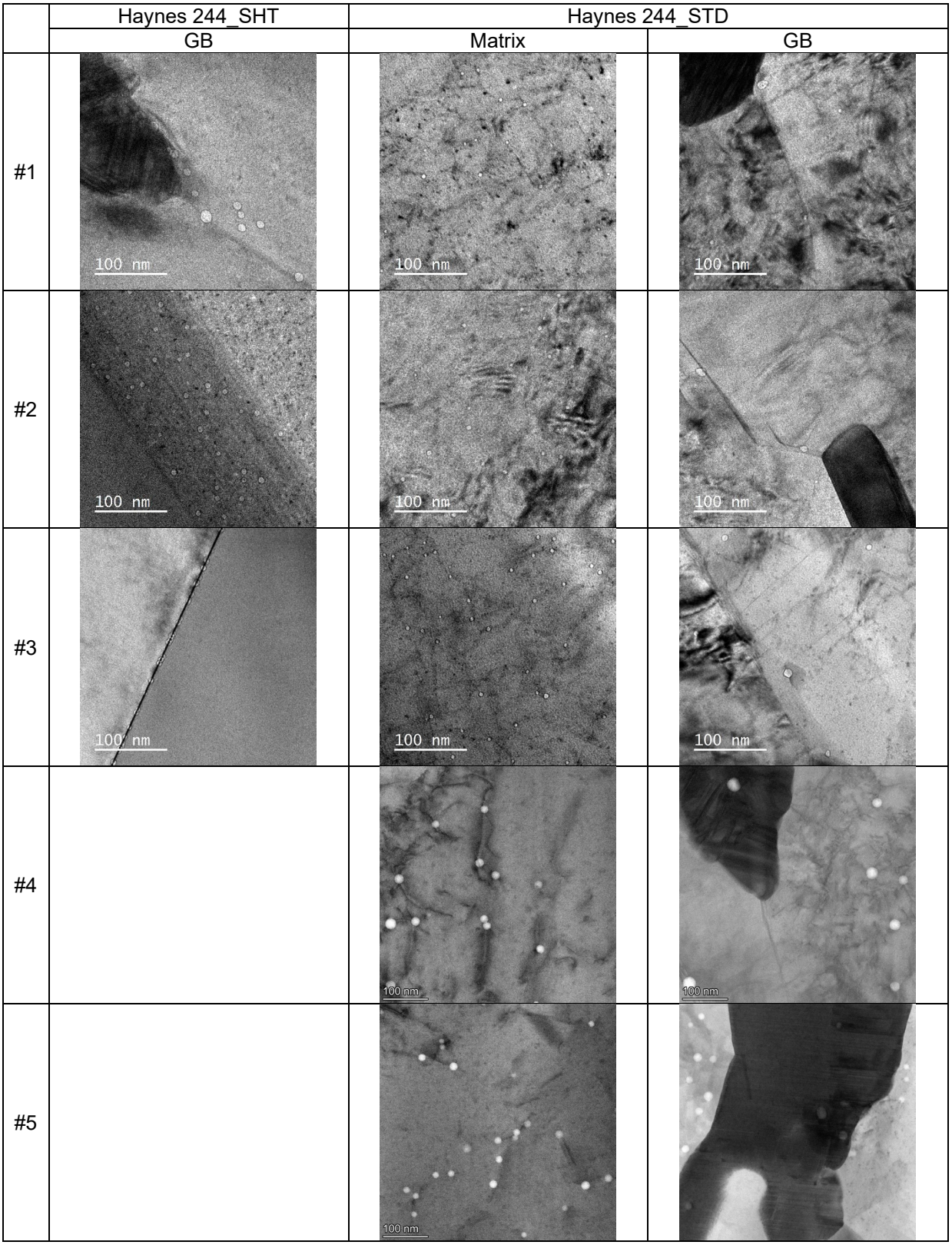

Figure 3. The TEM/STEM images of cavities in matrix and at GB in two Ni alloys for five different implantation conditions.

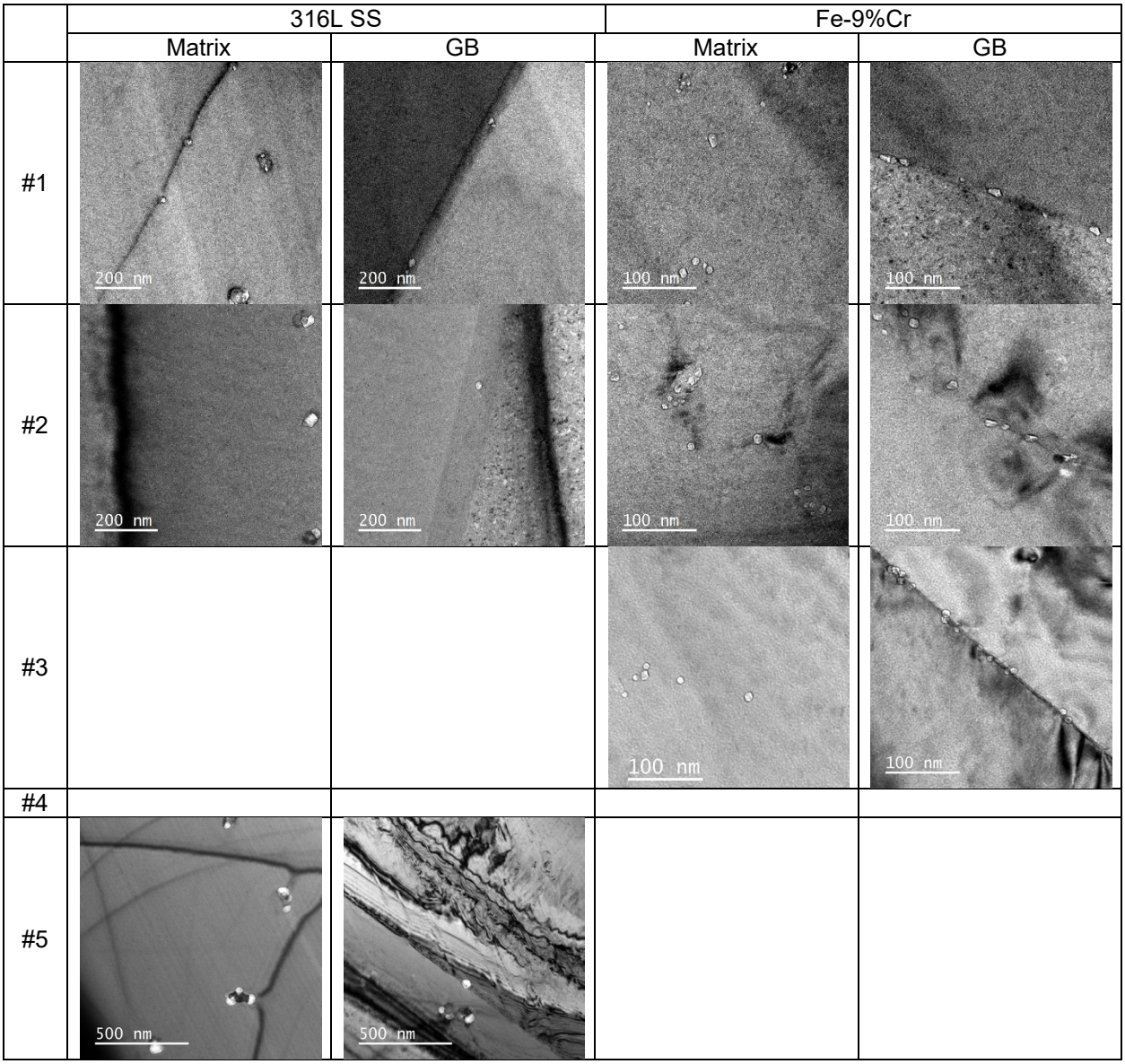

Figure 4. The TEM/STEM images of cavities in matrix and at GB in two Fe alloys for five different implantation conditions.

In Figure 7, the average size and number density of matrix cavities in all the alloys are plotted with the calculated equilibrium cavity curves for different stresses. Figure 7(a) shows the results for #1-#3 with the calculated curves for 0, 65 and 88MPa stress by using 100 appm average He concentration. Figure 7(b) shows the results for #4-#5 with the calculated curves for 0 and 56.5MPa stress by using 900 appm average He concentration. During calculation, the MLB equation was used as the equation of state for He, and 1J/m^2 surface energy was used. All the experimental data were below the equilibrium cavity curves, revealing that no voids were observed in all the alloys.

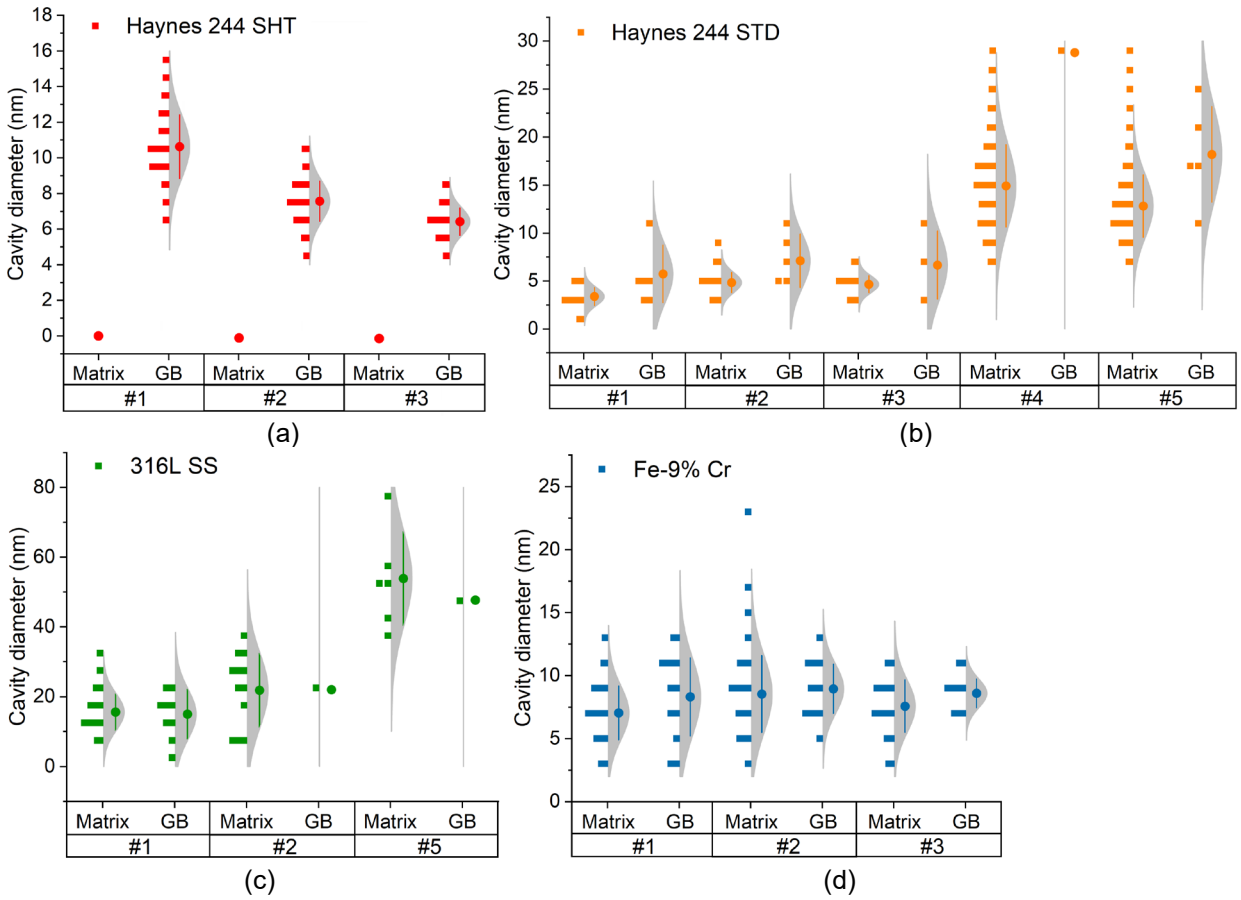

Figure 5. Size distributions with average sizes of cavities in matrix and at GB for five different implantation conditions in: (a) Haynes 244 SHT; (b) Haynes 244 STD; (c) 316L SS; (d) Fe-9%Cr.

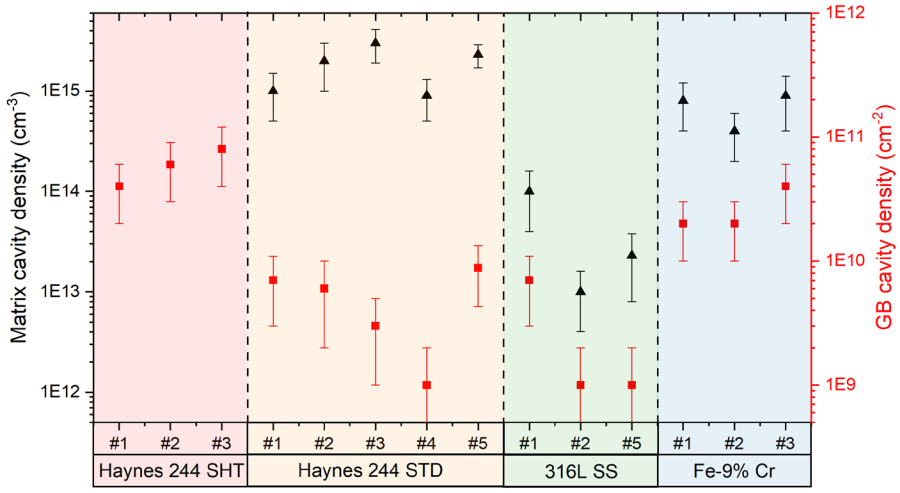

Figure 6. Number density of cavities in matrix and at GB in four Ni and Fe alloys for five different implantation conditions.

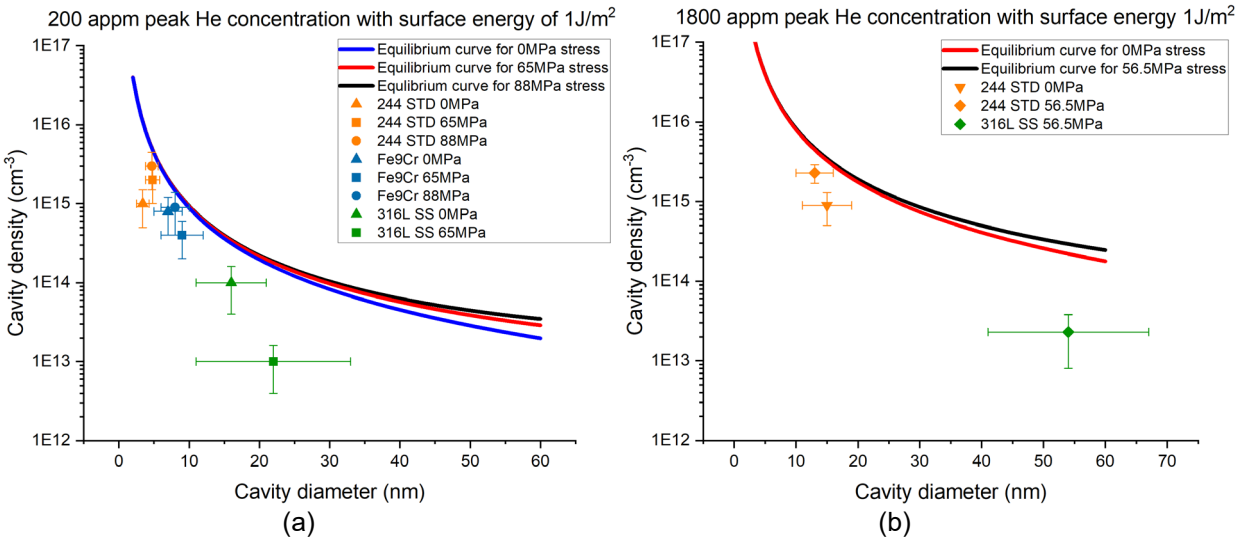

Figure 7. Average size and number density of matrix cavities in all the alloys for: (a) implantation conditions #1-#3 with equilibrium cavity curves calculated for 0, 65 and 88 MPa stress by using 100 appm average He concentration and 1J/m^2 surface energy; (b) implantation conditions #4-#5 with equilibrium cavity curves calculated for 0 and 56.5MPa stress by using 900 appm average He concentration and 1J/m^2 surface energy.

Future Work

We will finish characterizing the samples for all the implantation conditions in the next reporting period. Since no stress effect on grain boundary cavitation was observed in our experimental conditions, we suspect that dislocation lines (i.e., moderate plastic deformation) may be needed for He-vacancy clusters to diffuse to GBs. Significant network dislocations would be created during creep tests, which would explain the pronounced HTHE behaviour during historic creep testing during He implantation. However, our method of providing stress is in the stress relaxation (elastic stress) condition rather than the plastic deformation creep condition. Therefore, we will introduce pronounced dislocation densities by plastic deformation prior to He implantations in the future work to test this hypothesis.

References

[1] Z. Qi, S.J. Zinkle, Investigation of High Temperature He Embrittlement Effects in Nickel-based and Iron-based alloys, Fusion Materials Semiannual Progress Report for the Period Ending December 31, 2022, Oak Ridge National Laboratory, pp. 85-92.

[2] H. Ullmaier, The influence of helium on the bulk properties of fusion reactor structural materials, Nuclear Fusion 24(8) (1984) 1039.

[3] H. Schroeder, P. Batfalsky, The dependence of the high temperature mechanical properties of austenitic stainless steels on implanted helium, Journal of Nuclear Materials 117 (1983) 287-294.

7. PLASMA MATERIAL INTERACTIONS

7.1 THERMODYNAMIC ANALYSIS FOR THE SELECTIVE LASER SINTERING OF SiC—B. Lamm, T. Koyanagi (Oak Ridge National Laboratory)

OBJECTIVE

Use thermodynamic calculations to predict the likely behavior of SiC under selective laser sintering (SLS)-based additive manufacturing for fusion reactor structural applications.

SUMMARY

Thermodynamic equilibrium calculations were made to predict the behavior of SiC at various temperatures and pressures. The resulting phase diagram was analyzed to understand the species likely to be present under laser irradiation during the SLS advanced manufacturing process. An appropriate temperature-pressure window was identified to form an incongruent melt from SiC while minimizing vaporization of material.

Results

Process optimization of SLS process for SiC requires understanding of phase evolution during the densification process. The target microstructure for irradiation resistance and good high-temperature mechanical properties is high-purity SiC with minimal secondary phases. Commercial databases were used to perform a calculation of phase diagrams (CALPHAD) analysis of SiC over a range of pressures and temperatures (Figure 1). During the SLS process, laser irradiation is used to heat a small area of printed material to melt and/or sinter the material selectively. From the calculated SiC phase diagram, it was observed that SiC remains solid at 1 atm until heated to 2823°C. Above this temperature, a liquid melt forms composed of liquid silicon and solid carbon. This incongruent melt transition temperature is constant with pressure down to ~0.8 atm and up to at least 30 atm (the highest pressure simulated in this study). Melt point depression has been observed at extreme pressures (~10 GPa or ~0.1 Matm) but remains >2000°C to 60 GPa (0.6 Matm)[1]. At 1 atm, increasing temperature to 2868°C fully vaporizes silicon, forming a carbon + gas composition. The chamber pressure during SLS is assumed to be approximately 1 atm, however the laser and vapor formed under laser irradiation can exert extreme pressures [2]. The composition of the gas was calculated to be fairly consistent regardless of temperature or pressure. The primary constituent (~50 mol%) was SiC_2, followed by either Si_2C or Si, where both compounds could range from 20-25 mol%. As temperature increases, the amount of Si increases, decreasing the amount of Si_2C present. The remainder of the gas consists of oligomers of Si or C, all at ≤2 mol%. By 2879°C (phase line labeled ‘graphite’), all solid species have volatilized.

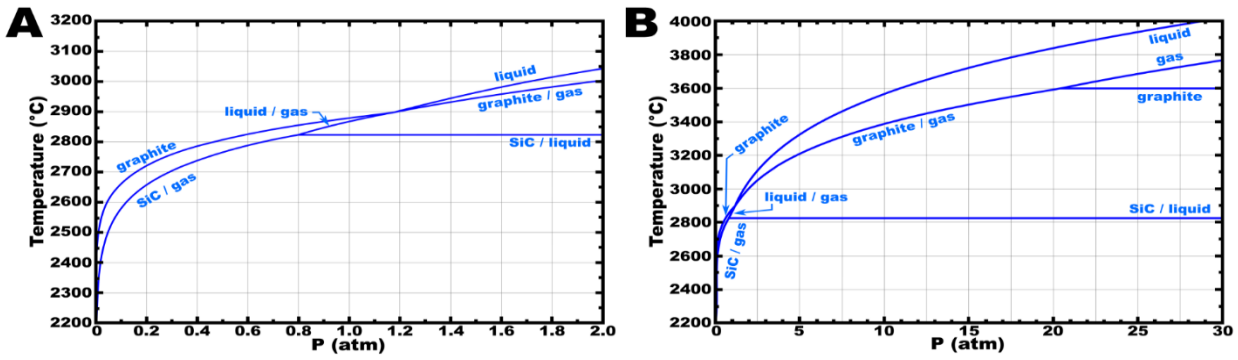

Figure 1. Temperature-pressure phase diagram for the Si-C binary at Si/(Si+C) of 0.5. The diagrams span (A) temperature T = 2200-3200°C and pressure P = 0-2 atm; (B) T = 2200-4000°C and P = 0-30 atm.

Decreasing pressure to <0.8 atm eliminates the liquid phase region, indicating that silicon is vaporized at the phase line labeled “SiC / gas” leaving solid graphite until temperatures increase to the “graphite” phase line. As a liquid phase is required for any particle solidification process to occur, it is not recommended that SLS of SiC be performed at reduced pressures. Increasing pressures to >1 atm increases the temperature range where the incongruent Si/C melt exists (bounded by the “SiC / liquid” and “graphite / gas” phase lines), so positive-pressure SLS of SiC might be advantageous.

It should also be noted that cooling rates will be important to control the phases present after laser irradiation. Sufficiently slow cooling rates could reproduce SiC by condensation of the Si/C incongruent melt; however, rapid cooling would kinetically trap the melt as solid Si and solid C.

Future Work

A manuscript on the SLS process of SiC will be submitted for publication. Further work will explore ways to monitor the surface temperature and pressure, as well as ways to densify the final part while preserving the phase-purity of SiC.

References

[1.] Daviau, K.; Lee, K., High-Pressure, High-Temperature Behavior of Silicon Carbide: A Review. *Crystals* 2018, *8* (5).

[2.] Juodkazis, S.; Nishimura, K.; Tanaka, S.; Misawa, H.; Gamaly, E. G.; Luther-Davies, B.; Hallo, L.; Nicolai, P.; Tikhonchuk, V. T., Laser-induced microexplosion confined in the bulk of a sapphire crystal: evidence of multimegabar pressures. *Phys Rev Lett* 2006**,** *96* (16), 166101.

8. CORROSION AND COMPATIBILITY IN FUSION SYSTEMS

8.1 FUSION CORROSION AND COMPATIBILITY SCIENCE STUDY OF MASS TRANSFER KINETICS BETWEEN SiC AND PRE-OXIDIZED FeCrAl AND PRE-OXIDIZED AND ALUMINIZED F82H IN FLOWING PbLi—M. Romedenne, C. De Lamater-Brotherton, B. Pint (Oak Ridge National Laboratory), Y. Zhang (Tennessee Technological University)

OBJECTIVE

This goal is to move compatibility testing in flowing PbLi towards more realistic blanket materials and temperatures. The first thermal convection loop (TCL) experiment with a peak temperature of 700°C showed a strong dissimilar materials interaction between SiC and bare FeCrAl. The second and now third TCLs reduced the peak temperature to 650°C and included aluminized F82H (Fe-8Cr-2W) specimens for 1000 and 2000 h to study reactions kinetics. The experiment began in early June and will complete 2000 h in early September 2023.

Experimental Procedure

Materials

Thermal convection loop and materials

The TCL (number 7 of a series of TCLs) (Figure 1) is operating at a peak temperature of 650°C (top of the hot leg) and at a minimum temperature of 550°C (bottom of the cold leg) and was made of pre-oxidized (8 h in air at 1050°C) APMT. The TCL contains pre-oxidized (2h at 800°C in air) APMT coupons and bare high purity chemical vapor deposited (CVD) SiC-SiC specimens. The alloy compositions (loop and specimens) are reported in Table 1. The specimens will be exposed for 2000 h in the TCL filled with 10 kg of flowing liquid eutectic PbLi provided by GMH Stachow-Metall GmbH (analyzed composition in Table 2). A total of 12 CVD SiC coupons and 4 APMT coupons are being exposed in the TCL. Aluminized F82H coupons (10) and tensile specimens (14) are also being exposed. The F82H specimens were aluminized using pack cementation for 30 min at 1050°C in a pack containing 20wt.% Cr-10wt.%Al powder, 2% NH_4Cl activator and 78% Al_2O_3 filler. After coating, the specimens were pre-oxidized for 2h at 800°C in air to form an alumina layer prior to PbLi exposure. The APMT coupons were pre-oxidized for 2h at 1000°C.

Figure 1. Picture of the operating TCL#7.

Table 1. Alloy compositions measured using inductively coupled plasma and combustion analyses in wt.%

Alloy	Fe	Cr	Al	Ni	Si	C	Others
APMT	69.0	21.6	4.9	0.12	0.53	0.03	2.8Mo, 0.1Mn, 0.2Hf, 0.1Y, 0.1Zr
APMT tube*	70.0	21.4	4.9	-	0.34	0.04	3.1Mo, 0.2Mn, 0.02Cu
F82H	88.9	8.1	0.02	0.06	0.08	0.10	1.8W, 0.45Mn, 0.20V, 0.09Ta, 0.01N
CVD SiC	-	-	-	0.01	69.8	30.2	0.003O

*reported by manufacturer [11]

Table 2. As-received PbLi composition measured using inductively coupled plasma and combustion analyses in at.%

Pb	Li	C	H	O	N
80.62	15.05	0.42	2.02	1.90	<0.01

Results

During the test, six thermowells at the top, middle, and bottom of each leg are used to estimate each specimen temperature, and the peak temperature of 650°C±1°C was controlled using the thermocouple located at the top of the hot leg. During operation, temperatures were measured by thermocouples in the six thermowells at the top, middle and bottom of the hot and cold legs (Figure 2). The TCL experiment is still in progress and is expected to end on the first week of September.

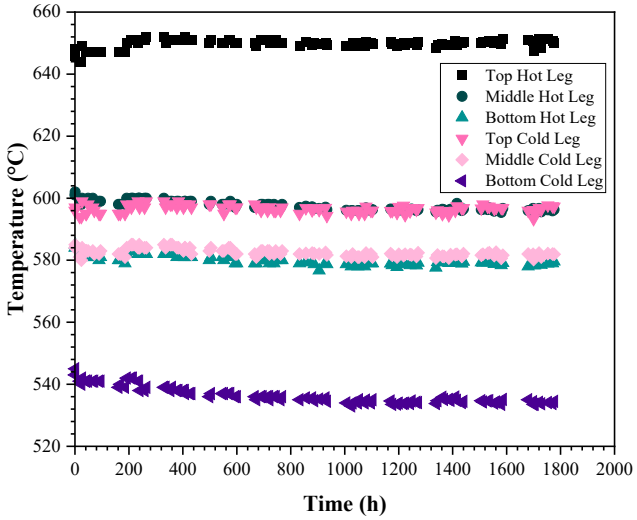

Figure 2. Measured temperatures around the TCL as a function of experiment time (Experiment in progress).

Conference Presentations

Initial results will be presented at an oral presentation at the International Symposium on Fusion Nuclear Technology (ISFNT) in September 2023 and more complete results at an invited talk at the International Conference on Fusion Reactor Materials (ICFRM) in October 2023.

Publication

M. Romedenne, Y. Zhang, Y.-F. Su, B. A. Pint, “Evaluation of the interaction between SiC, pre-oxidized FeCrAlMo with aluminized and pre-oxidized Fe-8Cr-2W in flowing PbLi,” Journal of Nuclear Materials 581 (2023) 154465.

9. MODELING AND COMPUTATIONAL STUDIES

9.1 HIGH-TEMPERATURE MOBILITY OF TUNGSTEN GRAIN BOUNDARIES—A. Qiu, T. Frolov, R. Rudd (Lawrence Livermore National Laboratory)

OBJECTIVE

The objective of this study is to assess the effect of hydrogen isotopes on mechanical properties of tungsten relevant to first-wall applications in a tokamak. We report progress on calculation of the mobility of tungsten grain boundaries at high temperature, a key property in the process of recrystallization. In prior work we studied tungsten grain boundary properties such as the energies of boundaries with various orientations and misorientations, including energies of grain boundary phases that differ in structure from those at low temperature. We have calculated properties associated with the grain boundary mobility including the response of grain boundaries to applied shear stress. Here we report direct calculation of the motion of curved grain boundaries at high temperature using molecular dynamics. We compute how the mobility increases with temperature and how the mobility depends on the grain boundary misorientation. These calculations form baseline data to calculate the change when hydrogen or other defects are present.

PROGRESS AND STATUS

Magnetic fusion energy first-wall applications need materials with high melting temperature, mechanical strength at elevated temperatures, high thermal conductivity, acceptable activation levels upon exposure to radiation, and resistance to surface sputtering. The refractory metal tungsten possesses these qualities, but it exhibits undesirable recrystallization and embrittlement. Recrystallization involves the nucleation of stress-free grains and the motion of grain boundaries. The grain boundary motion is driven by the reduction of associated free energies as the grain boundary sweeps up lattice defects. Grain boundary structure affects how the boundary responds to those driving forces, as described by the mobility. Beyond just defects in a grain boundary, boundaries undergo structural changes due to grain boundary phase transitions [1]. The phase affects various properties including the grain boundary mobility.

Grain boundary structure has conventionally been thought to be uniquely determined by the boundary's orientation and misorientation, up to defect content which would raise its energy. Here the misorientation is the rotational relationship between the lattices in the two abutting grains, and the orientation refers to the angles at which the boundary slices through them. The understanding of the thermodynamics of grain boundaries has been based on that minimal characterization. Over the past decade computational work has predicted grain boundary phase transformations in which a grain boundary with fixed orientation and misorientation change's structure dramatically in a first order transformation [1]. That prediction has recently been observed in experiments using high-resolution transmission electron microscopy [2]. A grain boundary was frozen in mid-transformation. The experiments were able to resolve the atomic structure of the grain boundary, showing half of the boundary to be in the ground state structure and the other half in a high-temperature phase. The structures of both phases agreed with atomistic calculations.

Much of the initial work developing approaches to find grain boundary phases was done on face-centered cubic metals [3-6]. More recently, the mechanisms of grain boundary phase transformation in tungsten have been identified [7,8]. Tungsten is body-centered cubic. Grain boundary phase transformation progresses by nucleation and growth. Initial studies of the impact of these phase transformations on the grain boundary mobility showed that the effect could be significant, changing the shear-coupled mobility by a factor of 3 and even changing its sign. While ultimately it may be possible to catalog all the phases of every coincident-site-lattice (CSL) boundary and compute the associated mobilities, we do not have the process sufficiently automated and computationally efficient at this point. In the meantime, we have applied a different approach, one that calculates the grain boundary mobility at elevated temperature directly as driven by free energy reduction using a technique that simulates the motion of the curved boundary surrounding a cylindrical homo-phase inclusion in a single crystal matrix.

Specifically, we have applied molecular dynamics (MD) to predict the grain boundary mobility at high temperature through direct simulation of how fast grain boundaries move in response to driving forces.

The driving force is the rate of change of the free energy per unit of motion as the grain boundary moves. The grain boundary motion is over-damped. The kinetic energy of the grain boundary is not important. The energy that is released as the grain boundary moves down the potential energy gradient is dissipated into thermal energy. The proportionality constant between the grain boundary velocity and the driving force is a material property, the grain boundary mobility.

The MD simulations were carried out using the Large-scale Atomic/Molecular Massively Parallel Simulator (LAMMPS) code [9] with the Zhou potential for tungsten [10]. This potential has been used for MD simulation of tungsten at tokamak conditions previously [4-6]. Thermal equilibrium was imposed using a Langevin thermostat and the equations of motion were integrated using a time step of 2 fs. Using an approached based on that in Reference [11], the initial configuration was taken to be a cylindrical grain. Both the metal in the grain and the metal surrounding the grain were perfect single crystals, but the two crystals were out of alignment by a misorientation angle of 30°, as shown in first panel on the left in Figure 1. Additional simulations were carried out with a misorientation of 15°. The atoms in the grain boundary have a higher energy than the other atoms in the system, so the amount the energy exceeds that of the bcc single crystal is proportional to the grain boundary area. The energy decreases if the grain gets smaller, producing a force that drives grain shrinkage. The simulations included 214752 atoms and were run at 3000K or higher temperatures. Our goal is to study grain boundary mobility at elevated temperatures. These simulations are at temperatures even higher than tokamak operating temperatures to facilitate the grain boundary motion within the time span of these simulations.

Snapshots from a simulation of shrinkage of a grain with 30° misorientation are shown in Figure 1. The grain may be seen to shrink in size over time, as expected since the decreasing grain size reduces the grain boundary free energy. The shape of the boundary exhibits some fluctuations, indicating the grain boundary motion is thermally activated. The shape remains roughly cylindrical. There is little grain rotation at this point.

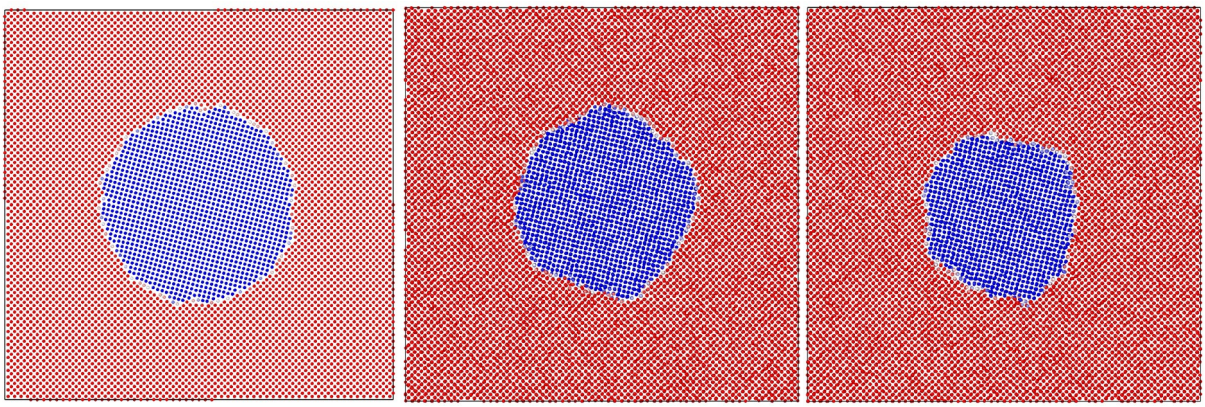

Figure 1. Grain shrinkage. A cylindrical tungsten grain is embedded in a single-crystal tungsten matrix at a 30° misorientation angle. Each dot represents an atom colored according to the local lattice orientation. The three panel are a sequence of snapshots as time increases in an MD simulation held in thermodynamic equilibrium at ambient pressure and a temperature of 3000K. The overall size of the embedded grain is shrinking over time, accompanied by fluctuations in the shape of the grain. The snapshots are from the times 0, 1 and 2 ns.

The grain shrinkage may be quantified through the cross-sectional area of the grain, as plotted in Figure 2. The figure shows the cross-sectional area as a function of time in simulations starting with the same grain with 30° misorientation but at different temperatures, ranging from 3000K to 3600K. The melting point of tungsten is 3700K. The grain may be seen to shrink more rapidly as the temperature increases. Starting from an initial diameter of ~ 13 nm, it takes 3.9 ns to shrink to half that size at 3000K, but only 0.1 ns at 3600K.

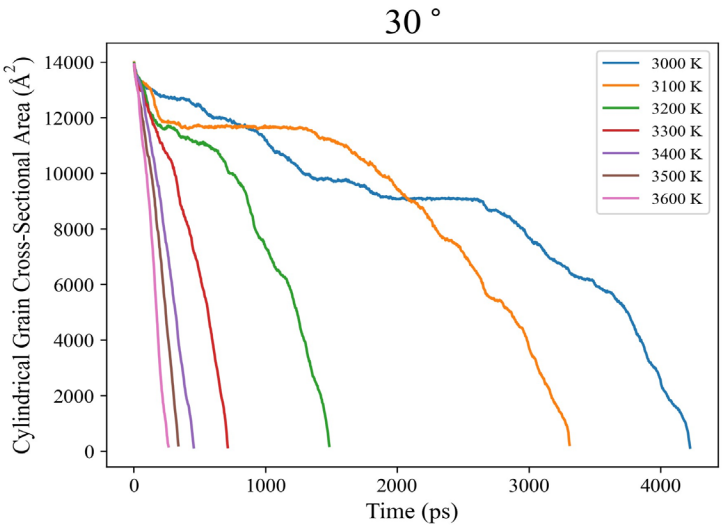

Figure 2. Grain cross-sectional area as a function of time at various temperatures. The evolution of an embedded grain during shrinkage is quantified by the cross-sectional area. This plot is the result of a series of simulations starting from the same grain misoriented by 30° in the matrix. The grain shrinkage rate increases dramatically as the temperature approaches the melting point of 3700K.

Similarly, the cross-sectional area as a function of time for a grain with 15° misorientation is plotted in Figure 3. Again, the grain shrinks more rapidly as the temperature increases. Starting from an initial diameter of ~ 13 nm, it takes 2.0 ns to shrink to half that size at 3000K, but only 0.3 ns at 3600K. This is faster than the shrinkage of the grain with 30° misorientation, but the temperature dependence is weaker. From these simulations of how the cross-sectional area decreases as a function of time, we can calculate the grain boundary mobility. We do not report the mobility values here since this work is on-going and it is best to see the overall trends before reporting final numbers, but the technique is working well.

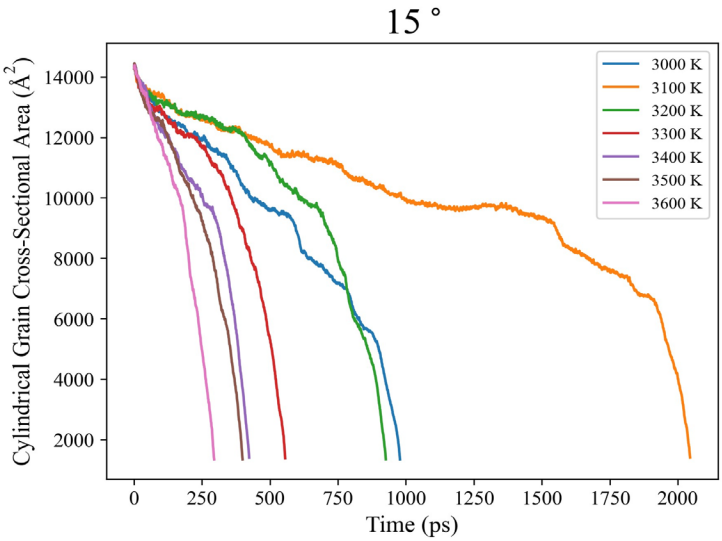

Figure 3. Grain cross-sectional area as a function of time at various temperatures. In this case the misorientation of the starting grain is less than in Figure 2: 15° here vs. 30° in there. Again, the grain shrinkage rate increases dramatically as the temperature approaches the melting point of 3700K. Overall, the shrinkage rate is faster for the lesser misorientation.

Future Work

The next topic to address is the mobilities of hydrogenated tungsten grain boundaries. We plan to address both the quantitative effect of the hydrogen on mobility and the mechanisms controlling mobility. The mobilities are provided to improve the parameterization of the recrystallization model being developed by the Marian group at the University of California, Los Angeles. This approach should provide new guidance on tungsten behavior in first-wall applications.

Acknowledgments

This work was performed under the auspices of the U.S. Department of Energy (US DOE) by Lawrence Livermore National Laboratory under Contract DE-AC52-07NA27344. This material is based upon work supported by the US DOE, Office of Science, Office of Fusion Energy Sciences.

References

[1] T. Frolov et al., Nature Commun. 4, 1899 (2013).
[2] T. Meiners, T. Frolov, R. E. Rudd, G. Dehm, and C. H. Liebscher, Nature 579, 375-378 (2020).
[3] Q. Zhu, A. Samanta, B. Li, R. E. Rudd, T. Frolov, Nature Commun. 9, 467 (2018).
[4] T. Frolov et al., Nanoscale 10, 8253 (2018).
[5] T. Frolov, Q. Zhu, T. Oppelstrup, J. Marian, and R. E. Rudd, Acta Mater. 159, 123-134 (2018).
[6] R. Freitas, R. E. Rudd, M. Asta, and T. Frolov, Phys. Rev. Mater. 2, 093603 (2018).
[7] I. S. Winter, T. Oppelstrup, T. Frolov, and R. E. Rudd, Acta Mater. 237, 118067 (2022).
[8] I. S. Winter, T. Oppelstrup, T. Frolov, and R. E. Rudd, Phys. Rev. Lett. 128, 035701 (2022).
[9] A. P. Thompson et al., Computer Physics Commun. 271, 108171 (2022).
[10] X. Zhou et al., Acta Mater. 49, 4005-4015 (2001).
[11] A. Qiu, I. Chesser, and E. Holm, Acta Mater. 257, 119075 (2023).

9.2 PREDICTIVE MODELING OF He BUBBLE ACCUMULATION IN NANOSTRUCTURED FERRITIC ALLOYS—K. Pitike, W. Setyawan (Pacific Northwest National Laboratory)

SUMMARY

The overall objective of this work is to develop a predictive model of helium bubble accumulation and distribution in irradiated nanostructured ferritic alloys under relevant fusion environments. As a first step, we have developed an accurate Fe-He machine learning potential (version (MLP)1) based of deep neural network that is intended to study defect binding in He clusters and small He_nV bubbles in pure BCC-Fe. This work was recently published in J. Nucl. Mater. [1]. In this reporting period, we employ MLP1 to calculate the activation energies of trap-mutation ((TM), a process in which an over-pressurized He cluster/bubble releases the pressure by creating one or more vacancies) in He_nV bubbles and He_n clusters. These activation energies are intended to be used in kinetic Monte Carlo or rate theory simulations to study the growth of He bubbles. We are actively writing a manuscript on the kinetics of TM, expected to be submitted in the next quarter. In addition, we are extending MLP1 to describe larger bubbles, by training MLP2 on configurations, with bubbles containing 1-9 vacancies and He gas interacting with various BCC-Fe surface terminations.

PROGRESS ANS STATUS

Experimental Procedure

Modelling trap-mutation in He_n clusters and He_nV bubbles in BCC-Fe with MLP1

Here we report our work on utilizing the previously developed Fe-He MLP [1] to study the self-trapping of He_n clusters and trap-mutation of He_nV bubbles.

It is well known that He atoms strongly bind with vacancies. In our previous work [1], through density functional theory (DFT) calculations, we have shown that a monovacancy at T=0 K, can accommodate up to 16 He atoms. The $He_{17}V$ bubble spontaneously trap-mutates into a $He_{17}V_2$ + SIA complex. We define a critical ratio of the number of He to vacancies (N_{He}/N_V) as the maximum ratio that can be accommodated by the cluster or bubble. Trap-mutation occurs because the pressure inside the bubble exceeds the surface tension plus the critical shear stress of the matrix. As temperature increases, the matrix material softens. Thus, it is expected that the critical ratio would decrease. A question arises: can a bubble trap-mutate when its' He to vacancy ratio is lower than the critical ratio? The developed MLP1 allows us to investigate this question through molecular dynamics simulations. Since MLP1 is trained with accurate DFT data, we expect the effective kinetics estimated using MLP1 to have near DFT accuracy. Here, we study the thermal stability of He_nV bubbles. Indeed, we find that bubbles with N_{He}/N_V lower than 16 can trap-mutate at elevated temperatures. Moreover, we find that trap-mutation reaction is a thermally activated process [2], with an associated activation energy barrier. We perform thermalization simulations for He_nV bubbles, where n=1 to 16, and record the time (Δt) needed to observe a trap-mutation event for each thermalization temperature. Figure 1 shows the plot of $\log(1/\Delta t)$ as a function of inverse temperature for these bubbles. The activation energy is then calculated using the Arrhenius equation:

$$k_B \log\left(\frac{1}{\Delta t}\right) = -E_a\left(\frac{1}{T}\right) + k_B \log(A)$$

k_B is the Boltzmann constant, Δt is the lifetime of a He_nV bubble before it trap mutates, E_a is the activation energy of the trap mutation reaction, T is the temperature of the system, A is the temperature independent preexponent factor which represents the attempt frequency of the trap-mutation event.

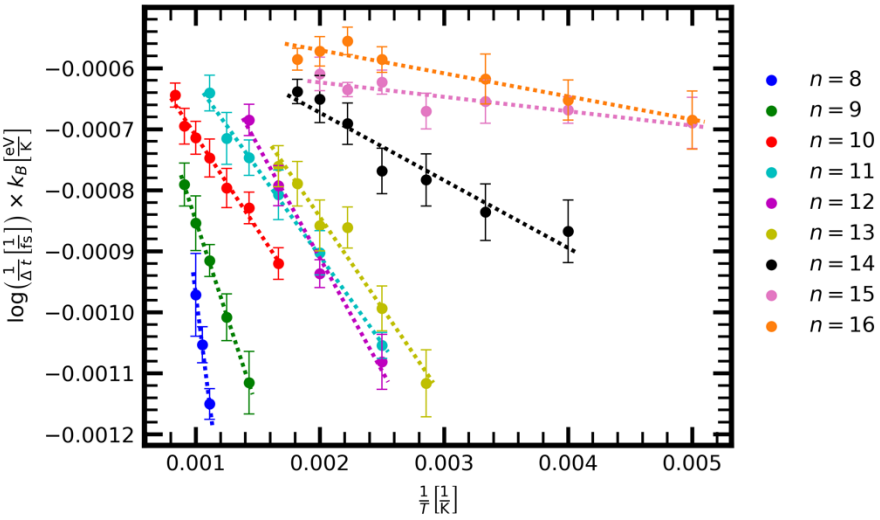

Figure 1. Arrhenius plot for the trap-mutation reactions of He$_n$*V* bubbles. The data is plotted in colored circles with associated linear fits plotted in dotted lines of same colors.

Hence, the slope of the lines in Figure 1 is the activation energy of trap mutation reactions for *n*=8 to *n*=16 bubbles. The error bars represent standard deviations (using sample variance), resulting from 10 simulations. Since the MLP is trained using the physically accurate DFT calculations, physical properties estimated employing MLP are expected to have near-DFT accuracy. These activation energies can be used to investigate the He bubble growth in ferritic steels through mesoscale kinetic Monte Carlo or rate theory simulations with high accuracy.

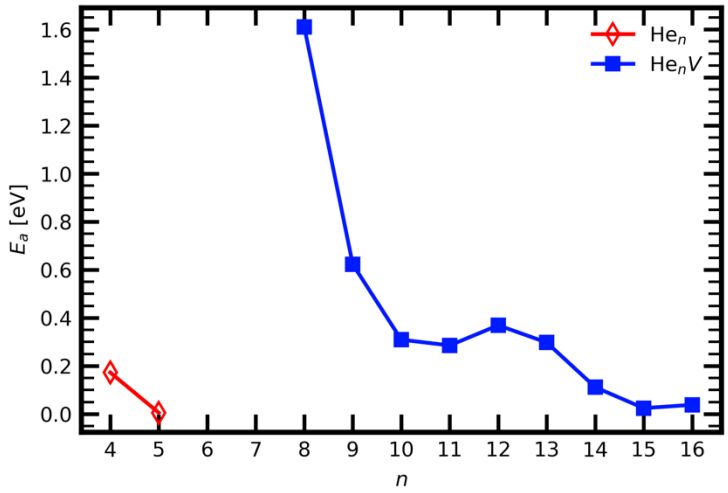

Figure 2. The activation energy, E_a values plotted against the number of He atoms, *n*, in He$_n$ cluster (red empty diamonds) and He$_n$*V* bubbles (blue filled squares).

Figure 2 presents the values of E_a plotted against the number of He atoms, *n*, in He$_n$ clusters and He$_n$*V* bubbles. For both clusters and bubbles, we find that E_a decreases with the number of He atoms. The activation energy in the case of bubbles non-monotonously decreases from 1.611 eV (*n*=8) to 0.038 eV (*n*=16). We find that E_a increases for *n*=12 and 16, compared to *n*=11 and 15, respectively. For bubbles with *n*<8, a TM event was not observed within a timespan of 3 ns, and 10 sample simulations. Similarly in the case of He$_n$ clusters, we find that the E_a decreases from 0.173 eV (*n*=4) to 0.005 eV (*n*=5).

We also find a major difference between the thermal stability of bubbles and clusters. All He_nV bubbles are stable, for T<1200 K, relative to dissociation of the bubble into [$He_{n-1}V$ + He_{tet}] complex. However, for T≥1000 K we find that He_3 and He_2 clusters dissociate into smaller [He_2 + He_{tet}] or [He_{tet} + He_{tet}] complexes, respectively.

Developing Fe-He machine learning potential to describe thermodynamics of He clusters and all He bubbles

Here we report our work on extending the Fe-He MLP1 to not only describe the thermodynamics of He_n clusters and small He_nV bubbles but also for large He_nV_m bubbles, that may contain more than one vacancy. In our previous report, we have presented the binding energies of He with He_nV_2 bubbles. In this report, we extend the binding energies to He_nV_3 bubbles. We have also trained MLP2 on DFT data, encompassing configurations from AIMD, He_nV_m bubbles, for m=1 to 3, several surface terminations of BCC-Fe, and He-gas interacting with surfaces. We also present the capability of MLP2 to accurately predict the binding energies of He_nV_m bubbles, for m=1 to 3.

Accurate estimation of the binding energies of He or vacancy (V) with He_n cluster or He_nV_m bubble is crucial to advance the fundamental understanding of radiation damage in nano structured ferritic alloys. First-principles based DFT is typically used to calculate the accurate binding energies. However, calculating the accurate binding energies for large He_nV_m bubbles is prohibitively expensive due to the computational cost of large supercells. Hence, a machine learning potential – trained on DFT data, obtained from relevant configurations – could be used to calculate accurate binding energies at a much smaller cost. In our previous work [1] we have developed a first Fe-He MLP to accurately describe the binding energies of He with He_n clusters and small He_nV bubbles with only one vacancy. Extending the MLP's ability to accurate estimation of binding energies for large He_nV_m bubbles can be achieved by further training of the MLP with atomic configurations that represent larger He bubbles. So far, we have sampled the atomic configurations of He_nV_m, m=1 to 9, bubbles using DFT. We have used m=1 to 3 bubbles for the training and reserved m=4 to 9 for testing. In the case on bubbles containing more than 1 vacancy, we have used a 5x5x5 supercell. We have also sampled slab configurations in which the vacuum is filled with varying concentration of He gas. The slab configurations are intended to mimic He-matrix interaction in large bubbles.

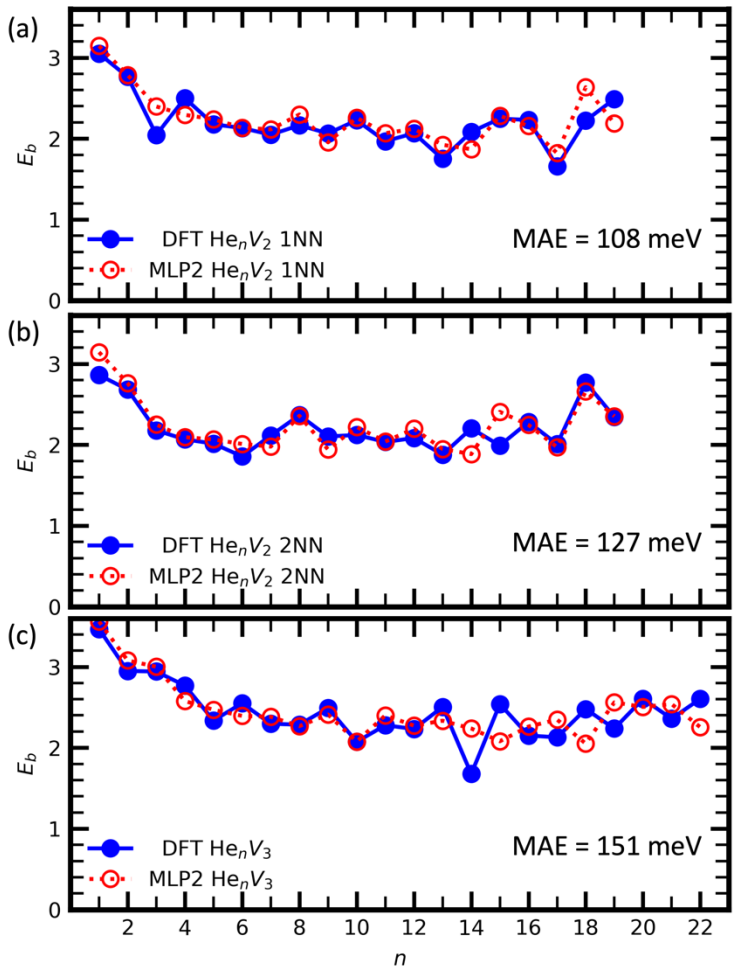

Figure 3. Binding energies of (a) He$_{n-1}V_2$ 1NN bubble + He, (b) He$_{n-1}V_2$ 2NN bubble + He, and (c) He$_{n-1}V_3$ bubble + He. The solid blue circles and empty red circles are calculated from DFT and MLP2, respectively. The mean absolute errors in predicting binding energies by MLP2 is given in each panel.

Figure 3 presents the values of binding energies of (a) He$_{n-1}V_2$ 1NN bubble + He, (b) He$_{n-1}V_2$ 2NN bubble + He, and (c) He$_{n-1}V_3$ bubble + He. The defect reactions to form larger bubbles and the equations to calculate their binding energies are:

Defect reactions:

$$\mathrm{He}_{n-1}V_2^{1\mathrm{NN}} + \mathrm{He} \rightarrow \mathrm{He}_n V_2^{1\mathrm{NN}}$$
$$\mathrm{He}_{n-1}V_2^{2\mathrm{NN}} + \mathrm{He} \rightarrow \mathrm{He}_n V_2^{2\mathrm{NN}}$$
$$\mathrm{He}_{n-1}V_3 + \mathrm{He} \rightarrow \mathrm{He}_n V_3$$

Binding energy equations:

$$E_b[\mathrm{He}_{n-1}V_2^{1\mathrm{NN}} + \mathrm{He}] = E_{\mathrm{DFT}}[\mathrm{He}_{n-1}V_2^{1\mathrm{NN}}] + E_{\mathrm{DFT}}[\mathrm{He}_{\mathrm{tet}}] - E_{\mathrm{DFT}}[\mathrm{He}_n V_2] - E_{\mathrm{DFT}}[\mathrm{Fe}_{\mathrm{pristine}}]$$
$$E_b[\mathrm{He}_{n-1}V_2^{2\mathrm{NN}} + \mathrm{He}] = E_{\mathrm{DFT}}[\mathrm{He}_{n-1}V_2^{2\mathrm{NN}}] + E_{\mathrm{DFT}}[\mathrm{He}_{\mathrm{tet}}] - E_{\mathrm{DFT}}[\mathrm{He}_n V_2] - E_{\mathrm{DFT}}[\mathrm{Fe}_{\mathrm{pristine}}]$$
$$E_b[\mathrm{He}_{n-1}V_3 + \mathrm{He}] = E_{\mathrm{DFT}}[\mathrm{He}_{n-1}V_3] + E_{\mathrm{DFT}}[\mathrm{He}_{\mathrm{tet}}] - E_{\mathrm{DFT}}[\mathrm{He}_n V_3] - E_{\mathrm{DFT}}[\mathrm{Fe}_{\mathrm{pristine}}]$$

$E_b[\mathrm{He}_{n-1}V_m + \mathrm{He}]$ is the binding energies of He with $\mathrm{He}_{n-1}V_m$ bubble to form a bigger He$_n$V$_m$ bubble. The superscripts 1NN and 2NN represent the relative first and second nearest neighboring vacancies in a

divacancy cluster. $E_{\mathrm{DFT}}[defect]$ represents the DFT total energy of a defect embedded in BCC-Fe matrix. $\mathrm{He}_{\mathrm{tet}}$, $\mathrm{Fe}_{\mathrm{pristine}}$ represents He present at thermodynamically stable tetrahedral interstitial position and ideal BCC-Fe structures, respectively.

For He_nV_2 bubble, 1NN and 2NN configurations are thermodynamically stable for *n*=1 to 17, and *n*=0,18,19. The binding energies of He with $He_{n-1}V_2$ bubble is shown in Figure 3 where the divacancy configuration is (a) 1NN, and (b) 2NN. We find that the MLP2 can predict the binding energies accurately with MAE = 101, 108, 127, and 151 meV for He binding with $\mathrm{He}_{n-1}V$, $\mathrm{He}_{n-1}V_2^{1\mathrm{NN}}$, $\mathrm{He}_{n-1}V_2^{2\mathrm{NN}}$, and $\mathrm{He}_{n-1}V_3$, respectively. These MAE values are 2 to 3 times smaller compared to the semi-empirical potentials [1]. Furthermore, we generally find that the binding energies of He with He_nV_m bubble increases with the value of *m*, for *m* ranging between 0 and 3. Simply put, He binding with a bubble containing a greater number of vacancies is thermodynamically stable.

Acknowledgments

This research was supported by the U.S. Department of Energy (US DOE), Office of Science, Office of Fusion Energy Sciences, through Contract No. AT2030110-13784 and was performed at the Pacific Northwest National Laboratory (PNNL), which is operated by Battelle for the US DOE under Contract No. DE-AC05-76RL0-1830. The research was performed using resources available through Research Computing at PNNL.

References

[1] K. C. Pitike, W. Setyawan, "Accurate Fe–He machine learning potential for studying He effects in BCC-Fe" J. Nucl. Mater. 574 (2023) 154183.

[2] J. Boisse, C. Domain, C.S. Becquart, “Modelling self trapping and trap mutation in tungsten using DFT and Molecular Dynamics with an empirical potential based on DFT”, J. Nucl. Mater. 455 (2014) 10-15.

10. IRRADIATION & TESTING ANALYSIS, METHODS, EXPERIMENTS, AND SCHEDULES

10.1 DETERMINATION OF TRANSMUTATION ISOTOPIC PRODUCTS FROM IRRADIATED TUNGSTEN—X.-Y. Yu, Y-R. Lin, L. Howard, Y. Katoh (Oak Ridge National Laboratory)

OBJECTIVE

The objective of this project is to determine the transmutation products of tungsten (W) post neutron irradiation exposure using high resolution time-of-flight secondary ion mass spectrometry (ToF-SIMS).

SUMMARY

We performed detailed ToF-SIMS spectral analysis of irradiated W specimens that were exposed to different doses to 1) demonstrate that SIMS has sufficient mass resolution to resolve isotopic peaks of W, rhenium (Re), and osmium (Os) that have close mass to charge ratios (*m/z*) and 2) SIMS detection is sensitive to obtain chemical makeup information and provide insights into transmutation pathways.

PROGRESS AND STATUS

Introduction

To comprehend the effects of neutron spectrum on clustering and precipitation in neutron-irradiated W specimens, a comprehensive ToF-SIMS investigation was conducted. This study involved examining two high-purity single-crystal W samples, each with a purity exceeding 99.99 wt.%. The TE01 and W18 specimens were subjected to different neutron spectra – shielded and unshielded, respectively. The W18 sample was irradiated at a temperature of 700°C, while the TE01 sample was irradiated at 753°C. The neutron fluence was consistently maintained at a level of 2.2-3.5x10^{25} n/m² (equivalent to 0.6-0.7 dpa).

Experimental Procedure

Materials

Post-irradiation, sample preparation took place in the Low Activation Materials Development and Analysis (LAMDA) laboratory at Oak Ridge National Laboratory (ORNL). For SIMS analysis, focused ion beam (FIB) techniques were employed to prepare lift-out bulk samples with dimensions of 20x15x10 μm^3. The sample was protected by capping it with platinum (Pt) before milling. The lift-out process involved initial milling and coarse surface polishing using a FEI Quanta 3D Dual Beam system operating at 30 kV. The lift-out materials were then welded with Pt deposition to either a molybdenum FIB lift-out grid or a silicon wafer with dimensions of 1x1 cm.

A ToF-SIMS V spectrometer (IONTOF GmbH, Münster, Germany) was used to analyze irradiated W samples. The SIMS analysis was performed using a 30 keV pulsed bismuth (Bi_3^+) primary beam ion under high vacuum of 4.8×10^{-8} mbar during measurements. The Bi_3^+ primary ion beam scanned over a 150 × 150 μm^2 area with a resolution of 256 by 256 pixels. The spectrum was acquired for 10 scans. The primary ion doses in all measurements were lower than the static limit, and the damage artifacts resulting from the Bi_3^+ primary ion beam was negligible. The mass resolutions of the detected peaks in the SIMS spectrum are in the range of 8000 to 11,000, varying from sample to sample depending on the sample roughness. Mass spectra were calibrated using CH^+, CH_2^+, Si^+, W^+, and Bi^+ in the positive ion mode using the SurfaceLab software version 7.0.

Results

Identification of W transmutation products

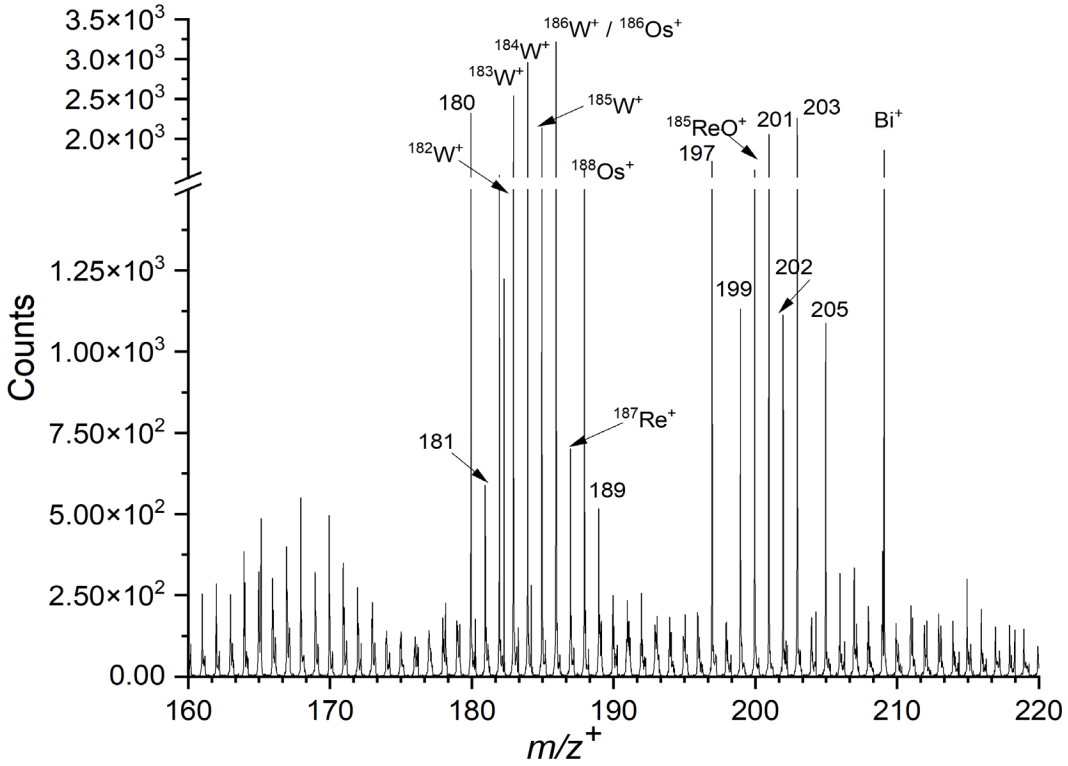

Figure 1. The ToF-SIMS spectrum of the W18 irradiated tungsten sample in the m/z^+ range of 160 – 220 in the positive ion mode.

Figure 1 depicts the ToF-SIMS spectrum of the W18 irradiated W sample in the m/z^+ range of 160 – 220 in the positive ion mode. The W isotopic peaks are evident including, m/z^+ 181.9457 $^{182}W^+$, m/z^+ 182.9471 $^{183}W^+$, m/z^+ 183.9468 $^{184}W^+$, m/z^+ 184.9489 $^{185}W^+$, m/z^+ 186.9566 $^{187}Re^+$, m/z^+ 187.9511 $^{188}Os^+$, m/z^+ 199.9575 $^{185}ReO^+$, and m/z^+ 209.9835 Bi^+. The peak of m/z^+ 209.9835 Bi^+ comes from the bismuth primary ion beam and it is used as a reference peak in calibration. The peak of m/z^+ 185.9463 can be assigned as either $^{186}W^+$ with a theoretical m/z^+ (m/z_{the}) of 185.95436 or $^{186}Os^+$ with a theoretical m/z^+ of 185.95384. The relative mass accuracy defined as $\Delta m=(m/z_{obs} - m/z_{the})/m/z_{the} \times 10^6$ (in ppm), where m/z_{obs} denotes the observed m/z in SIMS. Using this formula, the Δm is 32.5 ppm if the peak is assigned as $^{186}W^+$ or 29.8 ppm if the peak is assigned as $^{186}Os^+$. While acceptable, further refinement could involve modeling to effectively distinguish the two isotopic peaks with close mass to charge ratios. The preliminary SIMS analysis illustrates that the W isotopic peaks as well as transmutation product peaks, such as Re and Os, are observable with good mass resolution. Initial comparisons between the W18 and T01 samples show that W18 has higher abundances of W, Re, and O products than T01. This finding is in line with our previous scanning transmission electron microscopy (STEM) energy dispersive X-ray spectroscopy (EDS) results, which suggest that W18 (with an unshielded neutron spectrum) contains a larger amount of nuclear transmutation products compared to T01 (with a shielded neutron spectrum).

Future Work

Additional analysis and peak identification are currently ongoing. Results from the negative mode SIMS spectra will be reported.

11. IRRADIATION & TESTING METHODS, EXPERIMENTS AND SCHEDULES

11.1 HFIR IRRADIATION EXPERIMENTS—C. On (Oak Ridge National Laboratory)

OBJECTIVE

The goal of this report is to describe the progress of the neutron irradiation experiments that were performed in the High Flux Isotope Reactor (HFIR) and the operating status of HFIR.

SUMMARY

During the six-month period starting from January 1st to June 30th, 2023, a total of thirty-eight rabbit capsules continued their irradiation. The cycle 501 will be completed on June 17th, at which point two capsules will be removed from HFIR.

PROGRESS AND STATUS

Neutron irradiation experiments were performed in support of the research and development of fusion reactor materials using various materials irradiation facilities in the HFIR. The reactor operating history for the period from January 1-June 30, 2023, is detailed in Table 1.

Table 1. HFIR operating record for the semi-annual FY2023

Cycle Number	Cycle End Date	Power (MWD)
501	June 17	2115.76

All the fusion materials program irradiation experiments performed during this period (FY2023) used the nominally two-inch rabbit capsules, with no full-length target rod nor instrumented reflector position capsules within that period. Thirty-eight target-zone rabbit capsules remain in the reactor to complete their scheduled irradiations. Table 2 lists the capsules that were removed from HFIR at the end of cycle 501. The capsules listed in Table 3 were inserted either during or before FY2023 and will continue in FY2023 and beyond. Tables 2 and 3 give condensed information on the material, specimen type, temperature, fluence, and period of irradiation.

Table 2. The rabbit capsules removed from HFIR at the end of cycle 501

Experiment Designation	Primary Materials	Specimen Types	Irradiation Temperature (°C)	Max Exposure (dpa)	Number of Reactor Cycles	HFIR Cycles Start – End
FR51	Joint Tungsten Alloy	Disc (D3)	300	0.6	3	499 - 501
FR52	Joint Tungsten Alloy	Disc (D3)	500	0.6	3	499 - 501

Table 3. The HFIR fusion materials program rabbit capsules to continue irradiation in FY2023

Experiment Designation	Primary Materials	Specimen Types	Irradiation Temperature (°C)	Max Exposure (dpa)	Number of Reactor Cycles	HFIR Cycles Start – End
FH11	F82H-IEA / F82H-mod3	Tensile	300	80	46	496 - 541
FH12	F82H-IEA / F82H-mod3	Tensile	400	80	46	496 - 541

FH13	F82H-IEA / F82H-mod3	Tensile	500	80	46	496	-	541
FH21	F82H-IEA / F82H-mod3	Bend Bar	300	80	55	496	-	550
FH22	F82H-IEA / F82H-mod3	Bend Bar	300	80	55	496	-	550
FH23	F82H-IEA / F82H-mod3	Bend Bar	400	80	55	496	-	550
FH24	F82H-IEA / F82H-mod3	Bend Bar	400	80	55	496	-	550
FH25	F82H-IEA / F82H-mod3	Bend Bar	500	80	48	496	-	543
FH26	F82H-IEA / F82H-mod3	Bend Bar	500	80	48	496	-	543
FH31	F82H-IEA / F82H-mod3	Tensile	300	50	29	500	-	528
FH32	F82H-IEA / F82H-mod3	Tensile	400	50	29	500	-	528
FH33	F82H-IEA / F82H-mod3	Tensile	500	50	29	500	-	528
FH41	F82H-IEA / F82H-mod3	Bend Bar	300	50	35	500	-	534
FH42	F82H-IEA / F82H-mod3	Bend Bar	300	50	35	500	-	534
FH43	F82H-IEA / F82H-mod3	Bend Bar	400	50	29	500	-	528
FH44	F82H-IEA / F82H-mod3	Bend Bar	400	50	29	500	-	528
FH45	F82H-IEA / F82H-mod3	Bend Bar	500	50	29	500	-	528
FH46	F82H-IEA / F82H-mod3	Bend Bar	500	50	29	500	-	528
FMP07	F82H	Tensile	300	20	21	487	-	507
FMP08	F82H	Tensile	300	80	45	487	-	531
FMP11	F82H	Tensile	385	20	21	488	-	508
FMP12	F82H	Tensile	385	80	45	488	-	532
FMP14	F82H	Tensile	525	20	21	484	-	504
FMP17	F82H	Tensile/MPC*	650	80	45	484	-	528
FMP22	F82H	Bend Bar	300	20	21	488	-	508
FMP23	F82H	Bend Bar	300	80	45	488	-	532
FR12	Joint Tungsten Alloy	Disc (D6)	300	1.2	6	497	-	502
FR51	Joint Tungsten Alloy	Disc (D3)	300	0.6	3	499	-	501
FR52	Joint Tungsten Alloy	Disc (D3)	500	0.6	3	499	-	501
JCR11-03	SiC/SiC	Mini Bend Bar	950	200	100	487	-	586
JCR11-05	SiC/SiC	Mini Bend Bar	950	200	115	444	-	568
JCR11-08	SiC/SiC	Mini Bend Bar	950	200	115	444	-	560
JCR11-11	SiC/SiC	Mini Bend Bar	950	100	55	448	-	524
SCF4	SiC/SiC	Miniature Flexure Bar	250	100	90	457	-	547
SCF5	SiC/SiC	Miniature Flexure Bar	250	200	45	457	-	511
SCF8	SiC/SiC	Miniature Flexure Bar	600	100	45	457	-	502

SCF9	SiC/SiC	Miniature Flexure Bar	600	200	90	457	-	548
SCF11	SiC/SiC	Miniature Flexure Bar	950	100	57	458	-	517

*MPC= Multi-Purpose Coupon